LEABHARLANN CHOLÁISTE NA TRÍONÓIDE, BAILE ÁTHA CLIATH | TRINITY COLLEGE LIBRARY DUBLIN
Ollscoil Átha Cliath | The University of Dublin

Terms and Conditions of Use of Digitised Theses from Trinity College Library Dublin

Copyright statement

All material supplied by Trinity College Library is protected by copyright (under the Copyright and Related Rights Act, 2000 as amended) and other relevant Intellectual Property Rights. By accessing and using a Digitised Thesis from Trinity College Library you acknowledge that all Intellectual Property Rights in any Works supplied are the sole and exclusive property of the copyright and/or other IPR holder. Specific copyright holders may not be explicitly identified. Use of materials from other sources within a thesis should not be construed as a claim over them.

A non-exclusive, non-transferable licence is hereby granted to those using or reproducing, in whole or in part, the material for valid purposes, providing the copyright owners are acknowledged using the normal conventions. Where specific permission to use material is required, this is identified and such permission must be sought from the copyright holder or agency cited.

Liability statement

By using a Digitised Thesis, I accept that Trinity College Dublin bears no legal responsibility for the accuracy, legality or comprehensiveness of materials contained within the thesis, and that Trinity College Dublin accepts no liability for indirect, consequential, or incidental, damages or losses arising from use of the thesis for whatever reason. Information located in a thesis may be subject to specific use constraints, details of which may not be explicitly described. It is the responsibility of potential and actual users to be aware of such constraints and to abide by them. By making use of material from a digitised thesis, you accept these copyright and disclaimer provisions. Where it is brought to the attention of Trinity College Library that there may be a breach of copyright or other restraint, it is the policy to withdraw or take down access to a thesis while the issue is being resolved.

Access Agreement

By using a Digitised Thesis from Trinity College Library you are bound by the following Terms & Conditions. Please read them carefully.

I have read and I understand the following statement: All material supplied via a Digitised Thesis from Trinity College Library is protected by copyright and other intellectual property rights, and duplication or sale of all or part of any of a thesis is not permitted, except that material may be duplicated by you for your research use or for educational purposes in electronic or print form providing the copyright owners are acknowledged using the normal conventions. You must obtain permission for any other use. Electronic or print copies may not be offered, whether for sale or otherwise to anyone. This copy has been supplied on the understanding that it is copyright material and that no quotation from the thesis may be published without proper acknowledgement.

A Quasi Three Dimensional Numerical Model for Terrain Propagation

by

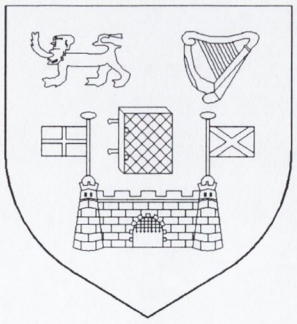
Ronan Bradley

Master of Science

A Thesis submitted to
The University of Dublin
for the degree of

Doctor of Philosophy

Department of Electrical and Electronic Engineering,
University of Dublin,
Trinity College



October, 2001

TRINITY COLLEGE
10 OCT 2002
LIBRARY DUBLIN
Thesis
6960

Declaration

This thesis has not been submitted as an exercise for a degree at any other University. Except where otherwise stated, the work described herein has been carried out by the author alone. This thesis may be borrowed or copied upon request with the permission of the Librarian, University of Dublin, Trinity College. The copyright belongs jointly to the University of Dublin and Ronan Bradley.

Signature of Author ..... R. Bradley .....

Ronan Bradley October, 2001

Summary

Numerical modeling techniques provide a powerful tool for the optimization of modern land mobile radio communications systems. Mathematically, propagation over terrain constitutes a three-dimensional vector field problem. However, the majority of conventional numerical modeling techniques make use of a two dimensional terrain approximation, leading to a scalar field representation, and as a consequence, make no allowance for depolarization phenomena.

This thesis introduces a novel geometrical approximation to the terrain surface, incorporating terrain gradients transverse to the direction of propagation, in a *quasi* three-dimensional approach. The propagation problem is solved for the approximate geometry by application of the Magnetic Field Integral Equation. An original approximate boundary condition is developed for fields of mixed polarization. The result is a method capable of predicting *copolar* losses through depolarization, and modeling the additional *cross-polar* field.

The method is tested against the Uniform Theory of Diffraction and shows excellent agreement. For terrain, predictions are consistent with measured *copolar* data, and indicate significant depolarizing effects over certain topographies. The new method is successfully combined with the Fast Far Field Approximation, achieving considerable reductions in run time, with numerical complexity being of the same order as for conventional two dimensional models. Several suggestions for further work are made.

Acknowledgements

I would like to acknowledge the encouragement, support, and patience of my supervisor Dr. Peter J Cullen, and wish him well in the future.

I would also like to thank the friends and colleagues with whom I shared many good times in the telecoms lab. I thank the EM axis that was Conor, Eamon and Luca (CEL), who were a constant source of counsel and technical assistance, and as readily a source of good humour, mindless diversion, reckless theoretical conjecture, and idle chin-wagging.

Others have been a source of good companionship in the lab and among these I must name Liam, who was gracious enough to endure our juvenile humour, the peerless Maxim, Alex, Derek, Irina, Eamon O'N, and going back some time Eugene and Liam, Sylvia, Peter, and Ken, and more recently my friend and night shift companion, Antanasis. Special thanks also go to Mark and Shane, whose ingenuity with ailing electronic appliances has never failed me.

There are others who I have known on a more fleeting basis, including the party posse at Aras an Phiarsaigh, and among the staff of the Electronic Engineering Dept., and I acknowledge them also.

Last but certainly not least, I thank Hannah for putting up with moods and absences over the last couple of years.

Contents

1 Introduction **1**

1.0.1 Overview 4

1.0.2 Key Contributions 6

2 Theoretical Foundations **8**

2.1 Review of basic electromagnetics 8

2.2 Volume Equivalence Principle 11

2.3 Surface Equivalence Principle 15

2.3.1 The Extinction Theorem 19

2.3.2 The Perfect Electrical Conductor 20

2.3.3 The Impedance Boundary 21

2.3.4 The Interior Field Equation 22

2.3.5 Homogeneous Bodies 24

3 3D Terrain Problem **28**

3.0.6 Topographical Propagation Effects 29

3.0.7 Hardware 31

3.0.8 Frequency Characteristics 31

3.0.9 Scalar/Vector Model 32

3.1 Empirical Methods 32

3.2 Geometrical Methods 33

3.2.1 Reflection 33

3.3 Non Planar Features 34

3.3.1 Geometrical Theory of Diffraction 35

3.4 Micro-cell 38
3.4.1 Curved Surface Diffraction 38
3.5 Fresnel/Kirchhoff Theory 40
3.5.1 Fresnel Zones 43
3.6 General Examples 46
3.6.1 Example Method 1 48
3.6.2 Example Method 2 49
3.7 Differential Equation Methods 50
3.7.1 Finite Element Method 50
3.7.2 Finite Difference Methods 51
3.7.3 The Parabolic Equation 51
3.8 3D Integral Equation 54
3.9 The Method of Moments 55
3.9.1 Point matching 57
3.9.2 Subsectional basis functions 57
3.10 Moment Method Applied to the
3D Vector Equation 57
3.10.1 The Fast Far Field Approximation 60
3.10.2 FMM 62
3.10.3 Low Resolution Methods 63
3.11 Machine Learning 64

4 Polarization Modes and the Corrugated Terrain Approximation 66

4.1 Numerical Comparison for a Planar Boundary 70
4.1.1 TM_y 71
4.1.2 TE_y 71
4.2 Reflection Coefficients 73
4.2.1 TM_y 75
4.2.2 TE_y 76
4.3 The PEC Boundary Condition 80
4.4 The Impedance Boundary Condition 80

4.5 Numerical Comparison 81
4.5.1 The TM_y Mode 81
4.5.2 TE_y : Coupled Equations v PMC 85
4.5.3 TE_y : Coupled Equations v Impedance 85
4.6 Discussion 87

5 A Quasi-3D Approach for PEC Surfaces. 88
5.1 Introduction 88
5.2 Analytical Transverse Integration for a
Point Source over a PEC Surface 89
5.3 New Terrain Model 94
5.4 Analytical Integration for Inclined Segments 95
5.5 Off Axial Scattering 99
5.5.1 Evaluation of Path Loss 104
5.6 Comparison with UTD 105
5.7 Terrain Predictions 110
5.8 Discussion 113

6 A Quasi-3D Approach for General Terrain. 114
6.1 The 3D MFIE 115
6.2 Incorporation of Reflection Coefficients and Boundary Conditions in 3D 116
6.3 Decoupling the 3DMFIE 124
6.4 Numerical Results for PEC/PMC Terrain 130
6.5 A PMC/Impedance Boundary Condition 136
6.6 Numerical Results for a PEC/Impedance
Terrain Approximation 137
6.6.1 Variation of Material Parameters 142
6.6.2 Definition of Incidence Plane 146
6.6.3 Field Components 149
6.7 Discussion 151

7 Application of the Fast Far Field Approximation to Q3D **153**

7.1 Formulation 154

7.2 Results 156

7.3 Conclusions 167

8 Discussion **170**

Chapter 1

Introduction

The principal concern of this thesis is the numerical treatment of large scale electromagnetic propagation problems. The class of problem tackled is that involving propagation over smoothly undulating surfaces bounding a lossy dielectric material distribution, embedded in a homogeneous space. As such these problems may be used to describe ultra high frequency (UHF) wave propagation over smoothly undulating terrain. Such problems are of great importance in channel characterization and the optimization of coverage in mobile communications and radio frequency planning.

By large, we mean problems of $\mathcal{O}(10) - \mathcal{O}(10^5)$ wavelengths. For such problems we are presented with a choice of either empirical methods [24], based on the results of field measurements for test profiles, or deterministic approaches utilizing detailed knowledge of the terrain profile, and the direct application of Electromagnetic theory. In the empirical approach simple formulae are used to give the path loss directly given input parameters such as transmitter and receiver heights, frequency, degree of undulation, and vegetation.

Deterministic approaches incorporate the physical variations in terrain height. This may be done using a high resolution discretization of the terrain, or by replacing the terrain itself with an approximate representation of canonical shapes. In the latter approach, scattering from these canonical forms is given using the theories of Geometrical Optics(GO), and the Uniform Geometrical Theory of Diffraction(UTD) [47]. The accuracy of the resulting solution may be increased by adding

detail to this representation. This also increases its complexity.

The preferred method of this thesis is deterministic in nature. Maxwell's equations for the field in the presence of a given material distribution are cast in the form of a surface integral equation. Replacing the volume problem with a surface problem allows for a considerable reduction in the number of problem unknowns. Further gains may be made using approximations to the surface boundary condition, height variation, and interaction terms, making the solution of large problems computationally feasible, while preserving the necessary level of accuracy. However, all conventional approaches to large scale, full wave, three dimensional propagation problems are severely limited by the heavy numerical burden associated with such computations. With such restrictions, terrain type problems are usually simplified using a corrugated two dimensional approximation to the surface. Such models are accurate to first order for smooth terrain and are conveniently solved for horizontal electric polarizations (TM_y) which have the benefit of allowing the surface to be represented by a perfect electrical conductor (PEC) for low angles of incidence. For horizontal magnetic polarizations (transverse electric - TE_y), the surface may be modeled as a perfect magnetic conductor (PMC) at grazing incidence, and for a wider range of propagation angles, may be modeled using the impedance boundary condition approximation [69]. Scalar integral equations result in both cases, and much effort has been put into the rapid solution of such problems and a battery of numerical optimization techniques developed [9] [15] [33] [12]. Where a terrain is being modeled, small scale random roughness, and the presence of buildings or vegetation, are also neglected, introducing a further degree of approximation. Atmospheric effects such as precipitation or ducting will be neglected, and this approximation is adequate at UHF and VHF for ranges of the order of 10 kilometers. Ducting contributions may arise where strong vertical atmospheric permittivity gradients are present, at lower UHF, however, such cases will be exceptional, particularly over land.

Considering the radial path connecting transmitter and mobile receiver, the bulk of the scattered field at the receiver comes from the region of terrain lying on or near the radial. This corresponds to a generalization of Fermat's principle, where extrema

in the total path length from source, to scattering surface, to receiver, will usually lie on or near the radial. The scattered field may be approximated to first order by the contributions from within the first Fresnel zone (Chapter 5). The two dimensional corrugated surface approximation is therefore appropriate in cases where (a) the terrain height variation in the transverse direction is everywhere small in comparison to the width of the first Fresnel zone, so that the terrain may be considered invariant in that direction. Further it requires (b) that the terrain height variations are such that off radial reflection, diffraction, and multipath effects, may be neglected.

The main objective of this thesis is not to increase further the efficiency of the scalar, corrugated terrain methods, but instead to build in more of the detail of the original three dimensional vector integral equation. Specifically the goal is to investigate the effect of gradients in the terrain profile transverse to the radial plane of propagation from source to receiver. This may be seen as a relaxation of constraint (a) above. It will be demonstrated in this thesis that this additional component of the interaction can be modeled within the scope of the one dimensional integral encountered in the corrugated model. Hence solutions may be made at a similar level of computational cost for large range problems. The modeling of such additional detail requires the retention of a vector equation formulation. This reflects the fact that the dual polarizations interact with each other and are modeled simultaneously. In the new method, the attenuation of both *copolar* and *cross-polar* signals for a specified propagation channel will be evaluated with a first order correction for transverse slopes in the terrain. Evaluating the depolarized field means that we may predict a quantity that is neglected entirely in the corrugated terrain method. The *cross-polar* field is not regarded as lost signal but is predicted in an entirely deterministic fashion.

Comparisons are made between this novel integral equation formulation, and solutions attained for certain canonical problems. Additional comparisons are made with conventional integral equations methods, and experimental data. In all cases the new method is found to show excellent agreement with standard methods and measurement where direct comparison is possible, and in addition provides a valuable insight into *cross-polarization* effects.

The mixed polarization method is successfully combined with the fast far field approximation (FAFFA) [46] [9] method. This widely used technique allows the grouping of interactions at large separations using a plane wave approximation. Hence we may combine the additional subtlety of the Q3D model with the efficiency of the FAFFA, enabling a practical long range propagation tool.

Unlike the corrugated terrain method, in the Q3D approach currents giving rise to significant side scattering effects are evaluated although at the present time the side scattered fields themselves are not. This would involve evaluating the field scattered from the region about one radial, to other terrain radial observation points. It is suggested how this method might be extended to ascertain the effect of these additional contributions in an even fuller approximation to the three dimensional problem, thereby accounting for both diffraction and multipath.

1.0.1 Overview

This thesis may loosely be divided into three sections. Chapters 2 and 3 introduce the necessary theory and techniques required to tackle the problem of three dimensional lossy dielectric type surfaces, and some recently developed methods for treating 3D surfaces are discussed. Chapters 4 to 6 deal with the particular problems encountered in modeling perfectly reflecting and non perfectly reflecting surfaces using the surface integral equation, where initially transverse gradients neglected, and later, they are accounted for. Chapters 7 and 8 show how these methods may be refined and/or extended, and some conclusions are drawn. Specifically the chapters may be summarized as follows:

Chapter 2 presents well established axioms and relations of electromagnetism that will be required in the remainder of the thesis. Volume and surface equivalence principles for an arbitrary inhomogeneity are derived and the transformation to an integral equation form is demonstrated.

Chapter 3 outlines the various methods available for the solution of coupled vector equations in the presence of a three dimensional boundary. The strengths and

limitations of empirical, GO/GTD, differential equation and integral equation methods are discussed. The methods of geometrical optics and UTD provide rapid solutions but both the geometrical approximation to the terrain, and the high frequency approximation itself, can lead to errors. It is shown that while current differential equation methods may treat diffraction they as yet do not account for mixed polarization effects. Despite the fact that a full three dimensional integral equation may be easily defined, the prohibitive computational burden is demonstrated with a range[1] dependence of $\mathcal{O}(R^2 \log R^2)$ even employing optimal FAFFA and FMM algorithms. The limitations of all methods with regard to measuring multipath and propagation delay characteristics are discussed.

Chapter 4 introduces our principal numerical tool, the method of moments for the solution of problems reduced to a one dimensional integral over a radial terrain profile. The Coupled Integral equation solution is tested by comparison with the method of plane wave expansion given by Clemmow [13]. The conditions for applicability of the PMC and impedance boundary condition for vertical electric polarizations is discussed with reference to frequency and material parameters and propagation angle. The efficacy of the PEC approximation for horizontal TM_y polarizations, and the PMC and impedance boundary approximations for vertical polarizations, is demonstrated within the framework of the integral equation. Numerical results are presented in each case for a test profile.

Chapter 5 describes how the two dimensional integral equation formulation for TM_y problems may be derived from the three dimensional problem by analytical integration over the transverse direction. It is shown that this approach may be extended from the 2D case, to account for a piece-wise planar surface comprising strips inclined to the plane of propagation. Numerical comparisons are made with GTD solutions for a PEC wedge, and corrugated terrain methods. Comparison is also made with experimental data. Results are presented for some hypothetical terrain topographies where a realistic transverse gradient is

[1] Range measured in wavelengths

selected.

Chapter 6 extends the method to treat fields propagating over non PEC surfaces with mixed polarizations in the same quasi three dimensional approach. Making an approximation to the plane of incidence for impinging field components on a terrain segment, the total impinging field at a match point is resolved, allowing the application of separate PEC, and PMC/Impedance boundary conditions for horizontal and vertical polarizations respectively. It is shown that these polarization components may be recombined by superposition to allow calculation of the total field. Numerical results are presented making comparison with solutions using the PEC and impedance approximation. Comparison is again made with experimental data. The relation between frequency, material parameters, and precise topography and the effect on *copolar* and *cross-polar* fields is investigated.

Chapter 7 combines the new model with techniques developed for the rapid solution of integral equation problems. This renders the method suitable for practical problems. It is demonstrated that the quasi three dimensional method is equally well suited to such optimization techniques.

Chapter 8 outlines possible areas of advance for the method drawing on the principles of a full three dimensional integral equation method but retaining the powerful approximation of reducing the problem to radial segments.

1.0.2 Key Contributions

The principal original contributions of the author may be summarized:

- The representation of the surface as a set of inclined planar strips tangential to the surface in the plane of propagation, and the extension of the principle of transverse analytical integration to cope with inclined tangent plates representing a piece-wise 2D surface.

- The application of the piece-wise 2D terrain to mixed polarization problems

and the resolution of the field on a strip into locally horizontal and vertically polarized components. The is demonstrated to facilitate the solution of a mixed polarization vector integral equation in a novel manner.

- The formulation of the above technique into a fast method employing the fast far field approximation(FAFFA).

- The proposed extension of the Q3D method to tackle off radial propagation effects by combination of discrete radial elements.

Chapter 2

Theoretical Foundations

2.1 Review of basic electromagnetics

We begin by stating Maxwell's equations of electromagnetism.

$$\nabla \wedge \mathcal{E}(\mathbf{r},t) = -\frac{\partial \mathcal{B}(\mathbf{r},t)}{\partial t} \tag{2.1}$$

$$\nabla \wedge \mathcal{H}(\mathbf{r},t) = \frac{\partial \mathcal{D}(\mathbf{r},t)}{\partial t} + \mathcal{J}(\mathbf{r},t) \tag{2.2}$$

$$\nabla \cdot \mathcal{D}(\mathbf{r},t) = \varrho(\mathbf{r},t) \tag{2.3}$$

$$\nabla \cdot \mathcal{B}(\mathbf{r},t) = 0 \tag{2.4}$$

where $\mathcal{E}(\mathbf{r},t)$ is the electric field vector in Volts/meter, $\mathcal{H}(\mathbf{r},t)$ is the magnetic field vector in Amperes/meter, $\mathcal{D}(\mathbf{r},t)$ is the dielectric displacement vector, in Coulombs/meter^2, $\mathcal{B}(\mathbf{r},t)$ is the magnetic flux density vector in Webers/meter^2, $\varrho(\mathbf{r},t)$ is the electric charge density in Coulombs/meter^3 and $\mathcal{J}(\mathbf{r},t)$ is the electric current density vector in Amperes/meter^2. These four equations along with the definitions of the material parameters (2.12-2.14), comprise a complete statement of the physics for all classical electromagnetic problems. The remainder of the literature[1] and the subject of this thesis are devoted to certain mathematical solutions of these equations.

We note that taking the divergence of (2.2) and substituting for (2.3) we may

[1] Anybody doubting the richness of Maxwell's equations may attempt an exhaustive study of classical electromagnetism.

derive the law of conservation of electromagnetic charge

$$\nabla \cdot \mathcal{J} = -\frac{\partial \rho}{\partial t} \tag{2.5}$$

Typically the source will be many wavelengths distant from the nearest portion of any scatterer and we will regard it as independent or decoupled from the rest of the problem. Rather, the role of the source will be represented by predefined incident electric or magnetic fields.

Formally we split the current $\mathcal{J}(\mathbf{r}, t)$

$$\mathcal{J} = \mathcal{J}^i + \mathcal{J}^c \tag{2.6}$$

where $\mathcal{J}^i$ and $\mathcal{J}^c$ are the impressed (source) current, and conduction current respectively. We will only be required to solve Maxwells equations in the region where $\mathcal{J}^i = 0$.

Essentially in this thesis we deal with time harmonic monochromatic problems[2], and so we may remove the time dependent factor[3] $e^{i\omega t}$ from the field, leaving a reduced, spatially dependent field $\mathbf{E}$. For example, the electric field $\mathcal{E}$ can be written in terms of its reduced, spatial field $\mathbf{E}$ as

$$\mathcal{E}(\mathbf{r}, t) = \mathrm{Re}\left[\mathbf{E}(\mathbf{r})\, e^{i\omega t}\right] \tag{2.7}$$

with similar expressions holding for other field quantities. We can write Maxwell's equations in the source free region in terms of the complex spatial field quantities

$$\nabla \wedge \mathbf{E}(\mathbf{r}) = -j\omega \mathbf{B}(\mathbf{r}) \tag{2.8}$$

$$\nabla \wedge \mathbf{H}(\mathbf{r}) = j\omega \mathbf{D}(\mathbf{r}) + \mathbf{J}^c(\mathbf{r}) \tag{2.9}$$

$$\nabla \cdot \mathbf{D}(\mathbf{r}) = \rho(\mathbf{r}) \tag{2.10}$$

$$\nabla \cdot \mathbf{B}(\mathbf{r}) = 0 \tag{2.11}$$

Harmonic impressed electric and magnetic current sources are represented by $\mathbf{J}^i$ and $\mathbf{K}^i$ respectively.

[2] We are evaluating only carrier signal strength

[3] Another popular form of time harmonic variations is $e^{-i\omega t}$, whose fields are related to those of the $e^{i\omega t}$ form by complex conjugation.

The relationships among the field quantities **E**, **D**, **B**, **H** and **J** depend on the constitutive parameters of the medium, namely ϵ, its permittivity, μ, its permeability and σ, its conductivity.

For a linear[4], passive[5] medium we can write

$$\mathbf{D}(\mathbf{r}) = \epsilon(\mathbf{r})\,\mathbf{E}(\mathbf{r}) \tag{2.12}$$

$$\mathbf{B}(\mathbf{r}) = \mu(\mathbf{r})\,\mathbf{H}(\mathbf{r}) \tag{2.13}$$

$$\mathbf{J}^c(\mathbf{r}) = \sigma(\mathbf{r})\,\mathbf{E}(\mathbf{r}) \tag{2.14}$$

ϵ, μ, and σ are in general tensor quantities of the spatial medium. If the medium is isotropic[6] the related fields are parallel with one another, the quantities ϵ, μ and σ reduce to scalars and this shall be sufficient for the remainder of our discussion.

Combining (2.12) and (2.13) with (2.8-2.11)

$$\nabla \wedge \mathbf{E}(\mathbf{r}) = -j\omega\mu(\mathbf{r})\mathbf{H}(\mathbf{r}) \tag{2.15}$$

$$\nabla \wedge \mathbf{H}(\mathbf{r}) = j\omega\epsilon(\mathbf{r})\mathbf{E}(\mathbf{r}) + \mathbf{J}^c \tag{2.16}$$

$$\nabla \cdot (\epsilon(\mathbf{r})\mathbf{E}(\mathbf{r})) = \rho(\mathbf{r}) \tag{2.17}$$

$$\nabla \cdot (\mu(\mathbf{r})\mathbf{H}(\mathbf{r})) = 0 \tag{2.18}$$

From here our approach depends on how we deal with the current in (2.16). In one approach we employ (2.14) to write the right hand side of (2.16) as

$$j\omega\epsilon(\mathbf{r})\mathbf{E}(\mathbf{r}) + \mathbf{J}^c = j\omega\epsilon_c(\mathbf{r})\mathbf{E} \tag{2.19}$$

where ϵ_c is the complex permittivity, given by

$$\epsilon_c = \epsilon - j\frac{\sigma}{\omega} \tag{2.20}$$

Taking the curl of equations (2.15) and (2.16) and substituting we have the second order vector differential equations

$$\nabla \wedge \left(\frac{1}{\mu}\nabla \wedge \mathbf{E}\right) - k_0^2\epsilon_c\mathbf{E} = 0 \tag{2.21}$$

$$\nabla \wedge \left(\frac{1}{\epsilon_c}\nabla \wedge \mathbf{H}\right) - k_0^2\mu\mathbf{H} = 0 \tag{2.22}$$

[4] A medium is *linear* if the constitutive parameters are not functions of the applied field strength.

[5] A passive medium will make no net electrical energy contribution to the system

[6] A medium is *isotropic* if its constitutive parameters are not dependent on polarization.

where the free space wavenumber $k_0 = \sqrt{\mu_0 \epsilon_0 \omega^2}$ and

$$\epsilon_0 = 8.854 \wedge 10^{-12} \text{ Farads/meter} \tag{2.23}$$

$$\mu_0 = 4\pi \wedge 10^{-7} \text{ Henries/meter} \tag{2.24}$$

are the permittivity and permeability of free space respectively, and inspection of the free space form of the above equation reveals that

$$v = c = \frac{1}{\sqrt{\mu_0 \epsilon_0}} \tag{2.25}$$

The spatial variation in μ and ϵ_c mean that these equations are difficult to solve in a direct analytical fashion apart from a limit range of symmetric permittivity/permeability profiles allowing separation of variables and modal expansion. It will be our preference to convert such equations into ones where fields are the sum of incident and scattered components radiating in a homogeneous environment. This leads to an integral equation formulation for the scattered fields with a simple kernel.

2.2 Volume Equivalence Principle

An alternative description of the current in (2.16) is used. Writing

$$\epsilon \mathbf{E} = \epsilon_0 \mathbf{E} + \epsilon_0 (\epsilon_r - 1) \mathbf{E} \tag{2.26}$$

and again using relation (2.14) for $\mathbf{J}^c$, the composite current $\mathbf{J}$ is defined

$$\mathbf{J} = j\omega \left(\left(\epsilon_r - \frac{i\sigma}{\omega \epsilon_0} \right) - 1 \right) \epsilon_0 \mathbf{E} = j\omega \left(\epsilon_{cr} - 1 \right) \epsilon_0 \mathbf{E} \tag{2.27}$$

and we note that this current accounts for both conduction and displacement currents. Further, defining a magnetic current

$$\mathbf{K} = j\omega \mu_0 (\mu_r - 1) \mathbf{H} \tag{2.28}$$

yields equations

$$\nabla \wedge \mathbf{E} = -j\omega \mu_0 \mathbf{H} - \mathbf{K} \tag{2.29}$$

$$\nabla \wedge \mathbf{H} = j\omega \epsilon_0 \mathbf{E} + \mathbf{J} \tag{2.30}$$

It is evident that the above equations describe propagation in a homogeneous enviroment characterized by material parameters μ_0 and ϵ_0, and where the source currents $\mathbf{J}$ and $\mathbf{K}$ radiate in that space. The currents have replaced the inhomogeneities of the original media.

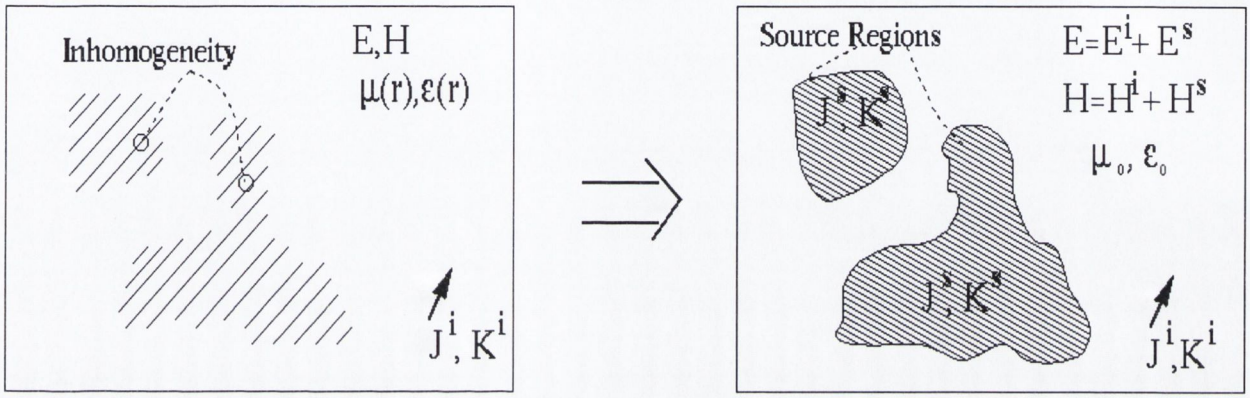


Figure 2-1: *Transformation of the inhomogeneous media problem into one involving homogeneous space with embedded scattering sources* $\mathbf{J}^s$ *and* $\mathbf{K}^s$. $\mathbf{J}^i$ *and* $\mathbf{K}^i$ *are sources external to the region of interest*

The procedure of representing an inhomogeneous volume by equivalent sources is known as the *volume equivalence principle.* The fields $\mathbf{E}$ and $\mathbf{H}$ may now be split

$$\mathbf{E} = \mathbf{E}^i + \mathbf{E}^s \tag{2.31}$$

$$\mathbf{H} = \mathbf{H}^i + \mathbf{H}^s \tag{2.32}$$

and with the sources $\mathbf{J}^i$ and $\mathbf{K}^i$ exterior to the volume of interest, fields $\mathbf{E}^i$ and $\mathbf{H}^i$ satisfy

$$\nabla \wedge \mathbf{E}^i = -j\omega\mu_0\mathbf{H}^i \tag{2.33}$$

$$\nabla \wedge \mathbf{H}^i = j\omega\epsilon_0\mathbf{E}^i \tag{2.34}$$

implying that $\mathbf{E}^i$ and $\mathbf{H}^i$ satisfy the two homogeneous vector wave equations

$$\nabla^2\mathbf{E}^i + k_0^2\mathbf{E}^i = 0 \tag{2.35}$$

$$\nabla^2 \mathbf{H}^i + k_0^2 \mathbf{H}^i = 0 \tag{2.36}$$

These fields are independent of the currents $\mathbf{J}$ and $\mathbf{K}$ and therefore of the inhomogeneities in the original medium. It is such solutions that will be used to represent the incident field from a remote source. The remaining components $\mathbf{E}^s$ and $\mathbf{H}^s$ are defined as scattered fields, the difference between the net and incident fields caused by the presence of inhomogeneities, or the source currents of the *volume equivalent* problem.

Subtracting (2.33) and (2.34) from (2.29) and (2.30) yields equations for the scattered fields

$$\nabla \wedge \mathbf{E}^s = -j\omega\mu_0 \mathbf{H}^s - \mathbf{K} \tag{2.37}$$

$$\nabla \wedge \mathbf{H}^s = j\omega\epsilon_0 \mathbf{E}^s + \mathbf{J} \tag{2.38}$$

but we note that $\mathbf{J}$ and $\mathbf{K}$ in these equations are dependent on the total field. Taking the divergence of (2.37) and (2.38)

$$\nabla \cdot \mathbf{H}^s = \frac{-\nabla \cdot \mathbf{K}}{j\omega\mu_0} \tag{2.39}$$

$$\nabla \cdot \mathbf{E}^s = \frac{-\nabla \cdot \mathbf{J}}{j\omega\epsilon_0} \tag{2.40}$$

Using these relations and taking the curl of (2.37) and (2.38), with substitution and some vector algebra it may be shown that

$$\nabla^2 \mathbf{E}^s + k_0^2 \mathbf{E}^s = j\omega\mu_0 \mathbf{J} - \frac{\nabla\nabla \cdot \mathbf{J}}{j\omega\epsilon_0} + \nabla \wedge \mathbf{K} \tag{2.41}$$

$$\nabla^2 \mathbf{H}^s + k_0^2 \mathbf{H}^s = j\omega\epsilon_0 \mathbf{K} - \frac{\nabla\nabla \cdot \mathbf{K}}{j\omega\mu_0} - \nabla \wedge \mathbf{J} \tag{2.42}$$

With the operator ∇ given in rectangular coordinates as [7]

$$\nabla = \frac{\partial}{\partial x}\hat{\mathbf{x}} + \frac{\partial}{\partial y}\hat{\mathbf{y}} + \frac{\partial}{\partial z}\hat{\mathbf{z}} \tag{2.43}$$

the dyadic operator $\nabla\nabla$ may be represented as the matrix formed of the outer quadratic product of ∇

[7] For the expression of the operator ∇ in cylindrical or spherical coordinates, see [4].

$$\nabla\nabla = \begin{pmatrix} \frac{\partial^2}{\partial x^2} & \frac{\partial^2}{\partial x \partial y} & \frac{\partial^2}{\partial x \partial z} \\ \frac{\partial^2}{\partial y \partial x} & \frac{\partial^2}{\partial y^2} & \frac{\partial^2}{\partial y \partial z} \\ \frac{\partial^2}{\partial z \partial x} & \frac{\partial^2}{\partial z \partial y} & \frac{\partial^2}{\partial z^2} \end{pmatrix}. \tag{2.44}$$

(2.41) and (2.42) are the key vector differential equations in this analysis. The left hand sides of these equations contain the Helmholtz operator. It can be shown that the solution of such equations may be constructed out of the solution of the scalar equation,

$$\nabla^2\psi + k_0^2\psi = -\delta(\mathbf{r}, \mathbf{r}') \tag{2.45}$$

for a Dirac delta function source, in a space V where the boundary recedes to infinity and where the radiation condition of Sommerfeld [65]

$$| r\psi | < K \tag{2.46}$$

$$r(\frac{\delta\psi}{\delta r} + ik_0\psi) \rightarrow 0 \quad as \quad r \rightarrow \infty \tag{2.47}$$

ensures that distant fields propagate outwards from the sources. It may be shown that the solution to (2.45) is given by the three dimensional free space Green's function

$$\psi = G(\mathbf{r}, \mathbf{r}') = \frac{e^{-ik_0|\mathbf{r}-\mathbf{r}'|}}{4\pi|\mathbf{r}-\mathbf{r}'|} \tag{2.48}$$

Where the vector radiation boundary condition [3]

$$\lim_{|\mathbf{r}|\rightarrow\infty} \left[\nabla \wedge \begin{pmatrix} \mathbf{E} \\ \mathbf{H} \end{pmatrix} + jk_0\hat{\mathbf{r}} \wedge \begin{pmatrix} \mathbf{E} \\ \mathbf{H} \end{pmatrix} \right] = 0 \tag{2.49}$$

is applicable, solutions to (2.41) and (2.42) may be constructed in an analogous fashion, and by appeal to linear superposition

$$\mathbf{E}^s = -\int_V d\mathbf{r}' G(\mathbf{r}, \mathbf{r}') \left[j\omega\mu_0\mathbf{J}(\mathbf{r}') - \frac{\nabla'\nabla' \cdot \mathbf{J}(\mathbf{r}')}{j\omega\epsilon_0} + \nabla' \wedge \mathbf{K}(\mathbf{r}') \right] \tag{2.50}$$

$$\mathbf{H}^s = -\int_V d\mathbf{r}' G(\mathbf{r}, \mathbf{r}') \left[j\omega\epsilon_0\mathbf{K}(\mathbf{r}') - \frac{\nabla'\nabla' \cdot \mathbf{K}(\mathbf{r}')}{j\omega\mu_0} - \nabla' \wedge \mathbf{J}(\mathbf{r}') \right] \tag{2.51}$$

Noting the commutation of the convolution and differential operators, and defining the vector potentials[8]

$$\mathbf{A} = \mathbf{J} * G = \int_V \mathbf{J}(\mathbf{r}')G(\mathbf{r}, \mathbf{r}')d\mathbf{r}' \tag{2.52}$$

[8]More often these potentials are postulated *a-priori*

$$\mathbf{F} = \mathbf{K} * G = \int_V \mathbf{K}(\mathbf{r}')G(\mathbf{r}, \mathbf{r}')d\mathbf{r}' \tag{2.53}$$

(2.50) and (2.51) may be written as

$$\mathbf{E}^s = \frac{\nabla\nabla \cdot \mathbf{A} + k_0^2\mathbf{A}}{j\omega\epsilon_0} - \nabla \wedge \mathbf{F} \tag{2.54}$$

$$\mathbf{H}^s = \frac{\nabla\nabla \cdot \mathbf{F} + k_0^2\mathbf{F}}{j\omega\mu_0} + \nabla \wedge \mathbf{A} \tag{2.55}$$

which constitute the vector integro-differential equations desired, in terms of vector potentials $\mathbf{A}$ and $\mathbf{F}$, functions of the unknown currents $\mathbf{J}$ and $\mathbf{K}$.

2.3 Surface Equivalence Principle

The above system of equations allows the description of a very general class of scattering problems in the form of volume integral equations where total fields are given by (2.31) and (2.32).

In many cases it is greatly beneficial to solve a problem in terms of a surface integral rather than a volume integral, the reduction in dimension leading to a considerable reduction in the total number of unknowns in a numerical discretization. The total region of inhomogeneity is first enclosed within a prescribed surface which may be purely fictitious or coincident with a real physical boundary. The intent is to model the scattering features of the enclosed volume using only the fields on the bounding surface, and to thereby evaluate the fields outside that boundary. In fact we are required to define a set of currents on the boundary that will replicate the original problem. For a fuller treatment of the following derivation see Ishimaru [29]. We consider the problem as depicted in Figure.2-2.

Sources $\mathbf{J}^i$ and $\mathbf{K}^i$ radiate in a space V_1 of constant material parameters ϵ_1 and μ_1, with boundaries S and S_∞, the surface S enclosing a region V_2 of inhomogeneity $\epsilon_2(\mathbf{r})$ $\mu_2(\mathbf{r})$. Fields $\mathbf{E}$ and $\mathbf{H}$ are the fields present in both regions caused by $\mathbf{J}^i$, $\mathbf{K}^i$ in the presence of the inhomogeneity. We also define the fields $\mathbf{E}_1$ and $\mathbf{H}_1$, those fields that would be excited at any point in the space, if the inhomogeneity were replaced with the medium ϵ_1 μ_1 and in the presence of arbitrary sources $\mathbf{J}_1$ and $\mathbf{K}_1$. The equations

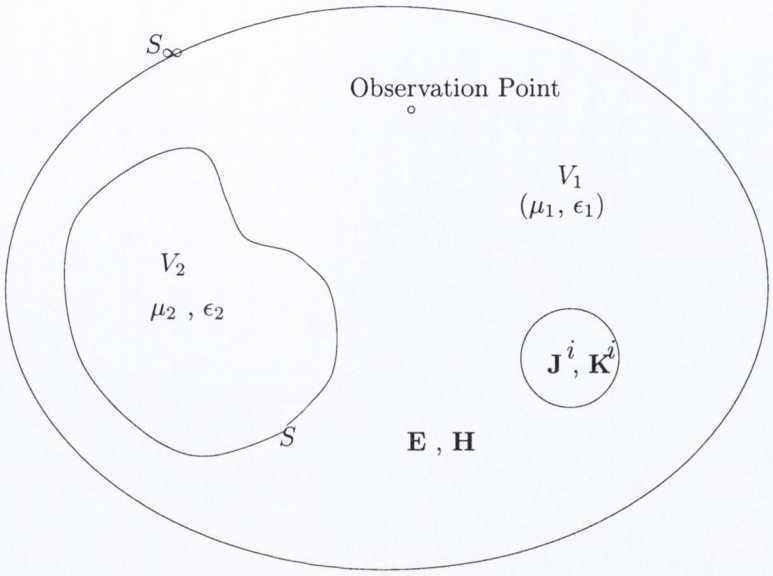


Figure 2-2: Problem involving inhomogeneous media V_2 surrounded by a homogeneous space V_1 in the presence of sources $\mathbf{J}^i$ and $\mathbf{K}^i$

for these fields in V_1 are respectively,

$$\nabla \wedge \mathbf{E} = -i\omega\mu_1\mathbf{H} - \mathbf{K}^i \tag{2.56}$$

$$\nabla \wedge \mathbf{H} = i\omega\epsilon_1\mathbf{E} + \mathbf{J}^i \tag{2.57}$$

$$\nabla \wedge \mathbf{E}_1 = -i\omega\mu_1\mathbf{H}_1 - \mathbf{K}_1 \tag{2.58}$$

$$\nabla \wedge \mathbf{H}_1 = i\omega\epsilon_1\mathbf{E}_1 + \mathbf{J}_1 \tag{2.59}$$

Hence

$$\mathbf{H}_1 \cdot \nabla \wedge \mathbf{E} = -i\omega\mu_1\mathbf{H}_1 \cdot \mathbf{H} - \mathbf{H}_1 \cdot \mathbf{K}^i \tag{2.60}$$

$$\mathbf{E}_1 \cdot \nabla \wedge \mathbf{H} = i\omega\epsilon_1\mathbf{E}_1 \cdot \mathbf{E} + \mathbf{E}_1 \cdot \mathbf{J}^i \tag{2.61}$$

$$\mathbf{H} \cdot \nabla \wedge \mathbf{E}_1 = -i\omega\mu_1\mathbf{H} \cdot \mathbf{H}_1 - \mathbf{H} \cdot \mathbf{K}_1 \tag{2.62}$$

$$\mathbf{E} \cdot \nabla \wedge \mathbf{H}_1 = i\omega\epsilon_1\mathbf{E} \cdot \mathbf{E}_1 + \mathbf{E} \cdot \mathbf{J}_1 \tag{2.63}$$

Taking (2.60)-(2.62) + (2.61) - (2.63) and some vector algebra,

$$\nabla \cdot (\mathbf{E} \wedge \mathbf{H}_1 - \mathbf{E}_1 \wedge \mathbf{H}) = \mathbf{E}_1 \cdot \mathbf{J}^i - \mathbf{H}_1 \cdot \mathbf{K}^i - \mathbf{E} \cdot \mathbf{J}_1 + \mathbf{H} \cdot \mathbf{K}_1 \tag{2.64}$$

and applying the divergence theorem for the volume V_1 enclosed by S and S_∞

$$\int_{S+S_\infty} (\mathbf{E} \wedge \mathbf{H}_1 - \mathbf{E}_1 \wedge \mathbf{H}) \cdot \hat{\mathbf{n}} dS = \int_{V_1} (\mathbf{E}_1 \cdot \mathbf{J}^i - \mathbf{H}_1 \cdot \mathbf{K}^i - \mathbf{E} \cdot \mathbf{J}_1 + \mathbf{H} \cdot \mathbf{K}_1) dV \tag{2.65}$$

In accordance with the radiation condition (2.49), the fields at infinity are vanishing and so we may neglect the integral over S_∞. With a little rearrangement

$$\int_S (\mathbf{E}_1 \cdot (\hat{\mathbf{n}} \wedge \mathbf{H}) - \mathbf{H}_1 \cdot (\mathbf{E} \wedge \hat{\mathbf{n}}))\, dS = \int_{V_1} (\mathbf{E}_1 \cdot \mathbf{J}^i - \mathbf{H}_1 \cdot \mathbf{K}^i - \mathbf{E} \cdot \mathbf{J}_1 + \mathbf{H} \cdot \mathbf{K}_1) dV \quad (2.66)$$

It is noted that the above is a reciprocity theorem and that it links the value of the fields $\mathbf{E}(\mathbf{r})$ and $\mathbf{H}(\mathbf{r})$ in V_1 with $\hat{\mathbf{n}} \wedge \mathbf{H}$ and $\mathbf{E} \wedge \hat{\mathbf{n}}$ on the surface S in terms of the homogeneous space solution of the wave equation for currents $\mathbf{J}_1(\mathbf{r})$ and $\mathbf{K}_1(\mathbf{r})$, and in relation to the sources $\mathbf{J}^i$ and $\mathbf{K}^i$. The nature of the relationship is revealed further if we choose currents

$$\mathbf{J}_1(\mathbf{r}) = \hat{\mathbf{u}} \delta(\mathbf{r} - \mathbf{r}') \quad (2.67)$$

$$\mathbf{K}_1(\mathbf{r}) = 0 \quad (2.68)$$

This yields $\mathbf{E}$ at an arbitrary point $\mathbf{r}$

$$\hat{\mathbf{u}} \cdot \mathbf{E}(\mathbf{r}) = \int_{V_1} (\mathbf{E}_1 \cdot \mathbf{J}^i - \mathbf{H}_1 \cdot \mathbf{K}^i) dV - \int_S (\mathbf{E}_1 \cdot (\hat{\mathbf{n}} \wedge \mathbf{H}) - \mathbf{H}_1 \cdot (\mathbf{E} \wedge \hat{\mathbf{n}}))\, dS \quad (2.69)$$

Considering the form of $\mathbf{J}_1$ and $\mathbf{K}_1$ the functions $\mathbf{E}_1$ and $\mathbf{H}_1$ are now given by the simple forms[9]

$$\mathbf{E}_1(\mathbf{r}') = \frac{\nabla' \nabla' \cdot + k_1^2}{i\omega\epsilon_1} \left(\hat{\mathbf{u}} \frac{e^{-ik_1 r}}{4\pi r} \right) \quad (2.70)$$

$$\mathbf{H}_1(\mathbf{r}') = \nabla' \wedge \left(\hat{\mathbf{u}} \frac{e^{-ik_1 r}}{4\pi r} \right) \quad (2.71)$$

where $k_1 = \sqrt{\epsilon_1 \mu_1}\omega$ is the wavenumber in V_1. These solutions may be substituted into (2.69), and exploiting symmetries of the Green's function and its derivatives with respect to interchange of $\mathbf{r}$ and $\mathbf{r}'$, and by moving the differentiations outside the integration it can be shown that

$$\hat{\mathbf{u}} \cdot \mathbf{E}(\mathbf{r}) = -\hat{\mathbf{u}} \cdot \frac{\nabla \nabla \cdot + k_1^2}{j\omega\epsilon_1} \int_S (\hat{\mathbf{n}} \wedge \mathbf{H}) \frac{e^{-ik_1 r}}{4\pi r} dS' + \hat{\mathbf{u}} \cdot \nabla \wedge \int_S (\mathbf{E} \wedge \hat{\mathbf{n}}) \frac{e^{-ik_1 r}}{4\pi r} dS' \quad (2.72)$$

$$+ \hat{\mathbf{u}} \cdot \frac{\nabla \nabla \cdot + k_1^2}{j\omega\epsilon_1} \int_{V_1} \frac{e^{-ik_1 r}}{4\pi r} \mathbf{J}^i dV' - \hat{\mathbf{u}} \cdot \nabla \wedge \int_{V_1} \frac{e^{-ik_1 r}}{4\pi r} \mathbf{K}^i dV'$$

[9] These forms come directly from the source field relationship applied to an elemental current $\mathbf{J}$ at $\mathbf{r}$

The direction of $\hat{\mathbf{u}}$ above was arbitrary. Inspecting the RHS of this equation we see that the terms containing the volume integrals simply give the total incident fields due to the source currents $\mathbf{J}^i$ and $\mathbf{K}^i$ in V_1. In general the source currents will be of simple form and so we may replace these integrals with the incident fields $\mathbf{E}^i$ and $\mathbf{H}^i$. The surface integrals take a similar form on substitution of exterior(+) surface currents $\mathbf{J}_{S+}$ and $\mathbf{K}_{S+}$ where

$$\mathbf{J}_{S+} = \hat{\mathbf{n}} \wedge \mathbf{H}_+ \tag{2.73}$$

$$\mathbf{K}_{S+} = \mathbf{E}_+ \wedge \hat{\mathbf{n}} \tag{2.74}$$

where the fields $\mathbf{H}_+$ and $\mathbf{E}_+$ are evaluated as the surface is approached from the outside and so the whole equation may be simplified to

$$\mathbf{E} = \mathbf{E}^i + \mathbf{E}^s_{S+} \tag{2.75}$$

where

$$\mathbf{E}^{\mathbf{s}}_{\mathbf{S}+} = \frac{\nabla\nabla\cdot + k_1^2}{j\omega\epsilon_1}\mathbf{A}_{S+} - \nabla \wedge \mathbf{F}_{S+} \tag{2.76}$$

where $\mathbf{A}_{S+}$ and $\mathbf{F}_{S+}$ denote the integrations over the surface S,

$$\mathbf{A}_{S+} = \int_S \mathbf{J}_{S+}\frac{e^{-ik_1 r}}{4\pi r}dS' \tag{2.77}$$

$$\mathbf{F}_{S+} = \int_S \mathbf{K}_{S+}\frac{e^{-ik_1 r}}{4\pi r}dS' \tag{2.78}$$

In (2.75) the interactions of the region of inhomogeneity are modelled using an integral over the fields on the bounding surface and this relation is known as the *surface equivalence principle.*

Letting the observation point $\mathbf{r}$ approach the boundary from the outside yields an equation for the exterior electric field at the surface

$$\mathbf{E}_+(s) = \mathbf{E}^i + \mathbf{E}^s_{S+}(s)[\mathbf{E}_+(s') \wedge \hat{\mathbf{n}}', \hat{\mathbf{n}}' \wedge \mathbf{H}_+(s')] \tag{2.79}$$

where $\mathbf{E}^s_{S+}(s)[.]$ is given by (2.83). This surface integral equation contains two unknowns and taken in isolation, cannot be solved.

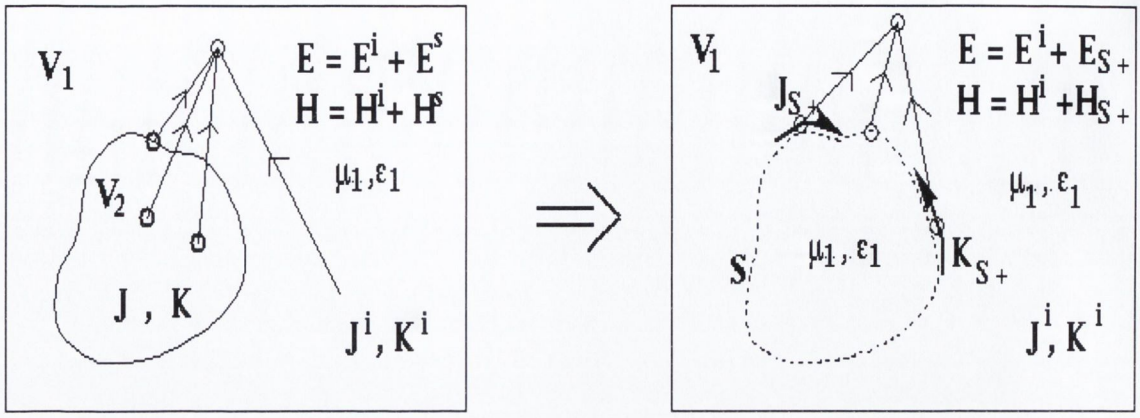


Figure 2-3: Transformation from volume equivalent to surface equivalent decription of a scattering problem.

2.3.1 The Extinction Theorem

We note that in the case where V_2 no longer contains inhomogeneity but instead is identical with region V_1 the fields on S are simply $\mathbf{E}^i$ and $\mathbf{H}^i$. (2.79) still holds and hence

$$\mathbf{E}_+(s) = \mathbf{E}^i(s) = \mathbf{E}^i + \mathbf{E}^s_{S+}(s)[\mathbf{E}^i(s') \wedge \hat{\mathbf{n}}', \hat{\mathbf{n}}' \wedge \mathbf{H}^i(s')] \tag{2.80}$$

and so clearly

$$\mathbf{E}^s_{S+}(s)[\mathbf{E}^i(s') \wedge \hat{\mathbf{n}}', \hat{\mathbf{n}}' \wedge \mathbf{H}^i(s')] = 0 \tag{2.81}$$

This is in fact a form of the *extinction theorem* indicating that the equivalent currents of the incident field excite no scattered field in V_1. Hence $\mathbf{E}^s_{S+}(s)[\mathbf{E}_+(s') \wedge \hat{\mathbf{n}}', \hat{\mathbf{n}}' \wedge \mathbf{H}_+(s')]$ in equation (2.75) might alternatively be replaced with $\mathbf{E}^s_+ = \mathbf{E}_{S+}(s)[\mathbf{E}^s_+(s') \wedge \hat{\mathbf{n}}', \hat{\mathbf{n}}' \wedge \mathbf{H}^s_+(s')]$, the integration being performed only over only the scattered components of the total field at the surface.

By similar analysis an equation may be formed for the field $\mathbf{H}$ as it approaches the surface.

$$\mathbf{H}_+ = \mathbf{H}^i + \mathbf{H}^s_{S+}[\mathbf{E}_+(s') \wedge \hat{\mathbf{n}}', \hat{\mathbf{n}}' \wedge \mathbf{H}_+(s')] \tag{2.82}$$

where

$$\mathbf{H}^{\mathbf{s}}_{S+} = \frac{\nabla\nabla\cdot + k_1^2}{j\omega\mu_1}\mathbf{F}_{S+} + \nabla \wedge \mathbf{A}_{S+} \tag{2.83}$$

(2.82) however, is not linearly independent of (2.79) so we retain a system of two unknown fields and one equation. (2.75) and (2.82) have the same form as a volume integral over a space μ_1, ϵ_1, with the embedded surface currents $\mathbf{J}_{S+}$ and $\mathbf{K}_{S+}$. The total field of the original problem in V_1 is then simply the sum of these fields and the incident field. This is known as the *equivalent exterior problem.* At this point the integral equation has not been solved but the unknown polarizations and conduction currents in V_2 have been replaced with unknown currents on a surface in a homogeneous space.

How we progress from this point is dependent on the specifics of the scattering problem. The simplest solutions arise where we have an additional constraint or boundary condition on the surface S.

2.3.2 The Perfect Electrical Conductor

Supposing that the surface actually bounds a region filled with or enclosed by a perfectly electrically conducting material ($\sigma \to \infty$), then it may be stated that the tangential electric field on the surface $\hat{\mathbf{n}} \wedge \mathbf{E}(s)$ is zero.

Taking the normal vector product of (2.79) at the surface, terms in $\mathbf{K}$ vanish leaving,

$$\hat{\mathbf{n}} \wedge \mathbf{E}^i(\mathbf{s}) = -\hat{\mathbf{n}} \wedge \frac{\nabla\nabla\cdot + k_1^2}{j\omega\epsilon_1}\int_S \mathbf{J}_s(s')\frac{e^{-ik_1 r}}{4\pi r}dS' \tag{2.84}$$

where we may solve for $\mathbf{J}$ in terms of the incident field, there being only one unknown. Likewise an equation in terms of the magnetic field may be derived

$$\hat{\mathbf{n}} \wedge \mathbf{H}(\mathbf{s}) = \hat{\mathbf{n}} \wedge \mathbf{H}^i(\mathbf{s}) + \hat{\mathbf{n}} \wedge \nabla \wedge \int_S \mathbf{J}_s(s')\frac{e^{-ik_1 r}}{4\pi r}dS' \tag{2.85}$$

Individually these equations only appeal to one of the conditions on the PEC boundary and hence they can lead to non-unique solutions for certain problems associated with resonances internal to the boundary S. This will occur where the geometry of

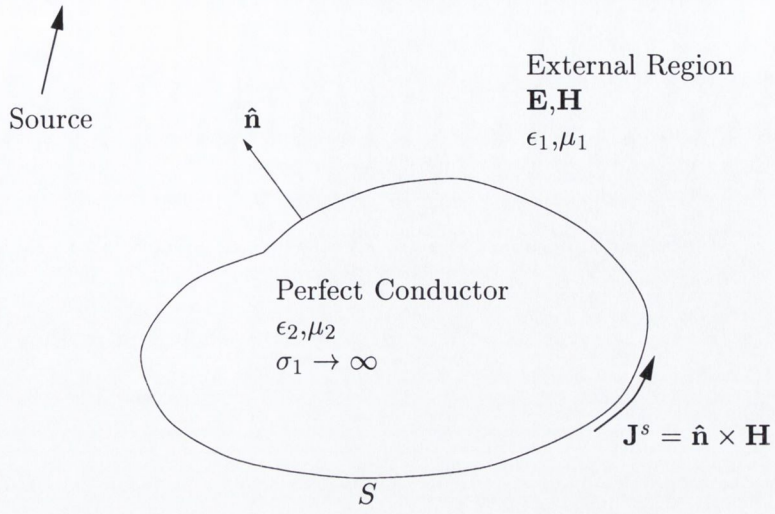


Figure 2-4: PEC body problem. **J** is the sole current lying on the surface S. Fields inside **S** are zero.

the scatterer, and the wavelength, are such as to correspond to waveguide modes inside the scatterer. The result is that an iterative matrix solver will take considerably longer to converge. In such cases we will prefer to solve for a linear combination of (2.84) and (2.85) in an approach known as the *combined field integral equation*(CFIE). Even using the CFIE, external resonances, or near resonances, may be excited, and these will again increase the number of required iterations. A method for dealing with such problems has been proposed by Lu and Chew [45]. For terrain problems however, the geometry will not correspond to resonance cavity structures, even for the most strongly undulating profiles, and the EFIE or MFIE will suffice.

(2.84) and (2.85), derived for PEC surfaces, are in fact applicable to a wider range of a surface type, notably to terrain in the case of grazing incidence propagation at VHF and UHF.

2.3.3 The Impedance Boundary

In other cases we will find it more appropriate to enforce a different condition on the boundary of region S known as the *impedance boundary condition*[10]. Without derivation, and assuming V_1 has the properties of free space the condition takes the

[10]The *impedance boundary condition* [54] is an approximate boundary condition derived from the principles of plane wave propagation.

form

$$\hat{\mathbf{n}} \wedge \mathbf{E} = -\eta_2 \mathbf{H}_{\hat{\mathbf{t}}} \tag{2.86}$$

where $\mathbf{H}_{\hat{\mathbf{t}}}$ is the component of $\mathbf{H}$ tangential to the surface and

$$\eta_2 = \sqrt{\frac{\mu_2}{\epsilon_2}} \tag{2.87}$$

is the characteristic impedance of the medium inside the surface. We may also define the characteristic impedance of region one as

$$\eta_1 = \sqrt{\frac{\mu_1}{\epsilon_1}} \tag{2.88}$$

In terms of the surface current definitions

$$\mathbf{K} = \eta_2 \mathbf{J} \wedge \hat{\mathbf{n}} \tag{2.89}$$

Once again an unknown is eliminated from (2.79) giving

$$\mathbf{E} = \mathbf{E}_i + \frac{\nabla\nabla\cdot + k_1^2}{j\omega\epsilon_1} \int_S G \frac{\mathbf{E}_{\hat{\mathbf{t}}}}{\eta_2} dS - \nabla \wedge \int_S G \mathbf{E}_{\hat{\mathbf{t}}} \wedge \hat{\mathbf{n}} dS \tag{2.90}$$

We may solve first for the tangential $\mathbf{E}$ field as we approach the surface and then the field at an exterior point will be given by (2.90).

The impedance boundary condition will be applicable where the interior permittivity is large by comparison with the exterior permittivity, and the dimensions and lossyness of the scatterer, are such as to ensure minimal re-emergence of energy transmitted into the interior medium.

2.3.4 The Interior Field Equation

Where the physical constraints of the problem do not lend themselves to the use of these or similar boundary conditions on S, in general it is possible to formulate a second equation for the fields inside the region V_2 in an analogous manner to the derivation of the *exterior equivalent problem.*

Rearranging the wave equation for an inhomogeneous space (2.21), and assuming that $\mu_2 = \mu_0$ is constant[11] throughout V_2

$$\nabla \wedge \nabla \wedge \mathbf{E} - k_c^2 \mathbf{E} = -i\omega\mu \mathbf{J} \tag{2.91}$$

[11] We are dealing with a non-magnetic homogeneous medium

where k_c is a function of $\mathbf{r}$. We may write a system of equations in matrix form defining a dyadic Green's functions for the electric field excited by an electric current source in the inhomogeneous space as

$$\nabla \wedge \nabla \wedge \overline{\overline{G_{e,J}}} - k_c^2 \overline{\overline{G_{e\,J}}} = -\omega\mu\delta(\mathbf{r}, \mathbf{r}')\overline{\overline{I}} \tag{2.92}$$

where $\overline{\overline{I}}$ is the 3×3 identity matrix, and this is analogous to the definition of the free space Green's function as the solution of the scalar Helmholtz equation in the presence of a $\delta(\mathbf{r}, \mathbf{r}')$ input source, with a radiation boundary condition applied at infinity. The $\mathbf{E}$ field due to a current distribution $\mathbf{J}$ may be obtained

$$\mathbf{E} = \int_V \overline{\overline{G}}_{e,J} \mathbf{J} dV \tag{2.93}$$

where the magnetic field is given by

$$\mathbf{H} = \frac{i}{\omega\mu} \nabla \wedge \mathbf{E} \tag{2.94}$$

We state the equations for the fields in the whole space excited by sources $\mathbf{J}_2$ and $\mathbf{K}_2$ residing in V_2 (Figure 2-2),

$$\nabla \wedge \mathbf{H}_2 = i\omega\epsilon_2 \mathbf{E}_2 + \mathbf{J}_2 \tag{2.95}$$

$$\nabla \wedge \mathbf{E}_2 = -i\omega\mu \mathbf{H}_2 - \mathbf{K}_2 \tag{2.96}$$

with the fields of the original problem inside V_2 satisfying,

$$\nabla \wedge \mathbf{H} = i\omega\epsilon_2 \mathbf{E} \tag{2.97}$$

$$\nabla \wedge \mathbf{E} = -i\omega\mu \mathbf{H} \tag{2.98}$$

Following the analysis of (2.60) to (2.69) for the *exterior equivalent problem* it can be shown that

$$\int_S \left(\mathbf{E}_2 \cdot (\hat{\mathbf{n}}_- \wedge \mathbf{H}) - \mathbf{H}_2 \cdot (\mathbf{E} \wedge \hat{\mathbf{n}}_-) \right) dS = \int_{V_2} (\mathbf{H} \cdot \mathbf{K}_2 - \mathbf{E} \cdot \mathbf{J}_2) dV \tag{2.99}$$

where $\hat{\mathbf{n}}_-$ denotes the inward pointing normal. Choosing $\mathbf{J}_2$ and $\mathbf{K}_2$ as in (2.67) and (2.68) and expressing $\mathbf{E}_2$ and $\mathbf{H}_2$ in terms of the dyadic Greens function as in (2.93) and (2.94),

$$\hat{\mathbf{u}} \cdot \mathbf{E} = -\int_S \left[\int_{V_2} \overline{\overline{G}}_{e,J} \delta(\mathbf{r}, \mathbf{r}') \hat{\mathbf{u}} dV \right] \cdot (\hat{\mathbf{n}}_- \wedge \mathbf{H}) \tag{2.100}$$

$$+\int_S \left[\frac{i\nabla}{\omega\mu_2} \wedge \int_{V_2} \overline{\overline{G}}_{e,J}\delta(\mathbf{r},\mathbf{r}')\hat{\mathbf{u}}dV\right] \cdot (\mathbf{E} \wedge \hat{\mathbf{n}}_-)dS$$

and hence

$$\mathbf{E}(\mathbf{r}) = -\int_S \left(\overline{\overline{G}}(\hat{\mathbf{n}}_- \wedge \mathbf{H}) - \frac{i}{\omega\mu}\nabla \wedge \overline{\overline{G}} \cdot (\mathbf{E} \wedge \hat{\mathbf{n}})\right) dS \tag{2.101}$$

where the vector $\mathbf{u}$ is entirely arbitrary and has been factored out of the integral.

(2.101) defines a source field relationship for the field at a point inside S in terms of the tangential fields on the interior surface of S, and the inhomogeneous space, electric field/electric source, dyadic Green's function.

The considerable problem of finding the dyadic Green's function in this inhomogeneous space remains, and methods for its solution exist [32]. In many cases however, volume finite element methods[12] will be preferred for inhomogeneous bodies. Combining (2.79) and (2.101) we have a coupled system of equations as the surface S may be drawn exterior to all inhomogeneity, and so fields $\mathbf{E}$ and $\mathbf{H}$ will be continuous across S.

2.3.5 Homogeneous Bodies

We will be restricting our investigation to terrain problems where the material body may be assumed to be homogeneous, or otherwise where a homogeneous boundary condition may be applied.

Where the body is homogeneous the dyadic Green's function may be easily found by appeal to the source field relations (2.70),(2.71), applied in a medium with the constitutive parameters of V_2 distributed over the whole space. These have solutions given by (2.70) and (2.71) replacing k_1 with k_2.

Hence we may express the internal fields in terms of $\mathbf{A}_{S-}$ and $\mathbf{F}_{S-}$ as

$$\mathbf{E}_- = \frac{\nabla\nabla\cdot + k_2^2}{j\omega\epsilon_2}\mathbf{A}_{S-} - \nabla \wedge \mathbf{F}_{S-} \tag{2.102}$$

where

$$\mathbf{A}_{S-} = \int_S \mathbf{J}_{S-}\frac{e^{-ik_2 r}}{4\pi r}dS' \tag{2.103}$$

$$\mathbf{F}_{S-} = \int_S \mathbf{K}_{S-}\frac{e^{-ik_2 r}}{4\pi r}dS' \tag{2.104}$$

[12] These have the advantage that inhomogeneity can be treated at no extra cost.

and

$$\mathbf{J}_{S-} = \hat{\mathbf{n}}_- \wedge \mathbf{H}_- \tag{2.105}$$

$$\mathbf{K}_{S-} = \mathbf{E}_- \wedge \hat{\mathbf{n}}_- \tag{2.106}$$

Taking the limit as the observation point approaches the surface from the inside, (2.102) gives an integral equation for the electric field on the interior surface.

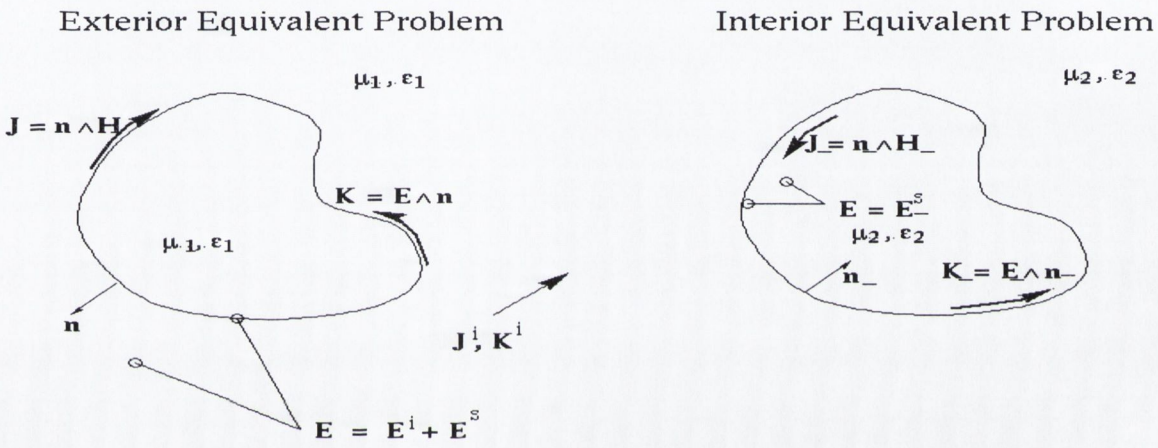


Figure 2-5: Internal and external equivalent problems for a homogeneous body.

A system of coupled equations may be formed by appeal to field continuity relations at the interface S. We need only deal with bodies having finite conductivity[13], ie where $\mathrm{Im}[\epsilon_c]$ is bounded. It will also be assumed that $\mathrm{Re}[\epsilon_c]$ is finite. Examining the fields depicted in Figure 2-6 where a small[14] rectangular box is drawn at the interface, we apply Stokes' theorem

$$\int_A \nabla \wedge \mathbf{U} \cdot \mathbf{dA} = \oint_C \mathbf{U} \cdot \mathbf{dl} \tag{2.107}$$

to the fields $\mathbf{E}$ and $\mathbf{H}$. Substituting $-i\omega\mu\mathbf{H}$ for $\nabla \wedge \mathbf{E}$,

$$\int_A \nabla \wedge \mathbf{E} \cdot \mathbf{dA} = -\int_A i\omega\mu\mathbf{H} \cdot \mathbf{dA} = \oint_C \mathbf{E} \cdot \mathbf{dl} \tag{2.108}$$

We allow that the length ΔL of the rectangle remains finite while its width and hence area tend to zero, and define vectors $\hat{t}$ upward tangential to the surface, and $\hat{p}$ upward

[13]The prescription for PEC surfaces has already been discussed

[14]compared to λ

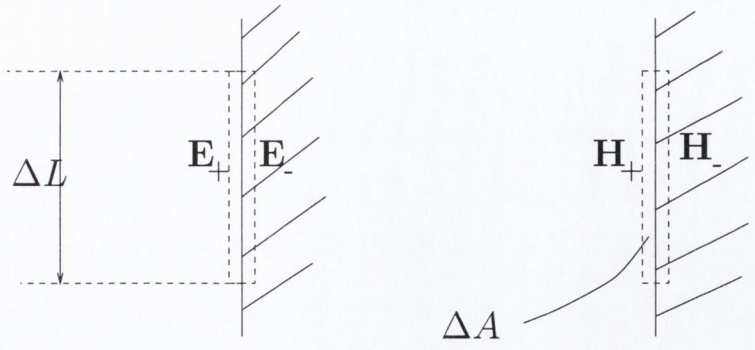


Figure 2-6: Continuity relation for **E** and **H** fields at surface boundary.

normal from the surface **A**, giving

$$-i\omega\mu_1\mathbf{H}_+ \cdot \hat{p}\frac{\Delta A}{2} - i\omega\mu_2\mathbf{H}_- \cdot \hat{p}\frac{\Delta A}{2} - = \mathbf{E}_+ \cdot \hat{t}\Delta L - \mathbf{E}_- \cdot \hat{t}\Delta L \to 0 \tag{2.109}$$

and given that $\mathbf{H}_+$, $\mathbf{H}_-$, μ_1, μ_2 and ω are finite, and ΔA vanishing, the LHS gives zero. This may only be satisfied where $\mathbf{E}_+ \cdot \hat{t} = \mathbf{E}_- \cdot \hat{t}$ and thus we have established the continuity of the **E** field at the boundary. A similar analysis holds for the magnetic field.

It is evident that tangential components of the electric and magnetic fields are continuous across the boundary, or

$$\hat{\mathbf{n}} \wedge (\mathbf{E}_+ - \mathbf{E}_-) = 0 \tag{2.110}$$

$$\hat{\mathbf{n}} \wedge (\mathbf{H}_+ - \mathbf{H}_-) = 0 \tag{2.111}$$

and so

$$\mathbf{K}_+ = \mathbf{E}_+ \wedge \hat{\mathbf{n}} = -(\mathbf{E}_- \wedge \hat{\mathbf{n}}_-) = -\mathbf{K}_- \tag{2.112}$$

$$\mathbf{J}_+ = \hat{\mathbf{n}} \wedge \mathbf{H}_+ = -(\hat{\mathbf{n}}_- \wedge \mathbf{H}_-) = -\mathbf{J}_- \tag{2.113}$$

Equations (2.79) and (2.101) now form a coupled system of equations for the electric field in terms of integrals over the same currents **J** and **K**. These are the coupled EFIE's (Electric Field Integral Equation)

$$\hat{\mathbf{n}} \wedge \mathbf{E}^i(\mathbf{r}) = -\mathbf{K}_1(\mathbf{r}) - \hat{\mathbf{n}} \wedge \left(\frac{\eta_1}{jk_1}(\nabla\nabla \cdot \mathbf{A}_1 + {k_1}^2\mathbf{A}_1) - \nabla \wedge \mathbf{F}_1\right)_{S^+} \tag{2.114}$$

$$0 = \mathbf{K}_1(\mathbf{r}) - \hat{\mathbf{n}} \wedge \left(\frac{\eta_2}{jk_2} (\nabla\nabla \cdot \mathbf{A}_2 + {k_2}^2 \mathbf{A}_2) - \nabla \wedge \mathbf{F}_2 \right)_{S^-} \tag{2.115}$$

and the coupled MFIEs

$$\hat{\mathbf{n}} \wedge \mathbf{H}^i(\mathbf{r}) = \mathbf{J}_1(\mathbf{r}) - \hat{\mathbf{n}} \wedge \left(\nabla \wedge \mathbf{A}_1 + \frac{\nabla\nabla \cdot \mathbf{F}_1 + {k_1}^2 \mathbf{F}_1}{jk_1\eta_1} \right)_{S^+} \tag{2.116}$$

$$0 = -\mathbf{J}_1(\mathbf{r}) - \hat{\mathbf{n}} \wedge \left(\nabla \wedge \mathbf{A}_2 + \frac{\nabla\nabla \cdot \mathbf{F}_2 + {k_2}^2 \mathbf{F}_2}{jk_2\eta_2} \right)_{S^-} \tag{2.117}$$

It is noted that the equations involve two different wave numbers k_1 and k_2 which in general may also be complex, for a lossy medium. Solving the problem through numerical discretization, care must be to sample at a sufficiently high frequency for both wavenumbers.

Chapter 3

3D Terrain Problem

This chapter outlines some recent solutions to the problem of propagation over irregular terrain, and the associated shortcomings of these methods, in particular, noting the advance towards accurate three dimensional modeling techniques.

Until very recently, in the absence of sufficiently efficient algorithms and the necessary computing power, terrain propagation has been modeled in a 2D approach, and many methods now exist for the solution of the 2D problem. The success of this approach depends on how invariant the terrain profile is in the transverse direction, and in favourable conditions almost perfect results may be achieved. A measure of the deficiencies of 2D methods is given by the relative errors such methods show against measurement. We note however that other factors such as buildings and vegetation may be the source of these errors. Experiment has shown directly [75] that 3D effects may make significant contributions. Successful as the 2D methodology has been, there can be little doubt that extending our description of the problem to fully characterize the three dimensional topography, and the vector characteristic of the EM field, will improve upon the accuracy of field predictions. In addition, multipath, fading, and delay spread, and polarization diversity characteristics may be investigated in a rigorous and deterministic manner.

This chapter is not intended as a detailed mathematical presentation. Instead, recent advances towards accurate 3D modeling are stated with particular reference to each of the three principal deterministic propagation methods, namely, GTD,

Differential Equation methods, and the principal method of this thesis, the Integral Equation method.

In all 3D terrain methods, radical approximations are required. It must be recalled however that the objective is to attain global coverage estimates and possibly other higher order channel characteristics. High resolution accuracy is not generally expected of field strength predictions, and local error levels of several dB are acceptable for mobile radio planning purposes. It must be remembered that factors other than terrain topography will influence field strength, such as buildings, vehicles, random and seasonal vegetation levels. It would be somewhat superfluous to strive for rigorously *exact* terrain modeling while these effects are ignored.

3.0.6 Topographical Propagation Effects

Propagation modeling for mobile communications is commonly subdivided into two domains. Long range macro-cell problems, where terrain variation tends to be the dominant factor, and short range, urban micro-cell environments, where scattering from buildings is the key concern. In this thesis we are interested in macro-cell propagation modeling. The terrain propagation problem is multi-faceted, and no single method can be said to tackle all its features. The surface topography may include hills, buildings, vegetation, and water amongst others features. On top of this, meteorological effects such as precipitation scattering/attenuation, and atmospheric ducting can come into play. Models of UHF and VHF ground wave propagation traditionally ignore these factors which are small at these frequencies (See Chapter 1), and they will henceforth be neglected from our consideration.

The principal effects influencing UHF/VHF terrain propagation, and those that should be accounted for in a deterministic scheme are,

- Line of sight propagation(LOS). Often the dominant propagation mechanism, where a LOS path exists between transmitter and receiver.

- Surface reflection, including reflection on the propagation axis, and off axial reflections.

- Diffraction over and around topographical features. Essential for the viability of mobile communications, providing coverage in geographical shadow regions
- Depolarization. The product of reflection/diffraction from inclined areas of terrain
- Building effects - diffraction, reflection, absorption, transmission.
- Vegetation effects - principally attenuation but occasionally also diffraction.
- Ground transmission/absorption - This is a very mild effect and can be modeled with an appropriate boundary condition. Likewise, for terrain inhomogeneity.
- Time variance of channel - effectively neglected in terrain problems, but will however be significant for a moving observer.

With adequate knowledge of the input parameters via traditional surveying, aerial photography, photogrammetric or GPS techniques, all of the above effects can be at least in part, included in the propagation model.

LOS transmission, axial reflection, and axial diffraction, are satisfactorily modeled using 2D schemes, within the approximation that terrain transverse gradients are zero. Moving beyond 2D then, of principal interest is how effectively we may model axial reflection and diffraction from transversely inclined regions of terrain and in addition, how we can account for off axial effects involving reflection, single or multiple, and diffraction. These contributions give rise to multipath and delay spread. Mild diffraction, scattering, and depolarization off glancing inclines will be the more commonly experienced phenomena in the terrain problem.

For our purposes terrain is judged to have a relatively sparse distribution of buildings and in the integral equation approach, these will be neglected, though they may be built into some terrain methods. Vegetation may have a more general distribution than buildings but again will be treated as sparse and is neglected in the initial formulation of the problem. In certain circumstances it may be accounted for *a-posteriori* with an additional attenuation factor dependent on local characteristics.

In general roughness will be neglected. It may be accounted for to some degree using a modification of the reflection coefficient that results in an additional attenuation of the coherently scattered field.

3.0.7 Hardware

To complete our description of the problem we must specify the communications apparatus. In a macro-cell, broad coverage is desired over ranges of up to 50km, and transmitters will be located on a high mast over a building or hill. Propagation will commonly be considered for a receiver at ground level with the mobile unit approximately 2 meters above that level. Unless otherwise specified, both transmitter and receiver will utilize vertical dipole antennas although the polarization of the receive antenna will naturally depend on its orientation, which is assumed to be upright.

3.0.8 Frequency Characteristics

Frequencies under investigation range from 144MHz to 1900MHz. For this range it is fair to say that terrain features are large by comparison with the wavelength, explaining the widespread application of high frequency techniques such as Ray Theory and GTD.

Modern communications systems are now principally digital and increasingly so, using wide band transmission. To accurately assess the effects of off axial propagation on the received signal, wide band modeling should be utilized. In GTD schemes such as ray tracing where off-axial reflections and diffractions are included, some characteristics of wide-band propagation may be inferred directly, by reference to path lengths, but the model must be considered approximate, as the theory of rays is fundamentally monochromatic, being based on continuous wave transmission.

For the differential equation and integral equation methods, the problem is first cast in continuous wave form. Provided accurate solutions are found at single frequencies, these may be used to evaluate the channel pulse response in the frequency domain, enabling the evaluation of wide band pulse response using the Fourier trans-

form. This is also possible with GTD methods. It will be deemed sufficient at this stage to find accurate solutions at single frequency, as this already presents considerable challenges. Once this is achieved, broad band analysis may readily follow.

3.0.9 Scalar/Vector Model

Electromagnetic fields are vector fields and in general a three dimensional terrain will couple vertical and horizontal polarizations. Where line of sight paths exist, or where terrain variations are small, the effect of this coupling will be negligible and is frequently neglected. Otherwise, significant *cross-polar* fields will exist and losses may arise in the *copolar* field. As such, any scalar modeling will give rise to systematic error. Correcting for this error is one of the goals of this thesis. Tackling the vector formulation invariably leads to more complex boundary conditions on the terrain surface. This is probably effected most easily in GTD, and is somewhat more complicated in differential equation and integral equation methods.

We now survey some present techniques for 3D terrain propagation.

3.1 Empirical Methods

The highly influential set of pathloss measurements made by Okumura et al. [53], and subsequent analysis by Hata, provide attenuation estimates for most problems although their principal concern was urban/suburban environments. Measurement based, they implicitly model 3D effects and are included for completeness. They used a parameter Δh denoting the difference in height between 10% and 90% points on a terrain height cumulative distribution function. They found terrain height variation led to an overall loss in field strength and an increase in variance. At 922MHz for $\Delta h = 50m$ they found a loss of 3dB over flat earth attenuation, with a variance of $\approx 10dB$ [24].

3.2 Geometrical Methods

Of all methods, the geometrical methods of Ray Optics, GTD [36], UTD [38] and PTD [69] provide perhaps the most intuitive picture of propagation phenomena, as they describe the progress of wavefronts through space and their subsequent interception, scattering, absorption, or diffraction and refraction. The methods of Geometrical Optics and Diffraction Theory introduce many concepts that help us greatly to understand the underlying mechanisms at play, and give many clues to how alternative methods may be understood and enhanced. Hence we make a slight digression to introduce some of its key features before returning to discuss geometrical methods recently applied to terrain.

The treatment of smaller objects and terrain may differ, but in all the methods the field at any point is given by the summation of all incoming rays which by appeal to Fermat's theorem will exist wherever there is an extremum in the path length from source, to obstacle, to observation point. Points along a ray wavefront have the same phase. The progress of a ray may be described in terms of the advance of that phase front, and a spatial attenuation factor due to the divergence of the ray, as

$$\mathbf{E}(\mathbf{r}) = \mathbf{E}_0 A(r) e^{-i\mathbf{k}\cdot\mathbf{r}} \tag{3.1}$$

$\mathbf{k}$ denoting the wavevector, where the ray has field strength and polarization $\mathbf{E}_0$ at its launch point, and the spatial spreading factor $A(r)$ depends on the range r from the ray launch point. $A(r)$ will also depend on the nature of that launch point, which may be a primary or secondary source of radiation. In some approaches, propagation over a terrain may be modeled by launching many of these rays from a source and following their progress as they interact with terrain features. This can lead to ray multiplication, which limits the number of subsequent scattering events that may be accounted for in the scheme.

3.2.1 Reflection

Having defined a ray, the first and simplest problem is to specify how it behaves at a planar interface. Provided the plane extends well beyond the region of interest or

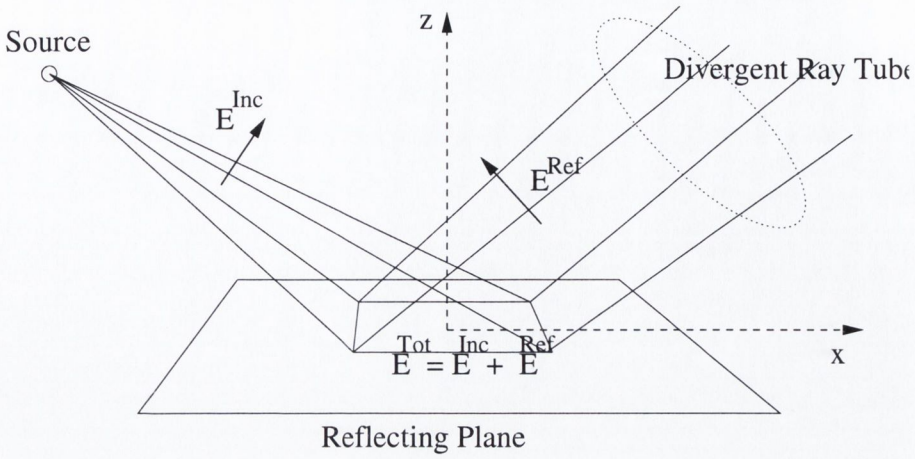


Figure 3-1: Reflection of a divergent ray tube from the central region of a flat plate

is large by comparison to the width of the ray tube in question, a simple reflection coefficient allows us to express the total field as a sum of incident and reflected rays, and by choosing a coordinate system aligned with the plane of incidence of the ray (Figure 3-1), we describe the total field for an incident wave, with explicit spatial dependence, $\mathbf{E}^{Inc}\, e^{-i(k_x x + k_z z)}$

$$\mathbf{E}^{Tot} = \mathbf{E}^{Inc}(e^{-ik_z z} + \mathbf{A}e^{ik_z z})e^{-ik_x x} \tag{3.2}$$

$$\mathbf{E}^{Tot} = (\mathbf{E}^{Inc}e^{-ik_z z} + \mathbf{E}^{Ref}e^{ik_z z})e^{-ik_x x} \tag{3.3}$$

where in general the reflection coefficient $\mathbf{A}$ is a matrix with polarization elements dependent on frequency, material parameters, and angle of incidence, and we distinguish it from $A(\mathbf{r})$, the spatial attenuation factor of (3.1), to which we will make no further reference.

3.3 Non Planar Features

Terrain features are modeled in terms of a limited set of canonical shapes, including plates, edges, wedges and cylinders. To account for the interaction of a ray with these shapes we introduce the Geometrical Theory of Diffraction.

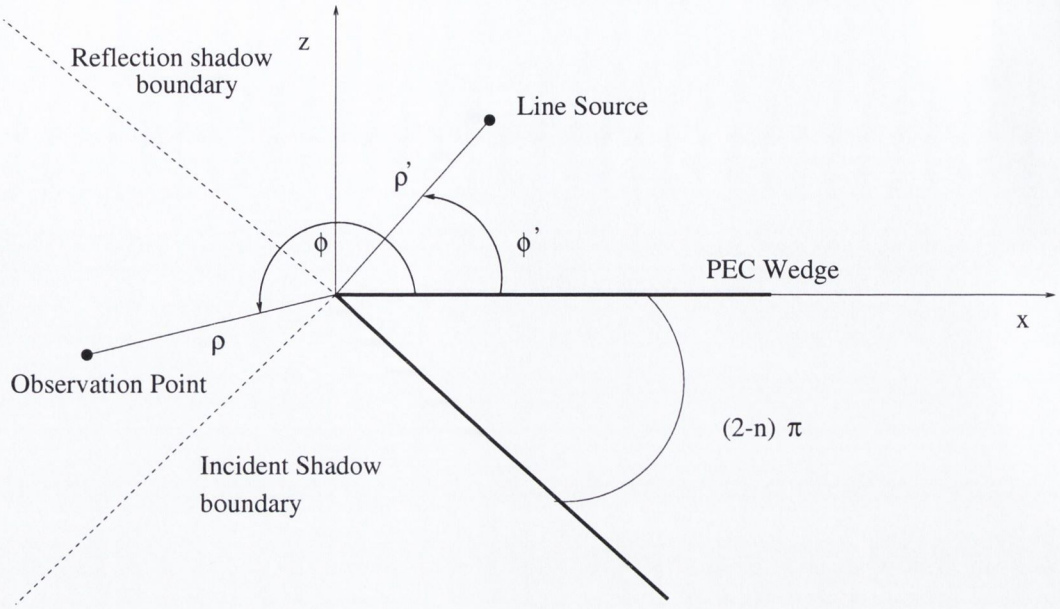


Figure 3-2: Geometry for wedge GTD

3.3.1 Geometrical Theory of Diffraction

Geometrical optics (GO), based only direct and reflected rays, is an approximate high frequency method for determining wave propagation and as λ approaches zero it becomes increasingly accurate, though at lower frequencies it is significantly in error as it predicts zero fields in the shadow regions. To explain the phenomenon of diffraction Keller postulated the Geometrical Theory of Diffraction (GTD)[36], which in addition to the fields of GO, includes diffracted rays. GTD solutions are derived by transforming the infinite series modal solutions available for canonical problems into contour integrals, the asymptotic evaluation of which provides the high frequency GTD solution. An introduction to GTD is given by Balanis [4].

We take the case of a PEC wedge illuminated by a TM_y line source, carrying an electric current I, and as such we will define a 2D diffraction scheme, which may be extended to 3D. Referring to Figure 3-2, the modal solution for the electric field E_y as,

$$E_y = -\frac{\omega\mu I}{4}\frac{1}{n}\sum_{m=0}^{\infty}\epsilon_m J_{m/n}(\beta\rho)\, H^{(2)}_{m/n}(\beta\rho')\left[\cos\frac{m}{n}(\phi-\phi') - \cos\frac{m}{n}(\phi+\phi')\right] \text{ for } \rho \leq \rho' \tag{3.4}$$

where

$$\epsilon_m = \begin{cases} 1 & m = 0 \\ 2 & m \neq 0 \end{cases} \tag{3.5}$$

For the case $\rho > \rho'$, ρ and ρ' are interchanged. This series converges slowly for large values of $\beta\rho$ and in such cases an asymptotic expansion in inverse powers of $\beta\rho$ is desirable. This is achieved by using the far field form of the Hankel functions and writing the Bessel functions as contour integrals, a process which transforms equation (3.4) into a contour integral amenable to evaluation via the method of steepest descent. Doing this, we arrive at a solution which is expressed in terms of a Geometric Optics field existing only in certain regions and a diffracted field which exists everywhere. The Geometrics optics field is given by

$$E_y^{GO} = \sqrt{\tfrac{2}{\pi\beta\rho'}} e^{-i\left(\beta\rho' - \frac{\pi}{4}\right)} \begin{cases} \text{Incident GO} & \text{Reflected GO} & \text{Region} \\ e^{i\beta\rho\cos(\phi-\phi')} & -e^{i\beta\rho\cos(\phi+\phi')} & 0 < \phi < \pi - \phi' \\ e^{i\beta\rho\cos(\phi-\phi')} & & \pi - \phi' < \phi < \pi + \phi' \\ 0 & & \pi + \phi' < \phi < n\pi \end{cases} \tag{3.6}$$

and the diffracted field, which exists everywhere in space, is given by

$$E_y^{GTD} = \frac{1}{n\pi\beta}\sqrt{\frac{1}{\rho\rho'}} e^{-i\beta(\rho'+\rho)} \sin\left(\frac{\pi}{n}\right) \left[\frac{1}{\cos\left(\frac{\pi}{n}\right) - \cos\left(\frac{\phi-\phi'}{n}\right)} - \frac{1}{\cos\left(\frac{\pi}{n}\right) - \cos\left(\frac{\phi+\phi'}{n}\right)} \right] \tag{3.7}$$

We note that equation (3.7) is invalid along $\phi = \phi' + \pi$ and $\phi = \pi - \phi'$ and gives unreliable answers in the *transition regions* around these lines, identified in figure 3-2 as the incident and reflected shadow boundaries respectively. This shortcoming is overcome by the Uniform Theory of Diffraction (UTD) [38] which, by evaluating the contour integrals using the Pauli-Clemmow modified method of steepest descent [17], introduces transition functions to remove the singularities associated with the shadow boundaries. The UTD solution for the diffracted field is

$$E_y^{UTD} = \sqrt{\frac{2}{\pi\beta\rho'}} e^{-i\left(\beta\rho' - \frac{\pi}{4}\right)} \left(V\left(\rho, \phi - \phi', n\right) - \quad V\left(\rho, \phi + \phi', n\right) \right) \tag{3.8}$$

where

$$V\left(\rho, \phi \mp \phi', n\right) = I_{-\pi}\left(\rho, \phi \mp \phi', n\right) + I_{+\pi}\left(\rho, \phi \mp \phi', n\right) \tag{3.9}$$

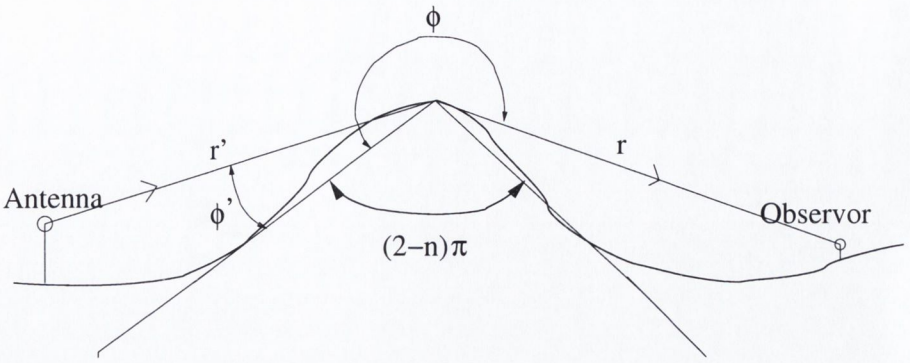


Figure 3-3: Wedge substituted for terrain peak on an undulating profile.

$$I_{\pm\pi}\left(\rho, \phi \mp \phi', n\right) \simeq \frac{e^{-i\left(\beta\rho+\frac{\pi}{4}\right)}}{jn\sqrt{2\pi}} \sqrt{g^{\pm}} \cot\left[\frac{\pi \pm (\phi \mp \phi')}{2n}\right] e^{i\beta\rho g^{\pm}} \int_{\sqrt{\beta\rho g^{\pm}}}^{\infty} e^{-i\tau^2} d\tau \quad (3.10)$$

where

$$g^{+} = 1 + \cos\left[(\phi \mp \phi') - 2n\pi N^{+}\right] \quad (3.11)$$

$$g^{-} = 1 + \cos\left[(\phi \mp \phi') - 2n\pi N^{-}\right] \quad (3.12)$$

with N^{+} or N^{-} being a positive or negative integer or zero which most closely satisfies

$$2n\pi N^{+} - (\phi \mp \phi') = \pi \quad (3.13)$$

$$2n\pi N^{-} - (\phi \mp \phi') = -\pi \quad (3.14)$$

These formulae may be extended to the case of 3D diffraction where the incident ray impinges on the wedge at some obliqueness angle β, defined as the angle between the line of incidence and the wedge vertex. For a point source excitation, the diffraction point on the wedge must first be identified, and is given by appeal to Fermat's principle. Formulae are given by Balanis [4].

The UTD solution is reliable in all regions but problems may arise where there are consecutive peaks in a profile, where the second peak lies in the transition region of the first, as the diffracted field is not adequately described by a plane wave. Such problems can be overcome by minor modification of the profile, or by utilizing a general uniform, double wedge diffraction coefficient [47]. Where one vertex is not sufficiently remote from another to be considered in its far-field, we are required to use slope diffraction formulae [4].

Diffraction over a hill top may thus be modeled, replacing the hill top with the vertex of a wedge. The total field over the terrain is given by the sum of direct, reflected and diffracted fields where such paths exist. The substitution of a wedge for an undulating terrain profile is illustrated in Figure 3-3.

3.4 Micro-cell

The combination of a theory of rays, reflections and diffractions is sufficient for the description of small urban micro-cells in most instances where topographical variations are small, or merely linear over the total range, and where buildings may be adequately constructed out of finite planar surfaces. GTD may also be extended to account for corners and curved edges. A large number of ray algorithms have been developed to model micro-cell propagation [57] [18] [20].

3.4.1 Curved Surface Diffraction

On occasions, particularly at low angles of propagation, hills may be approximated using edge/wedge diffraction. At considerable distances from the hilltop we are somewhat free in our choice of scatterer geometry, and may use a wedge or knife edge interchangeably.

This will not always be the case and frequently it will be more accurate to model a hill with a cylindrical arc, particularly where the hill is smooth, and gives rise to deep shadowing in the region only a moderate distance from the peak.

The asymptotic expression for high frequency scattering by a cylinder may be given by a series expansion where subsequent terms are identified with waves traveling further around the body of the cylinder. As the wave creeps around the cylinder it sheds energy, launching rays that propagate forward and away from the cylinder, along tangent lines. Where the creeping ray is deflected through an angle $\theta \geq (\lambda/\pi R)^{1/3}$, where R is the arc radius, energy loss through this ray launching is such that the asymptotic expression for the creeping wave fields may be approximated by the first term of the series expansion[30][52]. The trajectory of the ray is

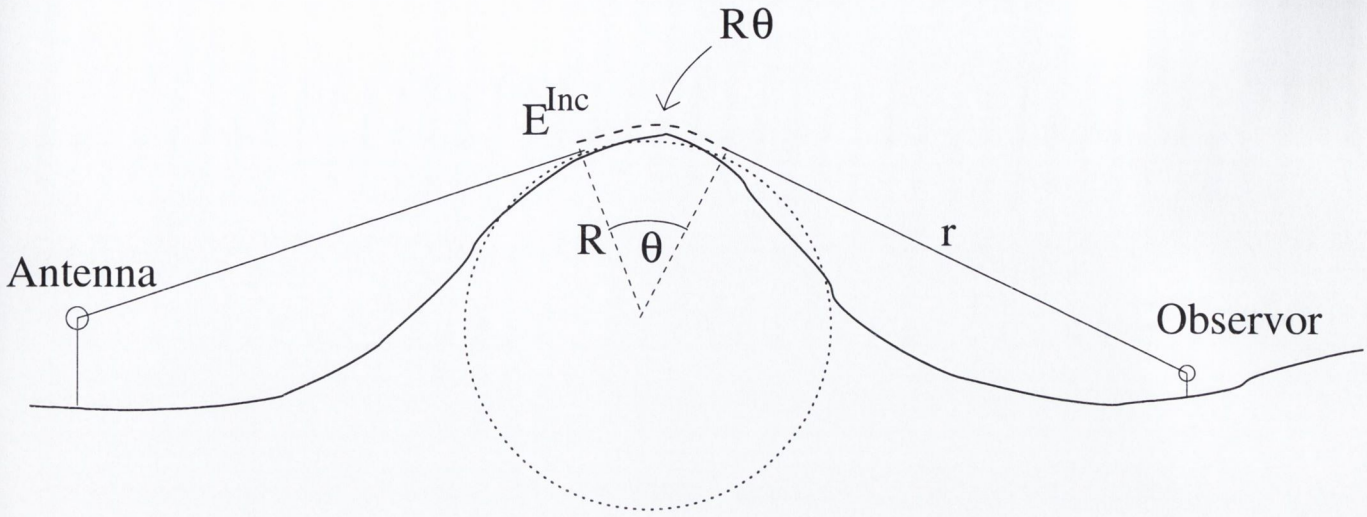


Figure 3-4: Creeping wave over a hill modeled using a circular cylinder.

that which grazes the surface, and may be envisaged in terms of a stretched piece of string connecting source, to observer over the hill[1](Figure 3-4).

As a result of the ray launching process the creeping wave suffers an exponential loss with θ. In addition, a diffraction coefficient couples the incident ray to the creeping wave, and the creeping wave to the scattered ray to give

$$\mathbf{E} = \mathbf{E}^{Inc} e^{-ik\theta R} \frac{e^{-ikr}}{\sqrt{r}} \frac{1}{\sqrt{k}} \mathbf{D} e^{-\phi\theta} \tag{3.15}$$

where for this polarization

$$\phi = \left(\frac{\pi R}{\lambda}\right)^{1/3} e^{i\pi/6} \times 2.338$$

$$D = \frac{1}{\sqrt{2\pi}} \left(\frac{\pi R}{\lambda}\right) e^{i\pi/6} \times 2.034$$

where r is the distance from the observer to the point from where the diffracted ray is launched, and where derivation of the constant coefficients from the series expansion may be found in [30] and [52], and these are dependent on the surface impedance. Perhaps the most significant feature is the exponential decay factor not found in other scattering geometries. Paths following a long angular arc are strongly attenuated. The same hill approximated in turn by a wedge, and a cylinder, will exhibit deeper shadowing in the latter case.

[1]These in fact constitute geodesic paths

Caution must be exercised however as the creeping ray approximation assumes a smooth, bare hill. The presence of buildings or vegetation can have a very significant effect on the overall attenuation [68] [22]. Some improvement may be achieved with a modification of D and ϕ in the light of additional knowledge of building and vegetation distributions[7].

Choosing the radius of cylinder to approximate a terrain peak presents problems and can lead to considerable variation in prediction. In one recently developed approach [55] a least squares method with a regression by parabola is used to find the radius of curvature at a terrain diffraction point. A selection criteria then determines if the diffraction point is to be modeled using a cylinder or a knife-edge 3.5. A cascaded series of such diffraction points is then used to model the terrain undulation. This constitutes an extension of the original cascaded cylinders method of Sharples and Mehler [63].

3.5 Fresnel/Kirchhoff Theory

Another approach providing an insight into propagation mechanisms, is that of Fresnel-Kirchoff diffraction. We consider a point source of scalar type, at considerable distance illuminating an aperture in an absorbing screen (Figure 3-5). The incident field is given

$$\phi^{Inc} = A\frac{e^{-ikr_0}}{r_0} \tag{3.16}$$

We impose several approximate conditions[2] advanced by Kirchoff, on the screen Ω_S and aperture Ap, namely that

- The incident field in the aperture is unperturbed by the presence of the screen.
- On the screen Ω_S, ϕ and its normal derivative $\frac{\partial \phi}{\partial n}$ vanish.
- A closed surface Ω is formed by the union of a fictitious hemispherical surface Ω_∞, receding to infinity, with the screen Ω_S and the aperture Ap. It is evi-

[2]Solutions to hyperbolic partial differential equations, such as the wave equation, are overdetermined if boundary conditions on the field and its normal derivative are both prescribed independently over a closed surface

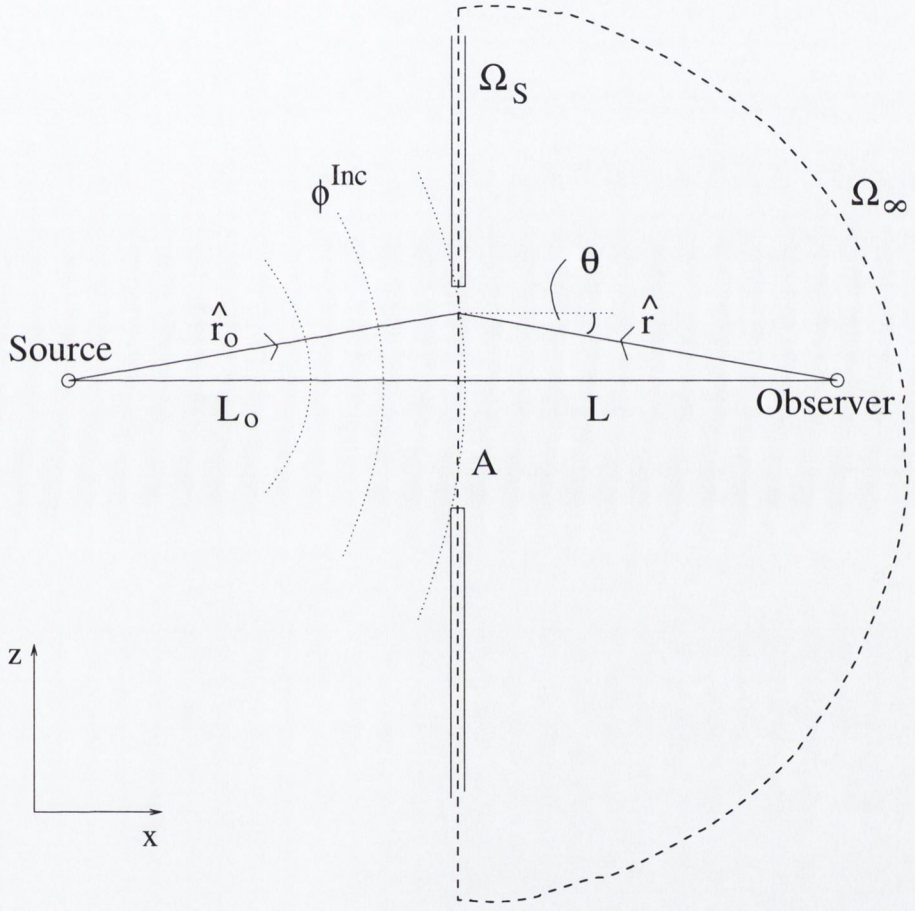


Figure 3-5: Diffraction of spherical wavefront through a planar aperture.

dent that as this boundary recedes to infinity, ϕ and $\frac{\partial\phi}{\partial n}$ on Ω_∞ may be made arbitrarily small as $\frac{1}{r}$. Further, considering the free space Green's function factor, the integrand will shrink as $\frac{1}{r^2}$. However, as the area of the receding hemispherical surface increases with $\frac{1}{r^2}$, we may not discount the integral from this boundary without some further assumption of the field on Ω_∞. Born[8] utilizes the fact that in any real problem the excitation may only have existed for some finite duration in time, and hence as the boundary may recede arbitrarily to infinity, we may consider that the excitation has not yet arrived at this boundary, and that the fields there are zero. This departure from pure monochromaticity[3] is not strictly necessary but shortens the discussion. In fact the radiation condition implies that the bracketed term in (3.17) will shrink as $1/r^3$ on the boundary, the two terms in brackets being almost equivalent as the angle between the vectors $\nabla\frac{e^{-ikr}}{r}$ and $\nabla\phi$ approaches π.

Using these approximations we apply Green's theorem to form the Helmholtz-Kirchoff integral equation for the field ϕ at an observation point, in terms of its normal derivative over the closed surface

$$\phi = \frac{1}{4\pi}\int_\Omega \left(\phi\nabla\frac{e^{-ikr}}{r} - \frac{e^{-ikr}}{r}\nabla\phi\right)\cdot\hat{\mathbf{n}}d\Omega \tag{3.17}$$

$$= \frac{1}{4\pi}\int_{Ap} \left(\phi^{Inc}\nabla\frac{e^{-ikr}}{r} - \frac{e^{-ikr}}{r}\nabla\phi^{Inc}\right)\cdot\hat{\mathbf{n}}dAp \tag{3.18}$$

If r and r_0 are large compared to the wavelength of the radiation, and substituting (3.16)

$$\phi = \frac{-iAk}{4\pi}\int_{Ap}\frac{e^{-ik(r+r_0)}}{rr_0}(\hat{\mathbf{r}} - \hat{\mathbf{r_0}})\cdot\hat{\mathbf{n}}dAp \tag{3.19}$$

This is known as the Fresnel-Kirchoff diffraction integral. The same idea may be applied where the relationship between the field on the aperture and its derivative is sufficiently simple, as in the case of a normally[4] incident plane wave Ae^{-ikx}

$$\phi = \frac{-ikAe^{-ikx'}}{4\pi}\int_{Ap}\frac{e^{ikr}}{r}(1+\cos\theta)dAp \tag{3.20}$$

[3] Alternatively we might envelope the radiation field by assuming a small material absorption in the spatial medium.

[4] The wave does not need to be normal

In two dimensions and where $\theta = 0$ this reduces to

$$\phi = -Ae^{-ikx'}\sqrt{\frac{i}{\lambda}}\int_{-a}^{a}\frac{e^{-ikr}}{\sqrt{r}}dz \tag{3.21}$$

where the aperture is of width $2a$. This allows us to extend the method to any incident field that may be expanded as a spectrum of plane waves. The method may be used to characterize scattering over building roof tops, or over terrain, where a hill may be modeled either with a single screen, or with a succession of screens at regular sampling intervals as in the method of Vogler [71], following the contour of the profile (Figure 3-6) and where the top of the aperture recedes to infinity. On each successive screen the field and its first derivative are set to zero. As the upper boundary recedes to infinity we require some method to truncate the integration domain, and the more rapidly this truncation can be effected the faster the numerical solution will be. The effect of simple truncation is to create spurious reflections from the upper boundary. Walfisch and Bertoni [72] suggest a gradual tappering of the field to prevent abrupt discontinuity. Whitteker [73] adds a small imaginary component to the wavenumber above a certain height, which may physically interpreted as adding a small material loss to the propagation medium. In addition Whitteker proposes bridging the terrain gaps between the knife-edges in order to more accurately model surface reflection effects.

The solution is marched forward from screen to screen. It is therefore an intrinsically forward scattering method.

3.5.1 Fresnel Zones

Another important concept that should be introduced at this stage is that of Fresnel zones. If we now consider a two dimensional aperture, symmetric about $z = 0$, as depicted in Figure 3-7 and where a is small compared to L, and ξ is an integration variable on the aperture, then we make the approximations

$$r = \sqrt{(z-\xi)^2 + L^2} = L\sqrt{1 + \frac{(z-\xi)^2}{L^2}}$$

$$\simeq L + \frac{(z-\xi)^2}{2L}$$

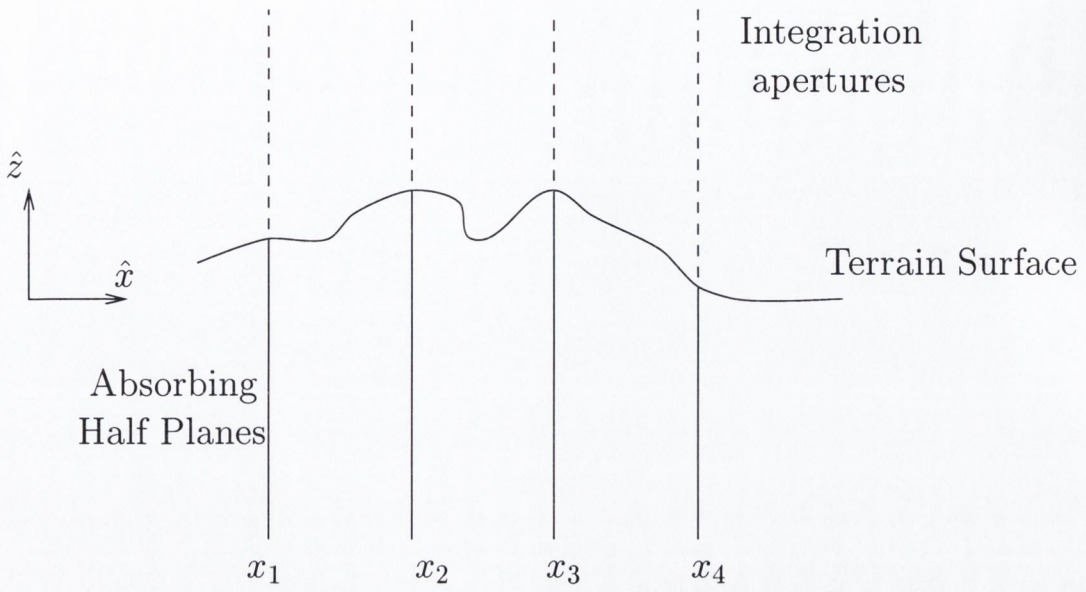


Figure 3-6: Terrain diffraction using absorbing half planes. Numerical integration over each aperture, truncated at the upper boundary, provides the field over the next aperture and so on.

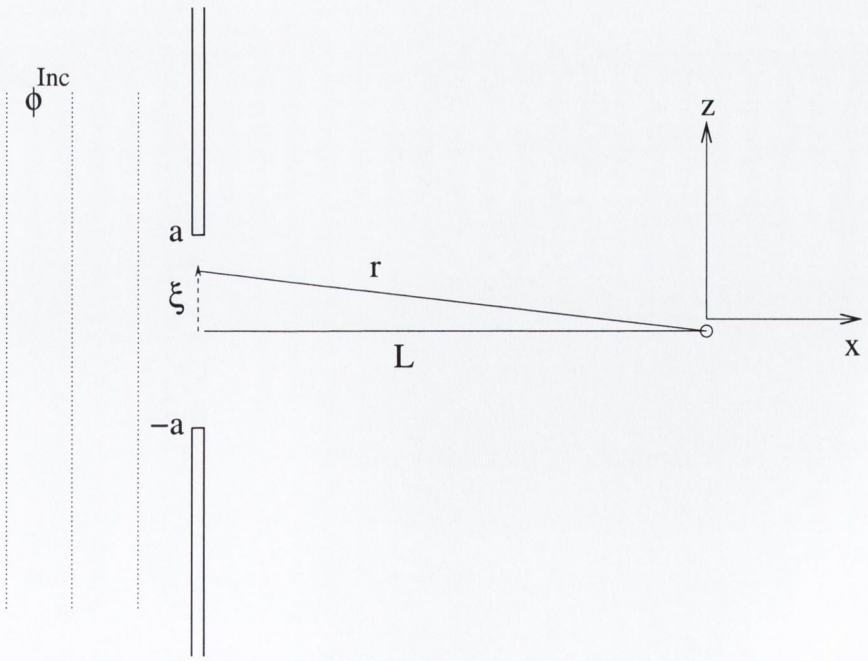


Figure 3-7: Illumination of a small aperture by a plane wave.

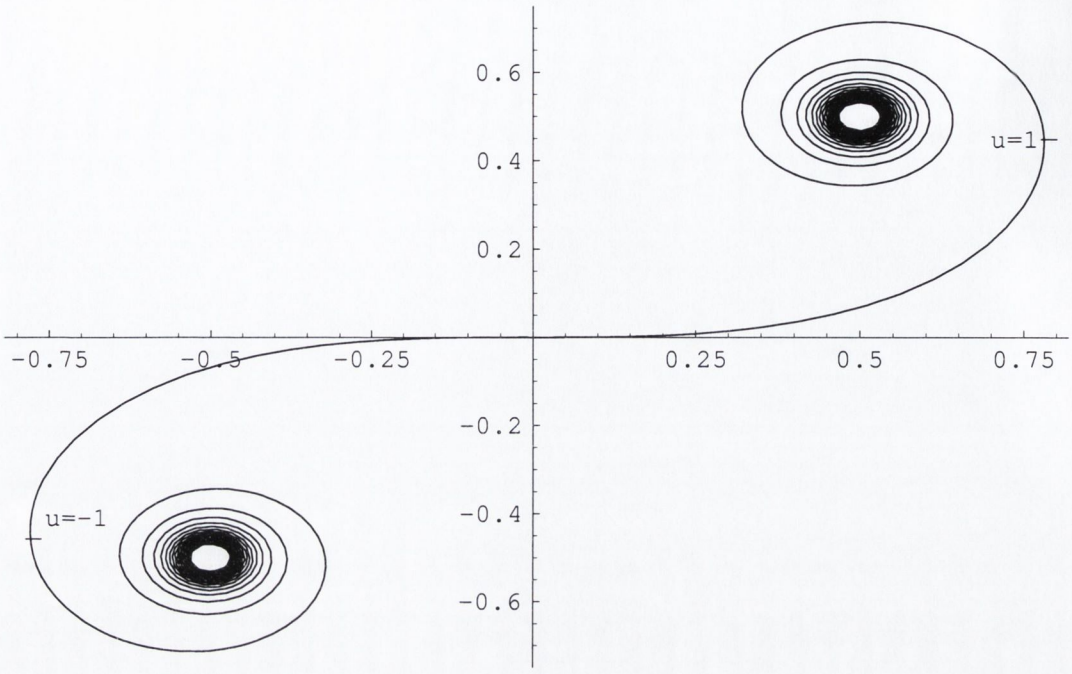


Figure 3-8: Cornu spiral for $0 <| u |< 10$

Considering the observation point at $z = 0$, we expand the integrand of (3.21)

$$\frac{e^{-ikr}}{\sqrt{r}} \to \frac{1}{\sqrt{L}} e^{-ik(L+\frac{\xi^2}{2L})} = \frac{e^{-ikL}}{\sqrt{L}} e^{-ik\frac{\xi^2}{2L}} \tag{3.22}$$

and factorizing functions of L out of the integral the field strength is given as

$$\phi = -A\sqrt{\frac{i}{\lambda L}} e^{-ikL} \int_{-a}^{a} e^{-ik\frac{\xi^2}{2L}} d\xi \tag{3.23}$$

Substituting $u = \sqrt{\frac{2}{\lambda L}}\xi$

$$\phi = -A\sqrt{\frac{i}{2}} e^{-ikL} \int_{u(-a)}^{u(a)} e^{-i\pi\frac{u^2}{2}} du \tag{3.24}$$

This integral is a complex sum of the Fresnel Integrals

$$S(u) = \int_0^u \sin\frac{\pi}{2}u^2 du \qquad C(u) = \int_0^u \cos\frac{\pi}{2}u^2 du$$

A parametric plot of $C(u)$ against $S(u)$ in the complex plane traces a curve known as the Cornu Spiral[5] shown in Figure **??**. It is evident that

$$C(u) = S(u) = -S(-u) = -C(-u) \to \frac{1}{2} \quad as \quad u \to \infty$$

[5]Introduced by M. Alfred Cornu in 1874

The integral in (3.23) is given by the vector connecting the points where $u = \pm u(a)$ where Figure 3-8 represents the Argand plane. The spiral tightens rapidly for larger $\mid u \mid$ and hence the integrand contributes less and less to this vector. In terms of the aperture the integral converges for finite symmetric apertures as they increase in size. This is because contributions from larger values of $|\xi|$ and hence $|u|$ are oscillatory in phase and tend to cancel each other, while systematically decreasing in size. The decrease in size is due to both the obliquity factor, and the increased range r. The value of ξ such that $r - L = \frac{n\lambda}{2}$ defines the point on the aperture giving a contribution shifted by $\frac{n\pi}{2}$ from the contribution at $\xi = 0$. For $n = 1$ this corresponds to a value of $u = 1$, and denotes the half width of the first Fresnel zone. These points are illustrated in Figure ?? and it is evident that they give a first order approximation to the limiting value where $u \to \infty$. The approximation improves as n increases and the aperture encloses a successively higher number of Fresnel zones.

This property of the 1 dimensional integral over a paraxial wavefront will be exploited later in the thesis and Fresnel zones, along with Fermat's principle, may be used to identify the principal areas contributing to a scattering integral.

3.6 General Examples

A terrain can be replaced by a set of canonical shapes. This is illustrated in Figure 3-9 in a 2D representation. With the first hill modeled by a wedge, and the second modeled by a cylinder, the field beyond the second hill is the product of multiple diffraction, with additional contributions arising due to reflections off the planar regions. It is seen that each successive scattering event introduces additional ray paths and in some situations very many of these paths will make a significant contribution. The picture is further complicated as we move to three dimensions, but with that said, at present, geometrical methods provide the most complete picture of 3D scattering, from either medium sized building environments or terrain.

In figure 3-10 we indicate some possible ray paths arising on a 3D terrain. In this case we have reflection by near planar surfaces, and diffraction over and around a smooth hill feature. The hill edges may be modeled using canonical shapes, but

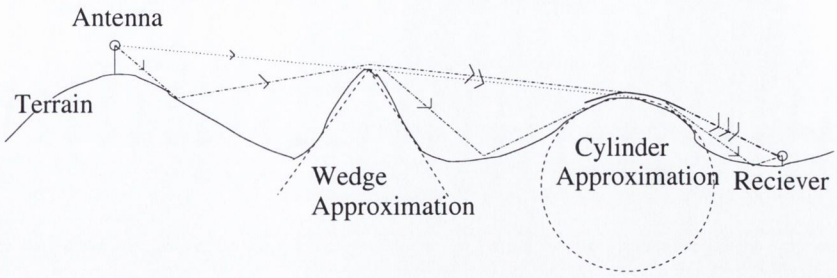


Figure 3-9: Approximation of terrain by canonical shapes, indicating multiplication of rays. Here that number is limited by the low number of diffraction and intervening reflection points.

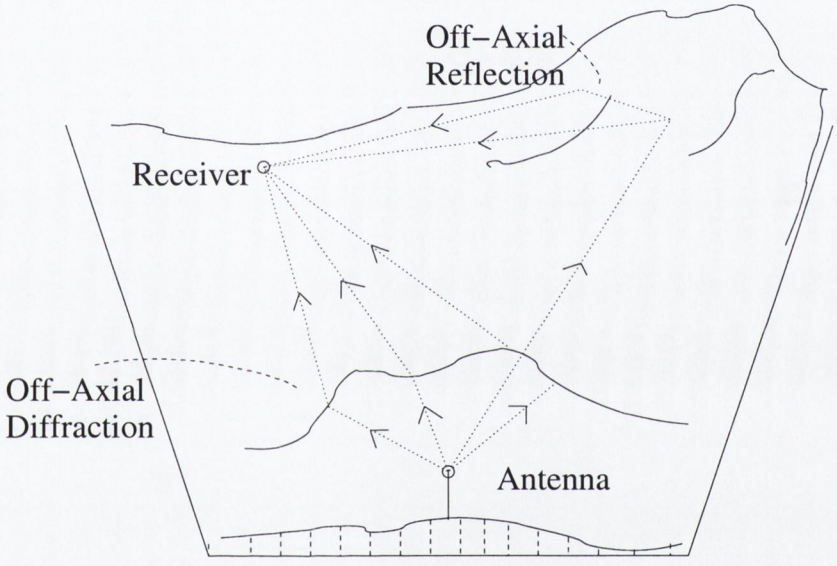


Figure 3-10: Off axial reflection and diffraction caused by multipath.

here the hill in the foreground presents several diffracting edges, inclined transversely to the direction of ray propagation. The most appropriate points of diffraction may be found employing a generalization of Fermat's Principle. The correct diffracting obstacle, wedge or cylinder, and its precise dimensions, and inclination angle must be carefully determined to attain accurate results in both near and far field regions. The reflection points are simpler to treat, but may become very numerous.

We now supply further details of two recent 3D GTD methods.

3.6.1 Example Method 1

A 3D integrated, macro and microcellular propagation model is reported by Tameh and Nix [19]. A terrain is represented as a connected set of trapezoidal tiles which we will refer to as pixels, each with large size by comparison with λ^2. In addition, the walls and roofs of buildings are likewise represented by planar scattering pixels. The profile discretization has a variable degree of resolution, zones of reduced resolution corresponding to concentric ellipses ranging outwards from source and receiver, where source and receiver locations define the foci of the ellipses. Hence this is a point to point ray method. Diffractions are computed in this model using UTD and hence we discuss it in this section. The method is however, a hybrid UTD/Radar Cross-section method.

Where a direct path exists from source to pixel to observation point, the scattering contribution is evaluated using the radar equation. This is a generalization of the plane wave reflection coefficient to cases where the reflecting surface is small compared to the overall problem geometry. The scattered field from a pixel is given in terms of an angular distribution of rays. The radar cross section describes the scattering from a pixel in terms of the far field plane wave amplitude σ scattered at angle θ_r, in terms of incidence angle[6] θ_i and θ_r where due consideration must be taken of the polarization of the incident field. The scattering cross section is tabulated for a standard plate and frequency. Terrain pixels will be approximated by this reference plate. The same approach has been used in 2D integral equation methods such as the Tabulated Interaction Method [11], where the interactions are given by the radar cross section of a 2D strip.

Where a direct path does not exist from the reflecting pixel to the receiver, the level of diffraction along the intervening path is evaluated. Only single reflections off terrain pixels are included but when this is combined with the diffraction effects, the method does include multiple scattering[7].

Diffraction around off axial geographical features (Figure 3-10) is not modeled.

[6] Angles are measured to the pixel normal

[7] In the sense of the scattered field integral of the integral equation

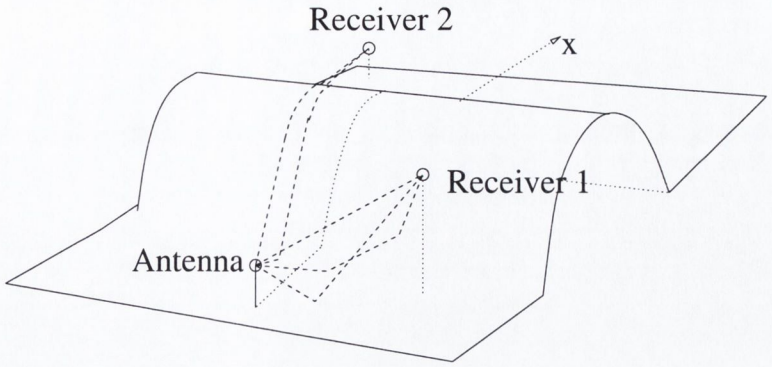


Figure 3-11: Multiple ray paths to two receivers for a 3D cylinder.

Also, cylindrical and spherical diffraction effects are not accounted for. The method is however ambitious in its scope, and goes as far as to work out path length propagated through foliage for each ray. The authors verify the considerable significance of this feature indicating foliage attenuations of up to $20dB$. Less clear is the benefit of modeling off axis effects, which appear to act principally as a smoothing effect, evening out deep shadowing, by the provision of alternative propagation paths. Of additional interest would be a quantification of the effect of neglecting buildings only, in rural areas.

3.6.2 Example Method 2

In another approach developed by Kam and Chew [35], GO and UTD are used in a ray scheme, where hilltops are modeled using cylindrical diffraction. They generalize the UTD formulation for a dielectric cylinder to 3D. Diffraction may be computed for paths crossing the cylinder obliquely as in Figure 3-11. From the generalization of Fermat's principle the path from source to observation point is a geodesic. The arc radius along this path must be computed to evaluate the level of diffraction. Such a scheme offers a method for evaluating effects such as diffraction around the shoulder of a hill as illustrated in Figure 3-10. Implementation for real terrain is likely to be cumbersome and not all profiles will readily lend themselves to description in terms of canonical geometric forms.

All of the above methods have significant shortcomings, notably the low order of scattering that is accounted for, and the adoption of the high frequency approximation. How limiting this will be, will depend on the problem geometry. Also, by the utilization of canonical shapes, we are not only using approximate propagation models, but a crude approximation to the topography itself. The error introduced here will depend on how amenable the terrain is to any canonical representation. Simple GTD methods are fast, but in the more elaborate schemes the multiplicity of rays is considerable. The necessary book keeping can be complex, and ultimately time consuming.

3.7 Differential Equation Methods

Derived from the most basic statement of the electromagnetic problem in terms of Maxwell's equations, differential equation methods can at least in theory provide exact solutions. In some cases, such as the Parabolic Equation, approximations will be made from the outset. Essentially this class of methods can be subdivided into Finite Difference Methods (Frequency Domain and Time Domain), and variational Finite Element methods.

3.7.1 Finite Element Method

This method involves subdividing the problem domain into simpler elements over which the differential equation may be satisfied. Some functional $F(\mathbf{E})$ is considered, which is stationary with respect to the solution $\mathbf{E}$. $\mathbf{E}$ may then be found by enforcing

$$\delta F(\mathbf{E}) = 0$$

when the appropriate boundary conditions have been applied. The resulting matrix is sparse and can be efficiently solved and stored.

The variational finite element method finds limited application for large problems like terrain, where the scattering body can be well modeled using a simple boundary condition. This leads to the reduction of order from a volumetric, to a surface

scattering problem. Although FEM can be applied using a surface boundary condition, rather than solving the equation inside the boundary, the necessity to satisfy the radiation condition and couple in the incident field, means that a large problem volume must be considered, exterior to the scatterer. Sparse as the matrix may be, it it likely to be excessively large for efficient solution. The method is ideal however, for inhomogeneous penetrable bodies, where the procedure is almost identical to the homogeneous case.

3.7.2 Finite Difference Methods

The problem domain, including the terrain surface and a substantial region of space above it, are discretized in the form of a grid. Derivatives of the field at points on the grid are given in terms of the fields and derivatives at neighbouring points, as finite differences. This yields a set of matrix equations which may be solved by a Crank-Nicholson scheme [25][48], after the imposition of boundary conditions. Commonly an impedance or PEC boundary condition may be applied at the terrain surface and a radiation condition on the space boundary. The matrix is sparse but once again, it is unmanageably large even for modest terrain problems as the entire matrix must be stored and solved simultaneously. This problem may be overcome if some approximation may be made to the wave equation which will render the finite difference matrix lower triangular. This is achieved in the Parabolic Equation method.

3.7.3 The Parabolic Equation

This is a popular terrain propagation and radar modeling method. For an excellent overview of this method see [44]. Making a paraxial approximation to the elliptic wave equation, it may be reduced to a parabolic form. This allows us to solve the equation over the problem domain in a step marching procedure given initial conditions and appropriate conditions on the terrain and upper space boundaries. Forward steps may be performed extremely efficiently using a Fourier Split[23] Step algorithm for both flat [37] and undulating [31] 2D surfaces. One feature of this method is the

simple fashion in which atmospheric inhomogeneity may be handled. This is not of primary concern here, and we state instead the 3D parabolic equation for propagation along a predominant direction $\hat{\mathbf{x}}$, where the spatial permittivity is that of free space[8],

$$\frac{\partial u}{\partial x}(x,y,z) = \frac{i}{2k_0}\left(\frac{\partial^2}{\partial z^2} + \frac{\partial^2}{\partial y^2}\right) u(x,y,z) \tag{3.25}$$

where u represents the reduced form of the scalar field

$$\phi = ue^{-ik_0 x}$$

with the fast phase factored out. Writing (3.25) in terms of finite differences yields the matrix equation [75]

$$\mathbf{A}U_{n+1} + U_{n+1}\mathbf{B} = \mathbf{D}U_n + U_n\mathbf{E} \tag{3.26}$$

where U^n is the matrix containing the values of u_n at each mesh point on screen n, and $\mathbf{A}$, $\mathbf{B}$, $\mathbf{D}$ and $\mathbf{E}$ are matrix operators. Each forward step requires the solution of this system, which may be solved by the method of Finite Differences using a Crank-Nickolson scheme. Zelley and Constantinou [75] have developed such a method for undulating 3D terrain. Other 3D parabolic equation solvers have been developed principally in underwater acoustics[40].

One difficulty however, is the treatment of the surface boundary. (3.25) describes a scalar field, which will be taken as representing the vertical polarization. In a 2D scheme it is not necessary to resolve the vertically polarized field at the terrain boundary. In the 3D extension, this is necessary to evaluate the vertically and horizontally polarized fields in the transverse plane(Figure 3-12. b)[9]

The vertically polarized component in the transverse plane should be resolved with respect to the surface normal and tangent vectors, in that plane, and the appropriate boundary condition applied for horizontal and vertical field components. This can not be achieved in a scalar description. The authors allowed that when the inclination of the terrain in the transverse plane exceeds 45%, the horizontal polarization boundary

[8] Any value might have been taken provided the space is homogeneous

[9] The problem of mesh points and terrain being non-coincident is not addressed here. A novel method of dealing with this has been proposed [75].

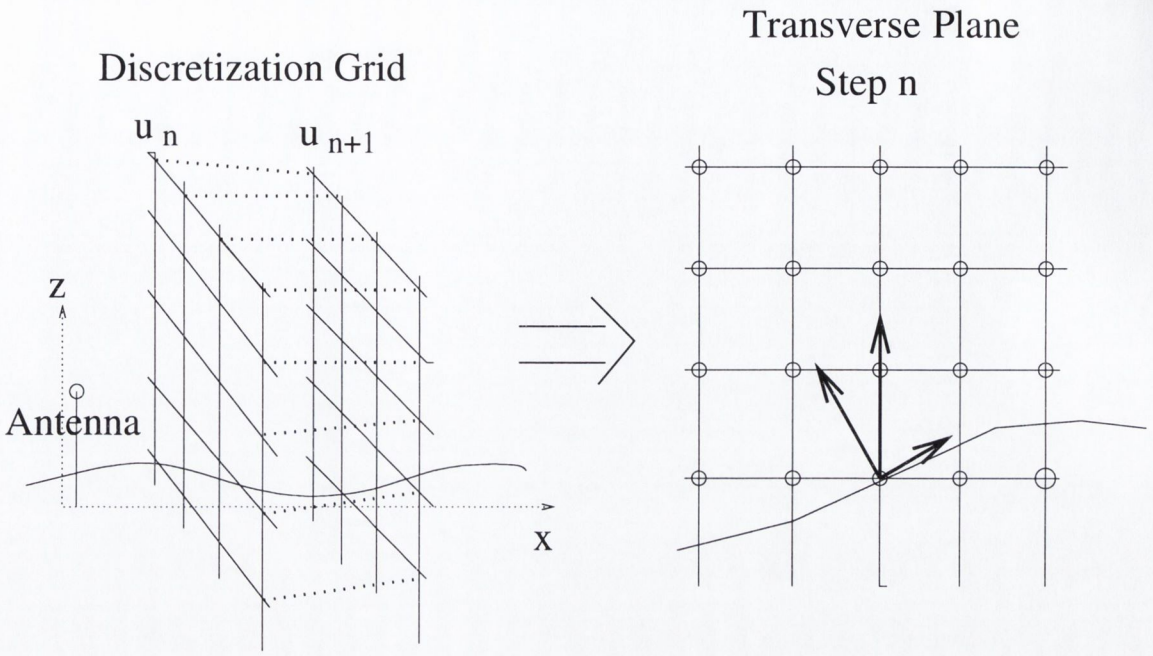


Figure 3-12: (a) Succession of 2D meshes forming the Parabolic Equation grid steps. (b) Problem of the scalar approximation to the vector field in the presence of transverse gradients

condition is applied. It is noted that such situations are extremely unlikely to arise and essentially this means the vertical polarization boundary condition is used at all times for each component. Using identical boundary conditions in this fashion has the effect of ignoring depolarization as the polarization vector suffers no rotation. With no energy coupled into the *cross-polar* field, the method has a tendency to overestimate the total *copolar* field.

Comparison made with measurements in an anechoic chamber indicated diffraction around an obstacle, the test case being PEC pyramid (4.25λ in height, 20λ wide and $\approx 80\lambda$ in length), can be well accounted for. It is noted that the test case is unlikely to be representative of a terrain geometry where gradients will be less extreme and sharp edges will not be present. As we saw earlier, these tend to increase the diffracted field strength in shadow regions. They do however present some results showing moderate improvement for undulating terrain, achieving a 7dB error reduction on one test profile, particularly where 2D algorithms are guilty of underestimation, a strong indication of off axial diffraction. Again the 3D diffraction

effects appear to smooth out deep shadowing to some degree. The model failed to show significant improvement at higher frequency and where the terrain was more mountainous, and it is suggested that this may be due to depolarization effects, further indicating the desirability of modeling such phenomena. Presumably also, off axial diffraction effects are reduced as the frequency is increased.

Levy [74] has also developed a 3D vector parabolic equation algorithm, at present limited to the treatment of smaller closed objects, for radar cross section analysis. In this case a coupled system of three scalar equations was used to model the electromagnetic interaction.

A drawback of both of the above treatments is that they require the solution of a matrix equation at each step, and this is performed using an iterative solver. This is computationally expensive. Some advantage may be gained if the problem may be recast in a form amenable to solution by the Fourier Split Step algorithm [37]. The author is at present unaware of such an implementation in a 3D terrain scheme. In addition it may be necessary to employ wide angle parabolic equation methods [43] to properly account for terrain multipath, and these are inevitably more computationally costly.

3.8 3D Integral Equation

In Chapter 2 it was shown that 3D scattering from an entirely general penetrable or impenetrable body, may be expressed in terms of a system of coupled integral equations (2.117). For a terrain problem the body in question is the terrain itself. Assuming either (a) that some energy is absorbed in the spatial medium, or (b) that transmission is for some finite duration, we may assume that at large distances from the source the fields are small and no energy is flowing back into the problem from beyond a certain range R[10]. Equation (2.117) may then be written in closed form as

$$\hat{\mathbf{n}}\wedge\mathbf{H}^{Inc}(\mathbf{r}) = \mathbf{J}_1(\mathbf{r}) - \hat{\mathbf{n}}\wedge\left(\nabla\wedge\int_{S(R)}\mathbf{J}G_1 dS + \frac{(\nabla\nabla\cdot + k_1^2)\int_{S(R)}\mathbf{K}G_1 dS}{jk_1\eta_1}\right) \tag{3.27}$$

[10]Later, a zero backscattering approximation may be adopted but this is not required to close the integral for a boundary receding to infinity

$$0 = -\mathbf{J}_1(\mathbf{r}) - \hat{\mathbf{n}} \wedge \left(\nabla \wedge \int_{S_-(R)} \mathbf{J} G_2 dS_- + \frac{(\nabla\nabla) \cdot + k_2^2 \int_{S_-(R)} \mathbf{K} G_2 dS_-}{jk_2\eta_2} \right) \tag{3.28}$$

where $S(R)$ denotes the earth/air interface lying within the range R, and $R \to \infty$. Where source and observation points are coincident, the scattered field is evaluated as we approach the surface along the exterior normal for S, and along the interior normal for S_-.

The integration is necessarily truncated to the region of interest or perhaps slightly beyond that desired region. Provided the flow of energy at the perimeter is predominantly outward from the transmitter we may still expect accurate predictions near the perimeter. The equations must now be converted into a discrete matrix system for numerical solution.

3.9 The Method of Moments

The principal tool that will be employed here to solve (3.27) and (3.28) is the Method of Moments(MoM). For an extended review of the MoM, the reader is referred to [59]. Any integral equation arising in electromagnetic wave scattering may be expressed as

$$L(f) = g \tag{3.29}$$

where L is an operator, g is the source or excitation (known function) and f is the field or response (unknown function to be determined). A problem of analysis involves the determination of f when L and g are given.

To introduce the Method of Moments, a definition of the inner product $\langle \cdot, \cdot \rangle$ of two functions is needed. The inner product is a scalar chosen to satisfy

$$\langle f, g \rangle = \langle g, f \rangle \tag{3.30}$$

$$\langle f, f^* \rangle \geq 0 \tag{3.31}$$

$$\langle \alpha f + \beta g, h \rangle = \alpha \langle f, h \rangle + \beta \langle g, h \rangle \tag{3.32}$$

where α and β are scalars and $*$ denotes a complex conjugate. The Method of Moments is a general procedure for solving equations $L(f) = g$. Let f be expanded in a series of functions $\{f_1, f_2, \cdots\}$ in the domain of L, as

$$f = \sum_n \alpha_n f_n \tag{3.33}$$

where the α_n are constants. The f_n are called *basis functions.* Hence the equation to be solved becomes

$$\sum_n \alpha_n L(f_n) = g \tag{3.34}$$

It is assumed that a suitable inner product $\langle f, g \rangle$ has been defined for the specific problem. A set of *test functions* [11] $\{w_1, w_2, \cdots\}$ is now defined and the following operation is performed

$$\sum_n \alpha_n \langle w_m, Lf_n \rangle = \langle w_m, g \rangle \tag{3.35}$$

with $m = 1, 2, \cdots$. This set of equations may be written in matrix form as [12]

$$\sum_n L_{mn} \alpha_n = g_m \tag{3.36}$$

or

$$L\alpha = g \tag{3.37}$$

where [13]

$$L = [L_{mn}] = [\langle w_m, Lf_n \rangle] \tag{3.38}$$

$$g = [g_m] = [\langle w_m, g \rangle] \tag{3.39}$$

The solution is then given by

$$\alpha = L^{-1} g \tag{3.40}$$

provided that the matrix L is non-singular. The solution

$$f = \sum_n \alpha_n f_n \tag{3.41}$$

may be exact or approximate depending upon the choice of the basis and test functions.

[11] The particular choice $w_n = f_n$ is known as Galerkin's method.

[12] Observe that the matrix may be either of infinite or finite order, depending on the definition of basis and testing functions.

[13] To express a vector v, the following notation is employed: $v = [v_n] = [v_1, v_2, \cdots]$.

3.9.1 Point matching

The integration involved in evaluating $\langle w_m, Lf_n \rangle$ of (3.38) is often difficult to perform in problems of practical interest. A way to obtain an approximate solution of (3.34) is to force the equation to be satisfied at discrete points in the region of interest. This procedure is called *point-matching* method. It is equivalent to use Dirac delta functions as test functions.

3.9.2 Subsectional basis functions

An approximation useful for practical problems involves the use of basis functions f_n each of which exists only over subsections of the domain of f. As a consequence, each α_n of the expansion (3.33) affects the approximation of the domain of f only over a subsection of the region of interest. This technique usually simplifies the evaluation of the matrix terms. Sometimes it is convenient to use the point-matching method in conjunction with subsectional bases.

3.10 Moment Method Applied to the 3D Vector Equation

Let us now examine the form of a MoM solution for a large 3D terrain problem. Breaking the terrain up into small elemental segments Δ_n (Figure 3-13), the problem is cast as a matrix equation. This inevitably introduces a measure of approximation, which can however be made arbitrarily small. Following from (3.41) the surface currents are expanded

$$\mathbf{J} = \sum_{1}^{N} \mathbf{J}_n f_n \tag{3.42}$$

$$\mathbf{K} = \sum_{1}^{N} \mathbf{K}_n f_n \tag{3.43}$$

where for our present discussion we shall not specify the form of the basis functions f_n other than to say that they are subsectional basis functions defined over the n^{th} terrain element. An appropriate choice of basis functions will impact significantly on

the efficiency and accuracy of our model. We will later utilize pulse basis functions defined over $\lambda/4$ elements, although much larger basis domains may be utilized in terrain integral equations [51].

For simplicity we will assume point matching is adequate, and that all interaction terms may be readily computed. The matrix equation takes the form

$$\begin{bmatrix} \mathbf{J}^{Inc} \\ 0 \end{bmatrix} = \begin{bmatrix} Z_{1,J} & Z_{1,K} \\ Z_{2,J} & Z_{2,K} \end{bmatrix} \begin{bmatrix} \mathbf{J} \\ \mathbf{K} \end{bmatrix} \tag{3.44}$$

where $\mathbf{J}^{Inc} = \hat{\mathbf{n}} \wedge \mathbf{H}^{Inc}$. and the matrix elements are given by

$$Z_{1/2,J} = -\hat{\mathbf{n}} \wedge \nabla \wedge \int_{\Delta_m} G_{1/2} f_m d\Delta_m \quad m \neq n \tag{3.45}$$

$$= \pm 1 - \hat{\mathbf{n}} \wedge \nabla \wedge \int_{\Delta_m} G_{1/2} f_m d\Delta_m \quad m = n \tag{3.46}$$

$$Z_{1/2,K} = \hat{\mathbf{n}} \wedge \frac{(\nabla\nabla \cdot + k_{1/2}^2) \int_{\Delta_m} G_{1/2} f_m d\Delta_m}{j k_{1/2} \eta_{1/2}} \quad \forall\ m \tag{3.47}$$

The precise values of the matrix elements will depend upon the basis functions employed. At first sight the required sampling rate in the optically denser medium would appear to be higher, in proportion to k_d, as the interior Green's function varies with $e^{-ik_d r}$. As the wavenumber in the Green's function beneath the surface is larger, $\lambda_d \propto 1/k_d$ is smaller, and Nyquist sampling intervals of $\lambda_d/2$ are necessary.

This can be avoided by analytical integration over larger segments, sufficient to sample $\mathbf{J}$ and $\mathbf{K}$, which will vary at most only fractionally faster than k_0 provided the terrain is smooth, and we are in the far field region. It is observed however, that when this approximation is most effective the same speed up may be achieved using a simpler, exterior boundary approximation.

2D terrain schemes allow facilitate a simple reduction of complexity to two uncoupled scalar equations, which have the further advantage of allowing a simple boundary condition to be applied, and the interior equation to be ignored. This is not possible in the 3D case, and either a new boundary condition must be developed, or the coupled system itself must be solved. The interactions above and below the surface are essentially the same in form and we may understand the key processes considering only the former.

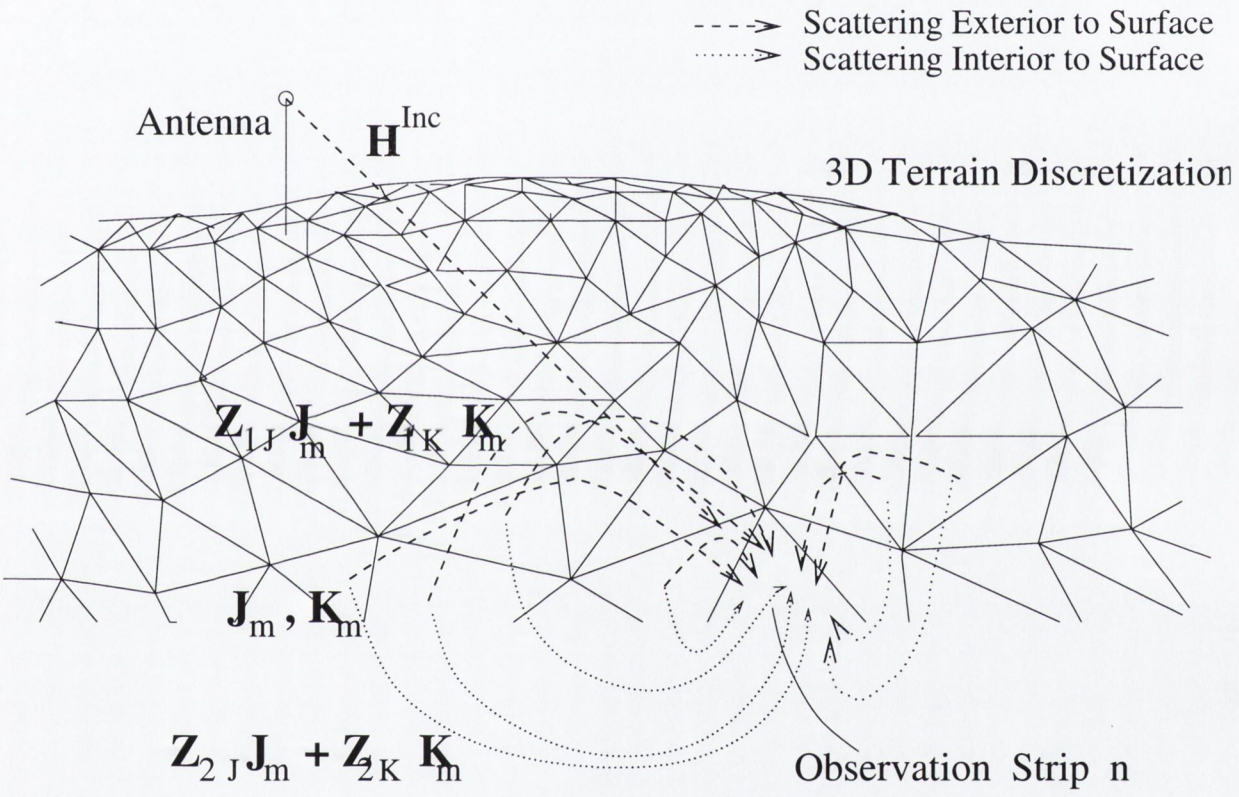


Figure 3-13: Depiction of a 3D Coupled Integral Equation Scheme showing a small number of scattering contributions to the integral interior and exterior to the surface.

In a rigorous approach, if any scale of surface complexity down to that of the order of a wavelength, is to be modeled, the Nyquist minimum sampling rate of $\lambda/2$ must be satisfied. In fact $\lambda/4$ may be found necessary[14]. The key problem now is that of calculating the scattered field at an observation point, in the presence of a vast number of subscatterers. Considering a flat, circular plate problem, measured in terms of its maximum range R/λ, if the discretization mesh is made out of Isosceles triangular elements with short side length $\lambda/4$ the total number required to cover the problem area will be $N = 32\pi R^2$. This figure will be extremely large even for a modest terrain range, and at relatively low frequency. Our troubles are further compounded when we consider that the numerical complexity of solving the matrix system is of the order $\mathcal{O}(N^2)$, not to mention memory storage requirements. Further to this the fact that we must solve for two vector unknowns, a total of six field components.

From the outset it is evident that some more efficient scheme is needed although complete solutions of (3.44) can be achieved for electrically small bodies.

3.10.1 The Fast Far Field Approximation

We consider a group of subscatterers l', in a portion of the terrain, and an observation point at the center of another group l, at a distance R from the center of group l'. The field scattered to the observation point from the m^{th} subscatterer may be given by

$$\mathbf{E}^s_{l,m} = \frac{e^{-ikr}}{4\pi r}\mathbf{U}(\mathbf{J}_m + \mathbf{K}_m) \tag{3.48}$$

where U denotes the reduced impedance matrix element $(Z_{1,J}\cdot + Z_{1,K}\cdot)$, and we make the approximation

$$\frac{e^{-ikr}}{4\pi r} = \frac{e^{-ikR}}{4\pi R}e^{ikr'_m\cos\theta'_m} \tag{3.49}$$

The total field scattered to the observer from this subgroup will then be

$$\mathbf{E}^s_l = \frac{e^{-ikR}}{4\pi R}\sum_{m\in l'} e^{-ikr'_m\cos\theta'_m}\mathbf{U}_m(\mathbf{J}_m + \mathbf{K}_m) \tag{3.50}$$

[14]For the EFIE applied to closed bodies this may increase up to lambda/20

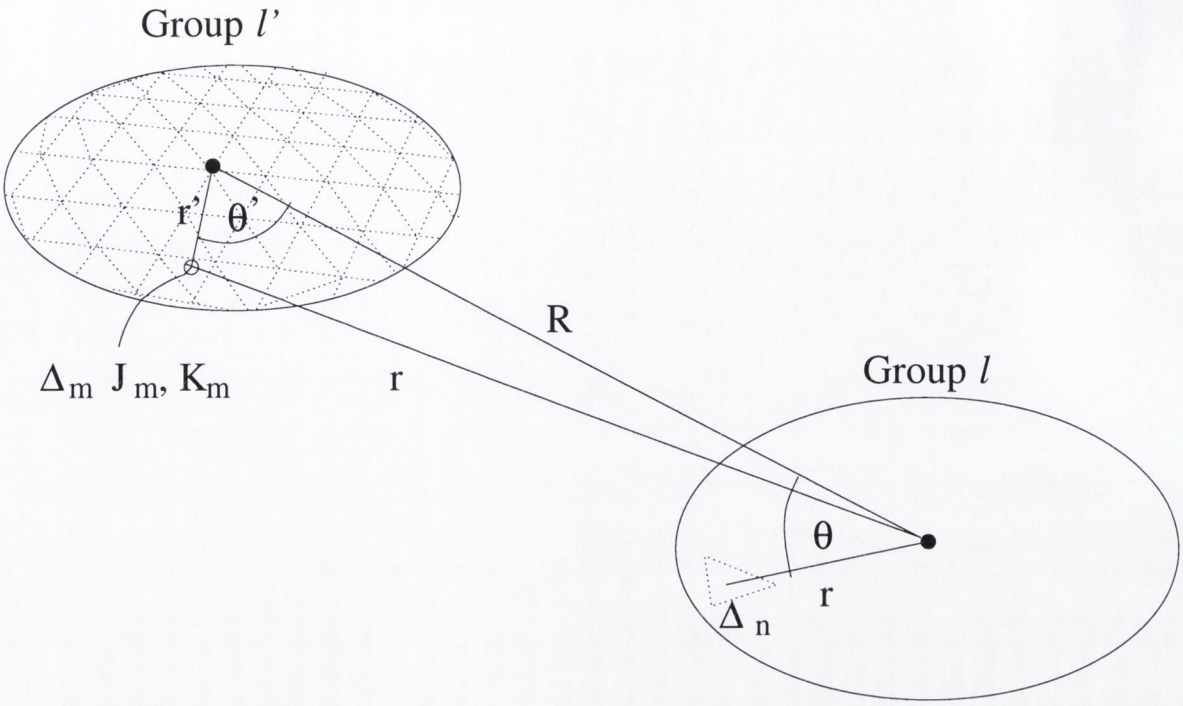


Figure 3-14: Scattering and observation groups in a FAFFA scheme

where **U** denotes the reduced impedance matrix **Z**. It is found that this approximation is good provided the error in the phase for any individual subscatterer is less than $\pi/16$ and it was shown by Fraunhoffer that this condition is satisfied where $R \geq \frac{2d^2}{\lambda}$ where $r' \leq d$. Group sizes are chosen to maintain a balance between increasing near field complexity, and the saving gained by using large groups. The balance between these factors is set by the Fraunhoffer limit. The true saving afforded by this approximation is evident when we consider that the field scattered to any element Δ_n in group l' may be given using a similar phase shift $e^{ikr_n \cos\theta_n}$ (Figure 3-14). To evaluate the field at any of these observation points the summation in (3.50) need only be calculated once.

In short, subscatterers may be aggregated into groups, and the scattering from one group to another evaluated in terms of an aggregation, multiplication by a complex range dependent dyadic matrix, and a subsequent distribution over the observation group. Considerable time savings are then possible. The method is constrained by the Fraunhoffer limit which forbids us from implementing the group interaction procedure, in the near field of the group. The size of the near field may be reduced by

decreasing the size of the groups, but the number of groups will increase as a result and the smaller the groupings become, the less efficient is the algorithm.

Already it will be obvious that by creating a multiple scale of groupings, we may recursively subdivide the near field and in addition the interactions inside each group, leading to a significant increase in efficiency, the trade off arising in increased algorithmic complexity. This has been implemented [62] for scatterers of moderate size. It is noted however that this method fails to become dramatically more efficient, before the number of unknowns, and interaction matrix, which must still be stored in full, becomes prohibitively large.

3.10.2 FMM

Another related scheme for aggregating the interactions is the Fast Multipole Method[56][60]. In this case the scattered field from of a group of subscatterers is modeled by the substitution of a weighted set of multipolar sources. Once the multipolar expansion for a scattering group is known, it may be re-used for any group in the far field of the scattering group at a given iteration. The range of the far field may be reduced arbitrarily by increasing the order of the expansion but in practice a compromise level of truncation will be adopted, leaving a manageable near field. In multilevel implementations this near field may be further subdivided along with the interactions internal to each group.

The FMM is ideal for smaller closed scatterers where a matrix system is solved using an iterative scheme like the Conjugate Gradient Algorithm. Here the FMM affords considerable levels of reuse, and numerical complexity may be reduced to $\mathcal{O}(N^{1.33})$, and further to $\mathcal{O}(NlogN)$ for the multilevel algorithm [66] [67]. For terrain however, reuse is more limited. Scattering takes place within a limited angular range about the earth plane[15]. Some form of forward scattering will normally be employed avoiding the need for a full matrix solver. Gains may be made, but considering that near field interactions may be neglected in an MFIE scheme over a smooth surface, far field interactions may be mediated adequately within the plane wave interaction

[15]This feature might also be used to accelerate the FMM for terrain

scheme of the FAFFA. In addition the complexity of Fast Multipole implementations methods increases considerably as we move from single to multi-level, and from 2D to 3D.

3.10.3 Low Resolution Methods

While the FAFFA and FMM make certain approximations they are essentially rigorous methods, where the error may be made arbitrarily small. Referring again to the total number of unknowns $N \approx 6 \wedge 32\pi R^2$, we find that even with FMM efficiency of $\mathcal{O}(N^{1.33})$, which carries its associated cost in complexity, or $\mathcal{O}(NlogN)$ for the multi-level algorithm, computation times are excessive with storage problems also arising. Some way must be found to reduce N directly. In 2D this has been achieved using TIM [11] or ANIM [39], where in the case of TIM the radar cross section is evaluated for a finite planar segment. This is distinct from the GTD method of Tameh et al. [19] in that the integral equation is fully solved in terms of reference currents, which are the product of a plane wave excitation of a strip. By dividing the terrain into a succession of identical strips these currents need only be computed once. The current on a strip is now given in terms of more than one basis current, but the basis subdomain is now large, and computational times are dramatically increased.

Efforts have been made [61] at applying a similar scheme in 3D. In this case the reference currents used are those of physical optics plane wave excitations. Dividing a terrain surface into a set of triangular elements as in Figure 3-13, where the triangles are now of the order of several, or perhaps many wavelengths is size, we suppose that the field impinging on any element may be expanded as a set of plane waves. For the i^{th} plane wave the associated physical optics current is given as $2\hat{\mathbf{n}} \wedge \mathbf{H}^i$ on the plate surface. The scattered field from such a current on a triangular plate may be given in analytic form. This provides an efficient method for calculating the scattered field, and is particularly attractive in the form of an MFIE where near field interactions are small. However, all near interactions may not be neglected. It may be demonstrated [61] that the near scattered field for a physical optics current distribution on a triangular patch may be given by a plane wave expansion derived

using the Gegenbauer addition theorem. Thus a complete plane wave interaction formulation is achieved and making the PO approximation, the currents on each triangular element are known, although they need not be numerically integrated over directly.

To date, results for this method do not conclusively demonstrate the viability of the PO expansion of the current, although it seems highly plausible that this should be possible. As such, no satisfactory 3D integral equation method for large terrain problems exists. 3D off axial effects are expected to be mild and we might expect that much of the improvement to the 2D approach may be made, including only 3D effects near the propagation axis. In the remainder of this thesis, an integral equation is introduced, that attempts to model 3D characteristics of a terrain surface, evaluating the scattered field along a terrain radial only. It is hoped that the main features of 3D terrain may be captured utilizing a quasi 3D approach based on the radial profile and its transverse gradients. The possibility exists however to extend the quasi 3D terrain radial method, to consider the effects off axial propagation, and this will be discussed in the final chapter of this thesis.

3.11 Machine Learning

A recent development in the field of propagation modeling has been the use of neural networks. It is assumed that propagation loss is a function of various parameters such as path profile, transmitter and receiver height, and obstacles on the terrain. Profile data is fed to the network, along with actual field measurements of field strength, and the network is trained as a predictor of propagation loss.

It is early days for such methods but results are reported indicating considerable improvement over the COST-231 prediction model. It is tempting to resist a method that makes no direct use of electromagnetic theory, but neural networks have already demonstrated some remarkable capabilities[16]. Anybody familiar with the appearance of pathloss predictions will be aware of some patterns, in some cases path loss profile

[16]Tests have shown neural networks superior to humans in judging gender from the picture of a face

bearing close resemblance to a superposition of the terrain profile on a range dependent attenuation. These techniques do however require a dedicated neural machine, where conventional methods aim to make accurate solutions attainable on a general purpose desktop PC.

Chapter 4

Polarization Modes and the Corrugated Terrain Approximation

We saw in the preceding chapter a number of approaches to solving the problem of propagation over three dimensional surfaces, and identified the major impediment to such calculations, namely the prohibitive computational cost. Even where the investigation was restricted to problems having simple boundary conditions, the number of unknowns will increase too rapidly with propagation range.

The most common way of overcoming this problem is to make a corrugated terrain approximation. Assuming that terrain gradients are not excessive, and that radial paraxial propagation dominates, a radial segment of a terrain profile running from the source to the receiver, may be isolated and treated as the profile of a two dimensional surface, invariant in the $\hat{\mathbf{y}}$ direction. The construction of the profile is illustrated in Figure 4-1. What is initially a geometric approximation to the surface, in fact leads to a reduction in complexity of the vector problem, and to a pair of separable scalar equations describing sources of orthogonal polarization. A source of arbitrary polarization may then be modeled by appeal to linear superposition.

Now consider the problem of solving equations (2.114) and (2.115) for the 2D geometry of Figure 4-1. Choosing the source orientations parallel or perpendicular to the corrugation direction $\hat{\mathbf{y}}$, the problem described becomes highly symmetric. We consider the case where the source is a horizontal electric dipole aligned along the

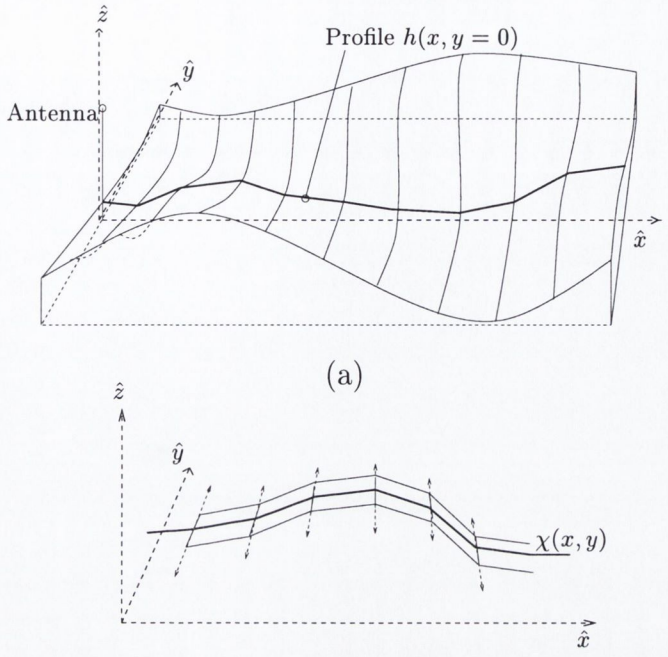


Figure 4-1: *(a) The surface height function $h(x, y)$ taken from measured data : (b)The corrugated surface function $\chi(x, y)$ constructed from h(x,0)*

$\hat{\mathbf{y}}$ direction. In terms of a spherical polar coordinate system (r, θ', ϕ') centered on, and aligned with the source ($\hat{z'}$ corresponding to $\hat{y}$), from the source field relationship (2.54) the incident field may be given by

$$E_r = \frac{I_0 L_0}{j\omega\epsilon} \frac{e^{-ikr}}{4\pi} \left(\frac{j2k}{r^2} + \frac{2}{r^3} \right) \cos\theta' \tag{4.1}$$

$$E_{\theta'} = \frac{I_0 L_0}{j\omega\epsilon} \frac{e^{-ikr}}{4\pi} \left(\frac{-k^2}{r} + \frac{jk}{r^2} + \frac{1}{r^3} \right) \sin\theta' \tag{4.2}$$

and in the far field of the transmitter the terms in higher powers of $\frac{1}{r}$ vanish leaving

$$E_{\theta'} = j(I_0 L_0)\omega\mu \frac{e^{-ikr}}{4\pi r} \sin\theta' \tag{4.3}$$

$$E_r \rightarrow 0 \tag{4.4}$$

where I_0 is the source current, L_0 the source length and where the *far field* relations above are satisfied when $\mid kr \mid \gg 1$. In the plane $\theta' = \pi/2$ the incident field is aligned along $\hat{y}$ and in the far field $\mathbf{E}^{Inc}$ is approximately cylindrical in the region of this plane. As such the problem locally resembles that of an infinite line source along the $\hat{\mathbf{y}}$ axis in a cylindrical waveguide, and in fact, in the plane $\hat{\mathbf{y}} = 0$ the problems differ

only by range dependence factor. The cylindrical problem may be described in terms of separable polarization modes. The geometry is invariant in the $\hat{\mathbf{y}}$ direction and as such, derivatives in (2.114) with respect to y are vanishing. The line source emits a cylindrical **E** field

$$E_y^{Inc} = jI_0\omega\mu\frac{e^{-ikr}}{\sqrt{\pi r}} \tag{4.5}$$

differing from (4.4) by the factor $A/\sqrt{R}$. With the assumption that the terrain is homogeneous, we may replace the 3D problem of (2.114) with

$$\begin{aligned} E_y^{Inc}(t) &= K_t(t) + jk_1\eta_1 A_{+y} + \left[\frac{\partial F_{+z}}{\partial x} - \frac{\partial F_{+x}}{\partial z}\right] \\ 0 &= -K_t(t) + jk_2\eta_2 A_{-y} + \left[\frac{\partial F_{-z}}{\partial x} - \frac{\partial F_{-x}}{\partial z}\right] \end{aligned} \tag{4.6}$$

where $\hat{\mathbf{t}}$ denotes the forward tangent vector along the radial, and interior and exterior wavenumbers are given by k_1 and k_2 respectively. The surface is now assumed invariant with respect to y. In this sense the terrain surface may be considered as forming the boundary of a cylindrical waveguide, closed at infinity.

The vector potentials now take the form,

$$A_{+/-y} = \int_{S_{+/-}} J_y G(k_{1/2} \mid \mathbf{r} - \mathbf{r}' \mid) dS_{+/-} \tag{4.7}$$

$$\mathbf{F}_{+/-t} = \int_{S_{+/-}} \hat{\mathbf{t}} K_t G(k_{1/2} \mid \mathbf{r} - \mathbf{r}' \mid) dS'_{+/-} \tag{4.8}$$

The functions J_y and K_t are invariant with respect to y, with **J** parallel to $\hat{y}$ and **K** parallel to the forward surface tangent vector $\hat{t}$. These quantities may therefore be factored through the y' integral in (4.7) and (4.8) leaving an integral over the free space Green's function, and noting that

$$\int_{-\infty}^{\infty} \frac{e^{-ik\sqrt{\rho^2+y^2}}}{4\pi\sqrt{\rho^2+y^2}} e^{-i\gamma y} dy = \frac{1}{4j} H_0^{(2)}(\rho\sqrt{k^2-\gamma^2}) \qquad k^2 > \gamma^2 \tag{4.9}$$

where $H_0^{(2)}(.)$ is the zero order Hankel function of the second kind, and ρ represents the vector $(r_x - r'_x, r_z - r'_z)$. The coupled equations (4.6) may be solved for the potentials

$$A_{+/-y} = \frac{1}{4i}\int_{C_{+/-}} J_y H_0^{(2)}(k_{1/2} \mid \rho - \rho' \mid) dt' \tag{4.10}$$

$$\mathbf{F}_{+/-t} = \frac{1}{4i}\int_{C_{+/-}} \hat{\mathbf{t}} K_t H_0^{(2)}(k_{1/2} \mid \rho - \rho' \mid) dt' \tag{4.11}$$

where C is the perimeter of the waveguide given by the 1D terrain profile. For terrain type problems we consider the contour C to be closed at infinity, where by the radiation condition the fields will be vanishingly small and may be neglected from the integral. It must be remembered that this integral will be approximate however, in the case of problems truncated at only moderately large distances from the antenna, and this can lead to errors in the calculated field.

Breaking a terrain profile into a succession of elemental strips Δ_n we expand the currents $\mathbf{J}$ and $\mathbf{K}$ in terms of pulse basis functions

$$\mathbf{J} = \sum_n j_n b_n \tag{4.12}$$

$$\mathbf{K} = \sum_n k_n b_n \tag{4.13}$$

$$b_n(t) = \begin{cases} 1 & t \in \Delta_n \\ 0 & t \notin \Delta_n \end{cases}$$

Equation (4.6) is then enforced at the center point of each strip, in the manner of a Galerkin point matching moment method solution, and equation (4.6) is written in matrix form as,

$$\begin{bmatrix} \mathbf{E}^{Inc} \\ 0 \end{bmatrix} = \begin{bmatrix} A & B \\ C & D \end{bmatrix} \begin{bmatrix} \mathbf{j} \\ \mathbf{k} \end{bmatrix} \tag{4.14}$$

where the matrix elements take the form

$$A_{mn} = \frac{k_1 \eta_1}{4} \int_{\Delta_m} H_0^{(2)}(k_1 \rho) dt' \quad \forall\ m \tag{4.15}$$

$$B_{mn} = \frac{k_1}{4j} \int_{\Delta_m} (\cos\phi_n \frac{\Delta x}{\rho_m} + \sin\phi_n \frac{\Delta z}{R_m}) H_1^{(2)}(k_1 \rho) dt' \quad m \neq n \tag{4.16}$$

$$C_{mn} = \frac{k_2 \eta_2}{4} \int_{\Delta_m} H_0^{(2)}(k_2 \rho) dt' \quad \forall\ m \tag{4.17}$$

$$D_{mn} = \frac{k_2}{4j} \int_{\Delta_m} (\cos\phi_n \frac{\Delta x}{\rho_m} + \sin\phi_n \frac{\Delta z}{R_m}) H_1^{(2)}(k_2 \rho) dt' \quad m \neq n \tag{4.18}$$

$$B_{nn} = \frac{1}{2} \qquad D_{nn} = -\frac{1}{2} \tag{4.19}$$

where ϕ_n is angle between the vectors $\hat{\mathbf{t}}$ and $\hat{\mathbf{x}}$ at matchpoint n, $\Delta x = r_x - r'_x$,

$\Delta z = r_z - r'_z$ and $H_1^{(2)}(.)$ is the first order Hankel function of the second kind[1], and $\rho = \sqrt{\Delta x^2 + \Delta y^2}$.

Where the contribution from a strip onto itself in B and D is evaluated, the limit has been taken approaching the center of the strip along the normal, from the exterior(+) or interior(-) region. The singularity in the Hankel function may be integrated analytically [58] and is found to yield values of $\pm 1/2$ over a strip element small compared to the wavelength. The self terms A_{nn} and C_{nn} are evaluated utilizing the small argument power series expansion of the Hankel function[21] yielding

$$B_{nn}/D_{nn} = \frac{k_{1/2}\eta\Delta_n}{4}\left\{1 - i\frac{2}{\pi}\left[\log(\frac{\gamma k_{1/2}\Delta_n}{4}) - 1\right]\right\} \tag{4.20}$$

where γ is Euler's constant.

In the Hankel function integrals there are different wave numbers for the two media. Care must be taken that sampling is sufficient to correctly sum over the most rapid spatial variations encountered. For terrain problems where medium 1 is free space, medium two will have a higher value of wavenumber. In addition the wave number may be complex reflecting propagation losses in the terrain medium. In any event sampling at $\frac{\lambda_2}{8} \rightarrow \frac{\lambda_2}{4}$ will provide sufficient resolution provided terrain variations are small in comparison to λ_1.

4.1 Numerical Comparison for a Planar Boundary

The above coupled equation was applied to a flat terrain propagation problem with an electric line source at height 20 meters over a planar surface having material parameters $(\epsilon_r, \sigma) = (15.0, 0.005)$, which are representative of earth at the test frequency of 144MHz. The source is oriented along the $\hat{\mathbf{y}}$ direction. Comparison is made with an analytical solution by the method of plane wave expansion given by Clemmov[13], where geometrical optics theory is used to compute the reflection amplitudes of plane wave components at the lossy dielectric interface. The discretization step is chosen as $\frac{\lambda_2}{8}$. Plots are of path loss against range x at a height of $2m$ and are normalized with the factor $\frac{1}{\sqrt{R}}$, to simulate the range dependence of a more physically realistic point source.

4.1.1 TM_y

Results from the coupled integral equations agree well with the predictions of the plane wave expansion technique which we regard as our reference solution (Figure 4-2). It transpires that for this particular problem an accurate solution may be found by the simpler means of image theory, as we will effectively be able to make a perfect reflecting boundary approximation to the surface. The solution in Figure 4-2 was achieved using a forward scattering integral equation method only. Agreement

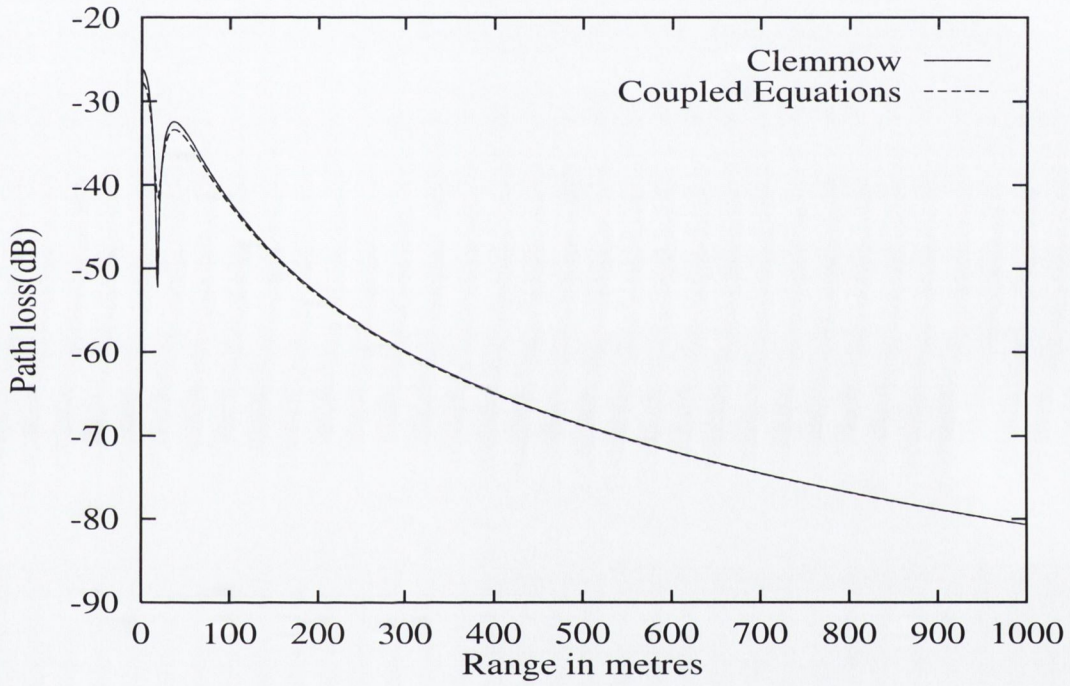


Figure 4-2: Pathloss over a flat terrain-like lossy dielectric surface comparing Coupled Integral Equation solution and analytical solution, for TM_y.

may be improved further in the region near to the source, using a forward/backward iterative solver. We note however that the method of Clemmow is approximate, in certain asymptotic limits and agreement will not be exact.

4.1.2 TE_y

A similar test is performed for the coupled magnetic field integral equations representing the field from a horizontal magnetic current source. Once again the solution

is compared with that of the plane wave expansion method. Figure (4-3) shows results for a single forward scattered coupled MFIE, and for a forward/backward[14] solution scheme. The forward/backward scheme is seen to show better agreement with the plane wave expansion method, in this case after four iterations.

The coupled field equations provide a very robust solution method for a wide range of problems. For practical purposes, problems are presented by the increased sampling rates, complex argument Hankel functions, and the multiplicity of fields involved. The method may however be enhanced with a range of FMM or FAFFA acceleration techniques. In general however we will prefer to simplify the problem by appeal to further approximations. The coupled equations however, may provide a reference solution for general terrain problems.

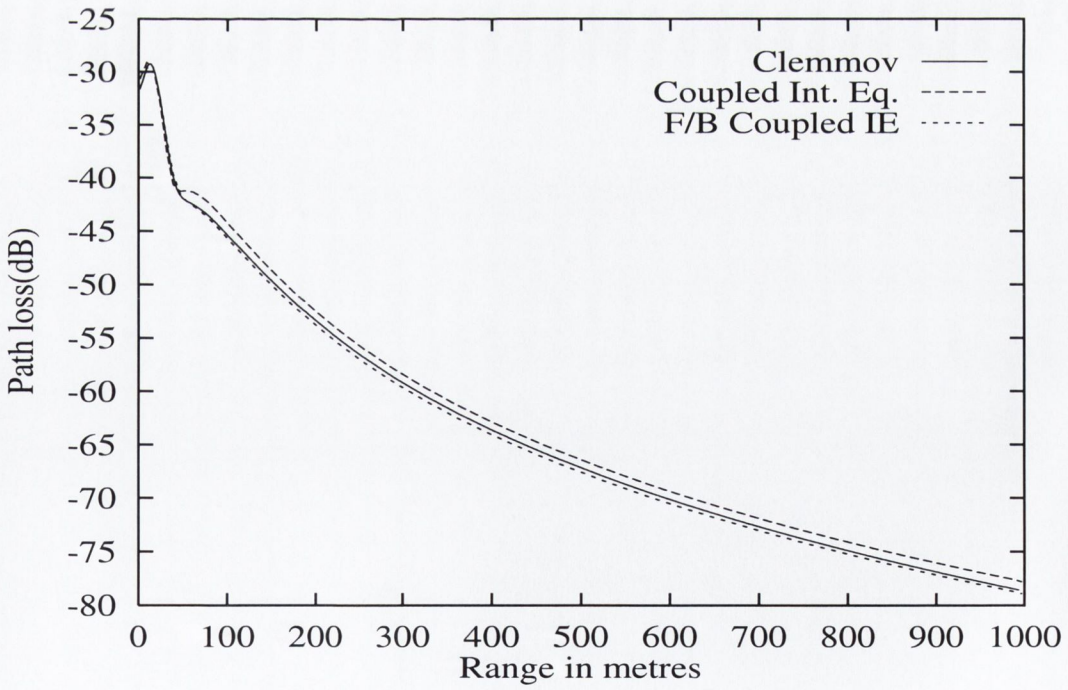


Figure 4-3: Pathloss over a terrain-like lossy dielectric surface comparing Coupled Integral Equation solution and analytical solution, for TE_y.

4.2 Reflection Coefficients

For the coupled equation problems treated above, the electric or magnetic fields in either space were polarized in the $\hat{y}$ direction. For infinite plane waves having this characteristic, and propagating in homogeneous space over an infinite planar surface, field continuity relations(2.3.5) at the boundary take a simple form. The total field may be given in terms of incident and reflected waves. This may be demonstrated by considering an incident plane wave of form,

$$\mathbf{E}^i = E^i_y \hat{y} e^{-ik_1(\sin\theta_i x - \cos\theta_i z)} \tag{4.21}$$

where θ_i is the angle of incidence measured to the normal of the interface. The only solutions to the free space wave equation above the plane are given in this form. In fact we may write the field scattered from the interface as

$$\mathbf{E}^r = A^r E^i_y \hat{y} e^{-ik_1(\sin\theta_r x + \cos\theta_r z)} \tag{4.22}$$

In the region beneath the boundary there is a transmitted wave taking the same form, as medium two is homogeneous

$$\mathbf{E}^t = A^t E^t_y \hat{y} e^{-ik_2(\sin\theta_t x - \cos\theta_t z)} \tag{4.23}$$

where the angle θ_t is in general complex as the medium may be lossy[34]. There is no impressed surface current on the boundary so the sum of incident and reflected fields must be continuous with the transmitted field at the boundary. As we are dealing with plane waves the tangential magnetic fields are easily derived,

$$H^i_x = \frac{k_1 \cos\theta_i}{\omega\mu_1} E^i_y \quad , \quad H^i_z = \frac{-k_1 \sin\theta_i}{\omega\mu_1} E^i_y \tag{4.24}$$

$$H^r_x = \frac{-k_1 \cos\theta_i}{\omega\mu_1} E^r_y \quad , \quad H^r_z = \frac{-k_1 \sin\theta_i}{\omega\mu_1} E^r_y \tag{4.25}$$

$$H^t_x = \frac{k_2 \cos\theta_i}{\omega\mu_2} E^t_y \quad , \quad H^t_z = \frac{-k_2 \sin\theta_i}{\omega\mu_2} E^t_y \tag{4.26}$$

Continuity of the field at the boundary $z = 0$ can hold only if

$$\exp(-ik_1 \sin\theta_i x) + A^r \exp(-ik_1 \sin\theta_r x) = A^t \exp(ik_2 \sin\theta_t x) \tag{4.27}$$

requiring

$$k_1 \sin\theta_i = k_1 \sin\theta_r = k_2 \sin\theta_t \tag{4.28}$$

and this implying $\theta_i = \theta_r$. This is a statement of Snell's laws of reflection and refraction at a boundary. The laws are quite general and hold where medium two may in fact be lossy, and k_2 is complex. In such cases the angle of transmission will be complex and the wave in medium two is in fact a non uniform plane wave where planes of constant phase and constant amplitude are no longer parallel. The wave will be attenuated or in the case of higher loss tangents, will be evanescent. In theory, k_2 might be evaluated for a particular medium by measuring its material parameters using electrostatic theory. In fact ϵ_c the complex relative permittivity of a material, varies with frequency. Provided a material is non magnetic($\mu = \mu_0$), Snell's law may been seen as a method of evaluating k_2 and hence ϵ_c, at a particular frequency. Such is the case in terrain type problems where a surface may contain polar molecules such as water or ionized minerals in solution, where ϵ_c has a strong dependence on ω (Table 4.2.2).

Applying the condition of continuity of the tangential magnetic field

$$\frac{-k_1}{\mu_1}\cos\theta_i + A^r\frac{k_1}{\mu_1}\cos\theta_r = -A^t\frac{k_2}{\mu_2}\cos\theta_t \tag{4.29}$$

Solving for the reflection and transmission coefficients of the plane wave we find, where $\mu_1 = \mu_2 = \mu_0$, and taking the refractive index $n_1 = \frac{k_1}{k_0} = 1$,

$$A^r = \frac{\cos\theta_i - \sqrt{n_2^2 - \sin^2\theta_i}}{\cos\theta_i + \sqrt{n_2^2 - \sin^2\theta_i}} \tag{4.30}$$

$$A^t = \frac{2\cos\theta_i}{\cos\theta_i + \sqrt{n_2^2 - \sin^2\theta_i}} \tag{4.31}$$

A similar analysis to the above may be carried out for the case where the incident, and therefore all, magnetic fields are polarized along $\hat{\mathbf{y}}$, yielding TE_y reflection and transmission coefficients,

$$B^r = \frac{n_2^2\cos\theta_i - \sqrt{n_2^2 - \sin^2\theta_i}}{n_2^2\cos\theta_i + \sqrt{n_2^2 - \sin^2\theta_i}} \tag{4.32}$$

$$B^t = \frac{2n_2^2\cos\theta_i}{n_2^2\cos\theta_i + \sqrt{n_2^2 - \sin^2\theta_i}} \tag{4.33}$$

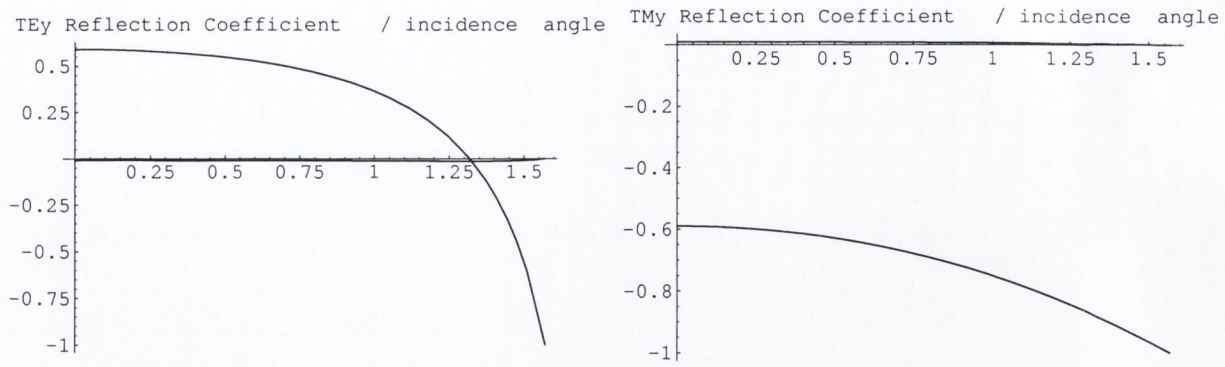


Figure 4-4: TE_y and TM_y reflection coefficients plotted against angle of incidence (radians). (15.0,0.005)

These coefficients may be applied to the treatment of incident fields which can be expanded as a set of plane waves and which are incident on a locally planar surface. We examine the nature of these coefficients for terrain like material parameters. In Figure 4-4 reflection coefficients are shown for $(\epsilon_r, \sigma) = (15.0, 0.005)$ at 144MHz.

On inspection of the above plots certain features are apparent. Firstly the coefficients are almost entirely real. In each case the imaginary part has also been plotted, but is small by comparison.

4.2.1 TM_y

The real part ranges from approximately $-0.6 \rightarrow -1.0$. For a coefficient of -1 clearly the incident and scattered fields combine to give a zero net tangential electric field at the boundary. We have a reflected wave of equal amplitude and opposite phase to the incident wave, in what is termed perfect reflection. The tangential electric field on the surface vanishes in the same way we might expect on the surface of a perfect electric conductor. In spite of the fact that the conductivity in this case is relatively low. For the horizontal electric polarization we have near perfect reflection as $\theta \rightarrow \pi/2$. The amplitude of this reflection tails off as we approach normal incidence where a considerable component of the energy is transmitted into the surface.

4.2.2 TE_y

In the case of the horizontal magnetic polarization(TE_y) the reflection coefficient has much stronger angular dependence with greatest angular variation where it approaches -1 at $\theta_i = \pi/2$. The point at which the real part is vanishing is known as the Brewster angle. Therefore, for very low incidence plane waves, the reflected wave will be equal and opposite in amplitude and the tangential magnetic field on the surface will be vanishing. This is analogous to the case of a perfect magnetic conductor(PMC). The greater angular variation means that problems involving this mode of propagation are not treated as simply as the TM_y case.

At very low grazing incidence, the reflection coefficient may be given as -1 irrespective of polarization[1]. It is also noted that as normal incidence is approached the modulus of TM_y and TE_y coefficients become equal, and they are opposite in sign. This is expected as at normal incidence, a ray may be described as either TM_y or TE_y. The difference in sign for the two reflection coefficients is consistent when we consider that the magnetic field vectors for incident and reflected rays with **E** polarized along $\hat{y}$, will be polarized in opposite directions.

We examine TM_y and TE_y reflection coefficients for different values of material parameter (ϵ_r, σ). Test cases, A(1.1,0.01), B(100.0,0.001), C(1.0,10.0) and D(100.0,100.0) (Figure. 4-5), are depicted in the Argand plane of ϵ_c. The approximate boundary characteristic are noted. In Figures 4-6 to 4-9 angular reflection coefficients are plotted for these values of complex permittivity.

[1]This is well known in fibre optic communications where at the core/cladding boundary, the interface of two non-conducting dielectrics, which differ in permittivity by only a fraction of 1%, grazing incidence light is guided over considerable distances with minimal leakage into the fiber cladding. In standard polarization diversity fibers this holds irrespective of field polarization.

Surface	ϵ_r	σ
Dry Ground	4	0.01
Concrete	4-6	$0.1 - 0.3$
Aerated Concrete	2-3	$0.1 - 0.5$
Damp Ground	30	0.01
Sea water	80	4.3
Fresh Water	80	0.01
Ice	3.2	0.005
Snow	1.2-1.5	0.003
Metallic Surface		10^7

Table 4.2.2 : Approximate material parameters [7][34] for a number of surfaces at UHF: The most obvious feature is that water content is the dominant factor in ground permitivity. Dry ground permitivity of 4-7 is comparable with that of concrete but can rise to 30 if ground is wet. This is not the case where water is in the solid phase. The converse is true for air content as indicated by the different values of permittivity for ice and snow, or concrete and aerated concrete. The same will hold true for dry, less densely packed earth.

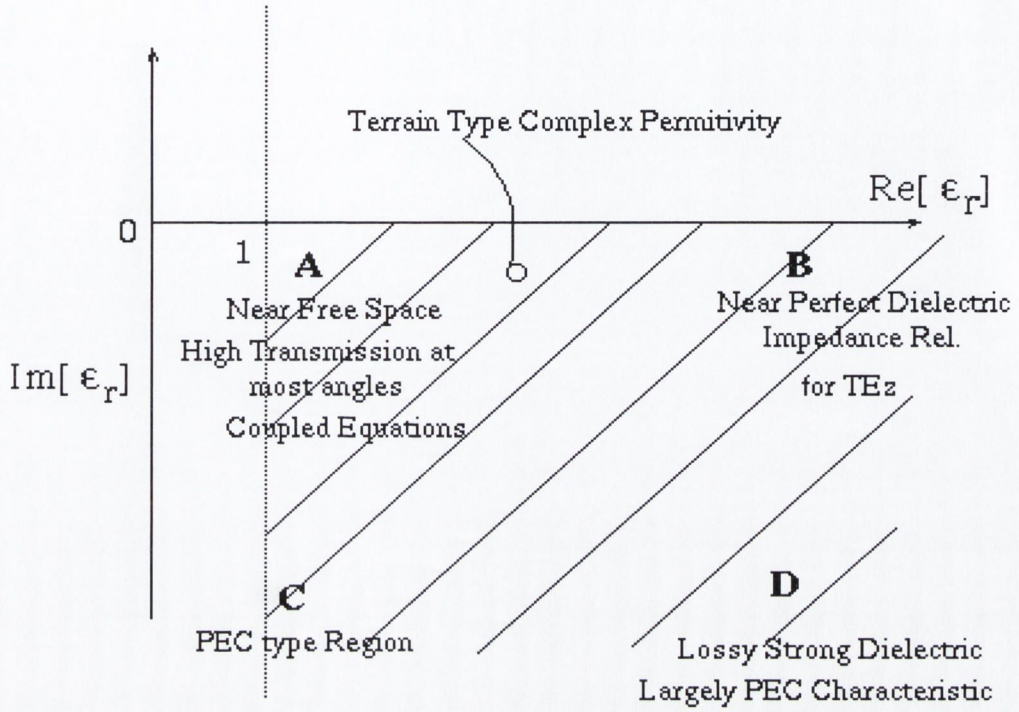


Figure 4-5: A range of complex permittivity values with associated characteristics and approximations.

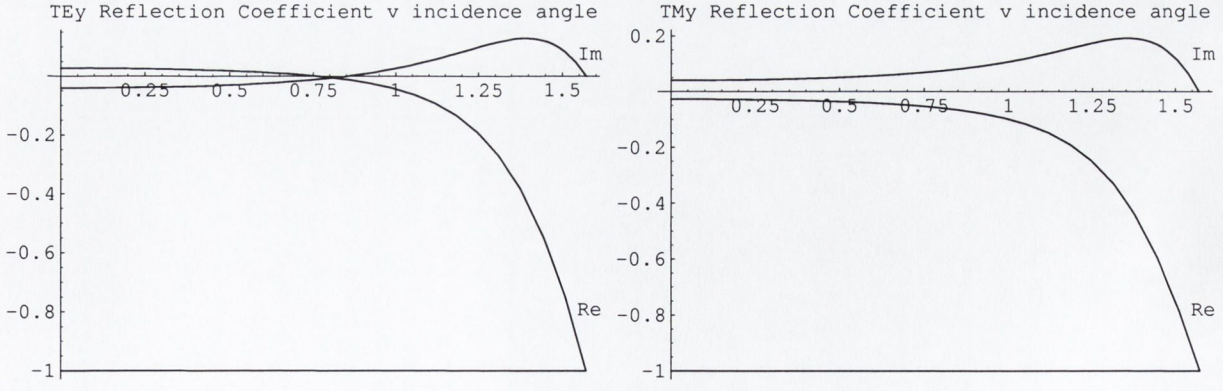


Figure 4-6: TE_y and TM_y reflection coefficients. Case A. Reflection coefficients are low at most angles, indicating high levels of transmission.

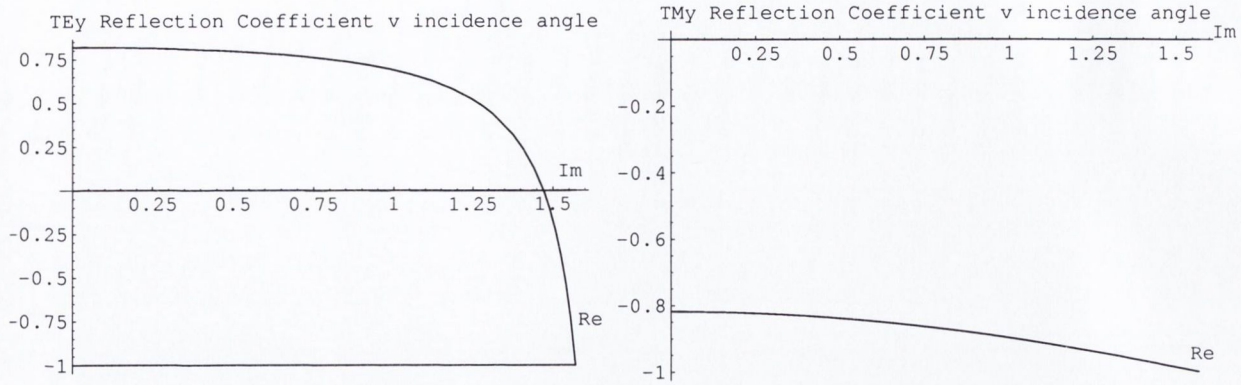


Figure 4-7: TE_y and TM_y reflection coefficients. Case B. Strong reflection at most angles, with wide variation around shallow incidence TE_y.

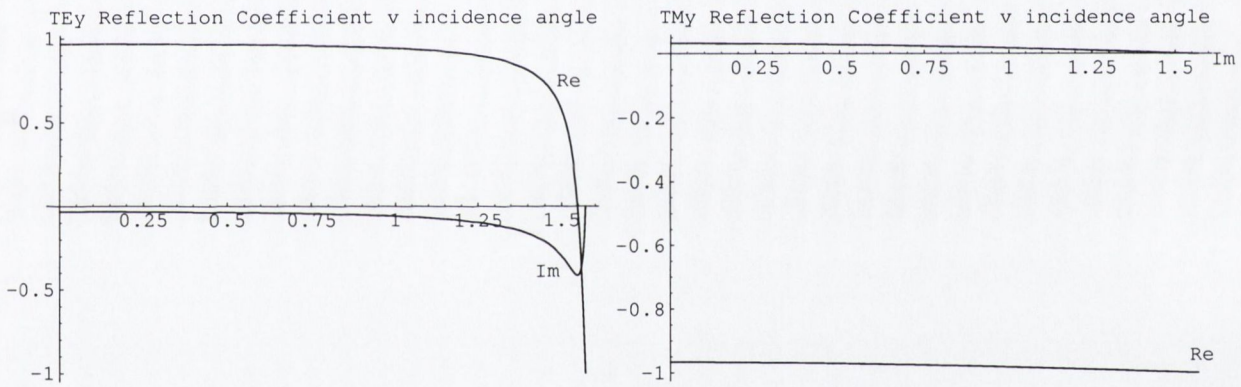


Figure 4-8: TE_y and TM_y reflection coefficients. Case C. PEC type reflection.

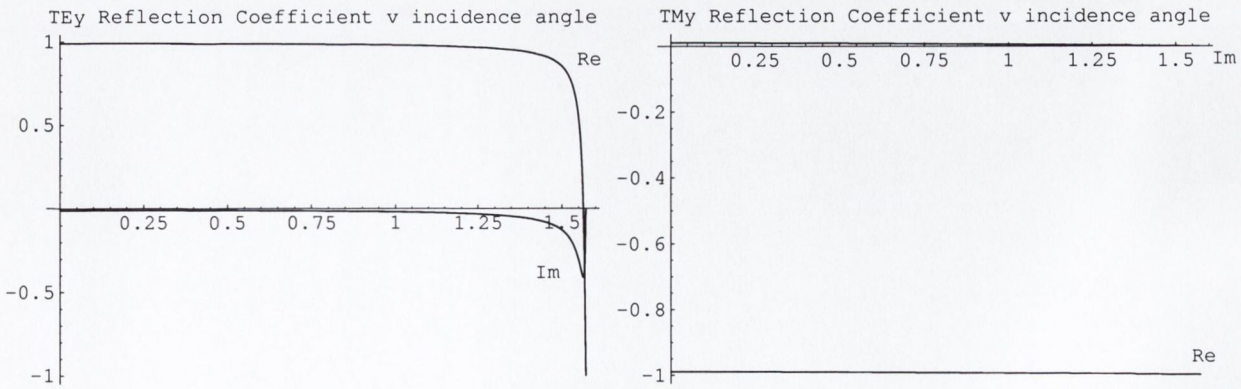


Figure 4-9: TE_y and TM_y reflection coefficients. Case D. PEC type reflection.

4.3 The PEC Boundary Condition

Having established that a planar terrain boundary behaves like a perfect electrical conductor for TM_y plane waves at near-grazing incidence, and given that locally a smooth boundary may be approximated by its tangent plane, and an arbitrary incidence field expanded as a set of plane waves, we apply the PEC surface approximation directly to the entire terrain boundary. (4.6) may be simplified setting $E_y = 0$, and therefore $\hat{\mathbf{n}} \wedge E_y \hat{\mathbf{y}} = 0$ across the boundary. The exterior equation now contains one unknown and takes the form

$$[\mathbf{E}] = [A][\mathbf{j}] \tag{4.34}$$

where matrix elements are the same as for the coupled equation.

4.4 The Impedance Boundary Condition

It is clear that the TE_y reflection coefficient(Figure 4-4) is angularly dependent for an earth like boundary, yet we desire an angularly independent boundary relationship for the integral equation. In fact this is available, considering the tangential components of the total **H** and **E** fields.

By analogy with (4.21)-(4.26), for the TE_y case the total tangential fields on the boundary are given as

$$H_y^T = (1 + B^r)H^i \tag{4.35}$$

$$E_x^T = \frac{k_1}{\omega\epsilon_1}\cos\theta_i(1 - B^r)H^i \tag{4.36}$$

where

$$B^r = \frac{\alpha - \beta}{\alpha + \beta} \tag{4.37}$$

$$\alpha = n_2^2\cos\theta_i \quad , \quad \beta = \sqrt{n_2^2 - \sin^2\theta_i} \tag{4.38}$$

Hence

$$\frac{E_x^T}{H_y^T} = \frac{k_1}{\omega\epsilon_1}\cos\theta_i\frac{1 - \frac{\alpha-\beta}{\alpha+\beta}}{1 + \frac{\alpha-\beta}{\alpha+\beta}} = \frac{k_1}{\omega\epsilon_1}\cos\theta_i\frac{\beta}{\alpha} \tag{4.39}$$

Now where n_2 is large

$$\beta = \sqrt{n_2^2 - \sin^2\theta_i} \approx n_2 \tag{4.40}$$

and so

$$\frac{\beta}{\alpha} \approx \frac{1}{n_2 \cos\theta_i} \tag{4.41}$$

Hence

$$\frac{E_x^T}{H_y^T} = \frac{k_1}{\omega\epsilon_1}\cos\theta_i \frac{1}{n_2\cos\theta_i} = \frac{k_1}{\omega\epsilon_1 n_2} \tag{4.42}$$

Where k_1 and ϵ_1 take their free space values, the RHS of (4.42) simplifies to η_2, the characteristic impedance of the interior medium, and (4.42) is a statement of the impedance boundary condition. By neglecting $\sin^2\theta_i$ with respect to n_2^2 we render the condition angularly independent, and as such, it is an approximate boundary condition, where the quality of the approximation increases with n_2. The derivation here differs from the original derivation of Schukin[64] developed almost simultaneously with that of Leontovich[42], where the initial assumption is of a total field propagating at low incidence over a planar boundary. In the same way that the PEC condition allowed the reduction of system (4.6) to a single equation (4.34), so the impedance relation allows the reduction of the TE_y exterior equation to

$$H_y^{Inc}(t) = -J_t(t) + \frac{jk_1}{\eta_1}F_{+y} + \left[\frac{\partial A_{+z}}{\partial x} - \frac{\partial A_{+x}}{\partial z}\right] \tag{4.43}$$

where

$$\mathbf{A}_{+t} = \int_{S_+} J_t \hat{\mathbf{t}} G(k_{1/2} \mid \mathbf{r}, \mathbf{r}' \mid) dS_+ \tag{4.44}$$

$$F_{+y} = \int_{S_+} \eta_2 J_t G(k_{1/2} \mid \mathbf{r}, \mathbf{r}' \mid) dS_+ \tag{4.45}$$

and so J_t is the only remaining unknown. In matrix form

$$[\mathbf{H}^{Inc}] = [B + \tfrac{\eta_2}{\eta_1^2}A][\mathbf{j}] \tag{4.46}$$

where the matrix components A and B are defined in (4.18). This forms the basis of the 2D impedance boundary algorithm.

4.5 Numerical Comparison

4.5.1 The TM_y Mode

We compare the solution in Figure 4-2 for a flat plate, with the solution using a PEC approximation, where a second image, equal and opposite in amplitude, is located

beneath the plane, and also to the solution by PEC integral equation is used. The methods show good agreement (Figure 4-10). In this example and for the remainder of this chapter we use the Forward/Backward iterative method, and in each case the solution has been iterated until convergence is achieved.

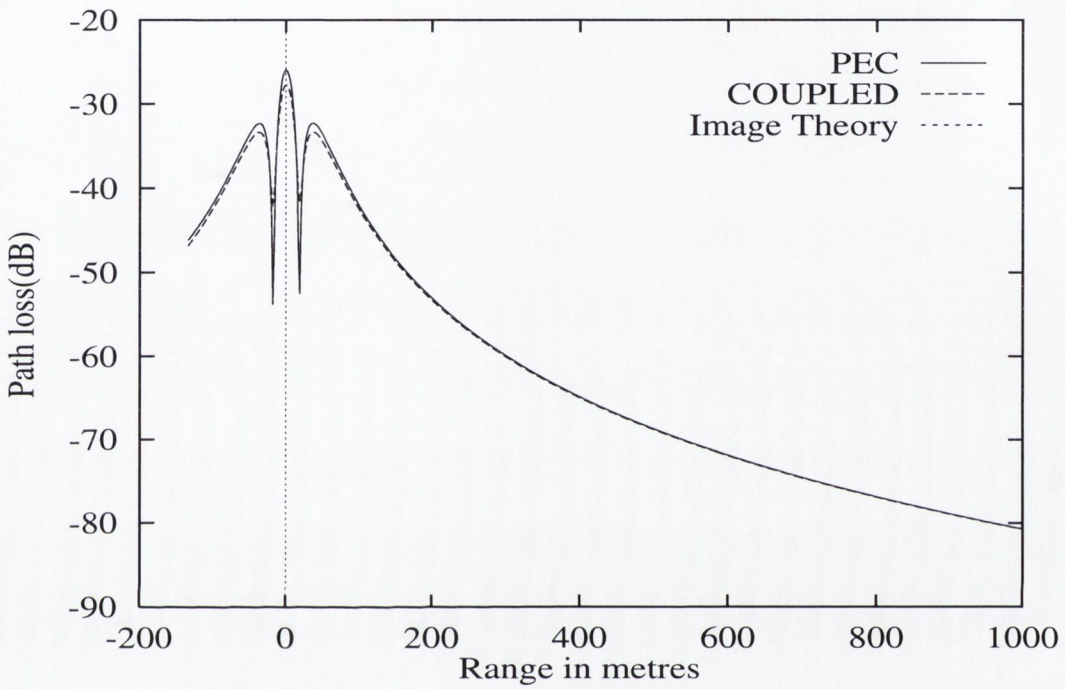


Figure 4-10: Pathloss over a terrain-like lossy dielectric plate comparing Coupled Equations, PEC Integral Equation and Image Theory for TM_y.

The plane wave expansion method is derived from the theory of reflection coefficients and as such we would expect good agreement with a theory that essentially replaces all angular reflection coefficients with -1. In fact the level of agreement is perhaps even greater than might be inferred from Figure 4-4 where the reflection coefficient rises to -0.6 at normal incidence. This difference is evident in Figure 4-10 in the small error in the near region of the source, where propagation is at lower angles of incidence.

The PEC surface approximation for TM_y is extremely well suited for terrain problems, where in the far field of the antenna, grazing incidence propagation dominates. Results are plotted (Figure 4-12) for propagation over a terrain with sinusoidal height variation(Figure 4-11) having material parameters $(15.0, 0.005)$, where the source and

receiver are again at $20m$ and $2m$ and at a frequency of 144MHz. The height variations for this profile may be considered moderate to strong.

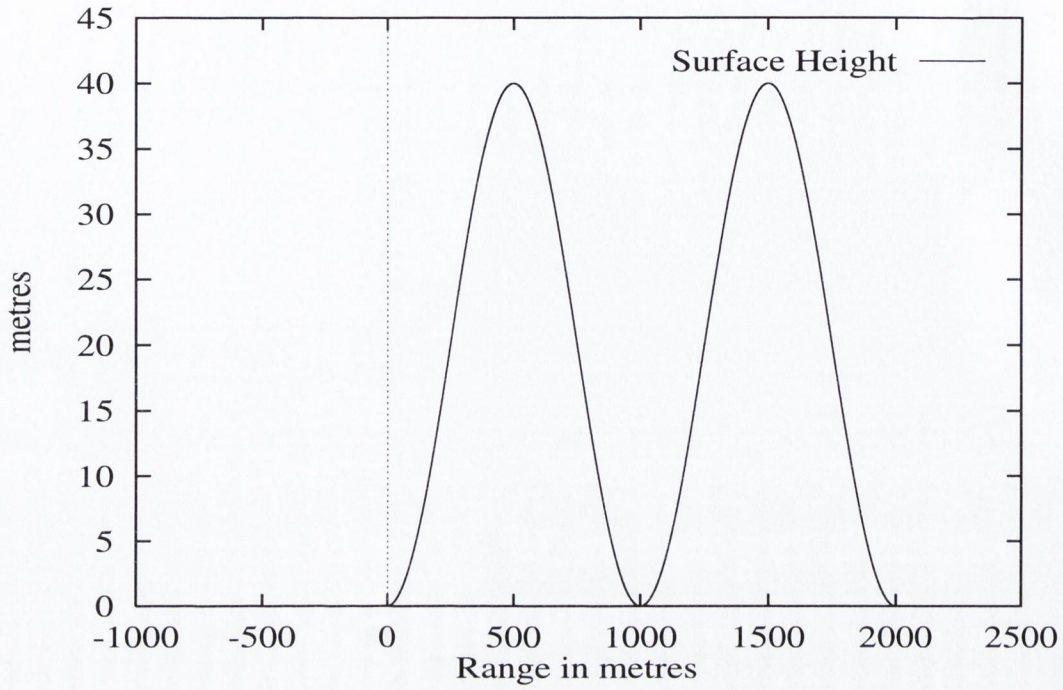


Figure 4-11: Test Profile

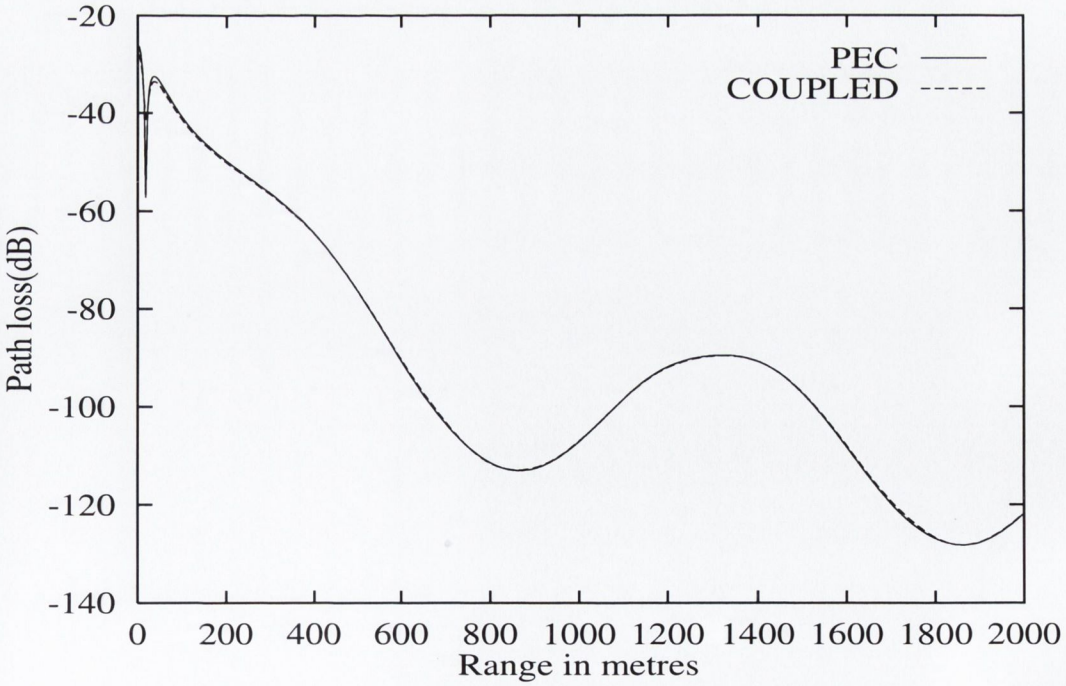


Figure 4-12: Pathloss - PEC v Coupled.

Apart from a very small discrepancy near the source, results for the coupled integral equation and the PEC integral equation are indistinguishable for this profile, indicating the strength of the PEC approximation. In fact the PEC approximation will be accurate for TM_y for practically any profile and frequency in the UHF and VHF bands and for higher frequencies.

4.5.2 TE_y : Coupled Equations v PMC

Figure 4-4 indicates that for TE_y, the reflection coefficient only approaches -1 at very shallow grazing incidence. This indicates that adopting a PMC approximation to a terrain boundary will only be effective for weakly undulating terrain. We test the PMC approximation against the coupled equation solution for a similar profile to Figure 4-11 where the maximum height variations of the sinusoids are reduced to $10m$. Results are plotted in Figure 4-13. Agreement between the PMC and coupled equation predictions is good, but less so than for the PEC/Coupled TM_y case, even for this weakly undulating profile. This suggests that errors may be significant for a more strongly undulating terrain, and this is born out in Figure 4-14 where the same test is performed on the original profile of Figure 4-11. The variations in the PMC solution still follow those of our reference solution, the coupled equation, but the error in this case can exceed $9dB$ in shadow regions.

4.5.3 TE_y : Coupled Equations v Impedance

Given the size of error seen in Figure 4-14 it is evident that a better boundary approximation is required, and this is available in the impedance boundary approximation. Comparison is made between the coupled solution and Impedance boundary solution for the same profile (Figure 4-11) and plotted in Figure 4-15 at 144MHz.

Again we have excellent agreement, as in the case of the PEC approximation to TM_y. This indicates that we will also be able to model TE_y propagation over terrain using a robust, simplifying boundary condition, and therefore avoid solving the interior field equation. The impedance boundary approximation has been utilized over many different boundaries and at many frequencies in terrain propagation

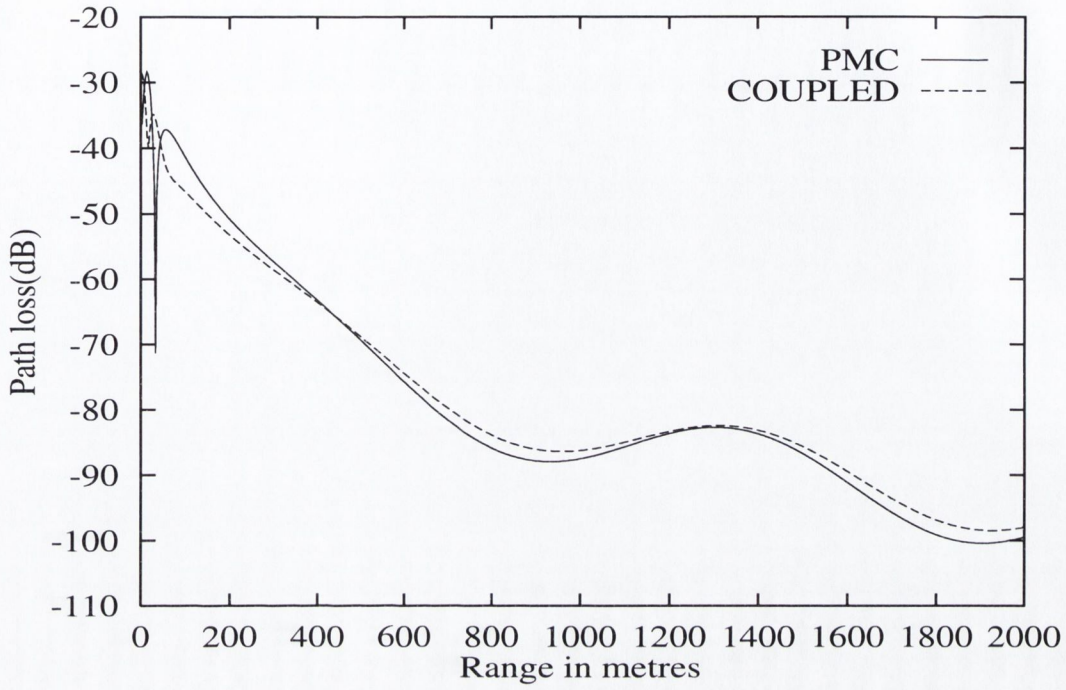


Figure 4-13: Pathloss PMC v Coupled for more gently undulating profile.

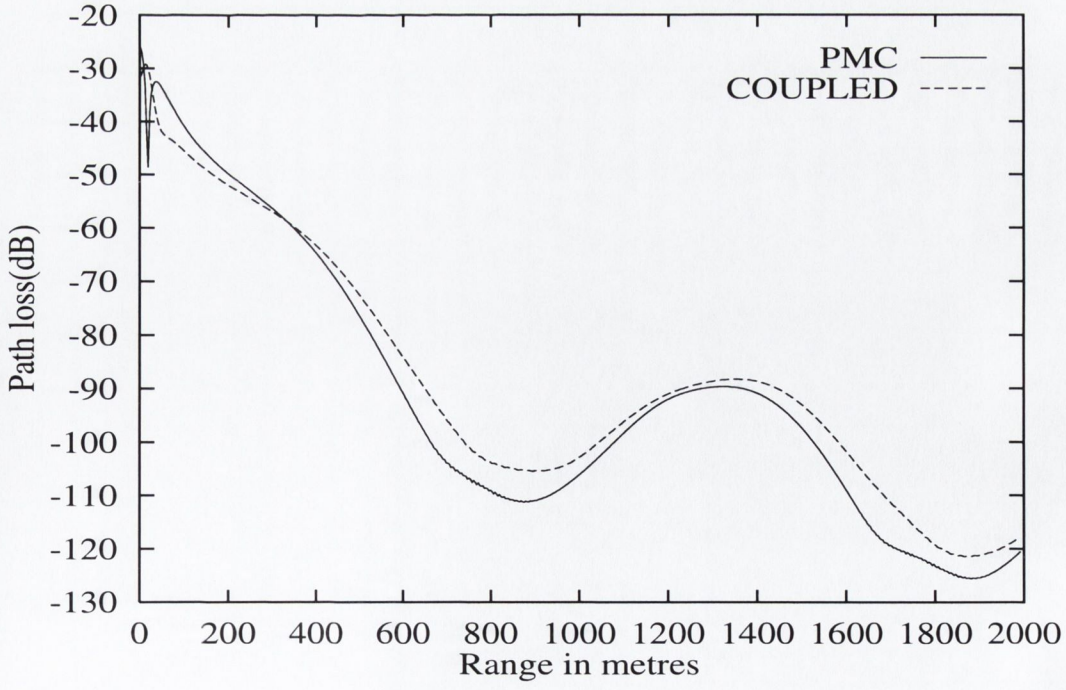


Figure 4-14: Pathloss - PMC v Coupled for profile of Figure 4-11.

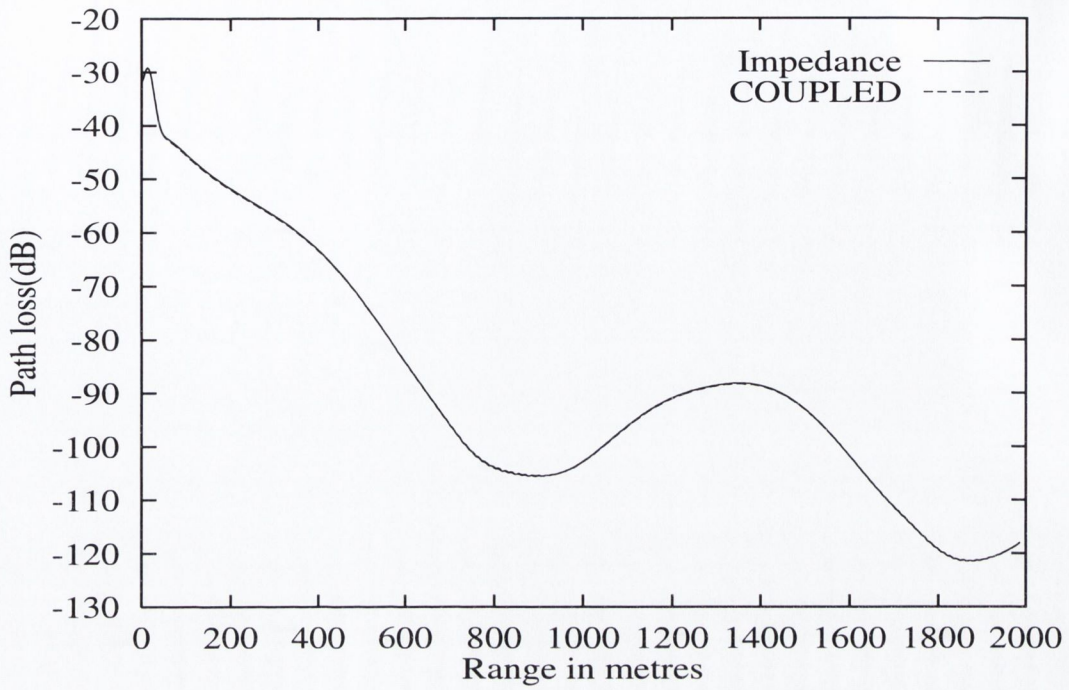


Figure 4-15: Pathloss - Impedance method v Coupled.

modeling[16] and other applications [28].

4.6 Discussion

The solution of 2D terrain problems by the method of coupled integral equations has been demonstrated. Analysis of plane wave reflection coefficients reveals that for terrain material parameters, the simplifying boundary approximations, of PEC for TM_y, and PMC or Impedance boundary for TE_y, may be applied to distinct polarization modes. Thus the problem is reduced to a single integral equation of scalar form. In Chapter 6 these boundary approximations will be incorporated into a quasi 3D dimensional vector integral equation. In this case however, they must be applied in combination, to separate polarization components as discrete polarization modes will no longer exist.

Chapter 5

A Quasi-3D Approach for PEC Surfaces.

5.1 Introduction

As we have seen, a large number of methods already exist for predicting path loss over smoothly undulating terrain. Such methods are used to gain an understanding of the behavior of the radio channel and for cellular mobile radio planning and site optimization. In the previous chapter we looked at existing full wave, and forward scattering approaches that make use of a 2D approximation, resulting in decoupled TM_y and TE_y polarization modes. In that case analytical integration was performed over y trivially (4.9), by solving for an infinite line source. Multiplying by a range dependence factor then recovers the point source solution.

We now demonstrate that for a point source excitation over a 2D PEC type surface, integration over the direction of corrugation can also be performed analytically in a local region about the source-observer radial[27]. The result is an alternative but essentially equivalent 2D formulation to (4.14). The fact that the interaction is localized to a small area about the radial, is akin to the theory of geometrical diffraction where scattering from an obstruction may be modeled by a local ray theory and an appropriate diffraction coefficient. Noting that GTD may be used to represent inclined wedges or plates in a three dimensional approach, it is deduced that scattering

from transversely inclined terrain strips might be modeled using the same analytical transverse integration. We demonstrate that this is indeed the case.

A model is adopted that replaces the 2D corrugated profile (Figure 4-1.b) with a succession of sloping linear strips (Figure 5-3) inclined in the transverse direction ($\hat{y}$) in a formalism characterizing first order *cross-polarization* effects. The new method will require only the same level of terrain resolution as the TM_z and TE_z methods and so we encounter the same order of numerical complexity as a 2D integral equation scheme.

We begin by demonstrating the analytical transverse integration in 5.2. The new surface model is introduced in section 5.3, and in section 5.4 we outline the formulation of the new quasi-3D integral equation approach. In section 5.6 comparison is made with UTD for an inclined wedge. In 5.7 the performance of the model is examined for undulating PEC surfaces at VHF and UHF.

5.2 Analytical Transverse Integration for a Point Source over a PEC Surface

We will work with the magnetic field integral equation (2.85) for a closed PEC surface, in the presence of an external source, which may be written in terms of the surface current $\mathbf{J}(\mathbf{r})$ at point $\mathbf{r}$,

$$\frac{1}{2}\mathbf{J}(\mathbf{r}) = \mathbf{J}^I(\mathbf{r}) + \mathbf{J}^S(\mathbf{r}) \tag{5.1}$$

in terms of the components $\mathbf{J}^I(\mathbf{r})$ and $\mathbf{J}^S(\mathbf{r})$ excited by incident and scattered fields respectively, where $\mathbf{J}^S(\mathbf{r})$ is defined in terms of the principal value integral

$$\mathbf{J}^S(\mathbf{r}) = \hat{\mathbf{n}} \times \oint_S \mathbf{J}(\mathbf{r}') \times \nabla' G(\mathbf{r}, \mathbf{r}') dS' \tag{5.2}$$

In fact the terrain will behave like a perfect electric conductor for horizontal electric polarizations and as a perfect magnetic conductor for low grazing vertical electric polarizations. The case is made here for purely PEC surfaces. A similar procedure may be applied for a PEC/PMC polarization dependent boundary by resolving field components on an elemental strip, and will be demonstrated in Chapter 6.

At this stage standard methods make the corrugated terrain approximation detailed in Chapter 4. We wish to solve (5.1) for the surface current along the profile $\mathbf{r} = (x, 0, \chi(x))$ where the terrain has been approximated by strips as illustrated in Figure 5-1. $\hat{\mathbf{r}}_2$ and r_2 represent the unit vector and amplitude of the vector $\mathbf{r}_2 = \mathbf{r} - \mathbf{r}'$

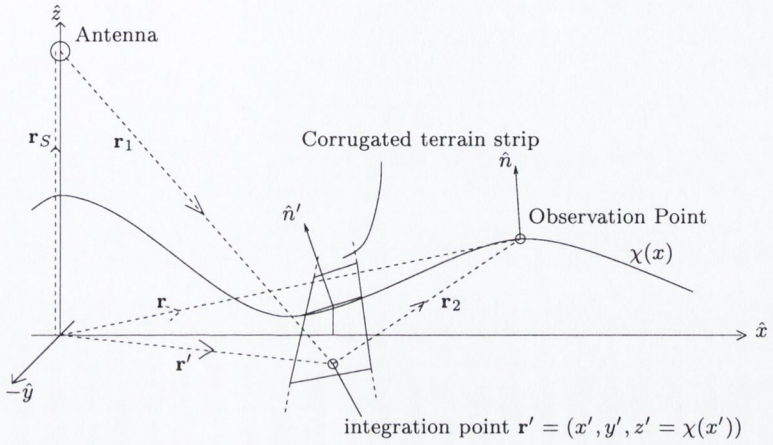


Figure 5-1: *Elemental terrain strip for a 2D profile, indicating vectors* $\mathbf{r}_1$, $\mathbf{r}_2$ *connecting antenna to integration point and integration to observation point respectively.*

connecting integration and observation points, respectively. In terms of these quantities and evaluating the derivative of the Green's function, (5.2) becomes

$$\mathbf{J}(\mathbf{r}) = 2\mathbf{J}^I(\mathbf{r}) + 2\int_\chi \left((\hat{\mathbf{n}} \cdot \hat{\mathbf{r}}_2)\mathbf{J}(\mathbf{r}') - (\hat{\mathbf{n}} \cdot \mathbf{J}(\mathbf{r}'))\,\hat{\mathbf{r}}_2\right)\left(\frac{1 + ikr_2}{4\pi r_2^2}\right)e^{-ikr_2}dy'dt' \ . \tag{5.3}$$

t representing the line element parameter where $dt = \sqrt{1 + (d\chi/dx)^2}dx$.

The surface is illuminated by an electric dipole source oriented in the $\hat{y}$ direction and at the antenna location $\mathbf{r}_S = (0, 0, z_S = \chi(0,0) + h_S)$ where h_S is the height of the antenna above the ground. The incident field is defined as the antenna far field and is given in spherical polar coordinates(system (r, θ', ϕ') aligned with source) as,

$$E^I_{\theta'} = j(I_0 L_0)\omega\mu\frac{e^{-ikr_1}}{4\pi r_1}\sin\theta' \tag{5.4}$$

$$E^I_r \to 0 \tag{5.5}$$

giving

$$\mathbf{H}^I = jI_0L_0\omega\frac{e^{-ikr_1}}{4\pi r_1}\sin\theta'\hat{\phi}' \tag{5.6}$$

Given the symmetry of the incident field and 2D channel, the surface current will have the following properties

$$\begin{aligned} \mathbf{J}_x(y') &= -\mathbf{J}_x(-y') \\ \mathbf{J}_y(y') &= \mathbf{J}_y(-y') \\ \mathbf{J}_z(y') &= -\mathbf{J}_z(-y') \end{aligned} \tag{5.7}$$

As a consequence of these symmetries and the fact that the $\hat{y}$ component of $\hat{\mathbf{n}}$ is zero, the x and z components of the scattered field in (5.3) from either side of the x-axis, will be equal and opposite. Therefore when determining the scattered field at the surface along the contour $\chi(\mathbf{r})$, the $\hat{x}$ and $\hat{z}$ components of $\mathbf{J}^S$ will be cancelled when the integration over y' is performed. The only non-zero component of the scattered current integral $\mathbf{J}^S$ is that in the direction $\hat{y}$. From (5.3) this is given by,

$$\begin{aligned} \mathbf{J}^S(x) &= \int_\chi \left(J_y(\mathbf{r}')(\hat{\mathbf{n}} \cdot \hat{\mathbf{r}}_2) + \frac{y'}{r_2}(\hat{\mathbf{n}} \cdot \mathbf{J}(\mathbf{r}')) \right) \times \frac{(1+ikr_2)}{4\pi r_2^2} e^{-ikr_2} dy' dt' \hat{\mathbf{y}} \\ &\approx \int_\chi J_y(\mathbf{r}')(\hat{\mathbf{n}} \cdot \hat{\mathbf{r}}_2) \frac{(1+ikr_2)}{4\pi r_2^2} e^{-ikr_2} dy' dt' \hat{\mathbf{y}} \end{aligned} \tag{5.8}$$

The approximation in (5.8) is exact for a cylindrical wave originating from a line source directed along the y-axis where $\hat{\mathbf{n}} \cdot \mathbf{J} = 0$. For the point source, the approximation is valid when the bulk of the scattering contributions come from the portion of the terrain in the vicinity of the x-axis, which will be true in the case of a corrugated terrain.

Due to the fact that the surface current $\mathbf{J}$ is excited by a point source, it is reasonable to assume an approximately spherical phase distribution for $\mathbf{J}$, with its center at the antenna location. This is a weaker approximation than physical optics, since we are only making an approximation to the phase variation of the surface current and not to its precise phase, and vector amplitude.

The derivative of the Green's function, having the spatial phase e^{-ikr_2}, also has a spherical phase front, but is centered on the observation point. We define the vector joining the antenna to the point on a strip $\mathbf{r}'_0 = (x', 0, \chi(x'))$, as $\mathbf{r}_1^a$ or $\mathbf{r}_1^a = \mathbf{r}'_0 - \mathbf{r}_S$ and the vector joining the observation point to the same point $\mathbf{r}'_0$ as $\mathbf{r}_2^a = \mathbf{r} - \mathbf{r}'_0$. We approximate the phase variation in $\mathbf{J}(\mathbf{r}')$ and $\nabla' G(\mid \mathbf{r} - \mathbf{r}' \mid)$ with respect to y' by

expanding the spherical phase fronts around $\mathbf{r}'_0$. The phase fronts are indicated in fig. 5-2 along with the quantities Δr_1 and Δr_2 the corrections to the path lengths r_1^a and r_2^a to attain the path lengths r_1 and r_2 respectively.

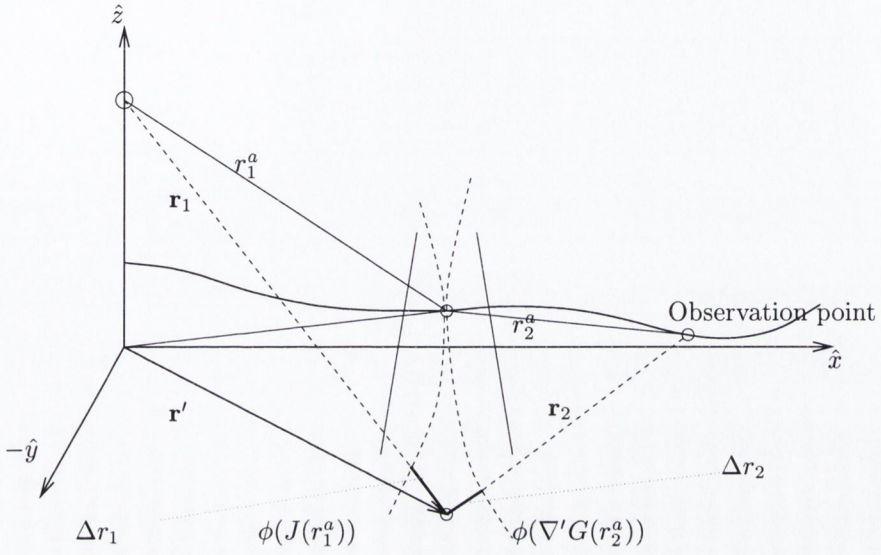


Figure 5-2: *Δr_1 and Δr_2, the corrections to the lengths r_1^a and r_2^a to attain the lengths r_1 and r_2, and the spherical phase fronts $\phi(\mathbf{J}(r_1^a))$ and $\phi(\nabla' G(r_2^a))$*

The phases of the two functions at the point $\mathbf{r}'$ are,

$$\mathbf{J}(\mathbf{r}') \approx \mathbf{J}(x', 0, \chi(x'))e^{-ik\Delta r_1(y')} \tag{5.9}$$

and,

$$\frac{1+ikr_2}{4\pi r_2^2}e^{-ikr_2} = \frac{1+ikr_2^a}{4\pi r_2^{a\,2}}e^{-ikr_2^a}e^{-ik\Delta r_2(y')} = f(r_2^a)e^{-ik\Delta r_2(y')} \tag{5.10}$$

and where we will make the general definition

$$f(r) = \frac{1+ikr}{4\pi r^2}e^{-ikr}$$

Provided $y' \ll r_1$ and $y' \ll r_2$ the series expansions of Δr_1 and Δr_2 are,

$$\begin{aligned} \Delta r_1 &\approx \frac{y'^2}{2r_1^a} \\ \Delta r_2 &\approx \frac{y'^2}{2r_2^a} \end{aligned} \tag{5.11}$$

The condition that $y' \ll r_2$ can be justified by the presence of the product $\hat{\mathbf{n}} \cdot \hat{\mathbf{r}}_2$ in the integral in (5.8). For a smooth surface, which is therefore locally approximately

planar, this product tends to zero in the near field. Therefore near field interactions are vanishingly small. For larger arguments of r_2 the bulk of the scattering takes place in the region where $\mid y' \mid$ is small, and so the relation $y' \ll r_2$ holds where required. To justify the relation $y' \ll r_1$ we note firstly that we are working in the far field of the antenna which is elevated above the terrain. Again, given that the scattering region contributing principally to the integral is narrow we may make the approximation $y' \ll r_1$ even near the antenna. This approximation will improve considerably as we move away from the antenna.

Referring to the quadratic expansions in y (5.11), the correction to the total *source* $\rightarrow$ *integration point* $\rightarrow$ *observation point* path length is

$$\Delta r_{12} = \Delta r_1 + \Delta r_2 \approx \frac{r_1^a + r_2^a}{2 r_1^a r_2^a} y'^2 \ , \tag{5.12}$$

Factoring out invariants in y' from the transverse integration in (5.8), we simplify the integral to

$$\mathbf{J}^S(x) = \int_{\chi(x')} \mathbf{J}(x')(\hat{\mathbf{n}} \cdot \hat{\mathbf{r}}_2^a) f(r_2^a) \times \int_{-\infty}^{\infty} e^{-ik\Delta r_{12}} dy' dt' \tag{5.13}$$

Now the y' integration takes the form of a Fresnel integral[21],

$$\int_{-\infty}^{\infty} e^{-ik\Delta r_{12}} dy' = e^{-i\pi/4} \sqrt{\frac{2\pi}{k} \frac{r_1^a r_2^a}{r_1^a + r_2^a}} \tag{5.14}$$

ultimately giving a scattered field,

$$\mathbf{J}^S(x) = \int_{\chi(x')} \mathbf{J}(x')(\hat{\mathbf{n}} \cdot \hat{\mathbf{r}}_2^a) f(r_2^a) \times e^{-i\frac{\pi}{4}} \sqrt{\frac{2\pi}{k} \frac{r_1^a r_2^a}{r_1^a + r_2^a}} dt' \tag{5.15}$$

and so the resulting integral equation for the surface current may be written,

$$\mathbf{J}(x) = 2\mathbf{J}^I(x) + 2 \int_{\chi(x')} \mathbf{J}(x')(\hat{\mathbf{n}} \cdot \hat{\mathbf{r}}_2^a) f(r_2^a) \times e^{-i\frac{\pi}{4}} \sqrt{\frac{2\pi}{k} \frac{r_1^a r_2^a}{r_1^a + r_2^a}} dt' \tag{5.16}$$

Considering the discretized problem we are now able to express the integral equation in matrix form as,

$$\mathbf{J} = 2\mathbf{J}^I + 2\mathbf{Z}\mathbf{J} \tag{5.17}$$

where $\mathbf{Z}$ is the impedance matrix characterizing the interaction between strips m and n having elements,

$$\mathbf{Z}_{mn} = (\hat{\mathbf{n}}_n \cdot \hat{\mathbf{r}}_{2\,mn}^a) f(r_{2\,mn}^a) e^{-i\pi/4} \sqrt{\frac{2\pi}{k} \frac{r_{1\,m} r_{2\,mn}}{r_{1\,m} + r_{2\,mn}}} \Delta t'_m \tag{5.18}$$

It may be demonstrated empirically that over a terrain with gentle slopes, the contributions to the scattering integral from the region $-\infty < x < 0$ are small by comparison to the forward propagating field from the antenna. This is particularly so where the antenna is located over high ground. A region of the profile preceding the antenna is included in the integral, consistent with the closure of the contour at infinity for the MFIE, or to eliminate under-terrain diffraction effects, in the case of the EFIE.

In addition backscattering effects may also be neglected, ie

$$\sum_{m=n+1}^{\infty} \mathbf{Z}_{mn}\mathbf{J}_m \approx 0 \tag{5.19}$$

Therefore (5.17) reduces to

$$\mathbf{J}_n \approx 2\mathbf{J}_n^I + 2\sum_{m=0}^{n-1} \mathbf{Z}_{mn}\mathbf{J}_m \tag{5.20}$$

which may be implemented directly as a recursive forward summation. $\lambda/4$ sampling rates are sufficient for accurate results. The numerical expense of the summation is high at order N^2 but this is only the simplest form of the algorithm and time saving techniques may be employed to good effect[9][2].

The efficacy of the transverse integral procedure for 2D profiles has been tested in [27] and good agreement with both UTD, and terrain field measurements is found. The results also agree with those of the alternative 2D formulation, in terms of a line source (Chapter 4), and we will not replicate them here.

5.3 New Terrain Model

We now extend this one dimensional integral method, to incorporate a first order correction accounting for transverse height variations in the surface. We require that the surface varies smoothly in the transverse direction, as is conventionally required in the direction of propagation. A piecewise locally 2D surface, constructed out of flat strips inclined in both the $\hat{x}$ and $\hat{y}$ directions (Figure 5-3) is used to approximate the 3D surface. The intersection of the plane $y = 0$ with the set of infinite strips is the 2D radial profile. The key advantage is that we can integrate over the y dimension

analytically making the same physical optics type approximation to the transverse phase variation of the current. The set of strips no longer forms a continuous surface, the effect being more pronounced as we move away from the $y = 0$ plane. However, the principal contributions to the forward scattered field will come from the region near $y = 0$. We note that our terrain data may have a resolution of 10 - 50m. Both the terrain height, and transverse gradients, are interpolated between each data point. As step sizes in the discrete matrix system are small ($\approx \lambda/4$), and so the height and transverse gradients vary only very slightly from one terrain element to the next, the discontinuities at principal scatter points near $y = 0$ will be small also, and they do not result in serious error. Indeed the approximation will be good provided the tangent plane approximation to the surface is satisfactory over the region about the radial lying within the largest first Fresnel zone, defined for any observation point considered. Scattering contributions from beyond this region are not included and are small in most cases. It is the combination of this terrain approximation and integration technique that distinguishes this as a quasi three dimensional method (Q3D).

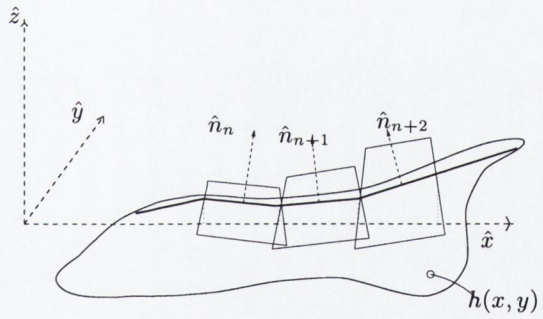


Figure 5-3: *The terrain surface around a radial is approximated by a set of flat strips with unit normals $\hat{n}_n$, inclined in both $\hat{x}$ and $\hat{y}$ directions.*

5.4 Analytical Integration for Inclined Segments

We now replace the smooth surface S in (5.2), with the surface χ which represents the radial height profile piecewise linearly as well as the transverse gradients across that

profile. Let $h(x,y)$ be the original surface height function. $\chi(x,y)$ is then defined,

$$\chi(x,y) = h(x,0) + y\frac{\partial h}{\partial y}\,|_{y=0}\,(x) \tag{5.21}$$

We then write the elemental surface area

$$\begin{aligned} d\chi &= \sqrt{(1+(\partial\chi/\partial y)^2)}\; dy\sqrt{1+(\partial\chi/\partial x)^2}\; dx \\ &= dY(x)\, dX(x) \end{aligned} \tag{5.22}$$

Referring to (5.2), in the plane $y = 0$

$$\begin{aligned} \mathbf{J}^S(x,0,\chi(x)) = \oint_{\chi} dX'(x') \int_{-\infty}^{\infty} ((\hat{\mathbf{n}}\cdot\hat{\mathbf{r}}_2)\mathbf{J}(\mathbf{r}') - (\hat{\mathbf{n}}\cdot\mathbf{J}(\mathbf{r}'))\hat{\mathbf{r}}_2) \\ \cdot\left(\frac{1+ikr_2}{4\pi r_2^2}\right) e^{-ikr_2}\, dY'(x') \end{aligned} \tag{5.23}$$

The discrete representation of the surface[1] χ is a set of strips n having variable unit normals $\hat{\mathbf{n}}_n$ truncated within the range $x_n \pm \frac{\Delta x_n}{2}$ (Figure 5-3). To proceed let the transverse phase variation of the current on an elemental strip (Figure 5-4) be approximated by the physical optics phase variation $Ae^{-ikr_1(y)}$, where A is an arbitrary complex coefficient and r_1 denotes the modulus of the vector $\mathbf{r}_1$ connecting source and scattering points. For an observation point $\mathbf{r}$, there will be a point on the strip near the plane $y = 0$, where the product $Ae^{-ikr_1(y')}G(\mathbf{r},\mathbf{r}')$ has a stationary phase with respect to a displacement in y'. Referring to Figure 5-4, most of the field scattered to $\mathbf{r}$ will originate from the neighbourhood of this point which we will define as the principal scattering point $\mathbf{r}^p$. It may be easily shown that $\mathbf{r}^p$ is the point minimizing the total path length $r_1 + r_2$, and

$$\mathbf{r}^p = (x', y^p, z^p)\ ,\quad z^p = \chi(x') + \frac{\partial\chi(x')}{\partial y'}y^p \tag{5.24}$$

[1] Integration over χ represents a summation of the principal value integrals over each strip element thereby avoiding integration over discontinuities. Note that the interaction between the different strips is still retained.

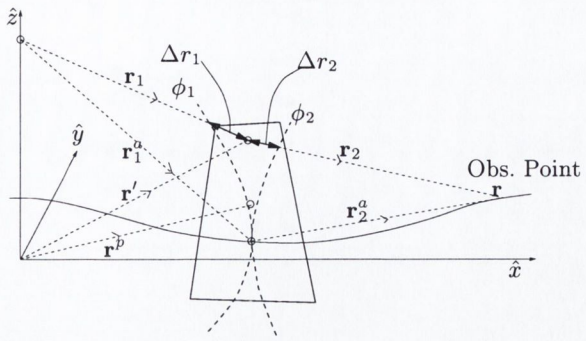


Figure 5-4: *A transversely inclined strip illustrating the vectors* $\mathbf{r}^p$, $\mathbf{r}_1$, $\mathbf{r}_2$, $\mathbf{r}_1^a$, $\mathbf{r}_2^a$, *phase fronts* ϕ_1 *and* ϕ_2 *and path length corrections* Δr_1 *and* Δr_2.

For a particular observation point and scattering strip the corresponding value of y^p is,

$$y^p = \frac{\partial \chi}{\partial y}\left(\frac{r_2^a(z_S - \chi(x')) + r_1^a(z - \chi(x'))}{r_1^a + r_2^a}\right) \tag{5.25}$$

where the source is located at $(0, 0, z_S)$ and the observer at $(x, 0, z)$. The vector $\mathbf{r_1^a}$ connects the source to the point $(x', 0, \chi(x'))$, and $\mathbf{r_2^a}$, that point to the observation point.

We will be using a quadratic power series expansion in y' to approximate the phase of the integrand. We require this quadratic phase approximation to be accurate over a range in y' up to

$$y' = \mid y^p \mid + \mid y^{F1} \mid \tag{5.26}$$

in order to include the principal scattering point and its first Fresnel zone width defined

$$\mid y^{F1} \mid \leq \sqrt{\frac{\lambda(r_1^a r_2^a)}{r_1^a + r_2^a}}$$

The quadratic phase expansion will be valid where

$$(\frac{y'}{r_1})^2 \ll 1 \qquad and \quad (\frac{y'}{r_2})^2 \ll 1 \tag{5.27}$$

For the value of y' given in (5.26)

$$(\frac{y'}{r_{1/2}})^2 = \frac{(y^p + y^{F1})^2}{r_{1/2}^2} \ll 1 \tag{5.28}$$

and this is guaranteed where r_2 is large. r_1 will always be large in comparison to y^{F1} and y^p. Where r_2 is small

$$y^{F1} \to \sqrt{\lambda} \tag{5.29}$$

and

$$y^p \to \frac{\partial \chi}{\partial y}(\frac{r_2}{r_1}(z_s - z') + \frac{\partial \chi}{\partial y} r_2) \tag{5.30}$$

and both of these quantities are again small in comparison to r_2. Thus the quadratic phase approximation will be adequate over the first Fresnel zone for an inclined strip.

The largest value of Fresnel zone associated with a profile length R is $y^{F1}_{max} \approx (1/2)\sqrt{\lambda R}$, indicating that we require the tangent plane approximation to the surface to hold over a region of $\approx 72m$ for $R = 10km$, at 144MHz. Such a transverse range is comparatively large. In such cases we may not simply define on-axial and off-axial scattering regions as the two will overlap. The interaction approximated by the Fresnel Integral may have substantial error but must still be viewed as an improvement on the corrugated terrain interaction term. It is also noted that at these lower frequencies, larger scale terrain obstructions will be of greater interest, the effects of more rapid, small scale terrain height variations being more important at higher frequency. As frequency rises the Fresnel zone width will be reduced to the extent that we may satisfactorily separate on and off-axial contributions at AMPS, GSM and 3G bands. We then approximate on-axial contributions with the Fresnel Integral, and neglect off-axial effects.

We have chosen a physical optics surface current phase variation as a best approximation to the unknown surface current phase variations. The accuracy of the transverse integration is reduced when the actual phase variations of the current depart from that of Physical Optics but the approximation is reasonable to first order and is, in any case no worse than the cylindrical phase front approximation used in 2D models.

5.5 Off Axial Scattering

Off axial scattering will not be included in this model. We consider here the impact of neglecting such contributions. We must gauge the magnitude of the integral over the unknown, off axial current.

Firstly we consider the issue of stationary phase points in the off axial integral over y'. Such points will not arise on profiles having gradients less than 45^o which we may comfortably consider beyond our scope[2]. Essentially, all stretched strings between source and observation points will move to the radial, or principal scattering points identified earlier. It was first indicated by Hufford[26] on transforming the surface integral to a 1D integral, that no stationary phase points would arise away from the axis where the current amplitude is slowly varying, and this was a key motivation for formulating the 2D integral approach. Hufford makes the qualification that there may be off axial points contributing a reflection, but it may be assumed that there will be no specular terrain reflections, back onto the axial path, and where reflections do occur they must be considered as *partial back-scattering* effects. The same is true of diffraction effects, which we will now consider. As in a 2D integral equation however, it is not simply sufficient to consider stationary phase points, and there will be other regions where the integrand is varying more gradually, and will make a contribution to the integral.

The case of a transverse Guassian hill profile is examined(Figure 5-5. We wish to assess the relative degree of scattering when the steepest portion of the profile is at various displacements in y' from the radial. We lack the mathematical machinery to do this rigorously, but we will take a line element across the hill profile in y', and integrate the physical optics phase and Green's function product, over a finite portion of this line element, corresponding to a Fresnel zone width, and these are indicated by the ellipses in Figure 5-5. In reality the creeping wave diffraction process around such a profile is highly complex. However, this heuristic analysis will give an indication of the relative magnitude of the interaction terms.

[2]Even in such cases further conditions would be required for an off axial stationary phase point to arise.

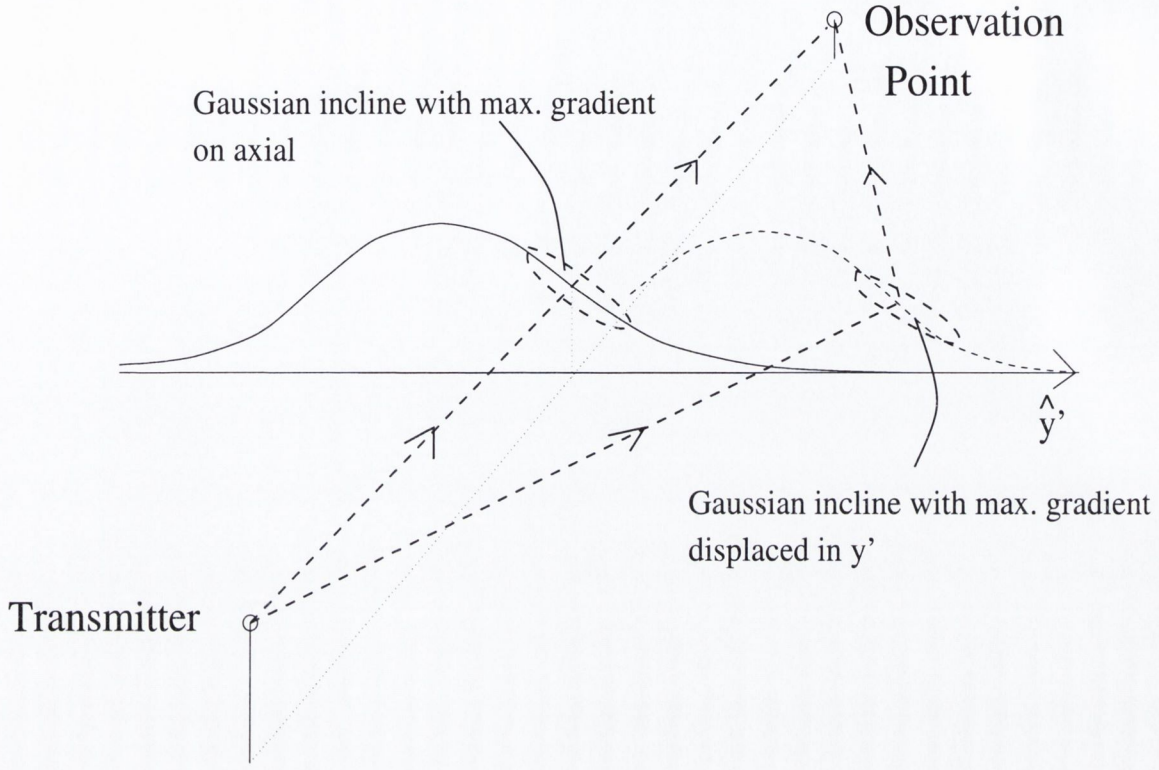


Figure 5-5: *Transverse Gaussian hill profiles with point of steepest inclination on axial, and shifted off axial.*

We take a moderately steep hill profile, having a peak of 50 meters, and maximum gradient of approximately 1/7. The antenna is located at a height of 50 meters, 2000 meters before the hill crest, and the observation point is at 2000 meters beyond the hill crest. The integral over one Fresnel zone width is evaluated, centered on the steepest portion of the hillside, which will be taken at a range of y' displacements, from on the axis itself(solid line, Figure 5-5), to a 300 meter displacement from the axis(broken line, Figure 5-5). The results are plotted on a logarithmic scale in Figure 5-6.

It is evident that the contribution to the integral falls off steadily as we move the transverse gradient away from the axis. A point is reached where the integral becomes oscillatory indicating rapid variation in the integrand with y'. Of course the situation is more complex when we consider the full scattering term in (5.23). We consider separately the factor

$$\mathbf{F} = ((\hat{\mathbf{n}} \cdot \hat{\mathbf{r}}_2)\mathbf{J}(\mathbf{r}') - (\hat{\mathbf{n}} \cdot \mathbf{J}(\mathbf{r}'))\hat{\mathbf{r}}_2) \tag{5.31}$$

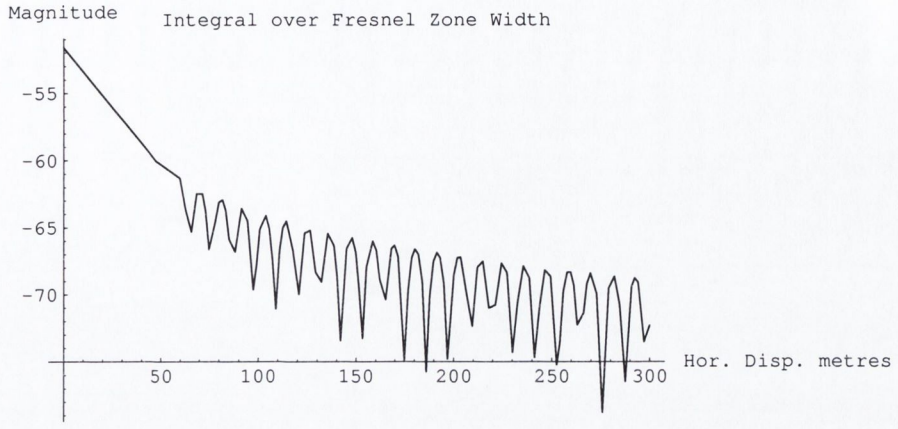


Figure 5-6: *Integral of physical optics current and Green's function from a portion of transversely inclined terrain, against displacement in y'*

The *copolar* current is J_y, so contributions to the *cross-polar* currents J_x and J_z will come from the components F_x and F_z. Now

$$F_x = (\hat{\mathbf{n}} \cdot \hat{\mathbf{r}}_2) J_x - (\hat{\mathbf{n}} \cdot \mathbf{J}(\mathbf{r}'))\hat{r}_x \tag{5.32}$$

$$F_z = (\hat{\mathbf{n}} \cdot \hat{\mathbf{r}}_2) J_z - (\hat{\mathbf{n}} \cdot \mathbf{J}(\mathbf{r}'))\hat{r}_z \tag{5.33}$$

We only need consider contributions for $\hat{r}_y \ll 1$, as we have seen that the integrand is rapidly oscillatory with y' for points where this constraint is not satisfied. This is not directly neglecting off axial effects, only those at excessively wide propagation angles. Hence, the first order components of these vectors are J_y, $\hat{n}_z$ and $\hat{r}_x$, with all others being second order, and the *cross-polar* components of $\mathbf{F}$ may be approximated

$$F_x = -n_y r_x J_y - n_z r_x J_z \tag{5.34}$$

$$F_z = n_x r_x J_z - n_y r_z J_y \tag{5.35}$$

and F_z is evidently of smaller magnitude than F_x. We notice that neither of the above are sensitive to the small quantity $\hat{r}_y$. This is significant in that contributions to the *cross-polar* current will come from the near axial stationary phase points, with no bias weighting in $\hat{r}_y$ to inclined off axial points. Neither are the above sensitive to J_x which will be greater at off axial points. This further indicates that there is

no reason to expect significant contributions to the *cross-polar* current from off axial regions for moderately undulating terrain. (5.35) indicates that it is primarily the gradient at the observation point that couples in *cross-polar* scattered current. It is such components that we are aiming to evaluate with Q3D. Similar relations hold in the expression for the field over the terrain. In (5.53) the *cross-polar* field is given by H_y, and it is evident that this will be insensitive to $\hat{r}_y$.

Where the on axial transverse gradient is zero, and there are non zero off axial gradients, then there will be a *cross-polar* field that is not predicted by Q3D, but the purpose of this discussion has been to indicate that such *cross-polar* contributions will be small. Further, it is statistically obvious that the majority of radial profiles will run across transversely inclined paths for the bulk of their length, apart from where we are dealing with trivially flat terrain. For paths that do fall directly on the crest of a hill it will still be the case that most of the points on the path will be on transverse inclination, and it is these points that will contribute most strongly to the *cross-polar* field.

Neglecting the amplitude variation with y', we factorize the spherical phase fronts of the current and the function $\nabla' G$,

$$\mathbf{J}(\mathbf{r}') \cdot e^{-ikr_2} = e^{-ik\Delta r_1} \mathbf{J}(x', 0, \chi(x')) \cdot e^{-ikr_2^a} e^{-ik\Delta r_2} \tag{5.36}$$

where we have defined the path length differences (Figure 5-4),

$$\begin{aligned} \Delta r_1 &= r_1 - r_1^a \\ \Delta r_2 &= r_2 - r_2^a \ . \end{aligned} \tag{5.37}$$

These quantities may be approximated as second order Taylor expansions in y',

$$\Delta r_1(y') \approx \frac{(\chi(x') - z_S)\frac{\partial \chi}{\partial y}}{r_1^a} y' + \frac{1}{2}\frac{1}{r_1^a} y'^2 \tag{5.38}$$

$$\Delta r_2(y') \approx \frac{(\chi(x') - z)\frac{\partial \chi}{\partial y}}{r_2^a} y' + \frac{1}{2}\frac{1}{r_2^a} y'^2 \tag{5.39}$$

the coefficients of y' and y'^2 approximating the first and second derivatives of r_1 and r_2 with respect to y at the point $\mathbf{r}^a$. These quantities are highly sensitive to the quadratic power of y' in the region $y' = 0$, unlike the terrain height function for a

smooth terrain, thus justifying the different orders of approximation with respect to y'.

As the derivatives are constant for a given surface strip we may denote the total phase shift with respect to y' as

$$e^{-ik(\Delta r_1(y')+\Delta r_2(y'))} = e^{-ik(ay'+by'^2)} \tag{5.40}$$

for

$$a = \frac{\partial \chi}{\partial y}\frac{r_2^a(\chi(x')-z_S)+r_1^a(\chi(x')-z)}{r_1^a r_2^a} \tag{5.41}$$

$$b = \frac{1}{2}\frac{r_1^a+r_2^a}{r_1^a r_2^a} \tag{5.42}$$

With $\mathbf{r}_2$ parameterized by

$$\mathbf{r}_2 = \left(x-x', -y', z-\chi(x')-\frac{\partial \chi}{\partial y}y'\right) \tag{5.43}$$

we arrive at a full expression for the integral (5.23) in terms of the parameter y'.

$$\mathbf{J}^S(x) = \oint_{\chi(x')} f(r_2^a(x'))$$

$$\cdot\left[\int_{-\infty}^{\infty} dY(x')e^{-ik(ay'+by'^2)}\left((\hat{\mathbf{n}}\cdot\hat{\mathbf{r}}_2)-\hat{\mathbf{n}}\,\hat{\mathbf{r}}_2\right)\right]$$

$$\times\mathbf{J}(r_1^a(x'))\,dX'(x') \tag{5.44}$$

where $f(.)$ is given in (5.10).

As $\hat{\mathbf{n}}$ is constant inside the y' integral we define the quantity,

$$\tilde{\mathbf{r}}_2 = \frac{1}{r^p}\int_{-\infty}^{\infty}\mathbf{r}_2 e^{-ik(ay'+by'^2)}dY(x') \tag{5.45}$$

$1/r^p$ has been factored out of the integral as an approximation to the near constant amplitude of $1/r_2$ over the small domain in y' contributing to the integral. On inspection of (5.43) there are two types of integral in (5.45). If we regard the wavenumber k as containing a vanishingly small imaginary part these integrals may be evaluated analytically. This is easily justified considering the amplitude factors that have been neglected or by introducing a small physical loss into the propagation medium. Hence we define[21]

$$A = \int_{-\infty}^{\infty} e^{-ik(ay'+by'^2)}dy' = e^{i(\frac{a^2k}{4b}-\frac{\pi}{4})}\sqrt{\frac{\pi}{bk}} \tag{5.46}$$

and

$$\begin{aligned} B &= \int_{-\infty}^{\infty} y' e^{-ik(ay'+by'^2)} dy' \\ &= -\frac{a}{2b} e^{i(\frac{a^2 k}{4b} - \frac{\pi}{4})} \sqrt{\frac{\pi}{bk}}\, Sign(a) \end{aligned} \tag{5.47}$$

and so,

$$\tilde{\mathbf{r}}_2 \approx \frac{\sqrt{(1+(\partial\chi(x')/\partial y)^2)}}{r^p} \begin{pmatrix} (x-x')A \\ -B \\ (z-\chi(x'))A - \frac{\partial\chi}{\partial y} B \end{pmatrix} \tag{5.48}$$

The resulting integral is

$$\mathbf{J}^S(x) = \oint_{\chi(x')} f(r_2^a) \cdot [(\hat{\mathbf{n}} \cdot \tilde{\mathbf{r}}) - \hat{\mathbf{n}}\,\tilde{\mathbf{r}}] \times \mathbf{J}(x') dX'(x') \tag{5.49}$$

The remaining integration is over one dimension but the presence of the dyadic matrix $\hat{\mathbf{n}}\tilde{\mathbf{r}}$ couples the different components in $\mathbf{J}$. Terms in n_y are included in the model. In matrix form,

$$\mathbf{ZJ} = \mathbf{J}^I \tag{5.50}$$

where for strips n and m the interaction matrix $\mathbf{Z}$ has the elements,

$$\mathbf{Z}_{mn} = -f(r_{2\,mn}^a)\Delta X'(x'_m) \cdot [(\hat{\mathbf{n}}_n \cdot \tilde{\mathbf{r}}_{mn}) - \hat{\mathbf{n}}_n\,\tilde{\mathbf{r}}_{mn}] \tag{5.51}$$

$$\mathbf{Z}_{nn} = \frac{1}{2} \tag{5.52}$$

For the case of smooth terrain topographies this may be evaluated as a recursive summation in a forward scattering scheme.

5.5.1 Evaluation of Path Loss

The magnetic field $\mathbf{H}(\mathbf{r})$ at an observation point over the surface can be computed directly from the surface current using

$$\mathbf{H}(\mathbf{r}) = \mathbf{H}^I(\mathbf{r}) + \int_S \mathbf{J}(\mathbf{r}') \times \nabla' G(\mathbf{r}, \mathbf{r}') ds' \tag{5.53}$$

Written in terms of the vector $\mathbf{J}$ in discrete form

$$\mathbf{H} = \mathbf{H}^I - \mathbf{Y} \cdot \mathbf{J}$$

$\mathbf{Y}$ having the elements

$$\mathbf{Y}_m = f(r_{2\,m})\Delta X'(x'_m)\tilde{\mathbf{r}}_{2\,m} \tag{5.54}$$

from which the path loss may be obtained.

5.6 Comparison with UTD

The Q3D propagation model is tested against 3D-UTD solutions[4] for propagation over an infinite smooth PEC wedge (Figure 5.6), having vertex aligned in the plane $x = 1000m$, and inclined to the y axis. For the results shown in Figure 5-8 and 5-9 the vertex of the wedge cuts the plane $y = 0$ at a height of 20m, and with line of vertex inclined at an angle of 0.01 radians to $\hat{y}$. Comparisons are made at 100MHz and pathloss is plotted from $x = 0$ under the antenna to a horizontal range of 2000m at a height of 2m above the surface (Figure 5-8) in the plane $y = 0$, and in addition over a vertical range of 250m, at horizontal range $x = 2000m$ (Figure 5-9). The antenna is at a height of $20m$, and is an electric dipole oriented along $\hat{y}$. Excellent agreement is found for both the *copolar* and *cross-polar* fields.

In addition, in Figure 5-10(a) we plot the pathloss for the same wedge with an inclination angle of 0.05 radians to the y axis, at a frequency of $1GHz$. Significantly the *cross-polar* field is larger than the *copolar* field at large distances from the source, and appears to have a lower rate of attenuation in both cases. The IE method bears out this UTD result. We note that for a horizontal electric field propagating over a perfectly reflecting surface, the total horizontal electric field decreases in magnitude sharply as we approach the surface, where it has zero magnitude. Specifically, the magnitude of the horizontal electric field component shrinks with the angle ϕ (Figure 3-2). This is also true of the vertical field, but the decrease is more gradual, and the total vertical field does not shrink to zero at the surface. At greater elevations from the surface, the *copolar*(horizontal) electric field is once again dominant. We note then, than in the case of a horizontal source over such a profile, most of the available energy for a low elevation receiver in the shadow region and at a significant distance from the vertex, will be in the *cross-polar* field. This is indicated clearly in the plots

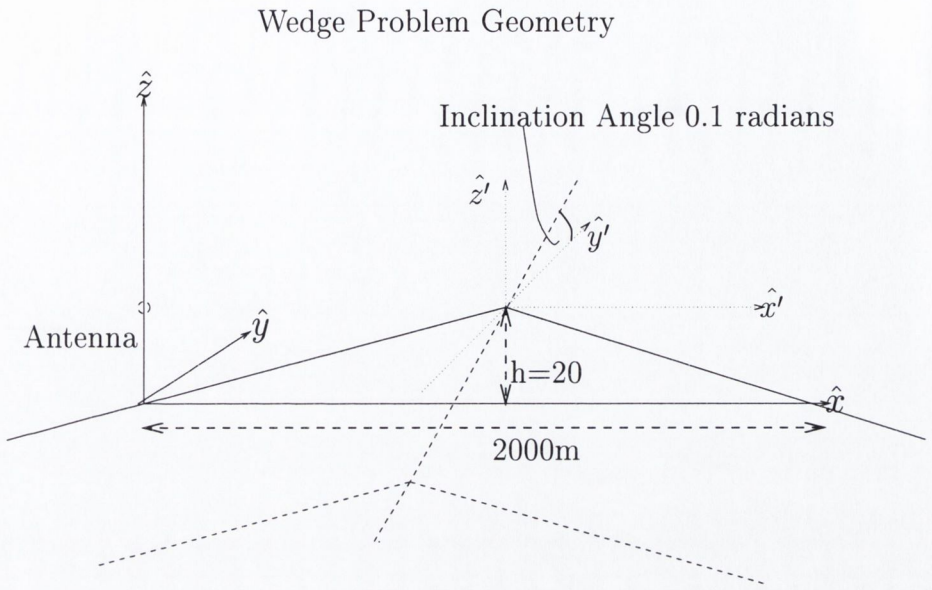


Figure 5-7: Geometry of inclined, infinite, conducting wedge.

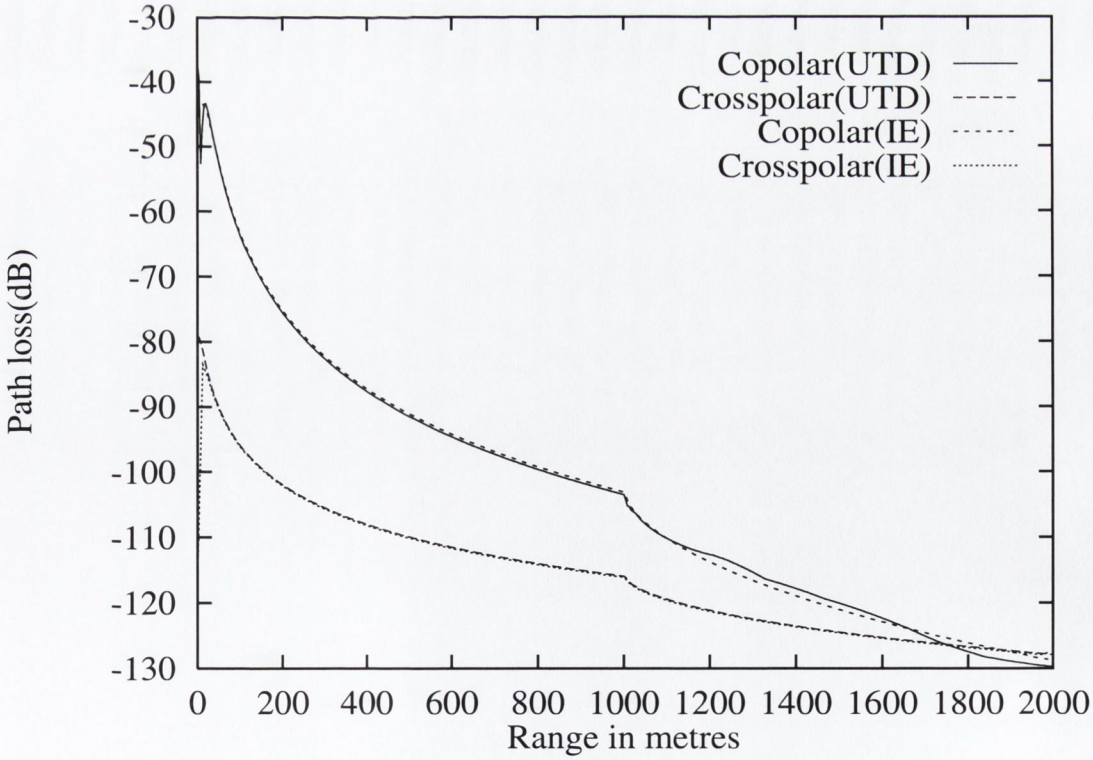


Figure 5-8: *Path loss against range prediction over a smooth sloping wedge using UTD and the Q3D IE at 100MHz.*

of field strength against height in Figure 5-9.

The local integral over the region $y' \approx y^p$ well replicates the predictions of the similarly localized UTD interaction. For the above examples, the solution for identical wedges with zero inclination exhibit zero *cross-polar* field, and an almost identical *copolar* field. The *copolar* field is not sensitive to small inclinations of the wedge, to first order.

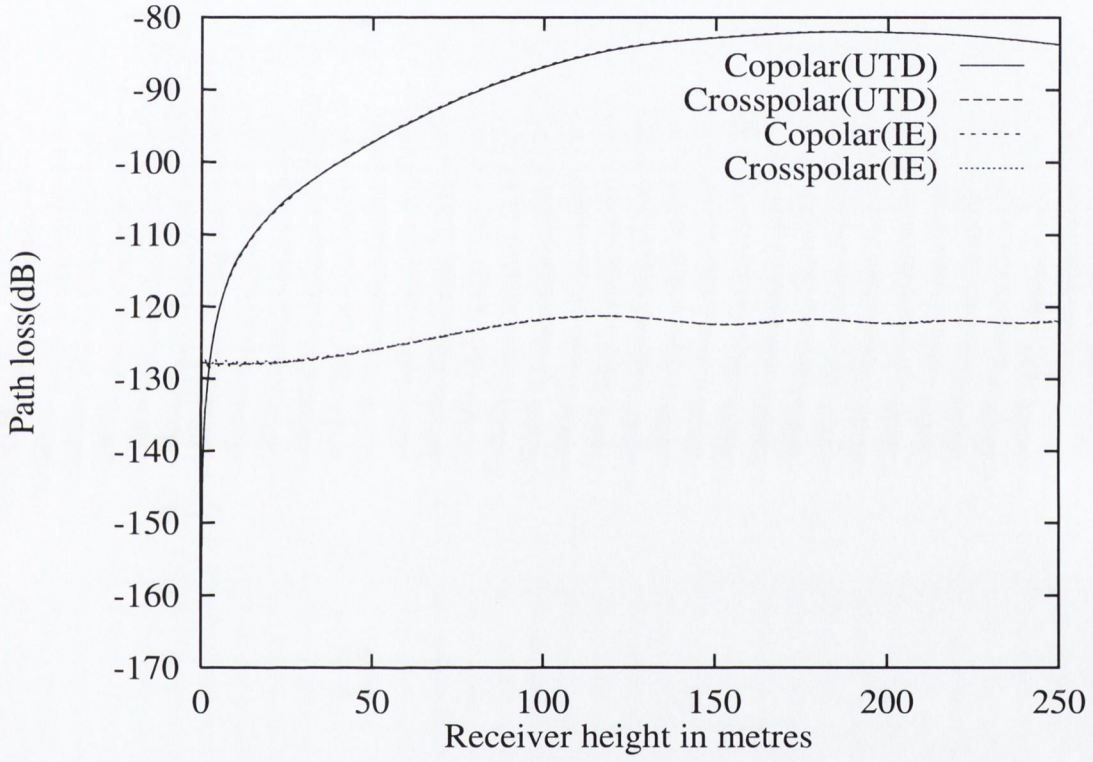
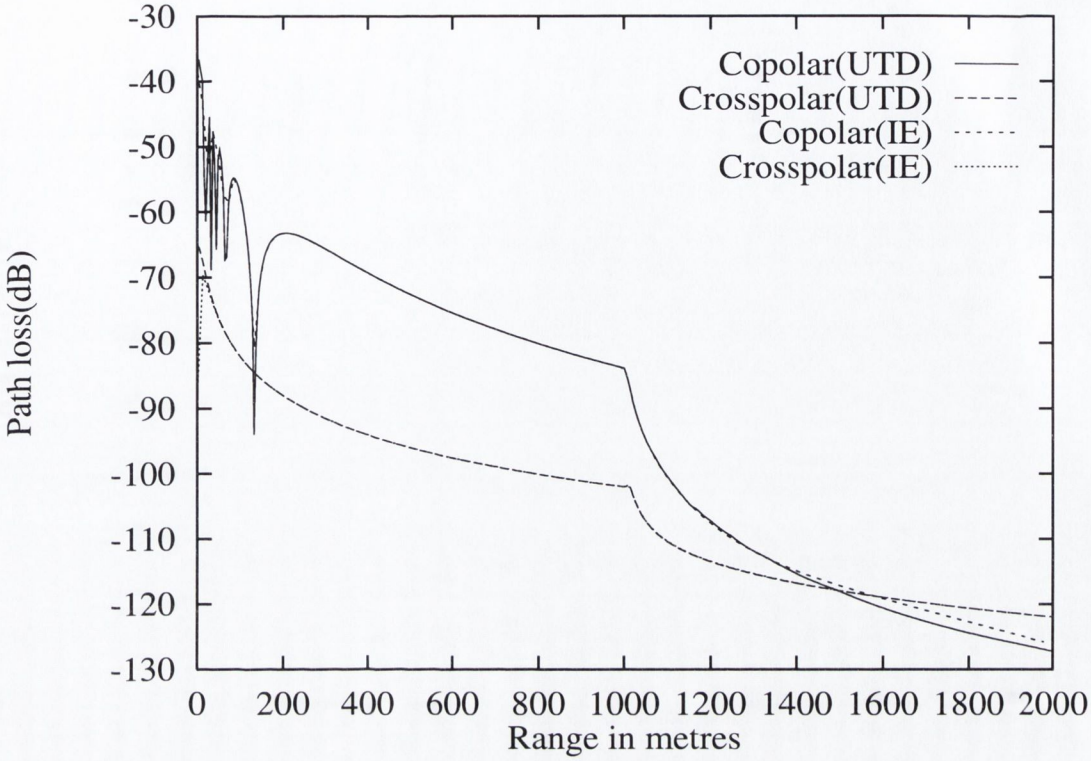
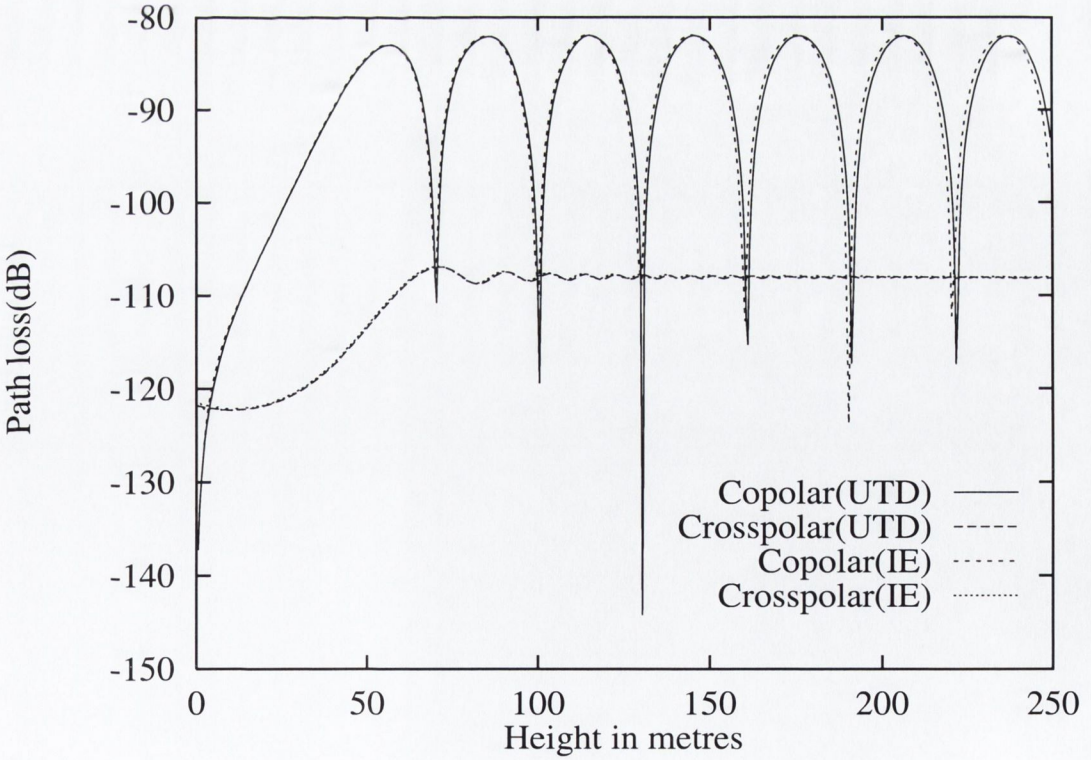


Figure 5-9: *Path loss against height prediction over a smooth sloping wedge using UTD and the Q3D IE at 100MHz.*



(a)



(b)

Figure 5-10: *Path loss prediction over a sloping wedge using UTD and the Q3D IE at 1GHz (a) against Range, (b) against Height*

5.7 Terrain Predictions

Comparisons are now made with experimental and numerical 2D solutions for terrain propagation. *Cross-polar* fields evaluated by the PEC-Q3D method are only indicative of those that might arise for terrain as the vertical electric polarizations coupled into the problem by the presence of the terrain, propagate over a terrain like material boundary with a PMC, rather than a PEC type boundary condition. However, it is possible that in some conditions the depolarizing propagation characteristics over a smoothly undulating PEC boundary may be required, and they are readily available using this technique.

No experimental data were available regarding the *cross-polar* field in the terrain examples. We present results at 144MHz and 435MHz. Predictions were made for the profile of Figure 5-11[27] and are plotted in Figures 5-12 and 5-13. Results are

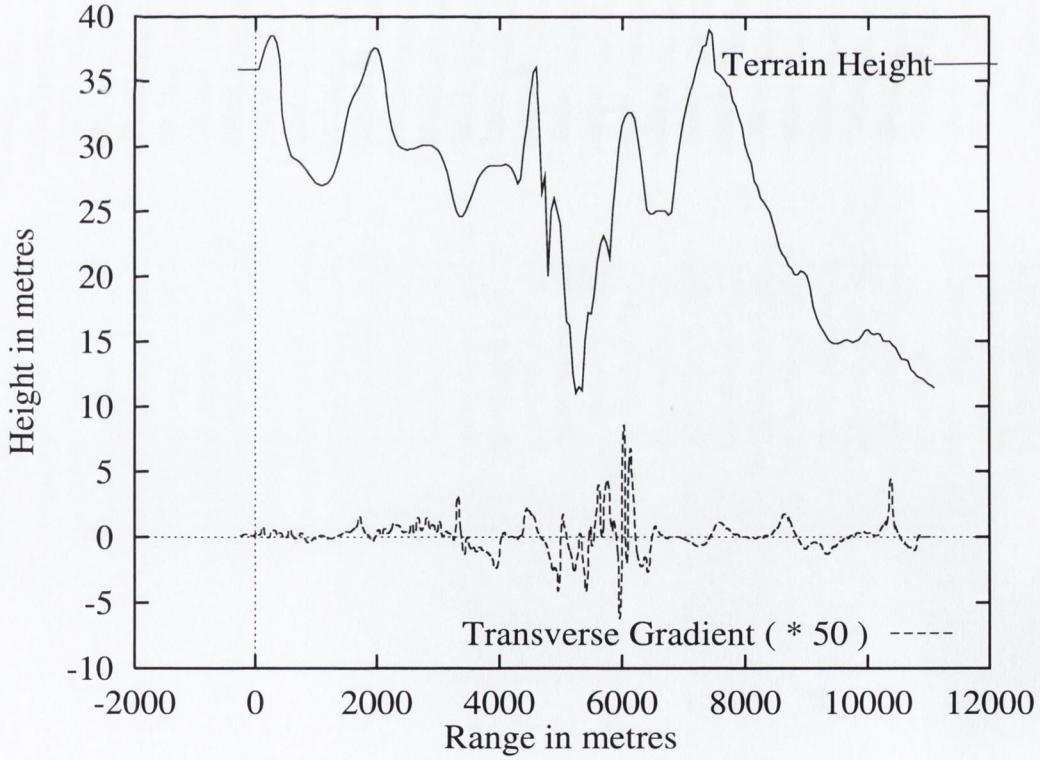


Figure 5-11: *Profile at Hjorring, Denmark with synthesized transverse gradient multiplied by a factor of 50*

for a horizontally polarized electric source and receiver at heights of 10.4m and 2.4m

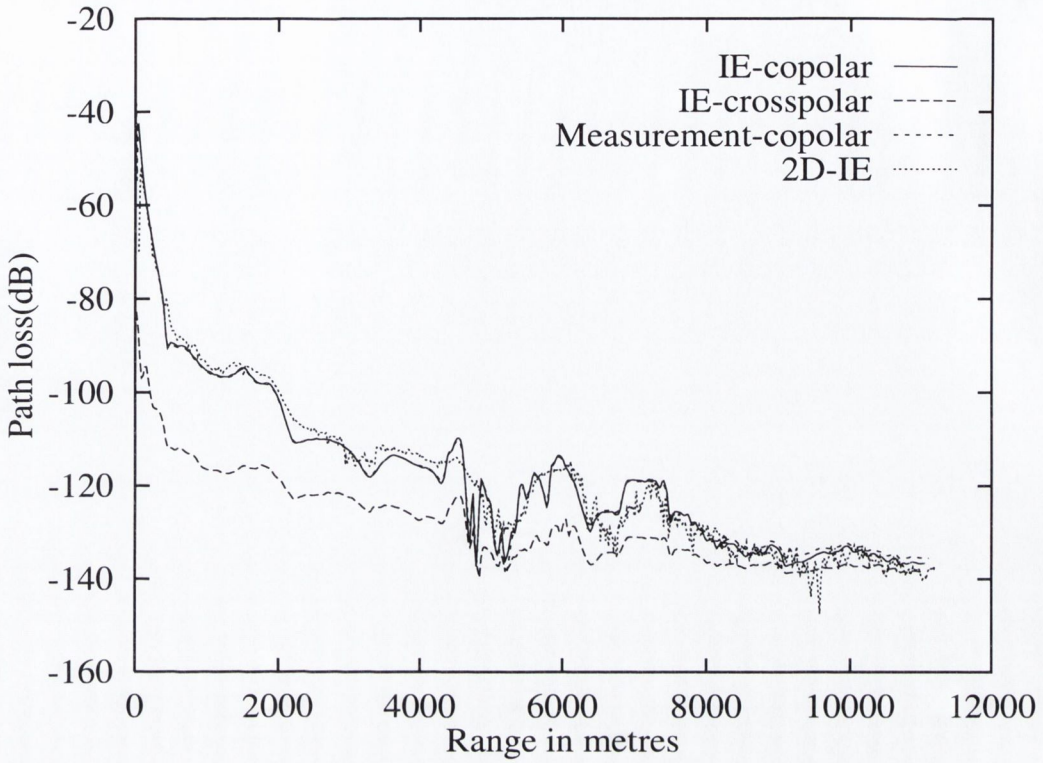


Figure 5-12: Copolar *and* Cross-polar *for Danish terrain at 144MHz*

respectively.

The authors were unable to obtain transverse gradient data for this profile. A transverse gradient profile has been synthesized (Figure 5-11) mimicking the variations of the known forward profile, by setting $\frac{\partial h}{\partial y}\Big|_x = \frac{\partial h}{\partial x}\Big|_{(R-x)}$ for a terrain of total range R. The intention here is to simulate a profile having the same statistical random variance characterists of transverse gradient as of forward gradient, where these quantities are assumed uncorrelated, and the statistical properties of terrain height variation are assumed to be isotropic. It will be sufficient to create a plausible test profile.

The measured data represents the field *copolar* with the transmitter.

We observe that the simpler 2D model compares well with measurement. The incorporation of comparable transverse gradients in the Q3D scheme introduces a small correction to the evaluated *copolar* field. The Q3D model predicts an additional *cross-polar* component which can be of comparable magnitude to the *copolar* at a distance and in shadow regions. At 435MHz the *cross-polar* component is generally

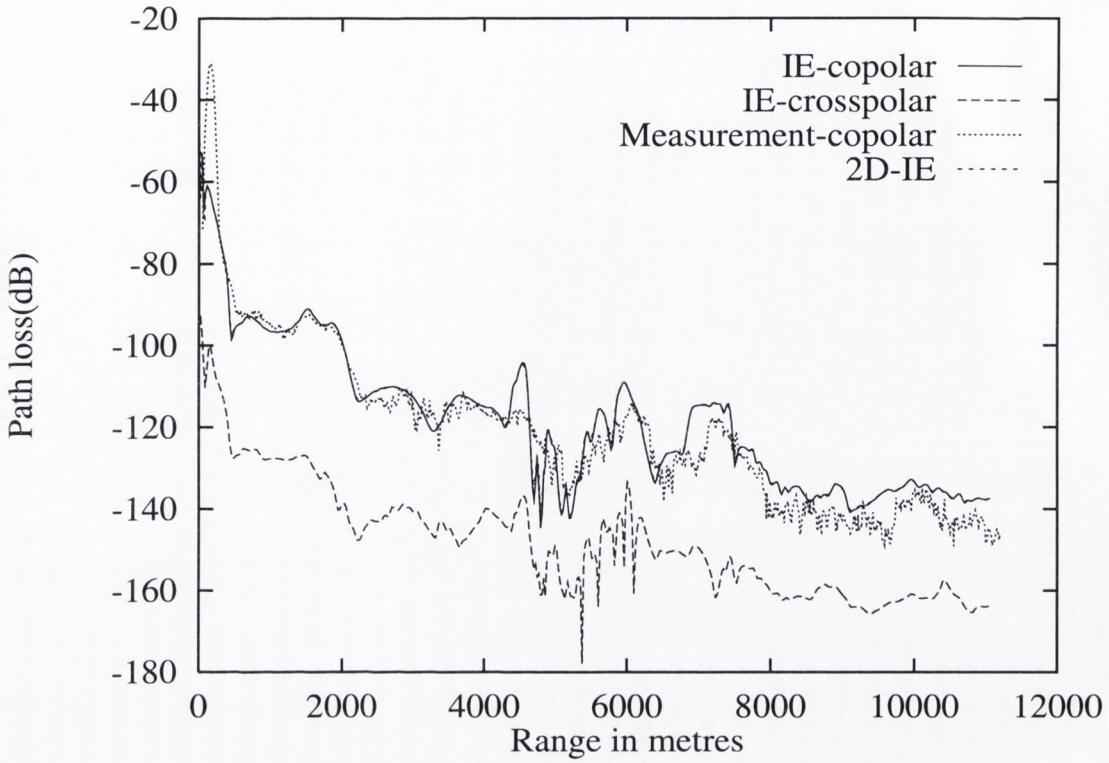


Figure 5-13: Copolar *and* Cross-polar *for Danish terrain at 435MHz*

significantly smaller than the *copolar*; however, in shadow regions it may differ by only a few dB. Again the rate of decay of the *cross-polar* field at low elevation is lower. This may be understood in terms of two mechanisms. Firstly, as in the case of the wedge, in the far field of a hilltop, the *cross-polar* field will scatter more effectively into low elevation shadow regions. Secondly, we consider that in the early portion of the profile, the bulk of the energy will be in the *copolar* field. In relative terms the *cross-polar* field will gain energy from the *copolar* field at successive scattering events although its absolute magnitude will tend to decrease. This is not to discount the possibility that subsequent scattering events might also cause destructive interference in the *cross-polar* field.

As expected, if we select vanishing transverse gradients in the Q3D model we retrieve the 2D solution.

5.8 Discussion

The three dimensional vector integral equation governing the propagation of UHF waves over an undulating PEC surface has been approximated by integration over the surface of a connected set of inclined planar segments, that model transverse gradients in the terrain profile. By analytical integration over each segment the computational problem is reduced to a 1D integral similar to that arising in corrugated two dimensional methods, but retaining a vector equation formulation that computes *copolar* and *cross-polar* field components. In this way a significant three-dimensional effect is included with little extra computational cost relative to existing scalar two-dimensional approaches.

The interaction matrix is dyadic in form, coupling the *copolar* to *cross-polar* fields. This depolarizing influence is demonstrated to produce significant *cross-polar* fields over representative surface topographies in the PEC approximation. The effect is seen to reduce however at higher frequency ranges. In general the *copolar* signal is largely uneffected by the inclusion of 3D surface scattering.

In the next chapter we will see how the Q3D integral approach may be combined with an approximate boundary condition more appropriate to terrain, characterizing the mixed polarity of the propagation field.

Chapter 6

A Quasi-3D Approach for General Terrain.

In previous chapters we outlined the problem of a full three dimensional approach to terrain scattering and have alluded to the fundamental impediments to its exact numerical solution, principally the exorbitant computational burden. We have also seen that approximating a propagation problem by taking a radial between source and observation point, we may reduce the numerical complexity to a reasonable level while retaining a sufficiently complete description to attain meaningful results.

In Chapter 5 this approach was extended to include transverse gradients in the surface of the terrain in our mathematical model, with the simplifying assumption that the terrain was a PEC surface. This approximation is not ideal for terrain problems where we have vertical electric polarizations, since the boundary behaves like a PMC or impedance surface. We now look to extend the technique of Chapter 5 to cope effectively with mixed polarization.

We will see that the solution is to carefully decouple horizontal and vertical field components defined with respect to a coordinate system in the surface, and to separately apply PEC, and PMC or impedance type conditions to these components respectively. By appeal to linear superposition these locally decoupled components may then be combined to yield a full mixed polarization scattered field. The same analytical integration in the transverse direction as in Chapter 5 may be used to

evaluate forward scattered fields. The result is a method applicable to a terrain with realistic material parameters, giving an indication of first order cross polarization interactions.

6.1 The 3D MFIE

Once again we approach the problem using the Magnetic Field Integral equation. Hence we are trying to solve the system of coupled equations (2.116-2.117)

$$\hat{\mathbf{n}} \wedge \mathbf{H}^{Inc} = \hat{\mathbf{n}} \wedge \mathbf{H} - \hat{\mathbf{n}} \wedge \left[\nabla \wedge (G_0 * \mathbf{J}) + \frac{\nabla\nabla \cdot + k_0^2}{ik_0\eta_0}(G_0 * \mathbf{K}) \right]_{S^+} \tag{6.1}$$

$$0 = \hat{\mathbf{n}} \wedge \mathbf{H} + \hat{\mathbf{n}} \wedge \left[\nabla \wedge (G_d * \mathbf{J}) + \frac{\nabla\nabla \cdot + k_d^2}{ik_d\eta_d}(G_d * \mathbf{K}) \right]_{S^-} \tag{6.2}$$

on the closed surface S, of a homogeneous, isotropic, dielectric body(ϵ_d, μ_d), for currents $\mathbf{J}$ and $\mathbf{K}$, where $\mathbf{J} = \hat{\mathbf{n}} \wedge \mathbf{H}$ and $\mathbf{K} = \mathbf{E} \wedge \hat{\mathbf{n}}$, and where

$$G_{0/d} * \mathbf{X} = \int_{S_{+/-}} \frac{e^{-ik_{0/d}|\mathbf{r}-\mathbf{r}'|}}{4\pi|\mathbf{r}-\mathbf{r}'|}\mathbf{X}dS$$

k_0 is the free space wavenumber, and $k_d = \sqrt{\epsilon_d}k_0$ is the wave number in the dielectric medium. $\mathbf{H}^{Inc}$ represents an arbitrary source of radiation located outside the dielectric body.

As we saw in Chapter 3, (6.1) and (6.2) can be solved directly as a system of coupled equations but this leads to considerably more computation and higher sampling rates due to the greater magnitude of k_d and the multiplicity of fields.

We recall that for the corrugated two dimensional problem we might set $\mathbf{K} \to 0$ for the horizontal electric polarization(PEC) problem, and similarly for the vertically polarized 2D problem we might employ the the PMC boundary condition setting $\mathbf{J} = 0$, or the impedance relation $\mathbf{K} = \eta\mathbf{J} \wedge \hat{\mathbf{n}}$. In each case an unknown is eliminated from the problem. Further approximations are required to reduce the 3D MFIE, of (6.1) in a similar fashion, for a realistic terrain boundary. As we are solving the MFIE we will henceforth refer the polarization to that of the $\mathbf{H}$ field, which is perpendicular to that of the $\mathbf{E}$ field.

6.2 Incorporation of Reflection Coefficients and Boundary Conditions in 3D

For any perfectly electrically conducting surface, we may state quite generally that the tangential electric field on the surface $|\mathbf{E}_{tang}| = |\mathbf{E} \wedge \hat{\mathbf{n}}| = 0$ and thereby eliminate $\mathbf{K}$ from our integral equation, irrespective of the polarization of incident and scattered fields. Highly conducting materials ($\sigma \to \infty$) possess this characteristic but as we saw in Chapter 4 this is far from true for terrain, which is in general only a weak electrical conductor. By examination of the Fresnel reflection coefficients derived using typical material parameters ϵ_d and μ_d (Chapter 4), or by measurement of surface reflection characteristics, we may determine that the reflection coefficient for plane waves with a vertical magnetic field polarization, ($\mathbf{H}_v$), is well approximated to -1 for grazing incidence. We are satisfied that we may extend this characteristic to any field that may be expanded as a set of grazing incidence plane waves and where propagation is over a smoothly undulating terrain[1]. In a 2D surface approximation all interactions may be described in terms of such vertically polarized $\mathbf{H}$ waves, allowing simplification to a scalar TM_Z integral equation. PMC or impedance surface modeling of the TE_Z component completes the solution for this approximation to the propagation channel.

The notion of vertical, $\mathbf{H}_v$, polarization identified with the TM_y mode of 2D waveguide propagation describes a *global* polarization characteristic. Dealing with a 3D problem for realistic terrain these modes can not be identified and polarizations are mixed. A *global* polarization may not be defined.

For a plane wave $\mathbf{H}e^{-i\mathbf{k}\cdot\mathbf{r}}$ propagating in a three dimensional space, the polarization vector is simply $\mathbf{H}$. If such a wave is incident on a planar surface having unit normal $\hat{\mathbf{n}}$, the resolution into vertical and horizontal polarizations, v and h is made with respect to the plane of incidence having unit normal vectors $\hat{\mathbf{h}} = \hat{\mathbf{n}} \wedge \hat{\mathbf{k}}$ (Figure 6-1). Here the v component is identified with that component of $\mathbf{H}$ that lies within the plane of incidence.

[1]The question of the validity of the PEC approximation for terrain with smaller radii of curvature is relevant but is not addressed here. This is distinct from the problem of modeling PEC vertices or edges.

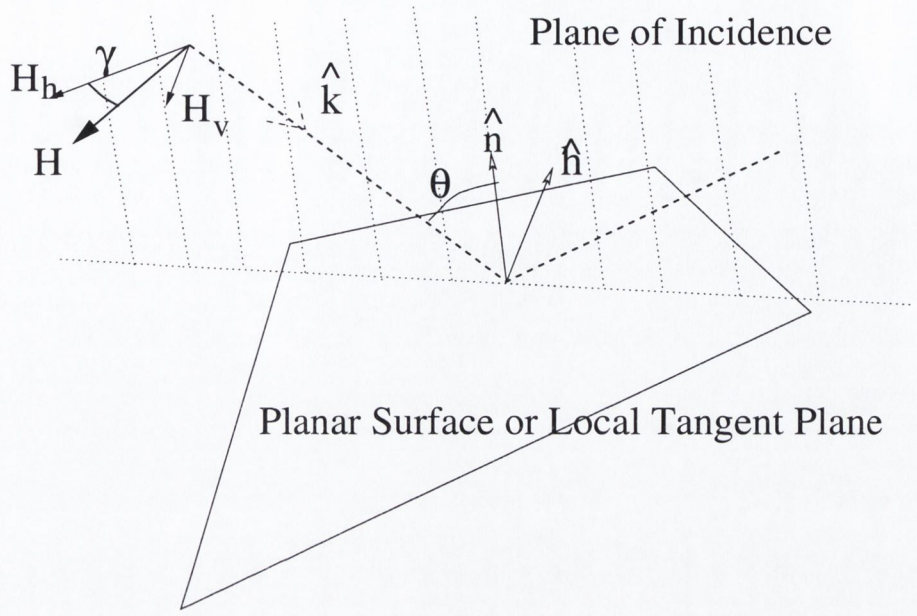


Figure 6-1: *Incident plane wave having vertical and horizontal magnetic field components impinging on a locally planar surface.*

Conventions on this differ and in some cases v is taken only as the component of the field lying in the plane of incidence and normal to the surface. Our choice of the former is based on the fact that reflection coefficients are specified with respect to the horizontal field [34], and only by considering both components of the vertical field in the incidence plane, do we deal with the complement of the horizontal field. In fact we note that for normal incidence there is no practical difference between v and h polarizations.

In a 3D problem the orientation of the polarization vector varies throughout. Locally however the total field, or a local plane wave component of the total field, may be ascribed a polarization vector. Essentially we are concerned with polarization vectors where the field meets the surface. For our class of problems the surface can locally be approximated using a tangent plane with appropriate material parameters. The impinging field $\mathbf{H}^I$ on this tangent plane is represented by a sum of plane waves which are a function of our spatial coordinates. It is defined in terms of components $\mathbf{H}_i^I$ at incidence angles[2] $\theta_i \in (\frac{\pi}{2}, \frac{\pi}{2} - \Delta\theta_{max})$ and $\phi_i \in (-\Delta\phi_{max}, +\Delta\phi_{max})$ (Figure 6-2)

[2]Angles in this and subsequent figures are exaggerated for clarity

where ϕ_i is the angle between the projection of $\hat{\mathbf{k}}_i$ onto the plane, and the forward tangent $\hat{\mathbf{t}}$, where $\hat{\mathbf{t}}$ is defined as the unit vector along the intersection of the tangent plane and the vertical plane containing source and observation points. The absence of incidence angles at $\theta_i > \pi/2$ indicates no propagation is expected from surface point to surface point beneath the interface as is the case in both PEC, PMC, and terrain high frequency problems, due to loss in the medium, high refractive index and low surface curvature. The limit on ϕ_i reflects the fact that we are concerned with paraxial propagation. For each impinging component i, the plane of incidence is defined in terms of its wave-vector $\mathbf{k}_i$ as the plane having unit normal $\hat{\mathbf{h}}_i = \hat{\mathbf{n}}(t) \wedge \hat{\mathbf{k}}_i$, t denoting the arclength parameter for the radial profile. The incidence planes for components $\mathbf{H}_i^I(\theta_i, \phi_i)$ and $\mathbf{H}_j^I(\theta_j, \phi_j)$ will coincide where $\phi_i = \phi_j$.

Each of the incident field components denoted by $\mathbf{H}_i^I(\mathbf{k}_i(\theta_i, \phi_i))$ may be of arbitrary polarization, where we have the free space propagating plane wave constraint on $\mathbf{E}_i^I$ and $\mathbf{H}_i^I$ that $\mathbf{H}_i^I = \frac{1}{\eta}\hat{\mathbf{k}}_i \wedge \mathbf{E}_i^I$ (the propagating wave has no longitudinal field components). We note that this relation does not hold for the total field.

This individual plane wave is now resolved with respect to the incident plane as in Figure 6-1, resulting horizontal and vertical components given by

$$\mathbf{H}_i^I = \mathbf{H}_i^I(\gamma_i) \exp\left(-i\hat{\mathbf{k}}_i(\theta_i, \phi_i) \cdot \hat{\mathbf{r}}\right) = (\mathbf{H}_{ih}^I + \mathbf{H}_{iv}^I) \exp\left(-i\hat{\mathbf{k}}_i(\theta_i, \phi_i) \cdot \hat{\mathbf{r}}\right) \tag{6.3}$$

$$\mathbf{H}_{ih}^I = H_i^I \cos\gamma_i \, \hat{\mathbf{h}}_i \tag{6.4}$$

$$\mathbf{H}_{iv}^I = H_i^I \sin\gamma_i \, \hat{\mathbf{v}} \tag{6.5}$$

where

v

$$\gamma_i = \arccos(\hat{\mathbf{H}}_i^I \cdot \hat{\mathbf{h}}_i)$$

γ_i is the angle between the vector $\mathbf{H}_i^I$ and the horizontal direction $\hat{\mathbf{h}}_i$, and $\hat{\mathbf{v}}_i = \hat{\mathbf{k}}_i \wedge \hat{\mathbf{h}}_i$.
γ_i is the angle between the vector $\mathbf{H}_i^I$ and the horizontal direction $\hat{\mathbf{h}}_i$, and $\hat{\mathbf{v}}_i = \hat{\mathbf{k}}_i \wedge \hat{\mathbf{h}}_i$.

The reflection coefficients for each polarization component of $\mathbf{H}_i^I$ were derived from the continuity relations defined over a dielectric boundary in Chapter 4. Denoting the reflection coefficients for horizontal, vertical-normal, and vertical tangential magnetic components as Γ_h and Γ_n and Γ_t respectively, the total tangential surface field will

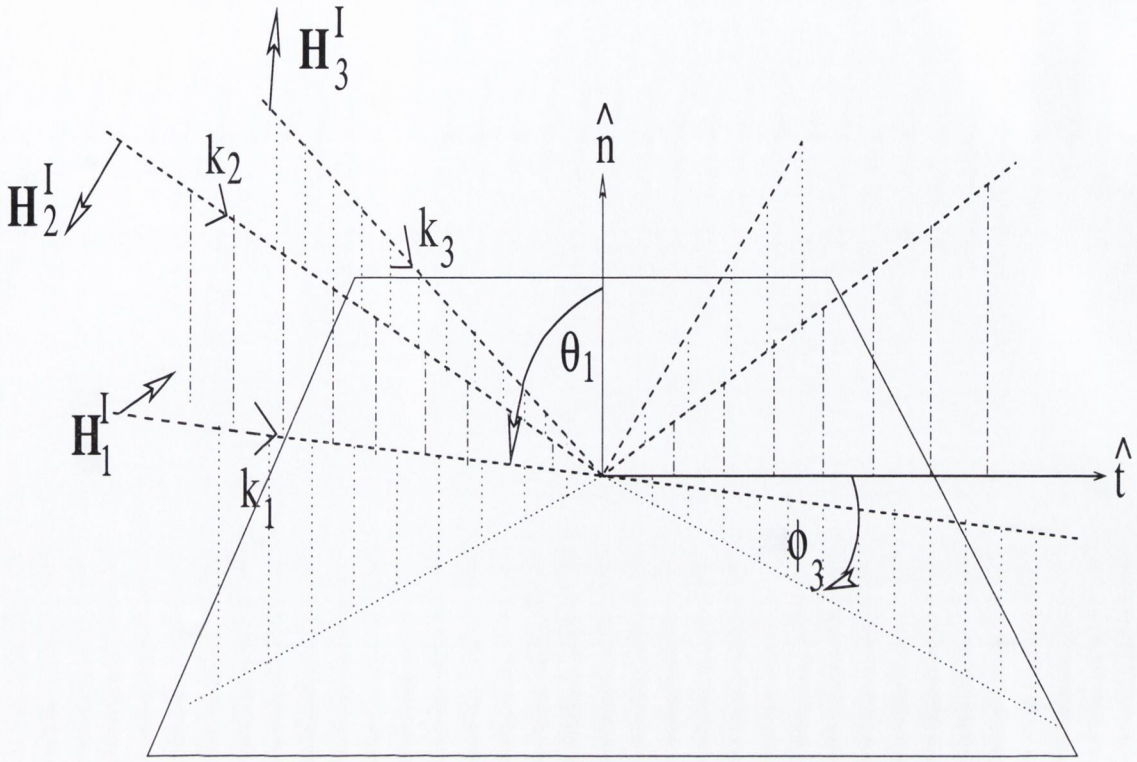


Figure 6-2: *Set of incident plane waves having vertical and horizontal magnetic field components and individual incidence planes.*

be given by the sum of impinging and reflected waves

$$\mathbf{H}^{Tot}_{i\,(tang)} = (\mathbf{H}^I_i + \mathbf{H}^R_i)_{(tang)}$$

$$= H^I_i \cos\gamma_i (1 + \Gamma_{hi})\hat{\mathbf{h}}_i + H^I_i \sin\gamma_i \cos\theta_i \,(1 + \Gamma_{ti})\hat{\mathbf{t}}_i \tag{6.6}$$

where $\hat{\mathbf{t}}_i = (\hat{\mathbf{h}}_i \wedge \hat{\mathbf{n}})$ and is the unit vector along the intersection of the plane of incidence and the surface tangent plane, and is used to define the tangential component of the vertically polarized field.

The coefficients Γ_{ti} and Γ_{hi} relate directly to A^r and B^r of Section 4.2

$$\Gamma_{ti} = -A^r \tag{6.7}$$

$$\Gamma_{hi} = B^r \tag{6.8}$$

As such Γ_{ti} is well approximated by 1 for all k_i near grazing incidence (Chapter 4. Figure 4-4), which indicates PEC type reflection. However, the coefficient Γ_{hi} has strong angular dependence(Chapter 4, Figure 4-4) but does approach -1 as $\theta_i \to \pi/2$.

This is equivalent to a PMC approximation as indicated by the cancellation of $\hat{\mathbf{h}}$ terms in (6.6). Making this approximation has been found satisfactory for a considerable range of terrain problems, and we proceed utilizing this approximation.

The boundary condition for the impinging wave contribution $\mathbf{H}_i$ may now be written in terms of the total tangential field components

$$\begin{aligned} \mathbf{H}_i^{Tot} \cdot \hat{\mathbf{h}} &= 0 \\ \mathbf{H}_i^{Tot} \cdot \hat{\mathbf{t}} &= 2\mathbf{H}_i^{I} \cdot \hat{\mathbf{t}} \end{aligned} \tag{6.9}$$

Rather than considering the set of waves as depicted in Figure 6-2 we simplify the analysis a little by considering only incident components propagating in the xz plane as is assumed in radial propagation problems, and where the surface normal also lies in the xz plane. Polarization vectors are arbitrary (Figure 6-3). This in fact describes

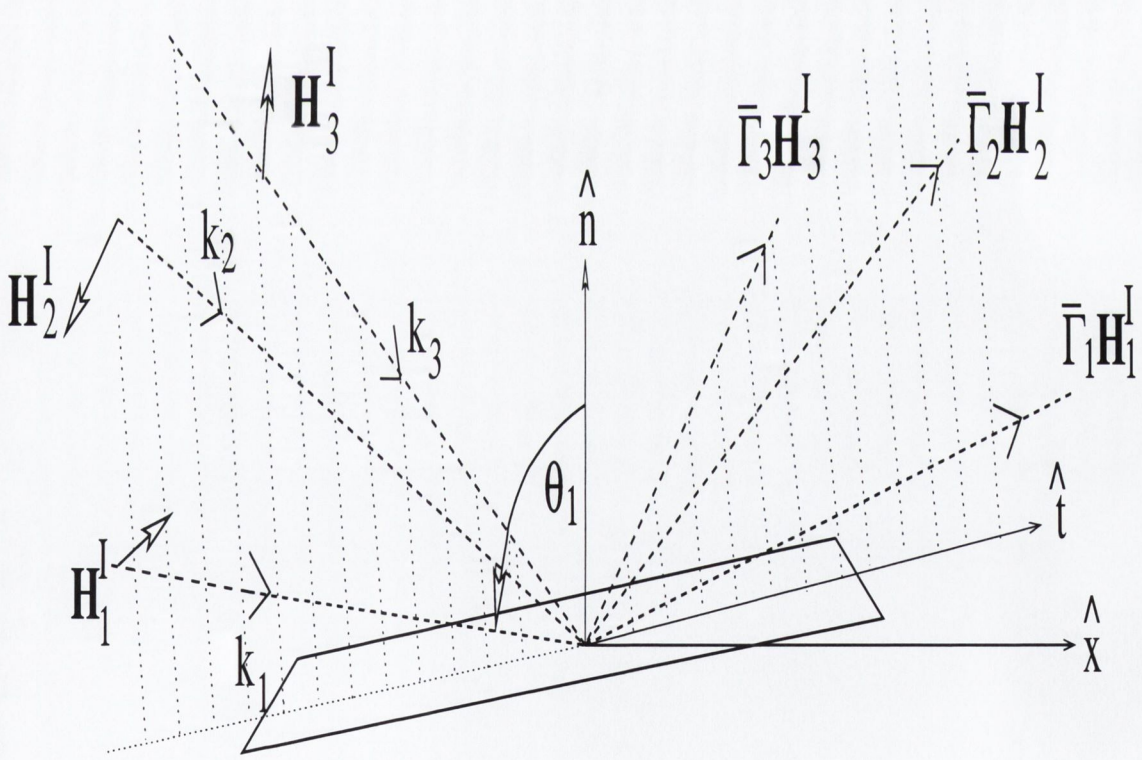


Figure 6-3: *Set of incident plane waves having vertical and horizontal magnetic field components, and common incident plane. Tensor reflection coefficients* $\overline{\Gamma}_i$. *The vectors* $\hat{\mathbf{h}}_i = \hat{\mathbf{h}}$ *are directly into the page for all components.*

a mixed polarization, two dimensional type problem. The impinging tangential field

on the surface depicted in Figure 6-3, is given by

$$\begin{aligned} \mathbf{H}^I_{(tang)} &= \sum_i \mathbf{H}^I_i(\gamma_i) e^{-i\mathbf{k}_i(\theta_i)\cdot\mathbf{r}} \\ &= \sum_i (H^I_{t\,i}\hat{\mathbf{t}}_i + H^I_{h\,i}\hat{\mathbf{h}}_i) e^{-i\mathbf{k}_i(\theta_i)\cdot\mathbf{r}} \end{aligned} \tag{6.10}$$

The reflected field may be described by a similar sum of outgoing waves, horizontally and vertically polarized, with amplitude and phase given by the tensor of Fresnel reflection coefficients $\overline{\Gamma}_i$ as illustrated in Figure 6-3. This tensor is diagonal considering the geometry of this problem and the non chiral nature of the planar material boundary.

$$\mathbf{H}^R_{(tang)} = \sum_i \left(\Gamma_{t\,i} H^I_{t\,i}\hat{\mathbf{t}}_i + \Gamma_{h\,i} H^I_{h\,i}\hat{\mathbf{h}}_i\right) e^{-i(\mathbf{k}_i(\theta_i) - 2k_{n\,i}\hat{\mathbf{n}})\cdot\mathbf{r}} \tag{6.11}$$

By linear superposition we may demand that the conditions (6.9) be satisfied for each impinging component and we may apply the weaker condition to the sum of all such components

$$\left(\sum_i \mathbf{H}^{Tot}_i\right) \cdot \hat{\mathbf{h}} = 0 \tag{6.12}$$

$$\left(\sum_i \mathbf{H}^{Tot}_i\right) \cdot \hat{\mathbf{t}} = 2\left(\sum_i \mathbf{H}^I_i\right) \cdot \hat{\mathbf{t}} \tag{6.13}$$

where $\hat{\mathbf{h}}_i = \hat{\mathbf{h}}$ and $\hat{\mathbf{t}}_i = \hat{\mathbf{t}}$ for all i. This condition is suitable for application in an integral equation method.

This case was simplified by the fact that the fields are in the same incidence plane. We consider now the effect of subjecting the tangent plane in Figure 6-3 to a small rotation with respect to the $y = 0$ plane as might be encountered in the case of a gently undulating terrain problem with transverse gradients. The vectors $\mathbf{k}_i$ are no longer coplanar with $\hat{\mathbf{n}}$ and the vectors $\hat{\mathbf{h}}_i$ take various directions indicating that we have a number of different incident planes. Each contribution i, may be resolved independently with respect to its incidence plane into h and v components, and these will be reflected with horizontal and vertical reflection coefficients respectively. The fields satisfy the set of conditions,

$$\mathbf{H}^{Tot}_i \cdot \hat{\mathbf{h}}_i = 0 \quad \forall\ i \tag{6.14}$$

$$\mathbf{H}^{Tot}_i \cdot \hat{\mathbf{t}}_i = 2\hat{\mathbf{H}}^I_i \cdot \hat{\mathbf{t}}_i \quad \forall \quad i \tag{6.15}$$

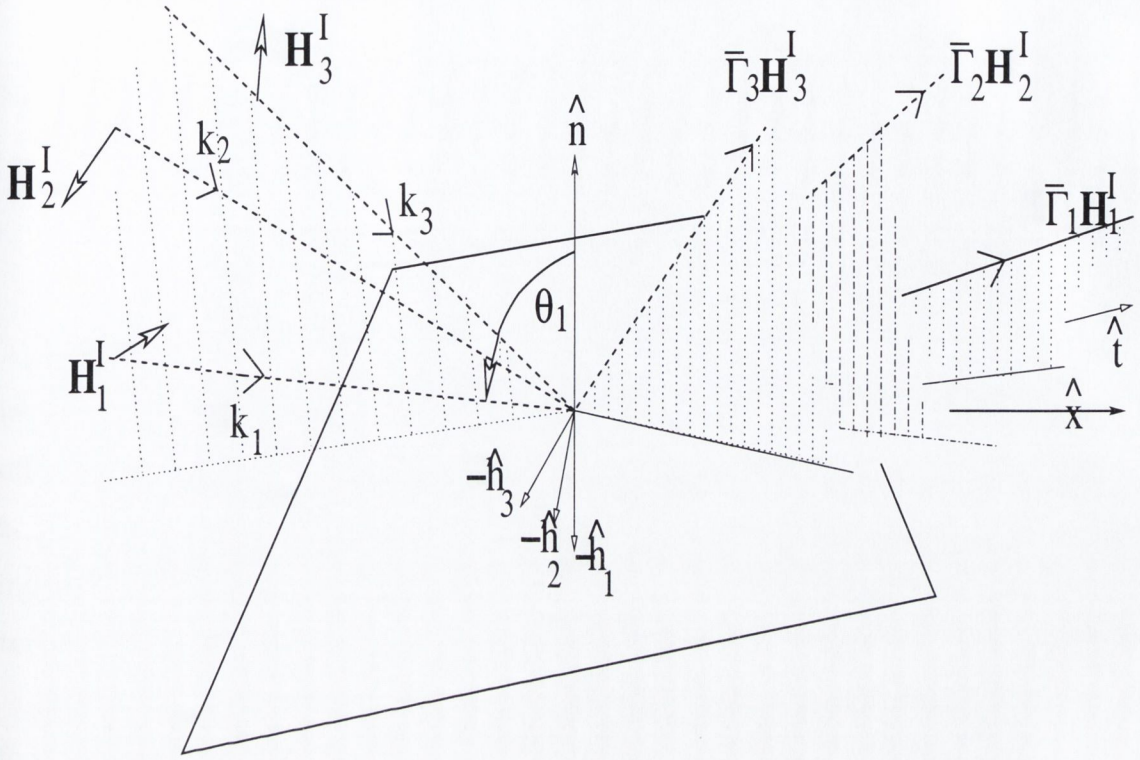


Figure 6-4: *Set of incident plane waves having vertical and horizontal magnetic field components impinging on a forward and transversely inclined plate. For clarity the orientation of the negative sense of the vectors* $\hat{\mathbf{h}}_i$ *is illustrated.*

and there is no single boundary condition on the surface. The mixture of polarization of each component i has also been changed with respect to the surface, in fact, this is the most significant effect that will later be captured in the model.

In order to use simple reflection characteristics in a Q3D integral equation problem we require a further approximation. We do not wish to define a distinct incidence plane and set of vectors $\hat{\mathbf{h}}_i$ and $\hat{\mathbf{t}}_i$ for each contribution i. Because we are dealing with a small angular distribution of impinging plane waves, ie paraxial propagation, the plane of incidence for all impinging waves will be approximated by that plane having the normal $\hat{\mathbf{h}} = \hat{\mathbf{n}} \wedge \hat{\mathbf{x}}$ where $\hat{\mathbf{x}}$ is the direction along which the radial profile is sampled. Essentially this $\hat{\mathbf{h}}$ is to approximate $\hat{\mathbf{n}} \wedge \mathbf{k}_i$, for all i. We inspect this more closely given what we know of these three vectors,

$$\hat{\mathbf{n}} = (n_x, n_y, n_z)\,, \qquad n_z \gg n_x, n_y$$

$$\hat{\mathbf{k}}_i = (k_{ix}, k_{iy}, k_{iz}), \quad k_{ix} \gg k_{iy}, k_{iz}$$

Neglecting quadratics in the small quantities,

$$\hat{\mathbf{h}}(\hat{x}) = (\hat{\mathbf{n}} \wedge \mathbf{x}) \approx (0, n_z, -n_y)$$

$$\hat{\mathbf{h}}_i(\hat{k}_i) = (\hat{\mathbf{n}} \wedge \mathbf{k}_i) \approx (0, n_z, -n_y) - (n_z \frac{k_{yi}}{k_{xi}}, 0, 0)$$

Approximating $\hat{\mathbf{h}}(\hat{x})$ for $\hat{\mathbf{h}}(\hat{k}_i)$ we are neglecting k_{iy} with respect to n_y, which is in keeping with the fact that we are trying to model transverse gradients and not off-axial propagation. $\frac{k_{iy}}{k_{ix}} \ll 1$ in all cases. Using a radial propagation model k_{iy} is implicitly neglected *ab-initio*, however we can see that our approximation for the incidence plane is satisfactory where $k_{iy} \ll k_{ix}$ holds, and this is reasonable for most terrain type problems.

Importantly, $\hat{\mathbf{h}}_i = \hat{\mathbf{n}} \wedge \mathbf{k}_i$ is not sensitive to k_{iz} to first order. In fact, it will be found later that the method is largely insensitive to the use of $\hat{\mathbf{n}} \wedge \hat{\mathbf{k}}_{PO}$, where $\mathbf{k}_{PO}$ is the wave-vector of the incident field, $\hat{\mathbf{n}} \wedge \hat{\mathbf{x}}$, or $\hat{\mathbf{n}} \wedge \hat{\mathbf{t}}$ to define the incidence plane, and possibly $\hat{\mathbf{n}} \wedge \hat{\mathbf{k}}_{PO}$ provides the most physically informed definition (except in the antenna near field).

Taken together, $\hat{\mathbf{t}}$, $\hat{\mathbf{h}}$, and $\hat{\mathbf{n}}$, define a coordinate system in the local tangent plane, orthogonal to a second order of approximation. $\mathbf{H}$ is resolved with respect to this system to define the horizontal $\mathbf{H}_{\hat{h}}$, and vertical-tangential $\mathbf{H}_{\hat{t}}$, magnetic field components for all incoming fields. Conditions (6.14) and (6.15) now take the form,

$$\mathbf{H}^{Tot} \cdot \hat{\mathbf{h}} \approx 0 \tag{6.16}$$

$$\mathbf{H}^{Tot} \cdot \hat{\mathbf{t}} \approx 2\mathbf{H}^{I} \cdot \hat{\mathbf{t}} \tag{6.17}$$

where,

$$\mathbf{H}^{Tot} = \mathbf{H}^{I} + \mathbf{H}^{R} \tag{6.18}$$

and

$$\mathbf{H}^{I}_{(tang)} = \sum_i (H^I_{ti}\hat{\mathbf{t}} + H^I_{hi}\hat{\mathbf{h}}(\hat{x}))e^{-i\mathbf{k}_i(\theta_i)\cdot\mathbf{r}} \tag{6.19}$$

$$\mathbf{H}^{R}_{(tang)} = \sum_i \left(\Gamma_{ti} H^I_{ti}\hat{\mathbf{t}} + \Gamma_{hi} H^I_{hi}\hat{\mathbf{h}}(\hat{x})\right) e^{-i(\mathbf{k}_i(\theta_i) - 2k_{ni}\hat{\mathbf{n}})\cdot\mathbf{r}} \tag{6.20}$$

and this condition is now suitable for application to an integral equation, and is effectively a dual PEC/PMC boundary condition for the two respective polarizations.

In the same fashion as above it may demonstrated that within these approximations

$$\mathbf{E}^{Tot} \cdot \hat{\mathbf{h}} = 0 \tag{6.21}$$

$$\mathbf{E}^{Tot} \cdot \hat{\mathbf{t}} = 2\mathbf{E}^{I} \cdot \hat{\mathbf{t}} \tag{6.22}$$

where,

$$\mathbf{E}^{Tot} = \mathbf{E}^{I} + \mathbf{E}^{R} \tag{6.23}$$

and

$$\mathbf{E}^{I}_{(tang)} = \sum_{i} (E^{I}_{t\,i}\hat{\mathbf{t}} + E^{I}_{h\,i}\hat{\mathbf{h}}(\hat{x}))e^{-i\mathbf{k}_i(\theta_i)\cdot\mathbf{r}} \tag{6.24}$$

$$\mathbf{E}^{R}_{(tang)} = \sum_{i} \left(\Gamma^{E}_{t\,i} E^{I}_{t\,i}\hat{\mathbf{t}} + \Gamma^{E}_{h\,i} E^{I}_{h\,i}\hat{\mathbf{h}}(\hat{x})\right) e^{-i(\mathbf{k}_i(\theta_i) - 2k_{n\,i}\hat{\mathbf{n}})\cdot\mathbf{r}} \tag{6.25}$$

Although these relations come from geometric considerations, they allow us to solve for the current on the surface at a boundary match point, which in turn may be used to evaluate the scattered field from that region of the surface to another, in an integral equation scheme. We suppose that the field boundary conditions established from the above approximation may be extended to any region of the surface where a tangent plane approximation and impinging plane wave expansion may be satisfactorily defined, and where the terrain may be approximated by a set of sloping tangent plates.

6.3 Decoupling the 3DMFIE

Equipped with the simplifying boundary approximations of (6.16),(6.17) and (6.21),(6.22) we re-examine (6.1), the exterior MFIE. We now deal only with exterior quantities and redundant indices are dropped.

$$\hat{\mathbf{n}}\wedge\mathbf{H}^{Inc} = \mathbf{J} - \hat{\mathbf{n}}\wedge\nabla\wedge\int_{S+} G(\mathbf{r},\mathbf{r}')\mathbf{J}(\mathbf{r}')dS' - \hat{\mathbf{n}}\wedge\frac{\nabla\nabla\cdot + k^2}{ik\eta}\int_{S+} G(\mathbf{r},\mathbf{r}')\mathbf{K}(\mathbf{r})dS' \tag{6.26}$$

The first integral on the RHS is recognizable as that which we encountered in the purely PEC problem and essentially it may be treated in the same manner as in

Chapter 5. In addition we encounter a term containing $\mathbf{K}$ and the dyadic second derivative $\nabla\nabla$ of the Green's function. The equation is satisfied in the limit as we approach the surface along the normal from above and hence we may avoid a costly finite difference evaluation of the derivatives by moving them inside the integration and performing analytic differentiation. Differentiation is with respect to the observation point $\mathbf{r}$ and acts only on the Green's function $G(\mathbf{r}, \mathbf{r}')$. As such it may be used to form the dyadic function,

$$\nabla\nabla \cdot G = \overline{\overline{G}} = (G_{ij}) \tag{6.27}$$

where

$$\overline{\overline{G}}_{ij} = (\frac{3(1+ikr_2) - k^2r_2^2}{r_2^4})Gr_{2i}r_{2j} \tag{6.28}$$

$$\overline{\overline{G}}_{ii} = ((3(1+ikr_2) - k^2r_2^2)\hat{r}_{2i}^2 - (1+ikr_2))G/r_2^2 \tag{6.29}$$

where $\mathbf{r}_2$ is once again the vector connecting scatter and observation points. The matrix elements may be simplified in particular asymptotic limits. If the observation point is in the far field, the matrix takes the simpler form,

$$\overline{\overline{G}} \approx -\frac{k^2}{r_2^2}G(\mathbf{r}, \mathbf{r}') \begin{bmatrix} r_{2x}r_{2x} & r_{2x}r_{2y} & r_{2x}r_{2z} \\ r_{2y}r_{2x} & r_{2y}r_{2y} & r_{2y}r_{2z} \\ r_{2z}r_{2x} & r_{2z}r_{2y} & r_{2z}r_{2z} \end{bmatrix} \tag{6.30}$$

We may avoid integrating over the product of the dyadic (6.27) with $\mathbf{K}$ in the near field region, by exploiting symmetry properties of the Green's function and the commutation of differentiation and convolution operations. We apply the $\nabla\nabla\cdot$ operators sequentially to the integrand, ie

$$\nabla\nabla \cdot \int G\mathbf{K}dS' = \nabla \int \nabla \cdot (G\mathbf{K})dS' \tag{6.31}$$

$$= \nabla \int (\mathbf{K} \cdot \nabla G + G\nabla \cdot \mathbf{K})dS' \tag{6.32}$$

$\mathbf{K} = \mathbf{K}(\mathbf{r}')$ has no dependence on the observation point and therefore the derivative $\nabla \cdot \mathbf{K} = 0$. Hence

$$\nabla\nabla \cdot \int G\mathbf{K}dS' = \nabla \int \mathbf{K} \cdot \nabla G dS' \tag{6.33}$$

Now given the symmetry of the Green's function with respect to exchange of the source and observation points $\nabla' G = -\nabla G$, and the convolution relation

$$\int \nabla' G f(\mathbf{r}') dS' = -\int G \nabla' f(\mathbf{r}') dS' \tag{6.34}$$

we may write

$$\nabla \int \mathbf{K} \cdot \nabla G dS' = \int \nabla' \mathbf{K} \cdot \nabla G dS' \tag{6.35}$$

The term $\nabla' \mathbf{K}$ denotes the outer product matrix $\left[\frac{\partial K_i}{\partial x_j}\right]$, of the divergence operator ∇' with the surface current $\mathbf{K}$ where differentiation is with respect to the source point $\mathbf{r}'$. The elements of the matrix $\nabla' \mathbf{K}$, and in fact the possibility of defining such matrix elements, depends on the choice of basis functions and discretization used to define $\mathbf{K}$. Clearly for this operation to be possible they must possess a first derivative. It will also be advantageous if these derivatives are of simple form or vanishing.

The discretization is now chosen in keeping with Chapter 5, as a series of plates tangential to the terrain surface at a given match point. We select the segment of the plate in the interval $x(t_n - \frac{\Delta t}{2}, t_n + \frac{\Delta t}{2})$ where Δt will typically be equal to $\lambda/4$. We utilize the approximate orthogonal system $\hat{\mathbf{t}}_m, \hat{\mathbf{h}}_m, \hat{\mathbf{n}}_m$ discussed in Section 6.2, centered on the strip m where $\hat{\mathbf{h}}_m = \hat{\mathbf{n}}_m \wedge \hat{\mathbf{x}}$ and hence we may immediately neglect the components $\mathbf{J}_{\hat{n}}$ and $\mathbf{K}_{\hat{n}}$ as by definition the currents are purely tangential.

The currents are written in terms of basis functions b_n as

$$\mathbf{J} = \sum_n \mathbf{J}_n b_n \tag{6.36}$$

$$\mathbf{K} = \sum_n \mathbf{K}_n b_n \tag{6.37}$$

where

$$b_m(t', y') = p[t, t_m - \Delta t/2, t_m + \Delta t/2] e^{-ik\Delta r_1(y')} \tag{6.38}$$

$$p(t) = \begin{cases} 1 & t \in (t_m - \Delta t/2, t_m + \Delta t/2) \\ 0 & t \notin (t_m - \Delta t/2, t_m + \Delta t/2) \end{cases} \tag{6.39}$$

ie, a pulse function $p[]$ modified by a spherical physical optics type phase correction (Section 5.4).

The third term in (6.26) contains an integral over $G\mathbf{K}$. For any point at a significant distance from the source, $\exp(-ik\Delta r_1) = \exp(-ik|\mathbf{r}_1(y') - \mathbf{r}_1^{\mathbf{a}})|)$ is slowly varying

about $y' = 0$. If the scattering point is in the near field of the observation point, the variation of amplitude and phase in the Green's function dominates over that of the physical optics phase front of the basis function over the region of the first Fresnel zone, limited by r_2^a, and therefore we neglect $e^{-ik\Delta r_1}$, and integrate over y' yielding

$$\int_{\Delta t} \alpha \int_{y'=-\infty}^{\infty} \frac{e^{-ik\sqrt{\rho^2+(y')^2}}}{4\pi\sqrt{\rho^2+(y')^2}} e^{-ik\Delta r_1} dy' dt' \approx \frac{\alpha}{4i} \int_{\Delta t} H_0^{(2)}(|k\rho|) dt' \tag{6.40}$$

where ρ is the vector $(x_2, 0, z_2)$, where α relates dy' to $\hat{h}$ through

$$dh' = \sqrt{1 + (\frac{h_{m\,z}}{h_{m\,y}})^2} dy' = \alpha dy' \tag{6.41}$$

We now write (6.26) in discrete form as

$$\hat{\mathbf{n}}_n \wedge \mathbf{H}_n^{Inc} = \mathbf{J}_n - \hat{\mathbf{n}}_n \wedge \sum_m \int_{\Delta_m} \nabla G \wedge \mathbf{J}_m b_m \tag{6.42}$$

$$-\frac{\hat{\mathbf{n}}_n \wedge}{ik\eta} \left(\sum_{m \in NF} \int_{\Delta m} [\frac{\partial(\mathbf{K}_m b_m)}{\partial x_i'}] \cdot \nabla G + \sum_{m \in FF} \int_{\Delta m} \overline{\overline{G}} \cdot \mathbf{K}_m b_m \right)$$

$$-\frac{\hat{\mathbf{n}}_n \wedge k^2}{ik\eta} \left(\sum_{m \in NF} \alpha_m \int_{\Delta t_m} \frac{H_0^2}{4i} \mathbf{K}_m b_m + \sum_{m \in FF} \int_{\Delta_m} G \mathbf{K}_m b_m \right)$$

where NF and FF are near-field and far-field regions, with respect to $\mathbf{r}$.

The vectors $\mathbf{K}_m$ and $\mathbf{J}_n$ are constant on each strip and may be factored out of the integrals and derivatives leaving only the derivatives of the basis functions.

We are no longer working with the fields $\mathbf{H}^I$, $\mathbf{H}^R$, $\mathbf{E}^I$ or $\mathbf{E}^R$ of Section 6.2 but the fields $\mathbf{H}^{Tot}$ and $\mathbf{E}^{Tot}$ may be identified with $\mathbf{H}$ and $\mathbf{E}$. Utilizing conditions (6.17) and (6.22), horizontal field components at a match point are eliminated from our consideration. Therefore from the definitions of $\mathbf{J}$ and $\mathbf{K}$,

$$\mathbf{J}_t \approx 0 \tag{6.43}$$

$$\mathbf{K}_t \approx 0 \tag{6.44}$$

Inspecting the near field dyadic term of (6.42) in this coordinate system reveals,

$$\left[\frac{\partial b_m}{\partial x_i'} \mathbf{K}_m\right] \cdot \nabla G = -f(k, r_2) \begin{bmatrix} \frac{\partial b_m}{\partial t'}(0, K_{h\,m}, 0) \\ \frac{1}{\alpha_m} \frac{\partial b_m}{\partial y'}(0, K_{h\,m}, 0) \\ 0 \end{bmatrix} \cdot \begin{bmatrix} \hat{r}_{2\,t} \\ \hat{r}_{2\,h} \\ \hat{r}_{2\,n} \end{bmatrix} = -f \begin{bmatrix} \frac{\partial b_m}{\partial t'} K_{h\,m} \hat{r}_{2\,h} \\ \frac{1}{\alpha_m} \frac{\partial b_m}{\partial y'} K_{h\,m} \hat{r}_{2\,h} \\ 0 \end{bmatrix} \tag{6.45}$$

where the function $f(k, r_2) = \frac{1+ikr_2}{4\pi r_2^2} e^{-ikr_2}$.

Taking derivatives of the basis functions with respect to this system

$$\frac{\partial b_m}{\partial t'} = (\delta(t_m - \frac{\Delta t}{2}) - \delta(t_m + \frac{\Delta t}{2})) \exp(-ik\Delta r_1) \tag{6.46}$$

$$\frac{1}{\alpha_m}\frac{\partial b_m}{\partial y'} = -\frac{ik}{\alpha}\frac{\partial \Delta r_1}{\partial y'} \exp(-ik\Delta r_1) p[t_m, -\frac{\Delta t}{2}, +\frac{\Delta t}{2}] \tag{6.47}$$

and so it is necessary to evaluate the integral

$$-\int_{\Delta_m} f(k, r_2) \begin{bmatrix} (\delta(t_m - \frac{\Delta t}{2}) - \delta(t_m + \frac{\Delta t}{2})) \exp(-ik\Delta r_1) \\ -\frac{ik}{\alpha_m}\frac{\partial \Delta r_1}{\partial y'} \exp(-ik\Delta r_1) \\ 0 \end{bmatrix} K_{hm} \hat{r}_{2h} \alpha_m dy' dt' \tag{6.48}$$

Integrating through t' for the $\hat{\mathbf{t}}$ element of the vector in (6.48)

$$-\int_{-\infty}^{\infty}\int_{\Delta t_m} f(k, r_2)(\delta(t_m - \frac{\Delta t}{2}) - \delta(t_m + \frac{\Delta t}{2}))e^{-ik\Delta r_1} K_{hm}\hat{r}_{2h} dt' \alpha_m dy'$$

$$= -\int_{-\infty}^{\infty} (f(k, t_m - \Delta t/2) - f(k, t_m + \Delta t/2))e^{-ik\Delta r_1} K_{hm}\hat{r}_{2h}\alpha_m dy' \tag{6.49}$$

The function $f(k, r_2)$ is approximately even with respect to y' in the near field region, where it is dependent principally on y'^2. $e^{-ik\Delta r_1}$ is stationary near $y' = 0$, and K_{hm} is constant over the strip. $\hat{r}_{2h}$ is odd with respect to y', so when the y' integration is performed the above integrand is odd, and the integral may be neglected.

Considering the $\hat{h}$ element of the dyadic near field(6.48), Δr_1 is stationary with respect to y' at the point $\mathbf{r}_m$ and its first derivative is both vanishing and even, in this region. By the presence of $\hat{r}_{2h}$ then, this integrand is also odd, and shall be neglected. The dyadic near field is therefore neglected altogether.

In the fourth term on the RHS of (6.42) we have the integral

$$\frac{k}{4\eta}\int_{t'=t_m-\frac{\Delta t}{2}}^{t_m+\frac{\Delta t}{2}} H_0^{(2)}(kr_2) K_{hm} dt' = \frac{k}{4\eta} H_0^{(2)}(kr_{2mn}) K_{hm} \Delta t_m \tag{6.50}$$

which contributes a self interaction term

$$\mathcal{S}_n^K K_{hn} = \frac{k\Delta t_n}{4\eta}(1 - \frac{2i}{\pi}\left[ln(\frac{\gamma k \Delta t}{4} - 1\right])K_{hn}$$

As in Chapter 5 the self interaction term integral over $\mathbf{J}$ evaluates to

$$\int_{\delta_m} \nabla G \wedge \mathbf{J}_{hn} b_n = \frac{\mathbf{J}_{hn}}{2} \tag{6.51}$$

as the observation point approaches the surface along the exterior normal.

The transverse integrals over terms in $G\mathbf{K}$ and $\overline{\overline{G}} \cdot \mathbf{K}$ on the strip are performed analytically in the same manner as in Chapter 5, Section 5.4 and may be expressed in terms of the elements of $\tilde{\mathbf{r}}_\mathbf{2}$ (5.48). Firstly, as $r_{2x} \gg r_{2y}, r_{2z}$ over the region contributing principally to the integral(this term is evaluated in the far-field of the observation point)

$$\overline{\overline{G}} = -\frac{k^2}{r_2^2} G_{mn} \begin{bmatrix} r_{2x}r_{2x} & r_{2x}r_{2y} & r_{2x}r_{2z} \\ r_{2y}r_{2x} & r_{2y}r_{2y} & r_{2y}r_{2z} \\ r_{2z}r_{2x} & r_{2z}r_{2y} & r_{2z}r_{2z} \end{bmatrix}_{mn} \approx -\frac{k^2}{r_2^2} G_{mn} r_{2x} \begin{bmatrix} r_{2x} & r_{2y} & r_{2z} \\ r_{2y} & 0 & 0 \\ r_{2z} & 0 & 0 \end{bmatrix}_{mn} \tag{6.52}$$

and so

$$\int_{\Delta m} \overline{\overline{G}} \cdot \mathbf{K}_m \approx -k^2 G_{mn} \hat{r}_{2x} \begin{bmatrix} \tilde{r}_{2x} & \tilde{r}_{2y} & \tilde{r}_{2z} \\ \tilde{r}_{2y} & 0 & 0 \\ \tilde{r}_{2z} & 0 & 0 \end{bmatrix}_{mn} \cdot \mathbf{K}_m \Delta t_m \tag{6.53}$$

$$\int_{\Delta m} G \cdot \mathbf{K}_m \approx G_{mn} \mathbf{K}_m \tilde{r}_{2x} \Delta t_m \tag{6.54}$$

Scattering in the near field region under the antenna may be evaluated in terms of (6.40), as the height of the antenna itself ensures a radius of curvature of at least 20 meters in the current phase. As the modulus of r_2 increases we may revert to (6.54) which is in fact robust even in the comparatively near field. Other near field components will be vanishing. This is again true when we consider contributions from regions of the profile near the observer at a large distance from the source. Here the only significant near field contributions may be evaluated using 6.54.

With all terms evaluated, equation (6.42) is now resolved at a tangent strip to give,

$$K_{\hat{h}n} = (\mathbf{H}_n^{Inc} + \mathbf{H}_n^{Sca})_{\hat{h}} / \mathcal{S}_n^K \tag{6.55}$$

$$J_{\hat{h}n} = 2.0(\mathbf{H}_n^{Inc} + \mathbf{H}_n^{Sca})_{\hat{t}} \tag{6.56}$$

$$\mathbf{H}_n^{Sca} = -ik \sum_{m \neq n} G_{mn} \tilde{\mathbf{r}}_{2\,mn} \wedge \mathbf{J}_m \Delta t_m \tag{6.57}$$

$$-\frac{k}{i\eta} \sum_{m \in FF} G_{mn} \hat{r}_{2\,x} \begin{bmatrix} \tilde{r}_{2\,x} & \tilde{r}_{2\,y} & \tilde{r}_{2\,z} \\ \tilde{r}_{2\,y} & 0 & 0 \\ \tilde{r}_{2\,z} & 0 & 0 \end{bmatrix}_{mn} \cdot \mathbf{K}_m \Delta t_m$$

$$+\frac{k}{i\eta} \left(\sum_{m \in NF} \frac{H_{0\,mn}^2}{4i} \mathbf{K}_m \Delta t_m + \sum_{m \in FF} G_{mn} \tilde{r}_{2\,x} \mathbf{K}_m \Delta t_m \right)$$

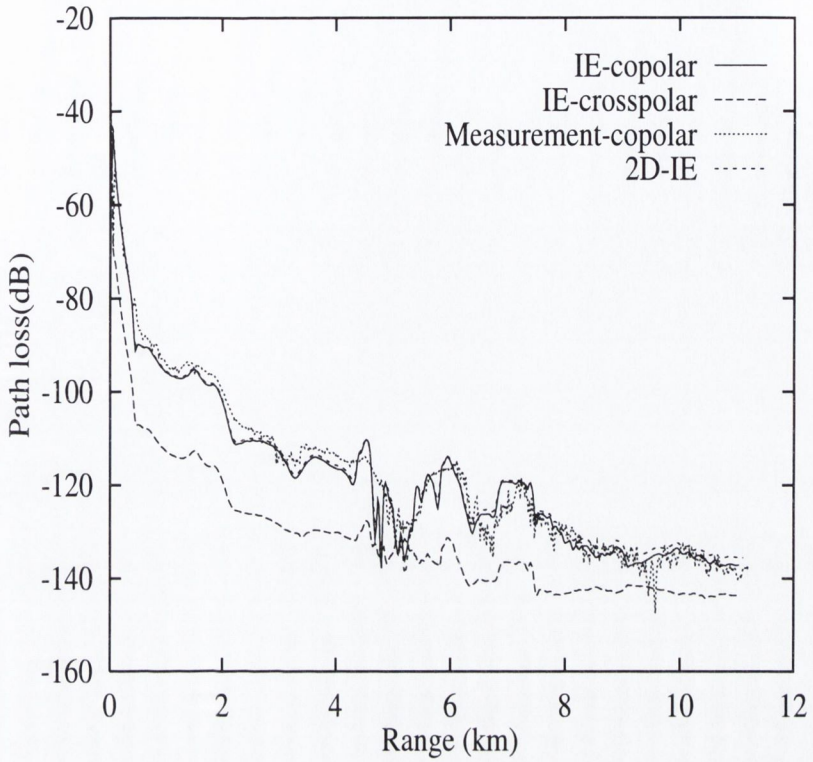
Essentially we have reduced a system of two coupled vector equations to one of two coupled scalar equations. In addition we have removed the necessity to simultaneously solve the interior field equation, and hence it is not necessary to sample the integrand at the smaller interval of $\frac{\lambda_d}{4}$. Having solved for $\mathbf{J}_h$ and $\mathbf{K}_h$ the field strength over the surface may be evaluated using the same integral, at observation points exterior to the surface.

6.4 Numerical Results for PEC/PMC Terrain

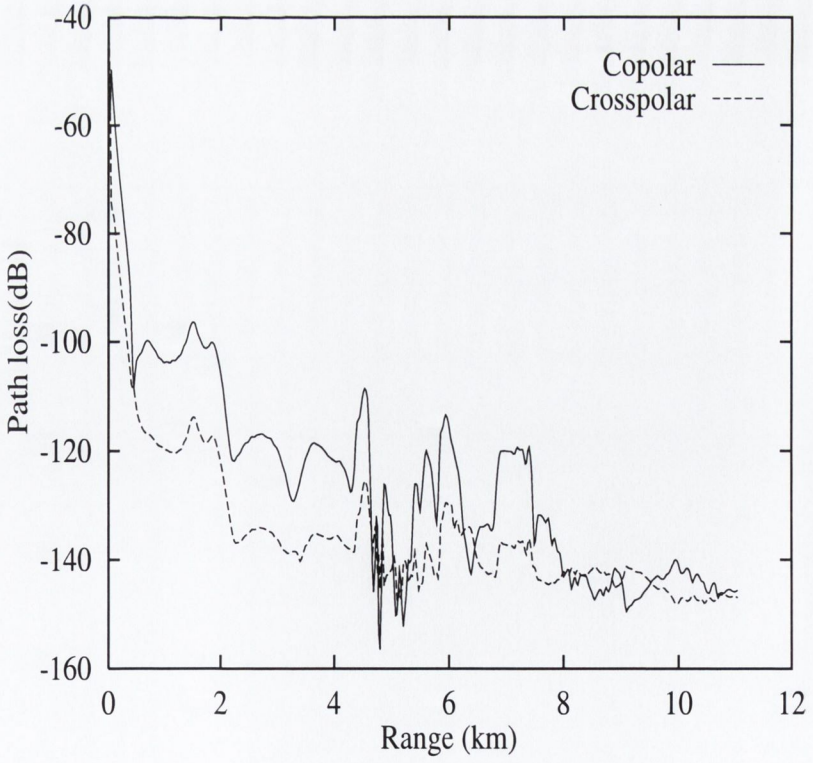
Comparisons are now made with experimental results and numerical 2D solutions for terrain propagation for a range of profiles and frequencies.

Again it is indicated that no experimental data were available regarding the *cross-polar* field in the terrain examples. Predictions were made for the gently undulating Danish profile of [27] at 144MHz and 435MHz using the PEC/PMC form of the algorithm and are plotted along with the 2D-IE solution and measured data, in Figure 6-5. Results are for a vertically polarized electric source and receiver at heights of 10.4m and 2.4m respectively.

The same transverse gradient profile has been synthesized as in Chapter 5. The measured data is of the field *copolar* with the transmitter, and it is assumed that it was measured to the upright vertical, and not upward normal to the terrain. In any case the difference between these two readings is negligible for the gently undulating terrain of this example. The point is made however, that on an incline, measuring the field normal to the surface is in effect measuring a mixture of the vertical *copolar* field, and the *cross-polar* field. The distinction is more important on steeper terrain



(a)



(b)

Figure 6-5: *(a)* Copolar *and* Cross-polar *for Danish terrain at 144MHz : (b) Double terrain height function also at 144MHz*

and where *copolar* and *cross-polar* fields are comparable in size. The *cross-polar* field is a vector quantity with an arbitrary orientation in the xy plane. The value plotted indicates the magnitude of this vector. For this field to be measured would require an electric dipole receiver to be rotated in the xy plane at the observation point until the direction of maximum received power is found. Vector components of this field are plotted and discussed in Section 6.6.3.

In the PEC/PMC approximation the transverse gradients only introduce a very small correction to the *copolar* field, and give good agreement with measurement. As expected the Q3D model predicts an additional *cross-polar* component which although weaker, has a lower rate of attenuation than the *copolar* field, and again may be of comparable strength in shadow regions (Figure 6-5.a). As we saw in chapter 6, this may be attributed to the fact that the *cross-polar* field propagates more efficiently along the surface and into the shadow regions, and increases at the expense of the stronger *copolar* field with subsequent scattering events.

At 144MHz the area average [3] difference between the *cross-polar* field and the *copolar* field is 11dB.

Figure 6-5.b represents predictions where the previous terrain height profile has been multiplied by a factor of two, creating a more strongly undulating terrain, but still having only $\approx 60m$ height variations over an 11km profile. The area weighted average difference between the *copolar* and *cross-polar* fields falls to $\approx 6dB$.

For the original profile at 435MHz (Figure 6-6) the difference in magnitude between the two components rises to $\approx 16db$. Again the rate of decay of the *cross-polar* field is lower.

Figure 6-8 illustrates predictions for two terrain topographies with known transverse gradient profiles, at 435MHz. The profiles were extracted from a three dimensional Irish terrain database (Figure 6-7. a), where the antenna was located on the peaks of this medium to strongly undulating profile, and the test profiles are plotted here in Figure 6-7. b.

Again the *copolar* field in the Q3D model differs only slightly from the solution

[3]Multiplying by a factor of 2 r / (R * R) representing the fact that the predictions at longer ranges are indicative of proportionately larger areas of coverage

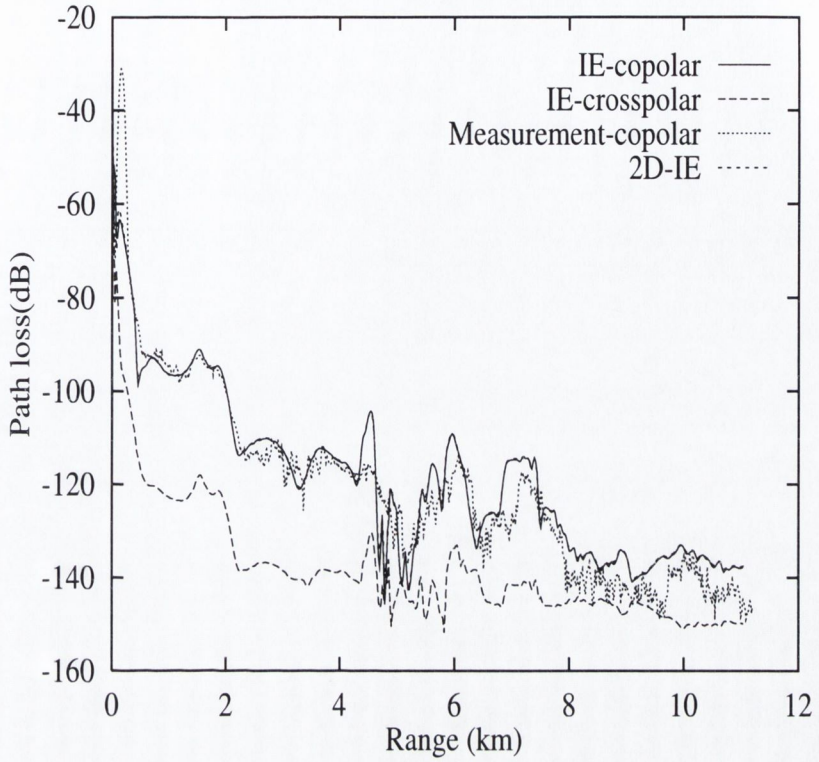
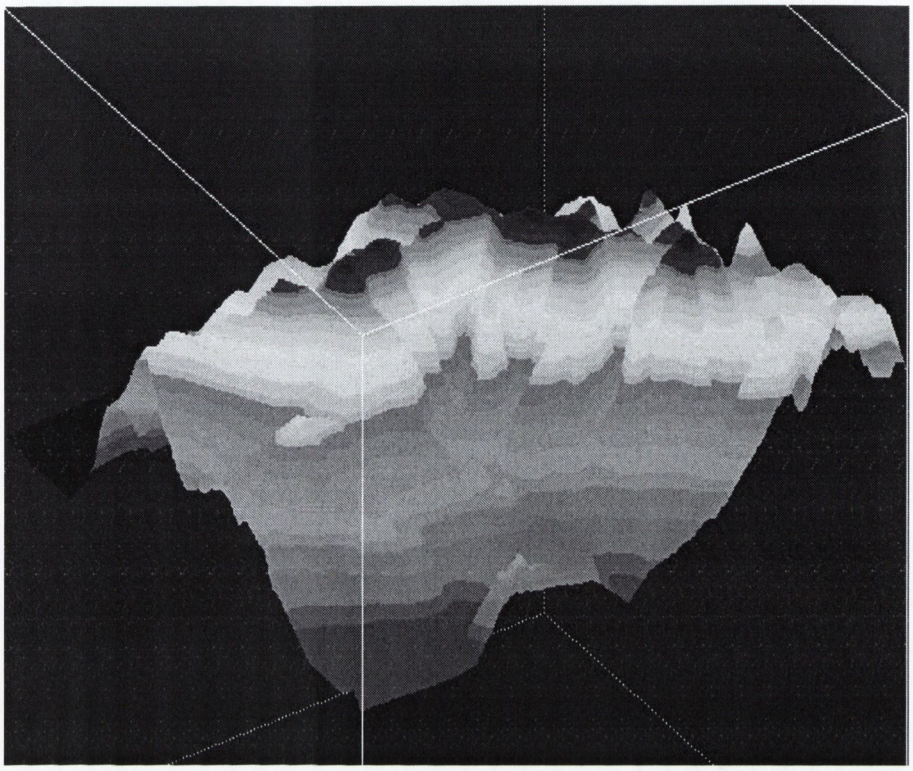


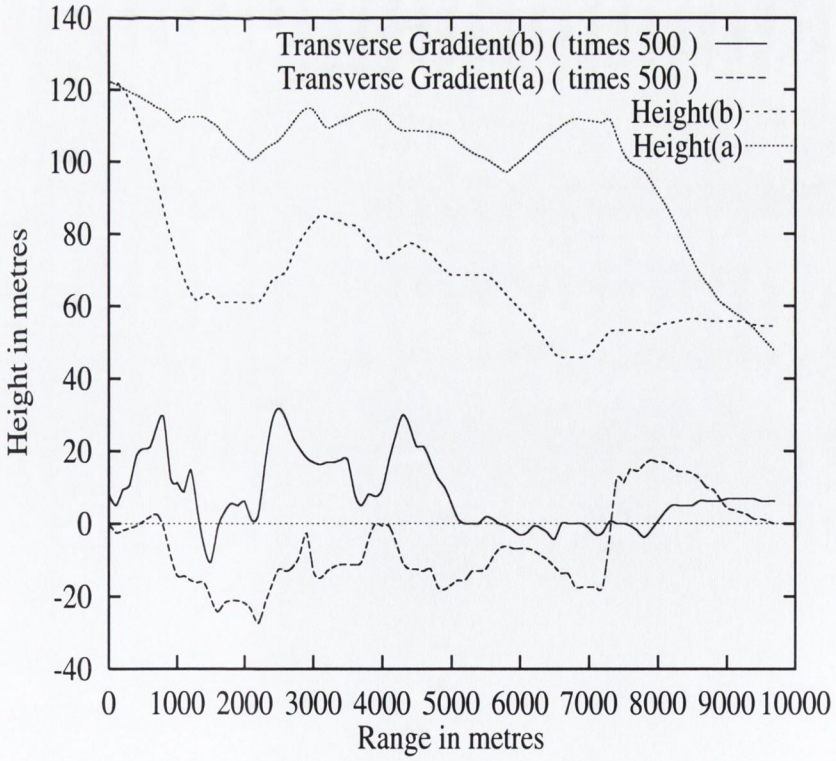
Figure 6-6: Copolar *and* Cross-polar *for Danish terrain at 435MHz*

attained using the 2D corrugated IE. This is not surprising as the current component J_y and the normal component n_z which principally dictate the *copolar* field strengths, vary only to second order on the introduction of the transverse surface gradient.

In Figure 6-8.a we can see that for certain topographies the *cross-polar* field may be dominant over considerable areas of coverage, in this case, over 40% of the profile, when area weighting is considered. In this case the cause may be identified as the sharp downward turn in the terrain profile around 7200m (Figure 6-8. b), which is accompanied by a swing from negative to positive transverse gradient. This appears to have the effect of rotating the plane of polarization of the scattered field, while the *copolar* field is deeply shadowed.

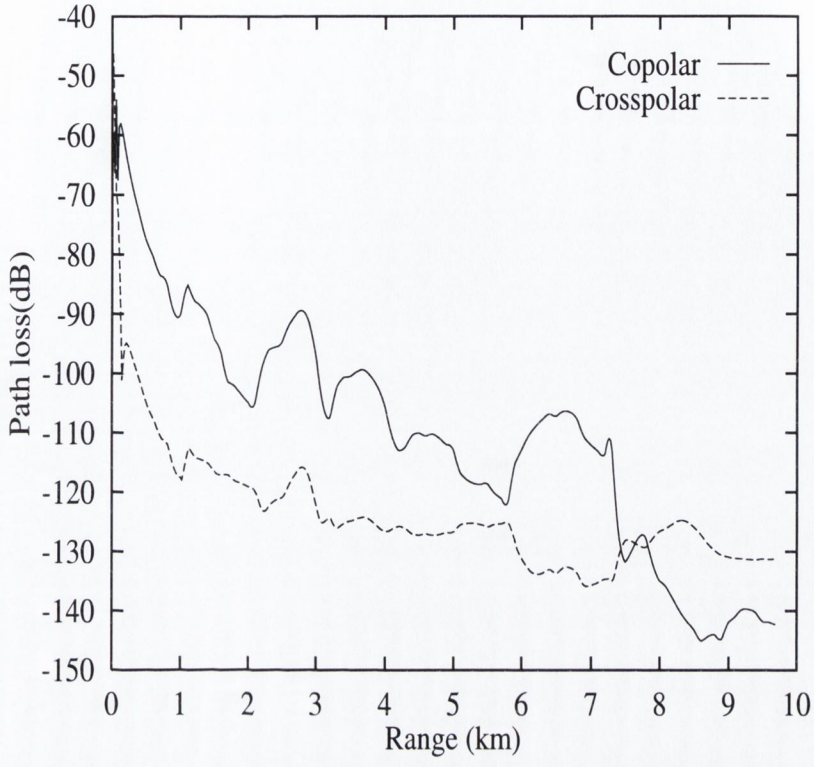


(a)

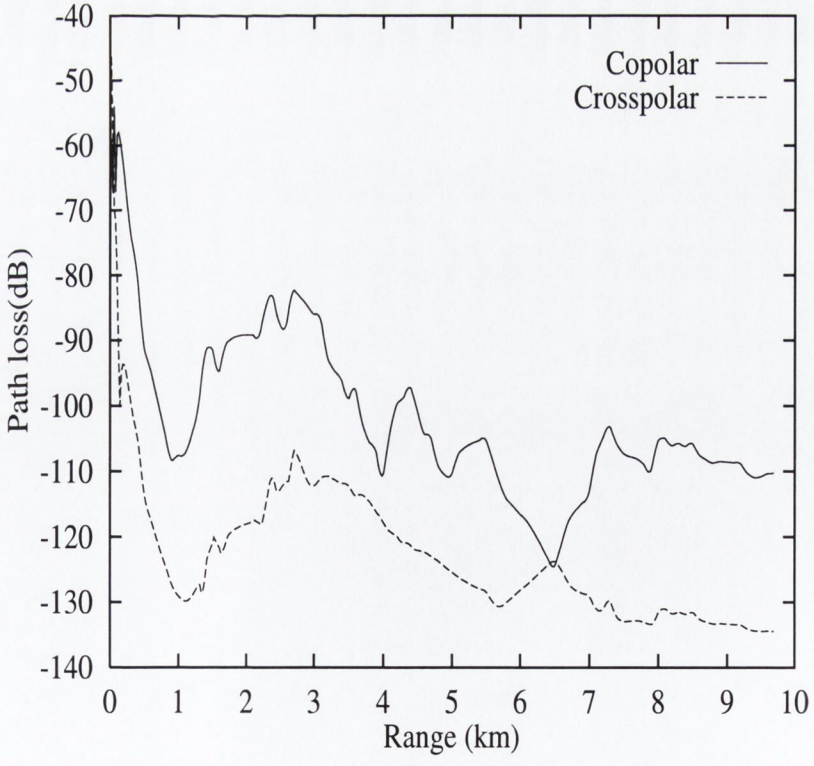


(b)

Figure 6-7: *Irish terrain (a) and two sample profiles with transverse gradients indicated (b).*



(a)



(b)

Figure 6-8: Copolar *and* Cross-polar *for two Irish terrain at 435MHz*

6.5 A PMC/Impedance Boundary Condition

The PEC/PMC type boundary condition used in Section 6.4 is acceptable for terrain having gradual surface height variations, where the reflection coefficient for horizontal magnetic polarizations may be approximated by -1. For terrain with larger gradients where incident and scattered fields may impinge on the surface at lower angles[4], $\theta_i \in (\pi/2, 70^o)$, which may be near or below the Brewster angle, it is necessary to provide a more robust approximation to the horizontal magnetic reflection coefficient. We step back to the analysis of Section 6.2. For the plane wave

$$\mathbf{H}_i^I = H_i^I(\cos\gamma_i\hat{\mathbf{h}}_i + \cos\theta_i \sin\gamma_i\hat{\mathbf{t}}_i + \sin\theta_i \sin\gamma_i\hat{\mathbf{n}}_i) \tag{6.58}$$

impinging on a planar surface, we recall from Chapter 4 section 4.4 that the total horizontal magnetic field $H_{h\,i}^{Tot}$, for an impinging plane wave component $\mathbf{H}_i^I$, satisfies an impedance boundary condition of the type,

$$H_{h\,i}^{Tot} = \frac{1}{\eta_d} E_{t\,i}^{Tot} \tag{6.59}$$

where $\eta_d = \sqrt{\mu_d/\epsilon_d}$. It was also demonstrated that this relation holds for a wide range of propagation angles. It is observed that $E_{h\,i}^{Tot}$ is independent of $H_{h\,i}^{Tot}$ which contributes only to $\mathbf{E}_v$ for scattering from a planar boundary. Given this independence, a similar analysis may be followed as in the development of the PEC/PMC compound boundary condition. The twin boundary conditions of (6.14) and (6.59), for individual impinging waves, may be extended by the single incident plane approximation $\hat{\mathbf{h}} = \hat{\mathbf{n}} \wedge \hat{\mathbf{x}}$ (Section 6.2), to define the boundary conditions

$$\mathbf{H}^{Tot} \cdot \hat{\mathbf{h}} = \frac{1}{\eta_d} \mathbf{E}_t^{Tot} \tag{6.60}$$

$$\mathbf{H}^{Tot} \cdot \hat{\mathbf{t}} = 2\mathbf{H}^I \cdot \hat{\mathbf{t}} \tag{6.61}$$

where $\mathbf{H}^{Tot}$ represents the total field on the surface due to all impinging and reflected components. The single incident plane approximation is accurate over a wider angular range than the PMC approximation to the surface boundary condition, and hence, it is of value to extend the Q3D treatment to a PEC/Impedance boundary condition.

[4]Even lower angles of incidence are possible but this range is likely to cover most terrain

This alternative approximation leads to a different integral equation formulation to (6.55) and (6.56). $\mathbf{H}^{Tot} \cdot \hat{\mathbf{h}}$ is no longer zero, and

$$J_t = -H_h = \frac{1}{\eta_d} E_t = \frac{1}{\eta} K_h \tag{6.62}$$

Referring once more to (6.42), and given that $K_t \approx 0$, the dyadic near and self terms may again be neglected, and without repeating the analysis of Sections 6.2 and 6.3 we make the substitution of $-\eta_d J_t$ for K_p yielding

$$J_{\hat{h}n} = 2.0(\mathbf{H}_n^{Inc} + \mathbf{H}_n^{Sca})_{\hat{t}_n} \tag{6.63}$$

$$J_{\hat{t}n} = -(\mathbf{H}_n^{Inc} + \mathbf{H}_n^{Sca})_{\hat{h}_n} / (\frac{1}{2} + \eta_d \mathcal{S}_n^K) \tag{6.64}$$

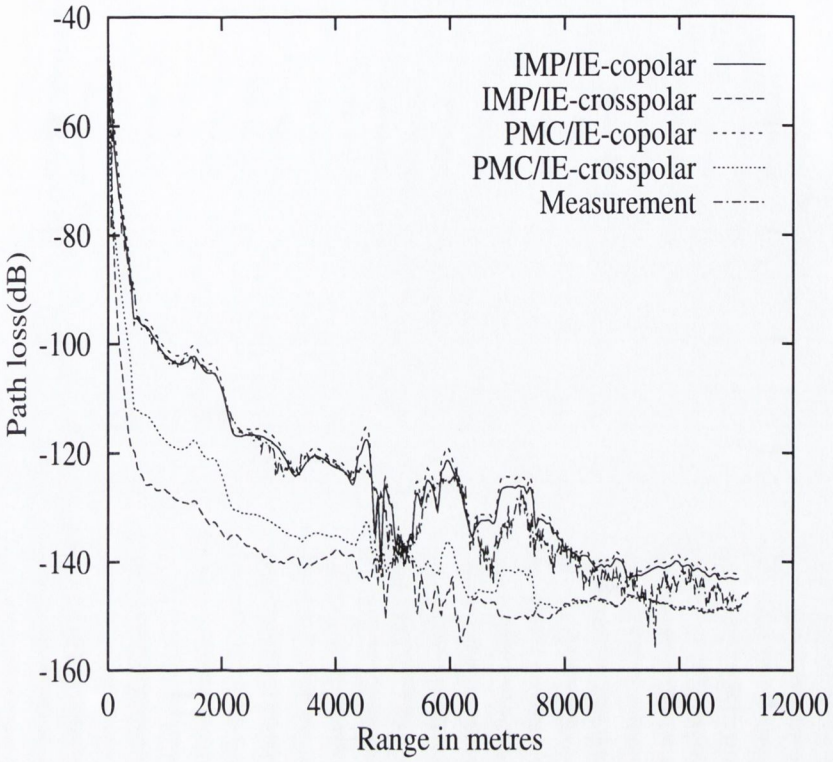
$$K_{\hat{h}n} = -\eta_d J_{tn} \tag{6.65}$$

The expression for the scattered field $\mathbf{H}_n^{Sca}$ is identical to (6.57).

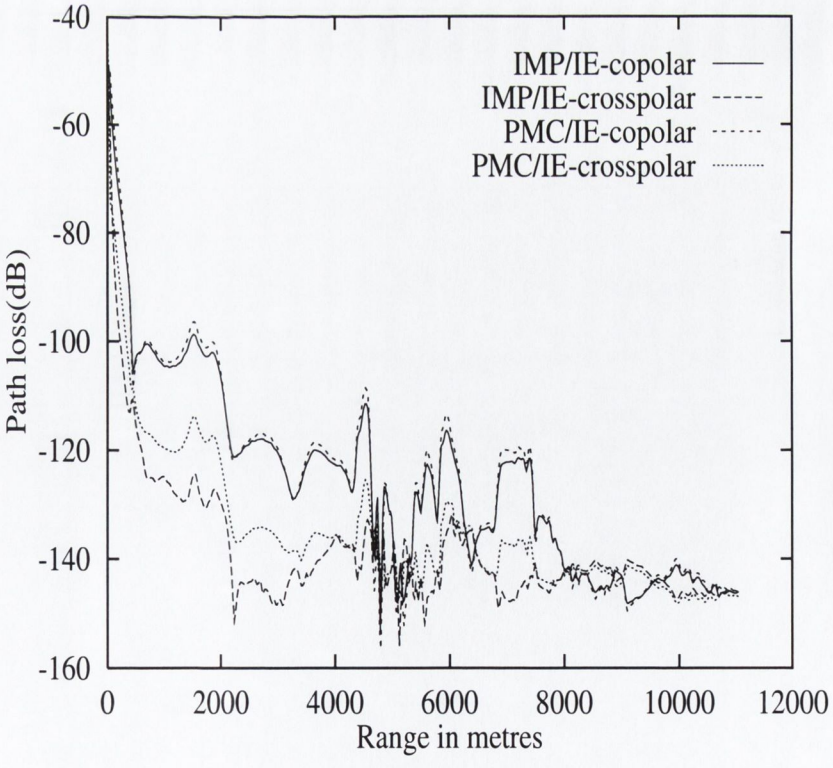
The equations for $\mathbf{J}_{\hat{h}n}$ and $\mathbf{K}_{\hat{h}n}$ are of the same form as in the PEC/PMC case with the additional current component, $J_{\hat{t}n}$. The forward scattered field is calculated over a different set of currents $\mathbf{J}_h$, $\mathbf{J}_t$ and $\mathbf{K}_h$.

6.6 Numerical Results for a PEC/Impedance Terrain Approximation

We repeat the tests of Section 6.4 using the PEC/Impedance boundary condition. Ground material parameters, where known, now provide an additional input parameter to the model. Otherwise, average ground parameters may be assumed. For our initial test intermediate values of $\epsilon_r = 15$, $\sigma = 0.005$ are adopted. Otherwise the profiles are identical to those of Section 6.4. Predictions were made for the profile of Figure 5-11 at 144MHz and 435MHz using the PEC/Impedance form of the algorithm and are plotted in Figure 6-9, along with the results of the PEC/PMC boundary. Results are for a vertically polarized electric source and receiver at heights of 10.4m and 2.4m respectively. Again the transverse gradient profile has been synthesized mimicking the variations of the known forward profile.



(a)



(b)

Figure 6-9: *(a)* Copolar *and* Cross-polar *for Danish terrain at 144MHz : (b) Double terrain height function also at 144MHz*

At 144MHz the area average difference between the *cross-polar* field and the *copolar* field is now 13 dB (Figure 6-9.a) versus 11dB for the PEC/PMC case. The difference between the *copolar* fields for PEC/PMC and PEC/Impedance methods, rarely exceeds 5dB. By comparison the difference between the predicted *cross-polar* fields may be over 12dB in the first few kilometers, converging however at greater ranges.

Figure 6-9.b represents predictions where once again the terrain height profile has been multiplied by a factor of two. The area average difference between the *copolar* and *cross-polar* fields in this case rises to $7.5dB$.

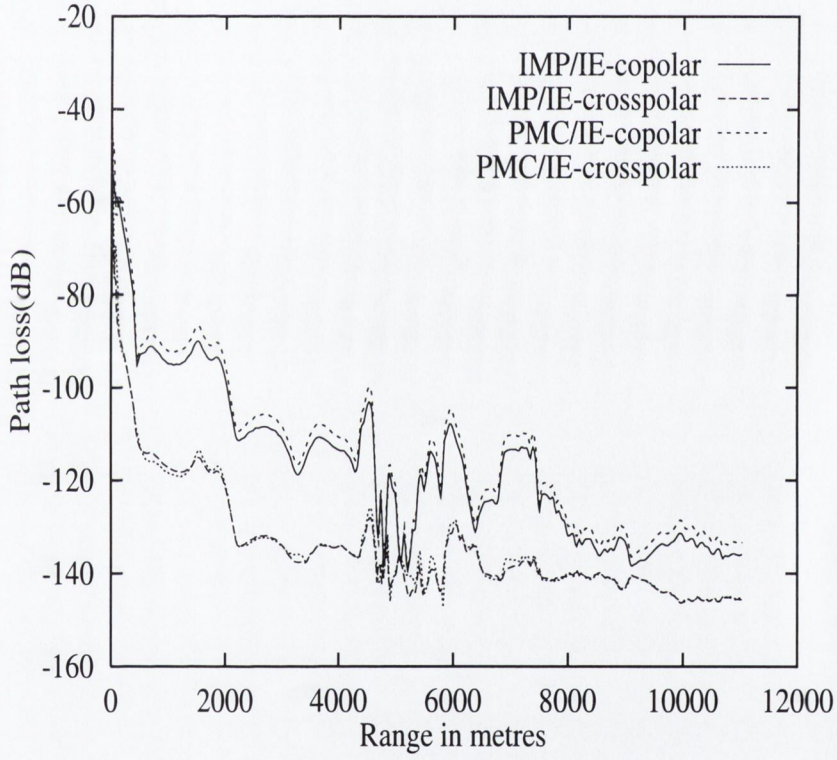
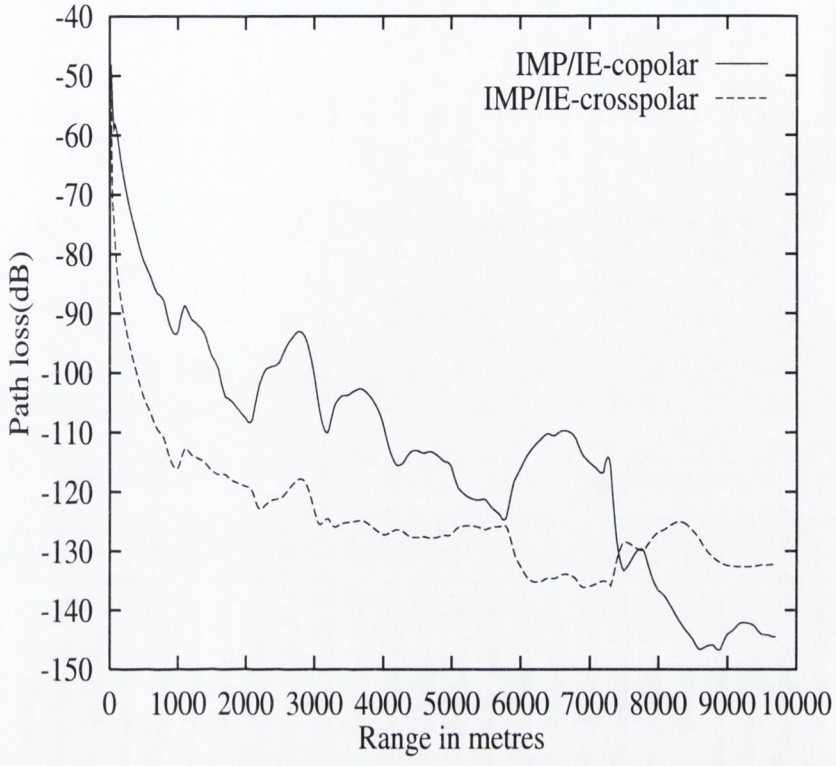


Figure 6-10: Copolar *and* Cross-polar *for Danish terrain at 435MHz*

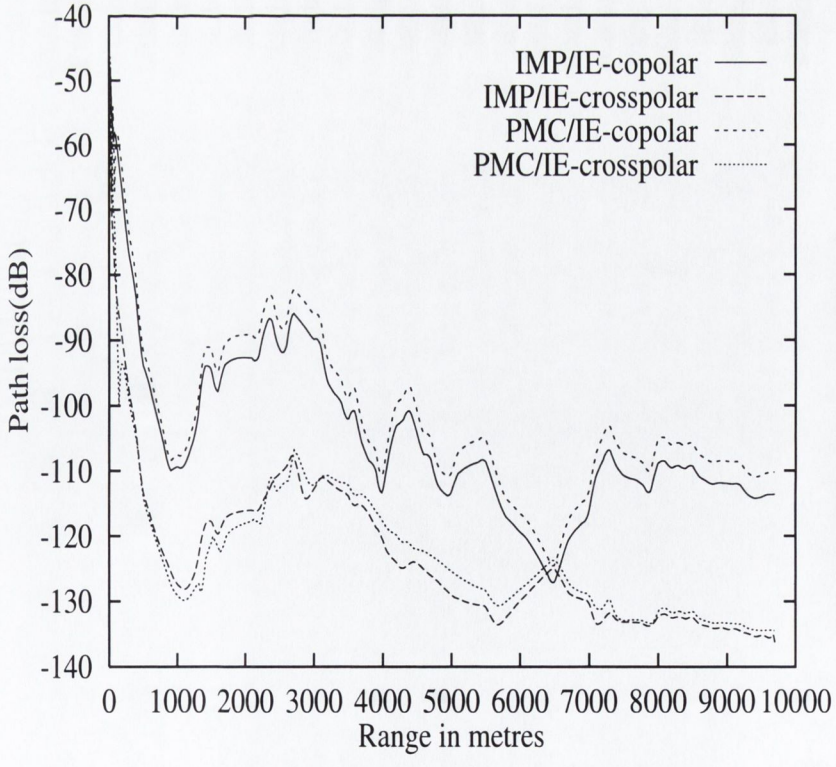
For the original profile at 435MHz the difference in magnitude between *copolar* and *cross-polar* components is now $\approx 14dB$, lower than in the PEC/PMC case at the same frequency(Figure 6-10). This is predominantly due to a 2dB drop in the predicted value of the *copolar* field taken against the PEC/PMC case. We note that measurements made in suburban areas indicate a *cross-polar* field 13dB lower than the *copolar* field[6][41][70]. Little may really be concluded from this as the

dominant depolarizing mechanisms in the suburban environment may not easily be determined. Again the *cross-polar* field decays more gradually than the *co-polar*. The results indicating a different rate of attenuation at least until the two fields become similar in magnitude, as consecutive scattering events tend to increase the *cross-polar* field at the expense of the larger, *copolar* field.

Figure 6-11 illustrates predictions at 435MHz, for the two Irish profiles, again, where predicted values are compared for PEC/PMC and PEC/Impedance conditions. In this case the difference in the *copolar* fields for PEC/PMC and PEC/IMP models is more noticeable at $\approx 3.5dB$. This indicates further the need to model the vertical polarization with an impedance type boundary approximation. We may expect the error to be greater for lower values of ϵ_r which may range from roughly 4 to 30. In addition, steeper gradients will further evince weakness in the PMC approximation. In these examples, the *cross-polar* fields are largely unchanged with an average difference of less than $1dB$.



(a)



(b)

Figure 6-11: Copolar *and* Cross-polar *for two Irish terrain at 435MHz*

6.6.1 Variation of Material Parameters

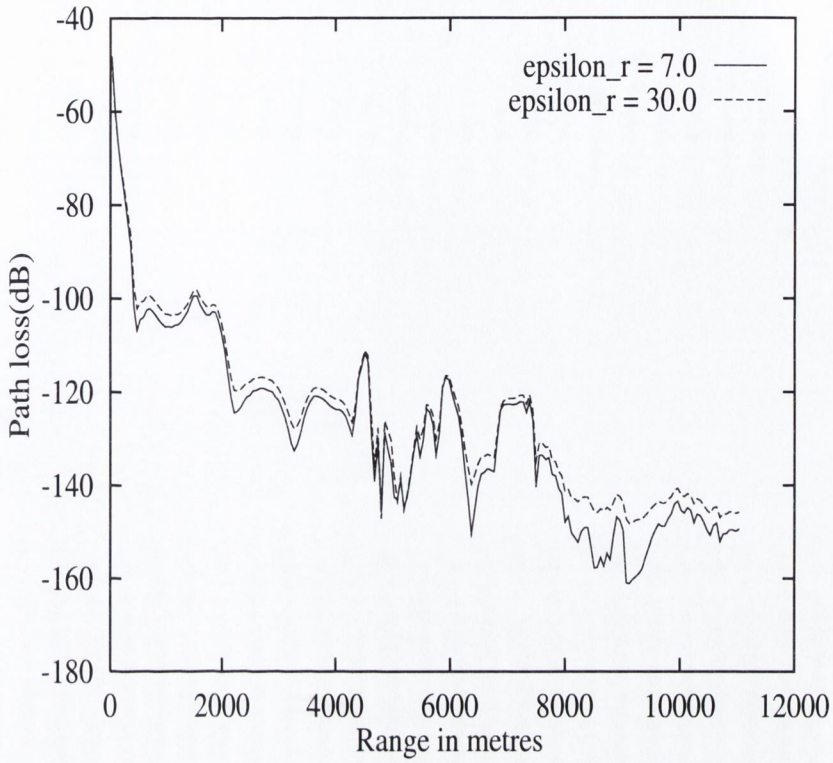
Comparisons are made at maximum and minimum likely ground permittivities of ($\epsilon_r = 7.0$, $\sigma = 0.005$) and (30.0, 0.005), at frequencies of 144MHz and 435MHz. More strongly undulating terrain profiles are tested as the effects of varying the refractive index will be more evident in such cases, differences only emerging at wider angles of propagation.

In Figure 6-12 tests are performed on the Hjorring profile with the height function scaled by a factor of 2, at 144MHz. The *copolar* field shows some considerable differences for the two values of ϵ_r, notably towards the end of the profile with errors of up to 12dB. The *cross-polar* field is more mildly affected by the change in permittivity. In this case, at the higher surface permittivity, the predicted *copolar* field is greater, while the *cross-polar* field shows a marginal reduction.

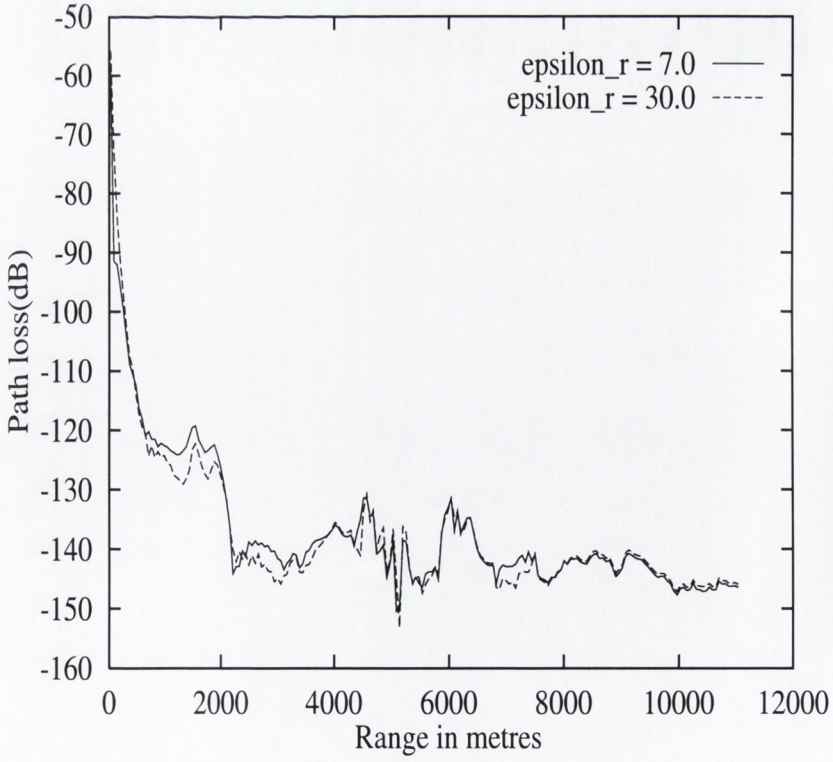
At 435MHz the sensitivity to ϵ_r is much less and differences only arise on a considerably steeper profile. The results of Figure 6-13 are for the Hjorring profile with height function scaled by a factor of 4. Differences of several dB arise at a few points on the *copolar* plot, but results are very similar for the two permittivitys, even for this strongly undulating profile. In this case the *copolar* field is marginally diminished at the higher permittivity, in contrast to the case at 144MHz. No sensitivity to ϵ_r is detected for the *cross-polar* field at 435MHz.

It was found that the effect of varying the terrain conductivity σ, within its realistic range of $0.001 - 0.03$, did not have any significant effect on these profiles, and hence results are not presented here. We note that for propagation over the sea, conductivity must be considered and factored into the surface impedance. It is generally true that the method may be applied to inhomogeneous surfaces by simply varying the surface impedance parameter.

Varying terrain permittivity is seen to have a mild effect on propagation estimates. No simple relationship between permittivity and field strength has been identified here. Some gains over PEC/PMC may be expected using the PEC/Impedance

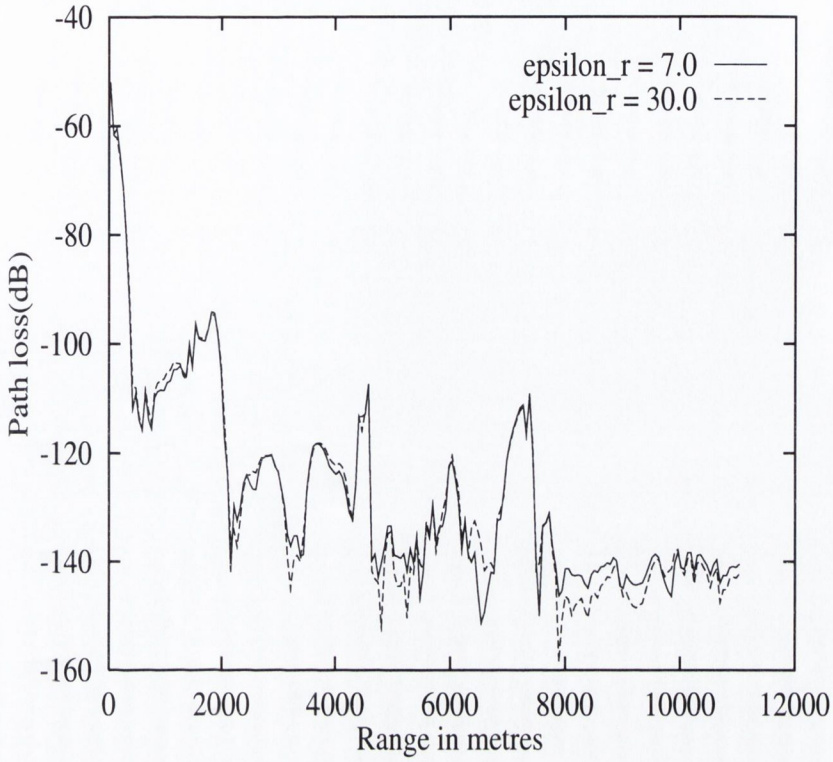


(a)

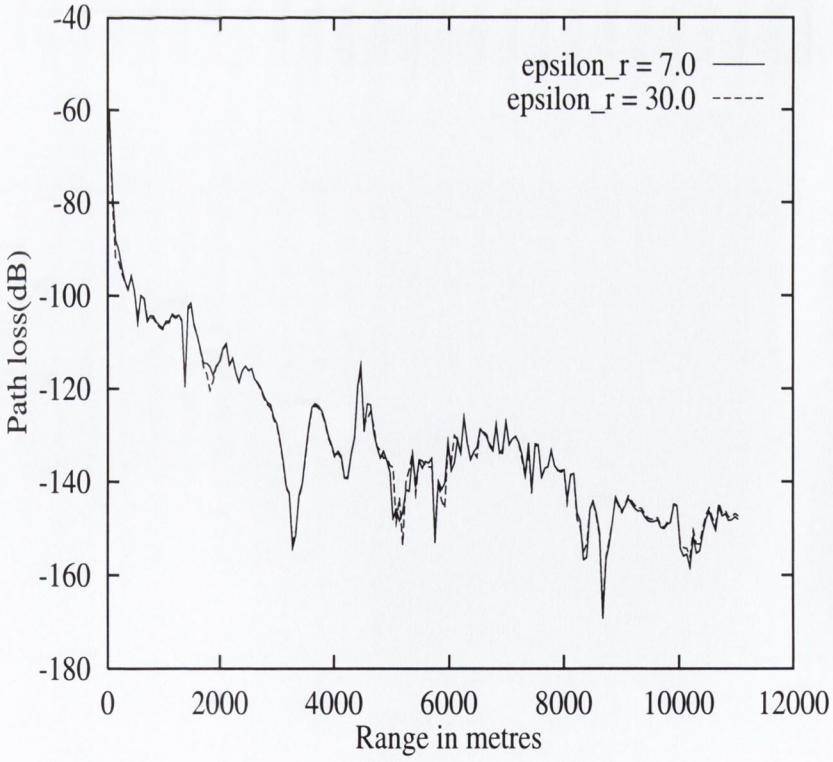


(b)

Figure 6-12: Copolar *(a) and* Cross-polar *(b) fields for Hjorring profile* ($\times 2$) *for* $\epsilon_r = 7.0$ *and* $\epsilon_r = 30.0$. $f = 144MHz$



(a)



(b)

Figure 6-13: Copolar *(a) and* Cross-polar *(b) fields for Hjorring profile* ($\times 4$) *for* $\epsilon_r = 7.0$ *and* $\epsilon_r = 30.0$. $f = 435MHz$

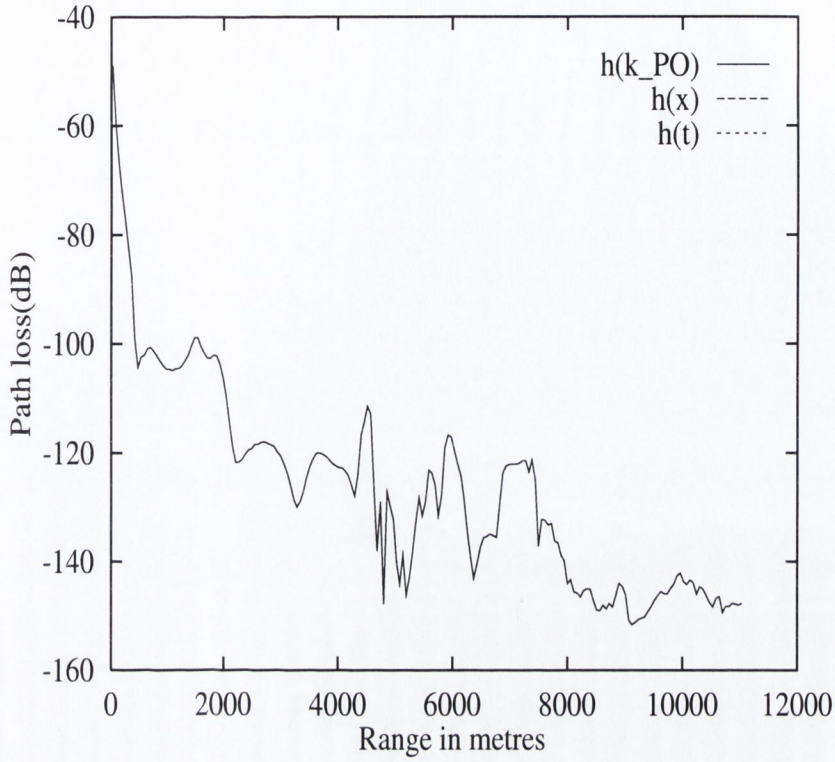
algorithm, but these are less significant at higher frequencies. However, testing the Q3D algorithm has required a more robust boundary approximation, and that has been achieved with the PEC/Impedance approach.

6.6.2 Definition of Incidence Plane

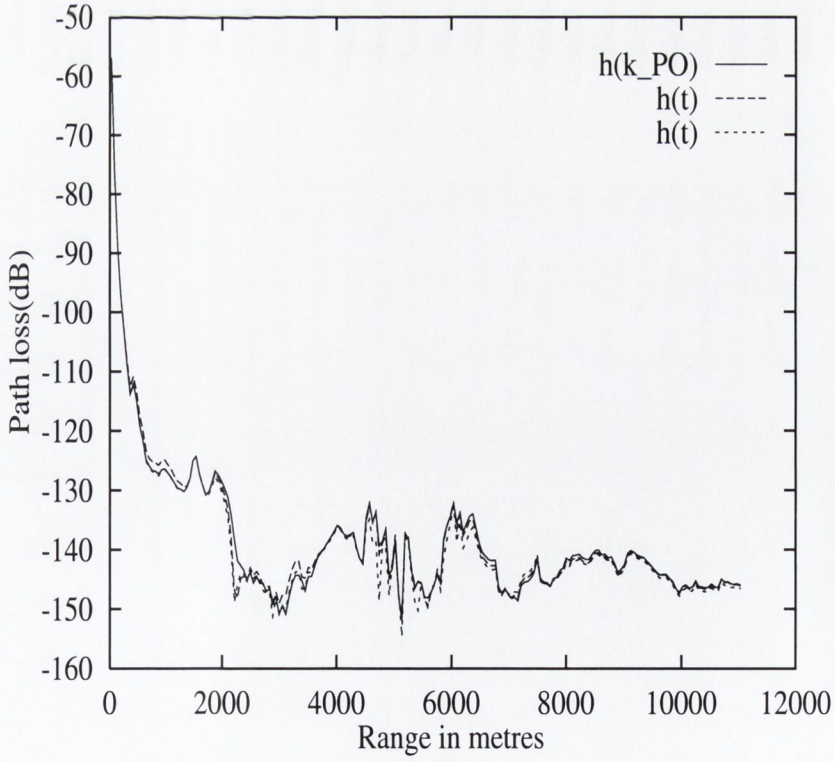
As was indicated in Section 6.2, the definition we use for the common incidence plane at a match point, given in terms of its normal vector $\hat{\mathbf{h}}$, although chosen to best approximate the incident plane in an average sense, was somewhat arbitrary. Choices, $\hat{\mathbf{n}} \wedge \hat{\mathbf{x}}$, $\hat{\mathbf{n}} \wedge \hat{\mathbf{t}}$, and $\hat{\mathbf{n}} \wedge \hat{\mathbf{k}}_{PO}$ are all reasonable. Given the arbitrary nature of this definition, we require that results do not vary significantly, on the basis of this choice.

We take the case where $\epsilon_r = 15.0$, at 144MHz(Figures 6-14), although permittivity will not be important in this test. Tests are on the Hjorring profile scaled by a factor of 2. We expect discrepancies to arise for more strongly undulating terrain. Plots are of *copolar* and *cross-polar* fields, given the three distinct definitions of $\hat{\mathbf{h}}$ listed above. In Figure 6-15 the test is repeated for the Hjorring profile scaled by 4, at 435MHz.

Both sets of plots indicate that the solution for either polarization is essentially invariant with respect to the definition of $\hat{\mathbf{h}}$, notably for the very strongly undulating terrain of Figure 6-15. With limited possibilities available for testing the accuracy of the Q3D model, this invariance gives a strong indication that approximating the incidence plane for all impinging components with a single incidence plane, is reasonable even for a strongly varying height profile. If this geometrical approximation is reasonable, we may also have confidence that the approximate boundary condition is satisfactory.

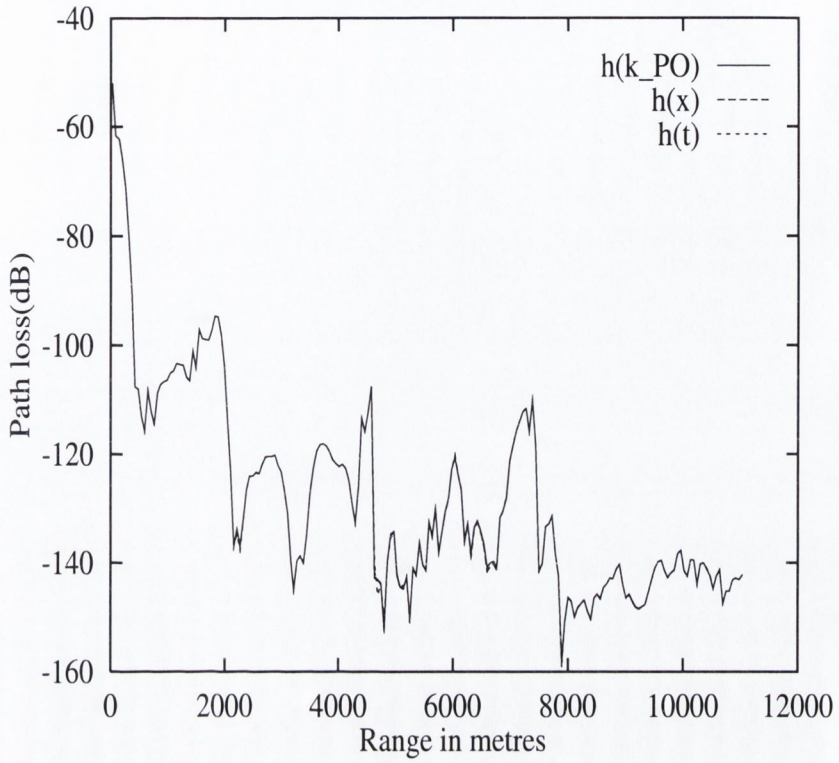


(a)

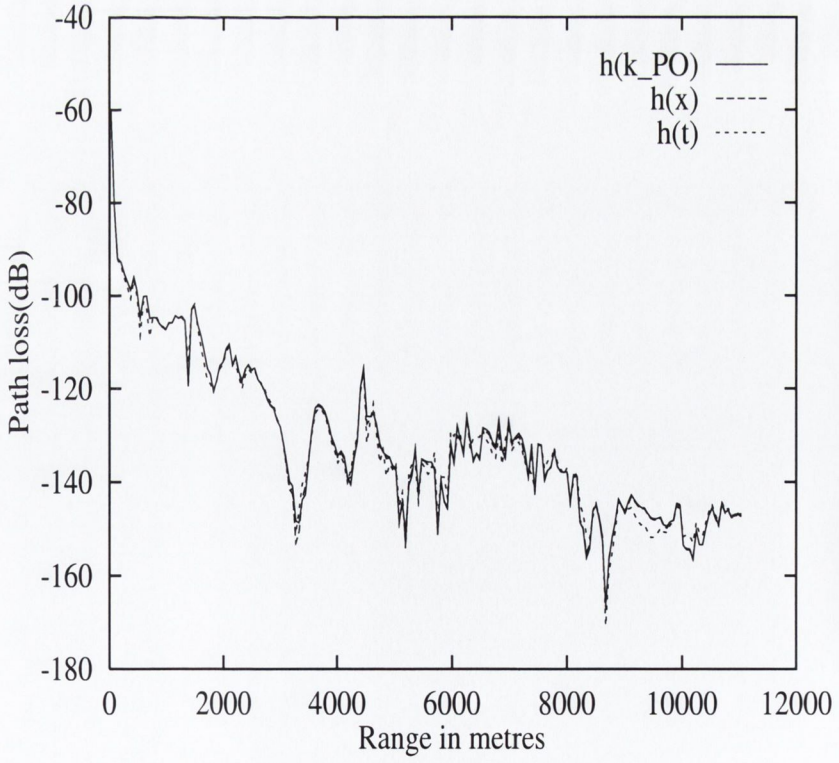


(b)

Figure 6-14: Copolar *(a) and* Cross-polar*(b) fields for Hjorring profile* ($\times 2$). $\epsilon_r = 15.0$, $f = 144MHz$ *for alternative definitions of* $\hat{\mathbf{h}}$



(a)



(b)

Figure 6-15: Copolar *(a) and* Cross-polar*(b) fields for Hjorring profile* ($\times 4$) *for alternative definitions of* $\hat{\mathbf{h}}$. $\epsilon = 30$, $f = 435MHz$ *for alternative definitions of* $\hat{\mathbf{h}}$

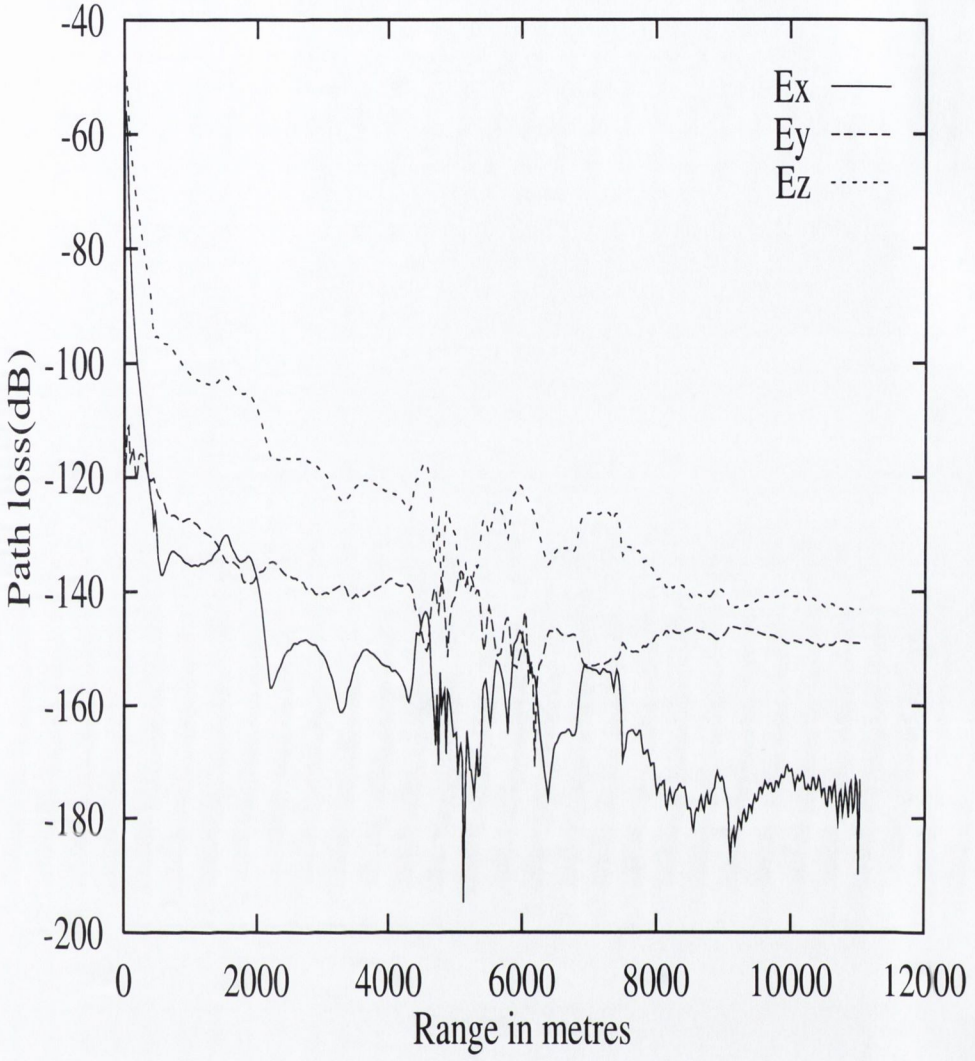


Figure 6-16: *Electric field components for Hjorring profile. $f = 144$ MHz*

6.6.3 Field Components

It was observed in Section 6.4 that the *cross-polar* field, constitutes a vector in the xy plane. The *cross-polar* plots indicate the amplitude of this vector, but we are free to examine its composition. In Figure 6-16 we plot the field components for $\hat{x}$, $\hat{y}$ and $\hat{z}$ directions, over the Hjorring profile at 144MHz. In Figure 6-17, the field components are plotted at 435MHz.

For both cases, in the near field of the antenna, the E_x component dominates the *cross-polar* field, and this is simply a result of the source geometry. As we progress along the radial, E_x falls off sharply, the **E** vector in the propagation plane being

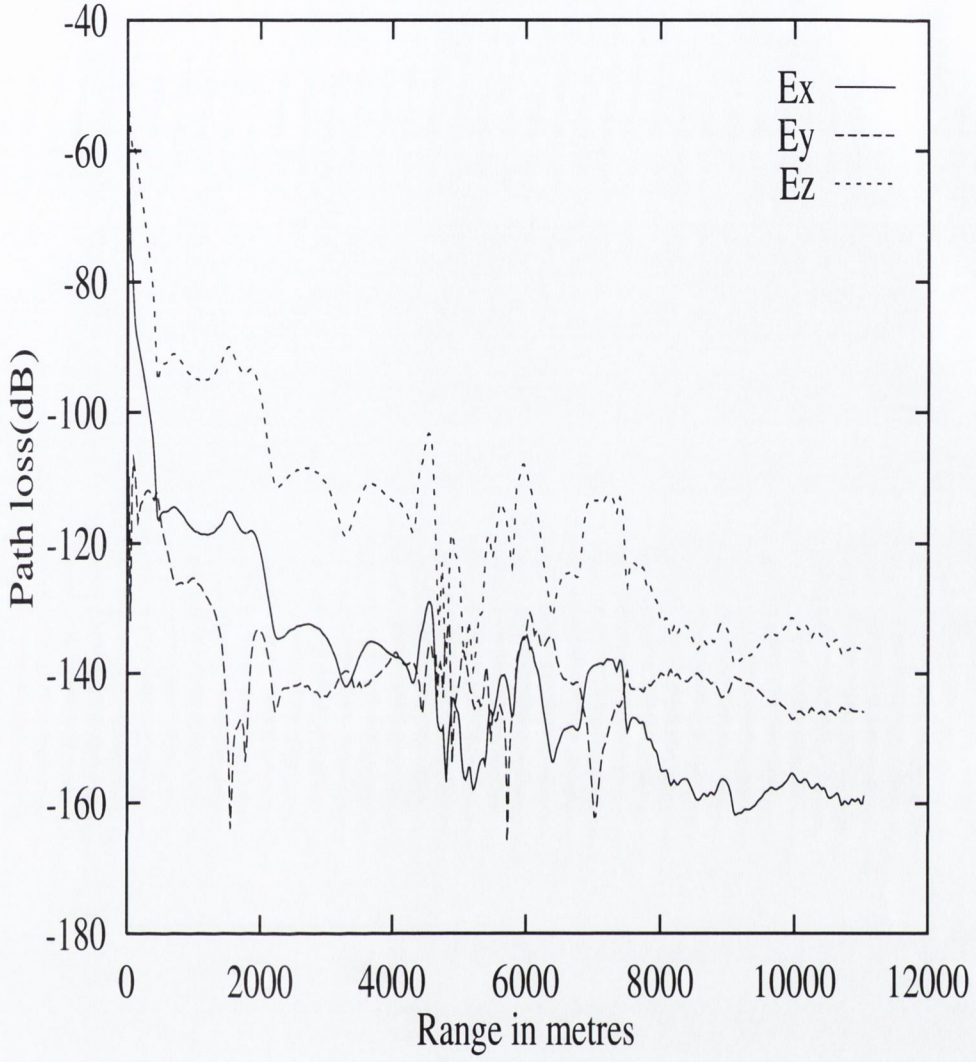


Figure 6-17: *Electric field components for Hjorring profile. $f = 435$ MHz*

almost vertical, with only a small wave *tilt*[5]. However, as successive scattering events occur, they contribute to the field E_y, which constitutes the bulk of the *cross-polar* field at greater ranges.

6.7 Discussion

The three dimensional vector integral equation governing the propagation of UHF waves over a smoothly undulating terrain has been approximated by integration over the surface of a connected set of inclined planar segments, modeling transverse gradients in the terrain profile using PEC/PMC and PEC/Impedance, compound boundary conditions, in an approach that is inclusive of terrain material parameters.

We have modeled a vertical electric point source, and successively utilized PEC/PMC, and PEC/Impedance boundary approximations for respective horizontal and vertical electric field components, at a local tangent plane. For vertically polarized electric field components propagating over Earth at UHF the reflection coefficient calculated from material parameters approaches -1 at grazing incidence but varies rapidly about this point, the amplitude decreasing linearly from 1 with θ_i in the region $\pi/2 > \theta > 80^o$, the phase remaining $\approx \pi$. In spite of this variation, a perfect reflecting boundary condition approximation may be adopted for this polarization at shallow incidence. Results compare well with the measured *copolar* field for gently undulating terrain, where much of the propagation takes place at angles of less than 1^o and the PMC approximation has been shown to be effective for modeling vertical electric polarizations [27] in such cases.

For wider angle propagation problems such as that arising on the steeper profiles, an impedance condition may be used for vertical electric polarizations. This allows us to incorporate ground material parameters in the model. While significant at lower frequency, varying ground permittivity appears to have little effect at 435MHz and beyond. The size of the *cross-polar* field is as expected, directly dependent on the level of terrain height variation and transverse gradients.

Off-radial propagation effects such as diffraction or multipath are not modeled in the Q3D approach but we do calculate to first order, currents that would contribute to such effects. This can be understood when we consider the calculation of the currents along many terrain radials, as one step in a Born Series method. It would

then be possible to integrate over these known currents to evaluate scattering to other radials, giving the next step in the series.

For a more complete solution some approximation to the interaction between the currents on terrain radials is required and this is discussed in Chapter 8. For more roughly textured surfaces where scattering is non specular we would anticipate a greater level of side scattering and depolarization.

For the results presented here $\lambda/5$ sampling was used and so the discontinuities between sloping surface segments are kept to a minimum. Longer segments would lead to greater discontinuities and an increase in the systematic error for more rugged surfaces. However, a number of interaction grouping techniques [9][51] may also be employed to dramatically reduce the computation times required for this method, and this is demonstrated in Chapter 7.

Chapter 7

Application of the Fast Far Field Approximation to Q3D

It was shown in the preceding two chapters that 3D terrain features may be modeled using a quasi three dimensional approximation to the terrain in the region of the antenna observer radial. Numerical complexity was of the same order as arises in the simpler 2D terrain propagation model, namely $\mathcal{O}(N^2)$, where $N = Samples/wavelength \times L$, where L is the length of line element from the source to the point of greatest range, measured in wavelengths. The Q3D solution is in fact slower than the 2D scalar model by a constant factor of ≈ 2.5, due to the multiplicity of fields, and more complicated interaction terms, and the run times encountered even at modest frequencies and problem ranges are prohibitive, taking days above $970MHz$ for the exact implementation. As was discussed in Chapter 3, both 2D and 3D techniques may be accelerated using approximation techniques such as the FMM and FAFFA. It is therefore natural to develop a rapid formulation of the Q3D method and bring it into line with the fast 2D terrain techniques. In the absence of a viable, fully 3D, vector integral equation method for terrain propagation, the Q3D approach will go some way to filling this gap in presently available propagation modeling techniques.

Very significant improvements in run time are possible with methods such as TIM and the NBS, but they rest on somewhat restrictive assumptions and are not an ideal

first candidates for a rapid Q3D algorithm. The FAFFA is the simplest method in formulation, yet highly robust, and it is this that will be applied to the Q3D model.

7.1 Formulation

In the Q3D method detailed in Chapter 6, the surface currents may be given in terms of the total magnetic field at the Earth-air interface via the exterior magnetic field integral equation. Hence, given an incident field $\mathbf{H}^{Inc}$, the MFIE is solved in terms of the scattered field

$$\mathbf{H}^s = \nabla \wedge \int_S G\mathbf{J}dS' \; + \; \frac{\nabla\nabla\cdot + k^2}{i\omega\mu_0}\int_S G\mathbf{K}dS' \tag{7.1}$$

and after discretization, the magnetic field scattered at the center of strip n is given by (6.65)

$$\mathbf{H}_n^s \approx -ik\sum_m G_{mn}\tilde{\mathbf{r}}_{2\,mn} \wedge \mathbf{J}_m\Delta t_m \tag{7.2}$$

$$+\frac{ik}{\eta}\sum_{m\in FF} G_{mn}\hat{r}_{2\,x}\begin{bmatrix}\tilde{r}_{2\,x} & \tilde{r}_{2\,y} & \tilde{r}_{2\,z}\\ \tilde{r}_{2\,y} & 0 & 0\\ \tilde{r}_{2\,z} & 0 & 0\end{bmatrix}_{mn}\mathbf{K}_m\Delta t_m$$

$$-\frac{ik}{\eta}\left(\sum_{m\in FF(n)} G_{mn}\tilde{r}_{x\,mn}\mathbf{K}_m\Delta t_m + \frac{1}{4i}\sum_{m\in NF(n)} H^{(2)}_{0\,mn}\mathbf{K}_m\Delta t_m\right)$$

where $\tilde{\mathbf{r}}_2$ has the definition given by (5.45). Now if we consider a small portion l' of the terrain containing a number of elemental strips as depicted in Figure 7-1, and define the vector $\mathbf{R}_{l'l}$ joining the principal scattering point $\mathbf{r}_p$ (5.24) on the central strip of group l', to the center of a subsequent group l. From Chapter 3, as amplitude terms in the current and Green's function are slowly varying, and $R_{l'l}$ is much greater than r'_m and r_n (Figure 7-1) we may approximate the Green's functions function, and Hankel functions thus,

$$G_{mn} = \frac{e^{-ikr_{mn}}}{4\pi r_{mn}} \approx e^{-ikr_n\cos\theta_n}e^{ikr'_m\cos\theta'_m}\frac{e^{-ikR_{l'l}}}{4\pi R_{l'l}} \tag{7.3}$$

$$H^{(2)}_{0\,mn} \approx \sqrt{\frac{2j}{\pi kr_{mn}}}e^{-ikr_{mn}} \approx e^{-ikr_n\cos\theta_n}e^{ikr'_m\cos\theta'_m}\sqrt{\frac{2j}{\pi kR_{l'l}}}e^{-ikR_{l'l}} \tag{7.4}$$

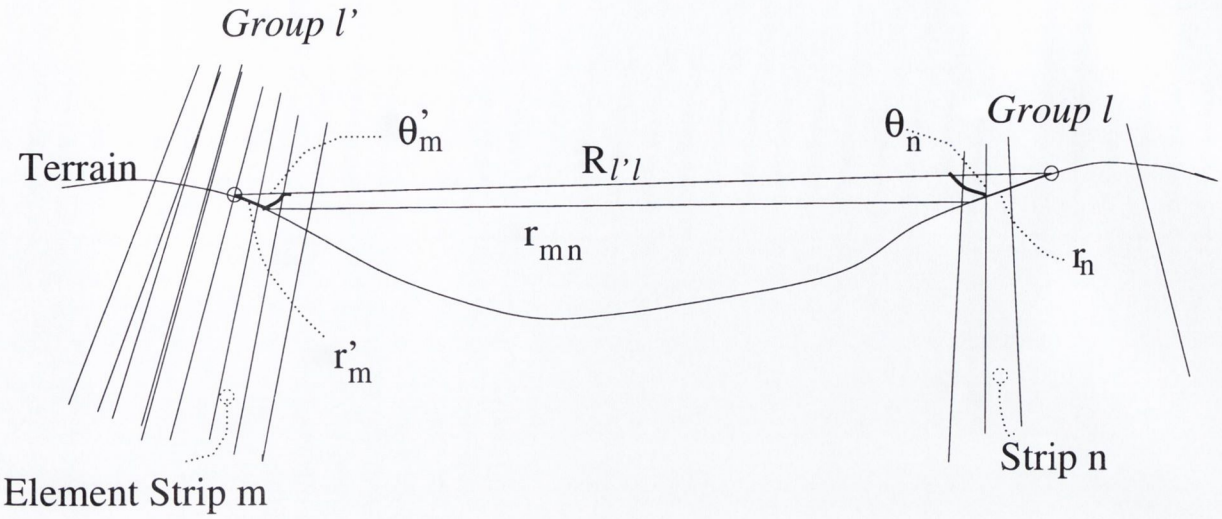


Figure 7-1: Grouping of inclined strip elements for Q3D FAFFA.

Having made this approximation to the phase variation in the interaction term, we further approximate the transverse gradient of all elements of group l' with the value of transverse gradient, $\frac{\partial \chi}{\partial y}$, at the central element of l'. In doing so, we are assuming small variation in the transverse gradients over a range of several meters, and this is reasonable. Hence, the complex vector $\tilde{\mathbf{R}}_{l'l}$, evaluated for the central point on group l', will be used to approximate $\tilde{\mathbf{r}}_{mn}$ for all points m in l', and observation points n in l.

The total field scattered to element n of group l from group l' may be given as

$$\mathbf{H}^s_{l'\,n} \approx -ik\Delta G_{l'l}\, e^{-ikr_n \cos\theta_n} \left(\tilde{\mathbf{R}}_{l'l} \wedge \sum_{m \in l'} e^{ikr'_m \cos\theta'_m} \mathbf{J}_m \right. \tag{7.5}$$

$$\left. -\frac{1}{\eta} \left(\tilde{\tilde{\mathbf{R}}}_{l'l} - \tilde{\mathbf{R}}_{l'l\,x} \cdot \right) \sum_{m \in l'} e^{ikr'_m \cos\theta'_m} \mathbf{K}_m \right) - \frac{k}{4\eta} \Delta e^{-ikr_n \cos\theta_n} H_{l'l} \sum_{m \in l'} e^{ikr'_m \cos\theta'_m} \mathbf{K}_m$$

where

$$\tilde{\tilde{\mathbf{R}}}_{l'l} = \begin{bmatrix} \tilde{R}_x & \tilde{R}_y & \tilde{R}_z \\ \tilde{R}_y & 0 & 0 \\ \tilde{R}_z & 0 & 0 \end{bmatrix}_{l'l}$$

and we are entitled to choose $\Delta_m = \Delta \, \forall \, m$ by appropriate choice of discretization.

Equation (7.5) forms the basis of the FAFFA algorithm. By comparison with FAFFA implementations in PEC EFIE problems [9], the range of validity of the approximation is less, as the approximation to the components of $\mathbf{r}$ and hence $\tilde{\mathbf{r}}$ is

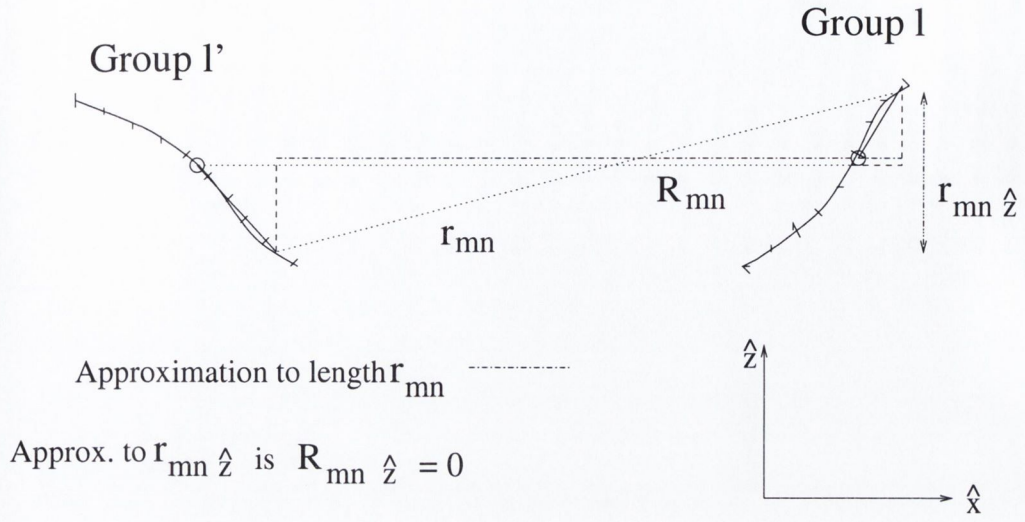


Figure 7-2: Error occurring in the approximation of $(\mathbf{r}_{mn})_{\hat{z}}$

weaker than the approximation to the phase of the Green's function. Considering the interaction depicted in Figure 7-2 the phase of the Green's function may be well approximated by (7.3), but the z component of $\mathbf{r}_{mn}$ will be approximated by zero in this case, as it will be for all $\mathbf{r}_{mn}$ connecting points m and n in groups l and l'. This error will be greatest in cases where both groups are at approximately the same elevation and $R_{l'l\,z} \approx 0$, but it will also be true that $r_{mn\,z}/r_{mn}$ is small, and so although the fractional error in the approximation to $r_{mn\,z}$ may be large, the overall fractional error in the approximation to $\mathbf{r}$ will be significantly smaller. Tests indicate that satisfactory results may be achieved where group sizes are restricted to less than 10 meters, for a gently undulating terrain. This will be true particularly when larger terrain features give the principal scattering contribution as opposed to small scale roughness.

7.2 Results

The FAFFA algorithm as applied to the Q3D approximation is tested against the full $\lambda/4$ resolution, forward scattering solution. Comparisons are made for two Danish terrain profiles [27](Figure 5-11 and Figure 7-3) exhibiting gentle terrain undulation. The measured *copolar* field is plotted in each case for completeness. The key

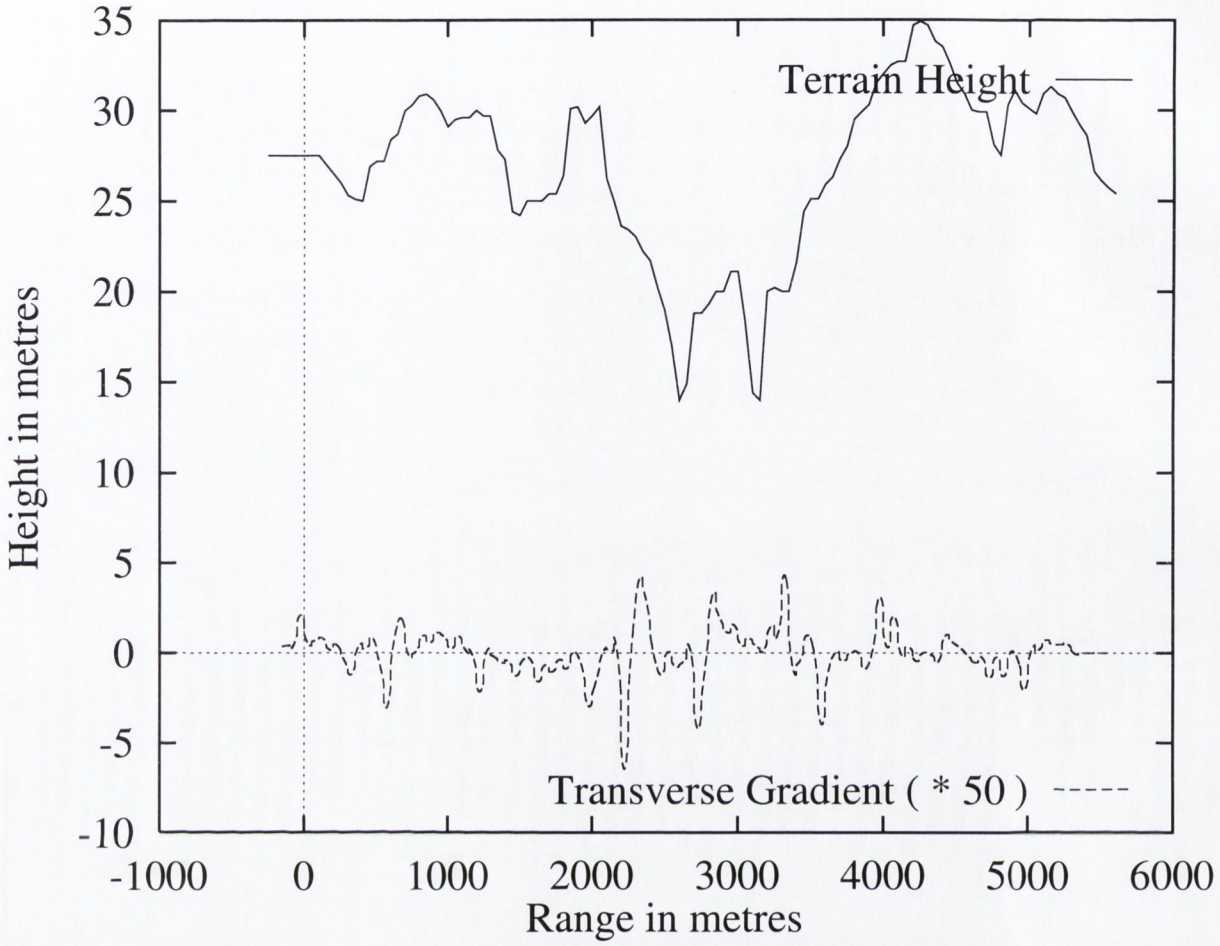


Figure 7-3: Jerslev profile and transverse gradient $\times 50$

comparison however, is between the exact Q3D, and Q3D FAFFA solutions. All simulations were carried out on an IBM RS6000, 266MHz work station, with Power II architecture. The comparisons in CPU time are given in Table 7.2 and Table 7.2.

The error arising between the Q3D FAFFA and the exact Q3D predictions is insignificant for the group sizes chosen in these examples. In fact the group sizes are perhaps somewhat conservative. Caution must be exercised however as the quality of the solution degrades rapidly if group size exceeds the Fraunhofer limit, with respect to the minimum separation between groups. Scattering from points within the minimum separation, must be calculated using the exact solution.

Hjorring	Frequency/MHz	Group Size	CPU (Exact)/s	CPU ((Faffa)/s
Figure 7-4	144	8	4342	629
Figure 7-5	435	16	36907	2539
Figure 7-6	970	32	183516	6385
Figure 7-7	1900	64	704105 (projected)	12046

Comparison of FAFFA and the exact Q3D methods for Hjorring terrain.

Jerslev	Frequency/MHz	Group Size	CPU (Exact)/s	CPU (Faffa)/s
Figure 7-8	144	8	1150	220
Figure 7-9	435	16	9962	799
Figure 7-10	970	32	49535	2170
Figure 7-11	1900	64	190015 (projected)	4823

Comparison of FAFFA and the exact Q3D methods for Jerslev terrain.

The effect of using larger group sizes is demonstrated in Figure 7-12 where comparison is made for the Hjorring terrain, between the exact Q3D method and a FAFFA implementation, taking group sizes of 256, at 970 MHz. In this case the run-time falls from 6385($N = 32$) to 1552 seconds and will only fall further to 1273 seconds for N=512. The fact that the saving is not greater than this is due to the considerable amount of time spent on the near field calculation. Performance can be greatly enhanced implementing a multi-level scheme to subdivide this large near field.

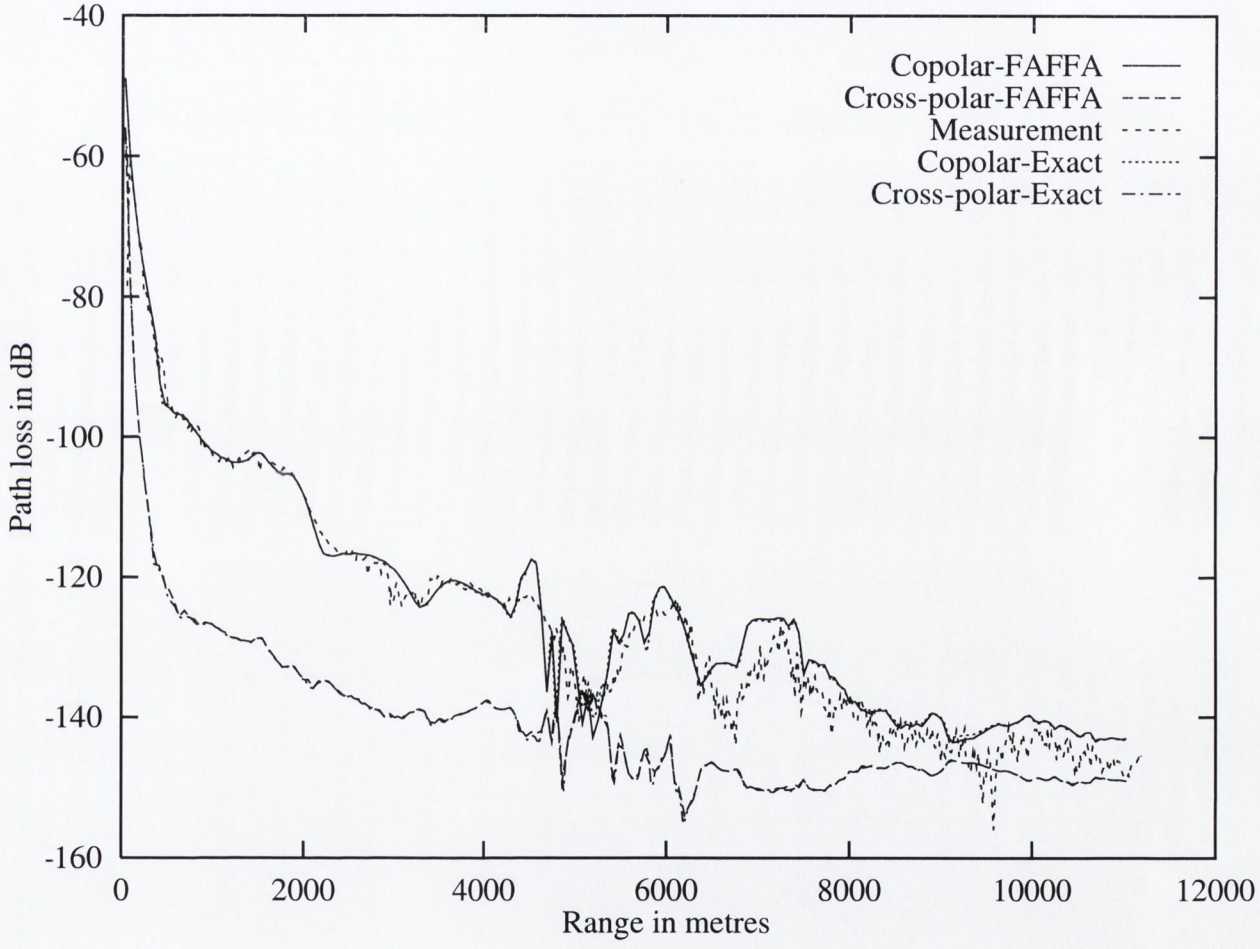


Figure 7-4: Hjorring profile at 144 MHz

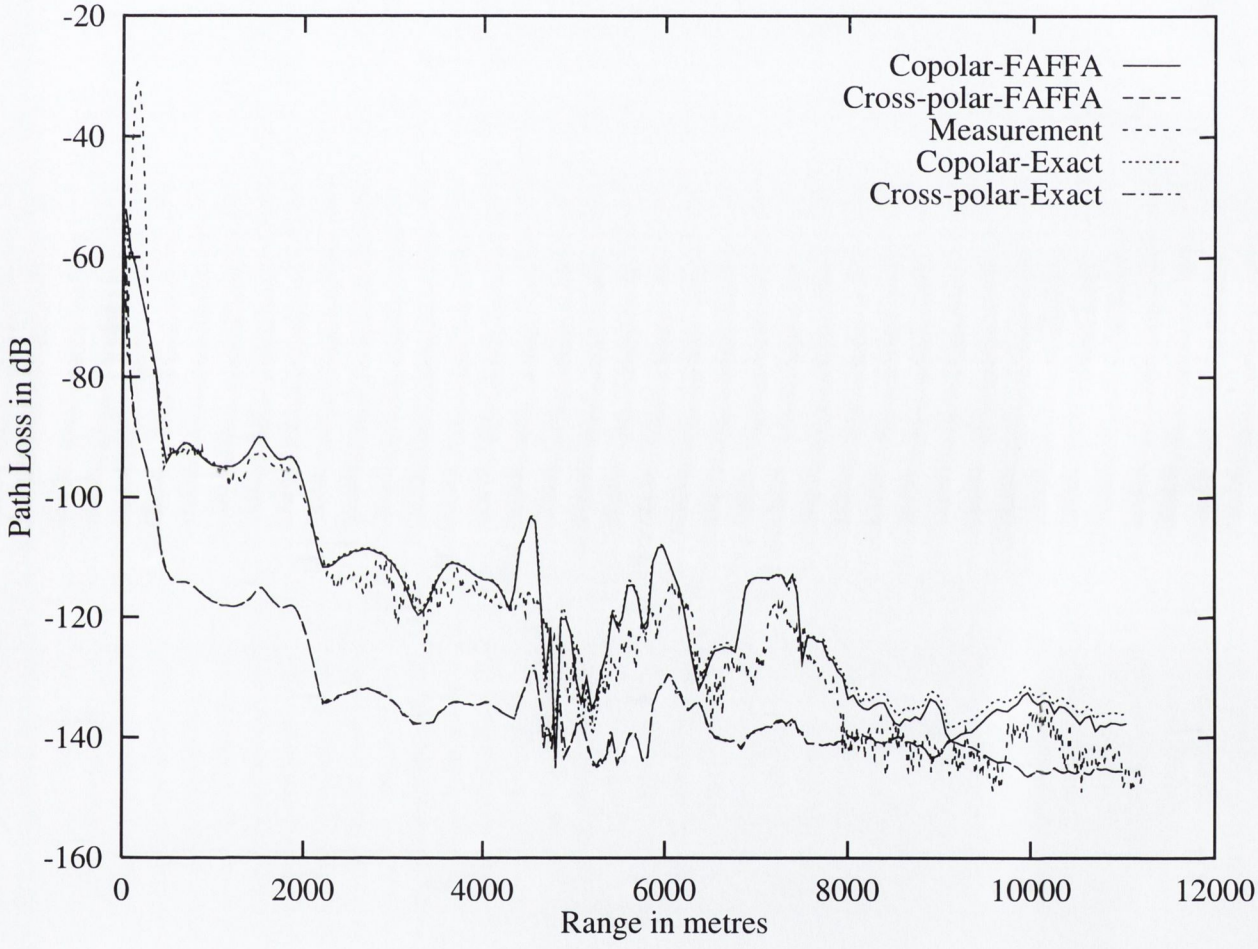


Figure 7-5: Hjorring profile at 435 MHz

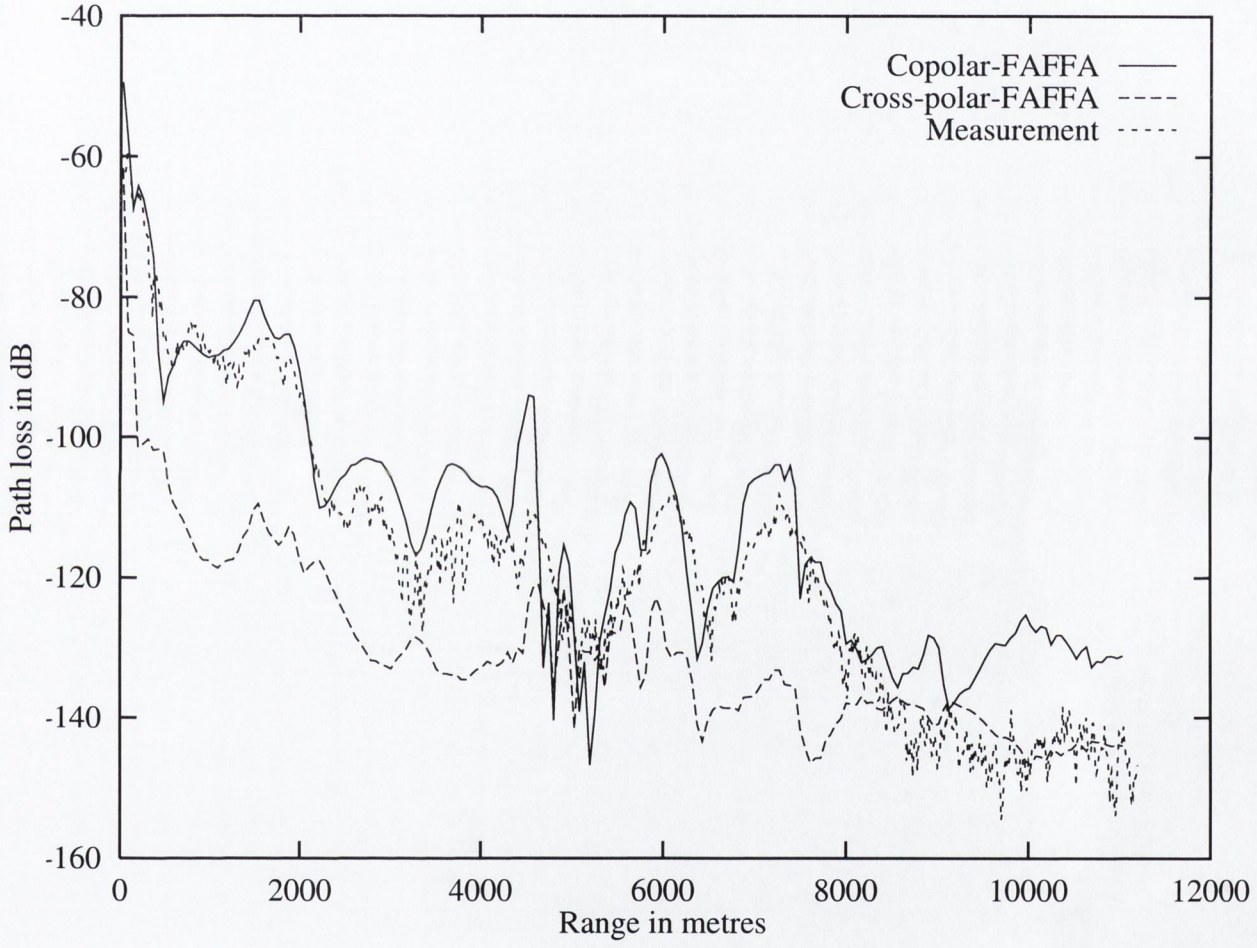


Figure 7-6: Hjorring profile at 970 MHz

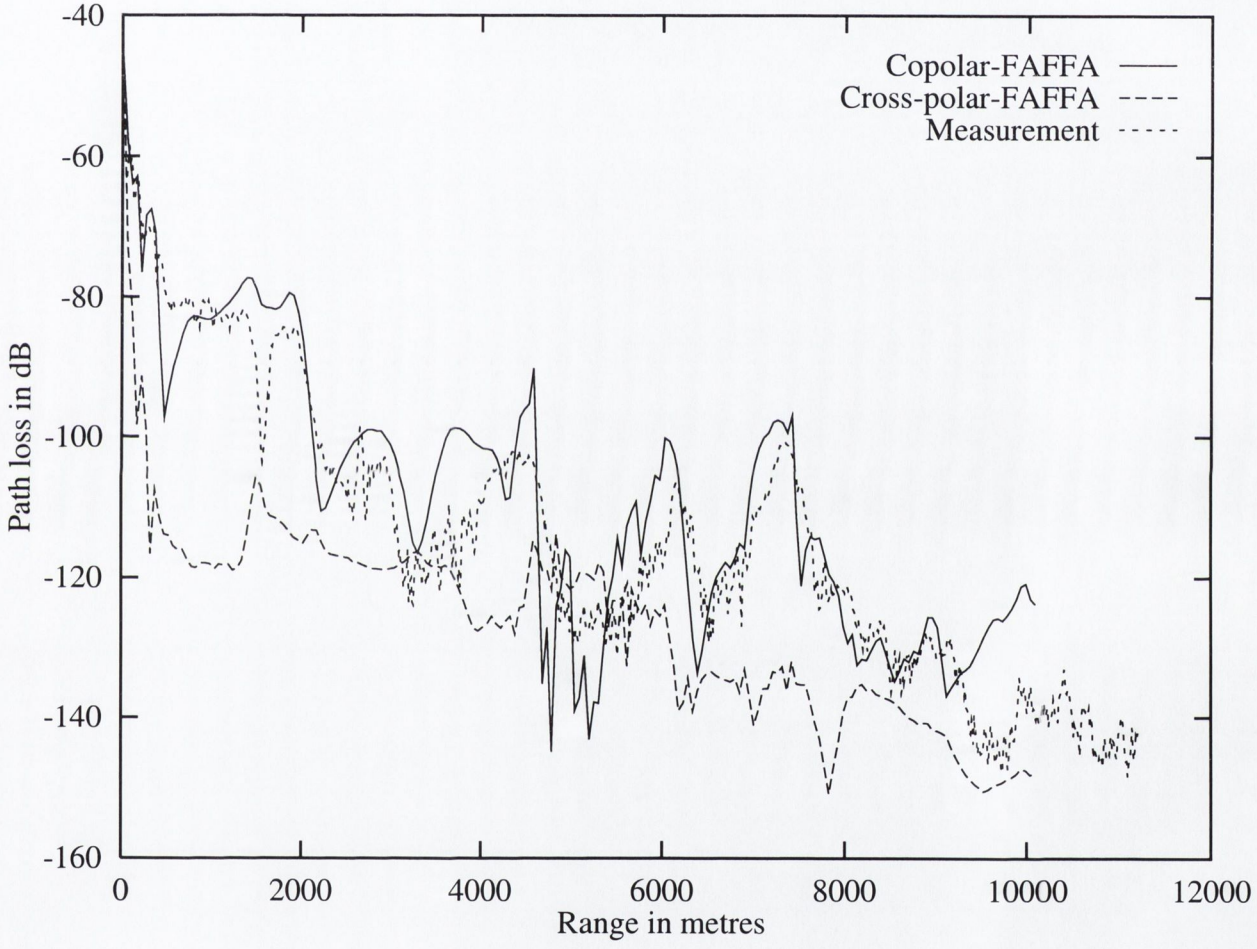


Figure 7-7: Hjorring profile at 1900 MHz

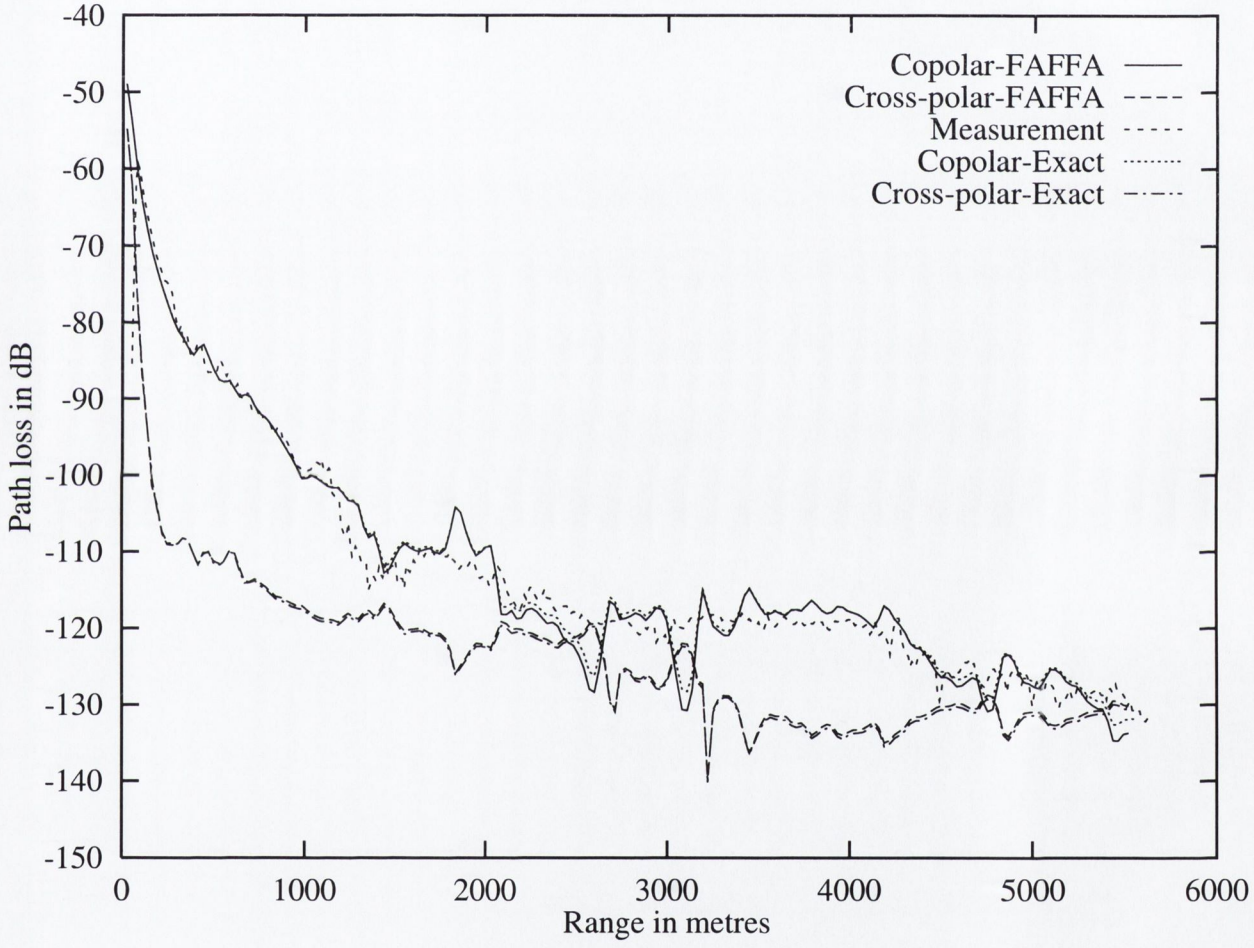


Figure 7-8: Jerslev profile at 144 MHz

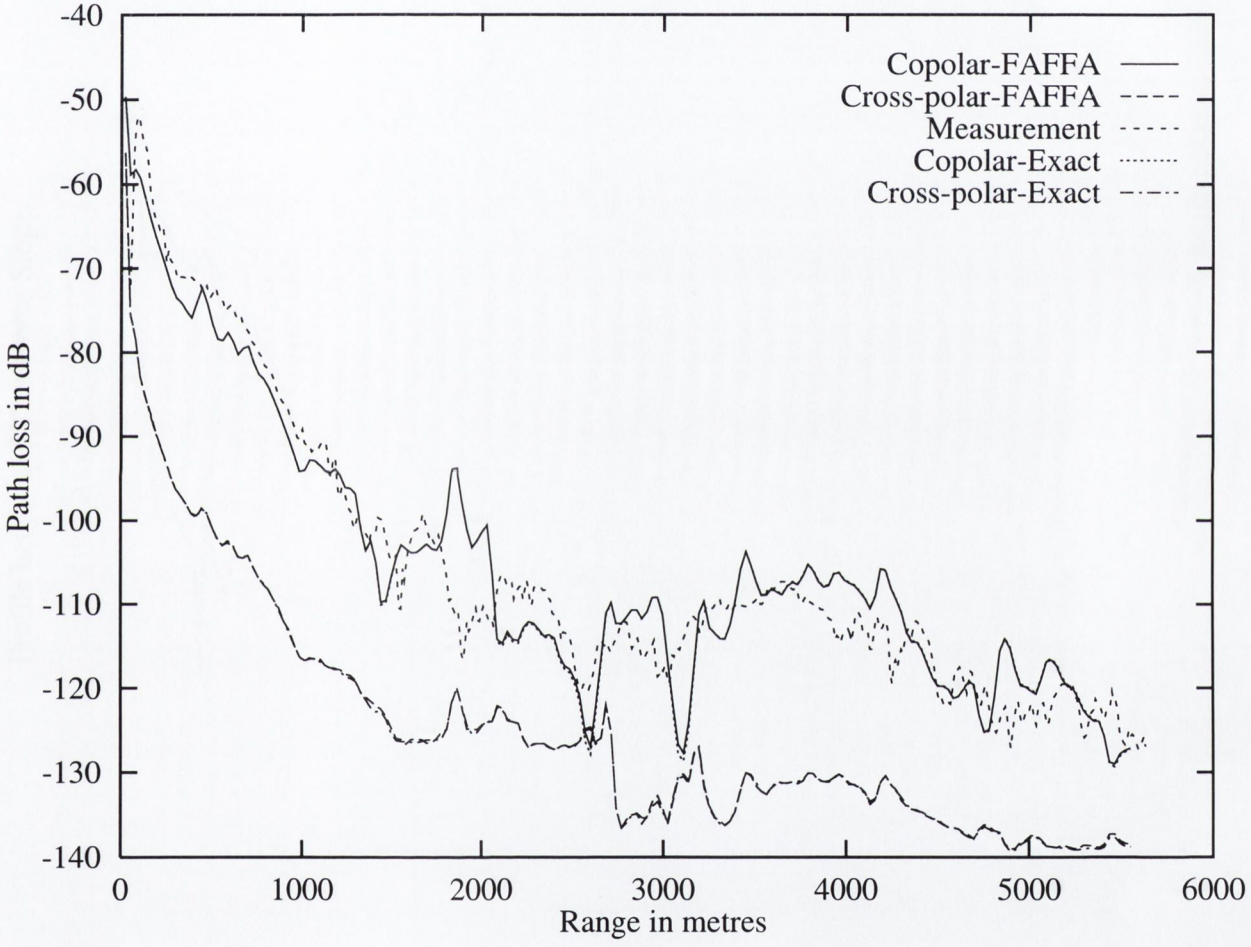


Figure 7-9: Jerslev profile at 435 MHz

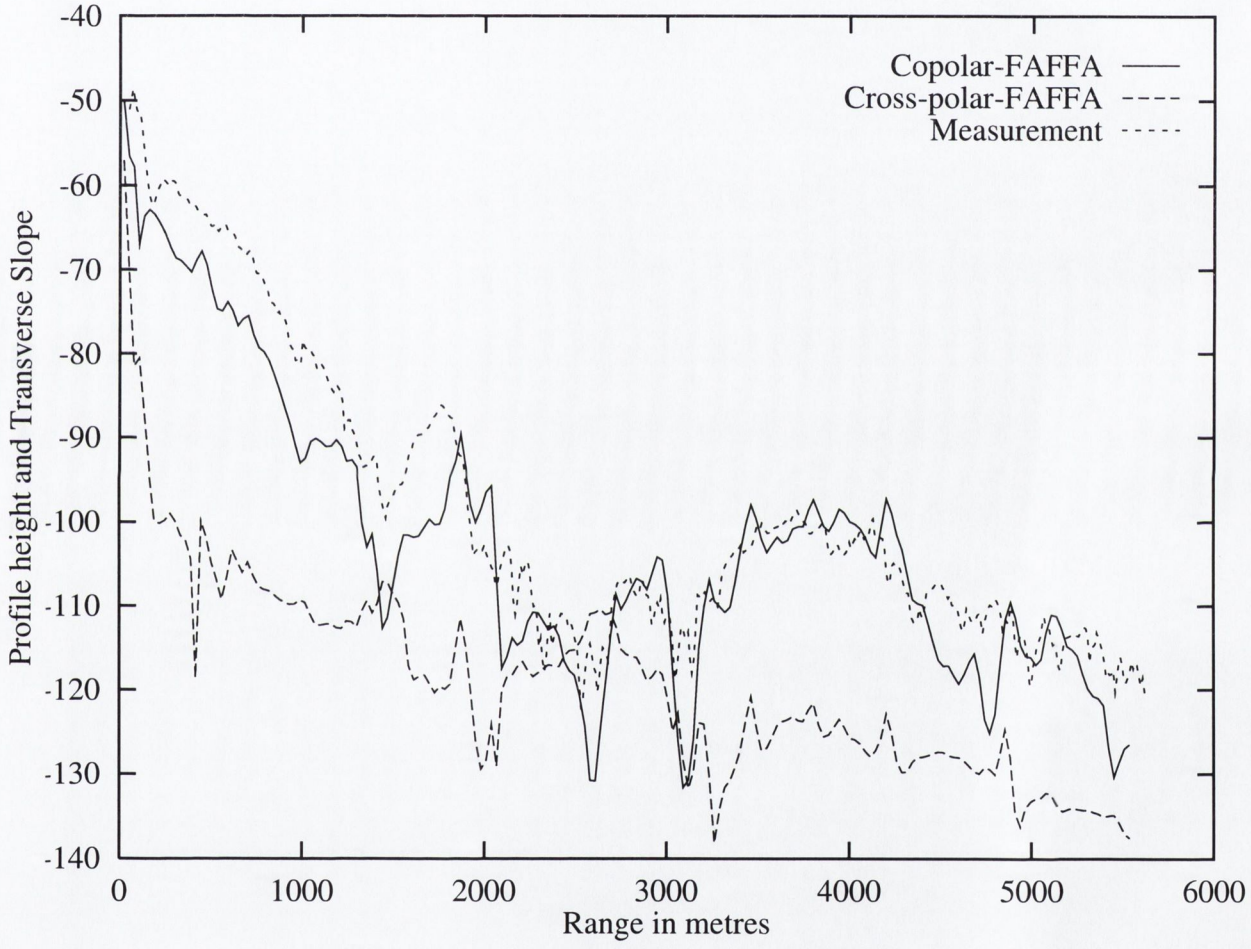


Figure 7-10: Jerslev profile at 970 MHz

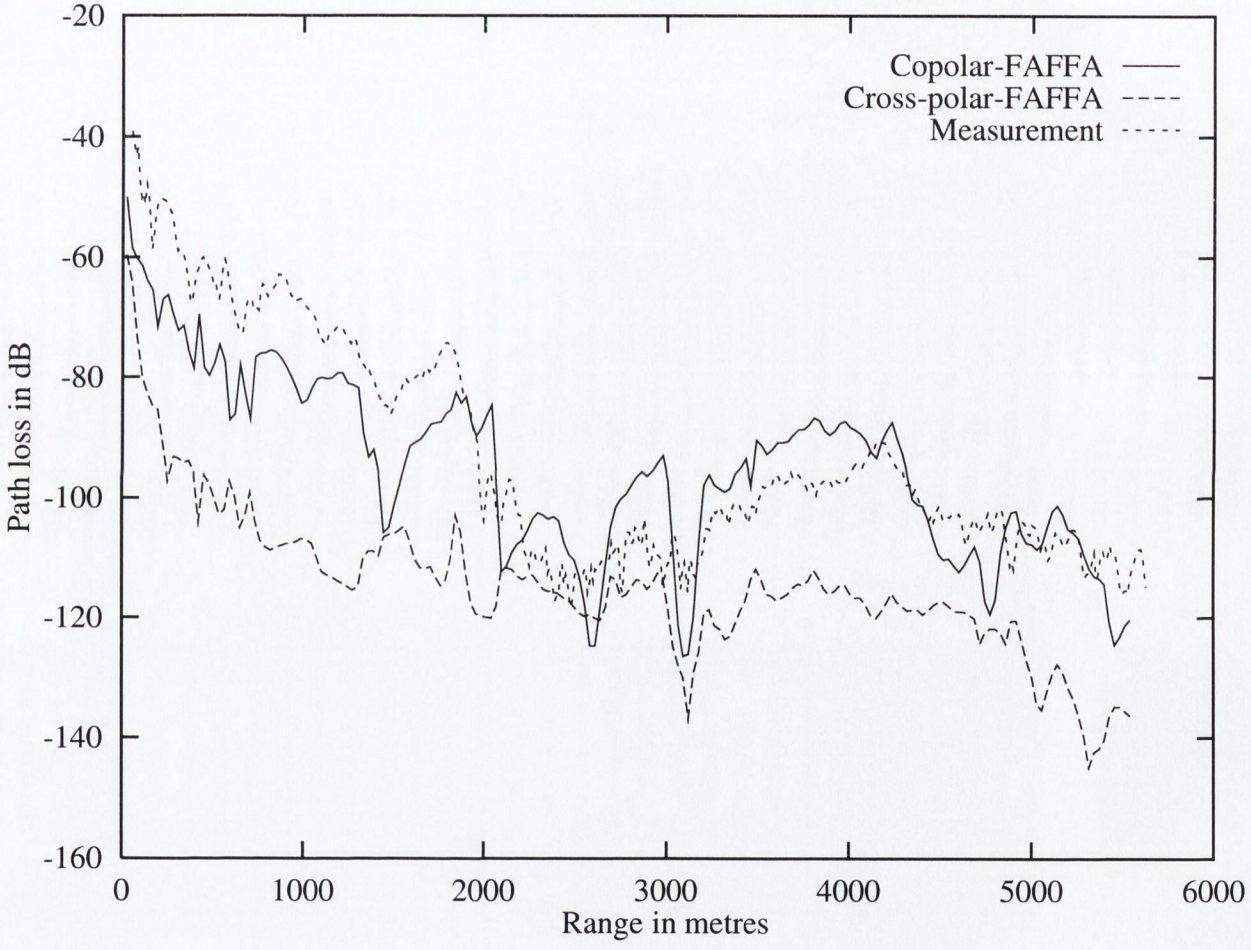


Figure 7-11: Jerslev profile at 1900 MHz

We note the error in the *copolar* fields towards the end of the profile. The *cross-polar* field is evidently somewhat less sensitive to the increase in group size, indicating that the Q3D interaction may be robustly incorporated into the FAFFA. In this example the error is small, and the solution quite acceptable but the terrain in question is relatively smooth. The tolerances will be reduced significantly on a harsher profile.

It is apparent that there is a systematic increase in error with frequency for these forward scattering solutions. For the profiles tested here, the author found no improvement in the coverage estimates, using the forward/backward iterative method. This indicates that the error at high frequency is not the result of slower convergence of the integral equation. Instead, it seems plausible that as frequency rises, the effect of smaller scale scattering features will come increasingly into play. Such detail is not included in the present IE scheme and this will give rise to an error, that will increase with frequency. This error might also be expected to increase with range as the effect of many such scatter events is multiplied. A related effect is scattering and attenuation by vegetation and and it is indicated [27] that measurements were carried out when there were still leaves on the trees. Such losses will again increase with frequency. It might also be worth including earth curvature on such smooth profiles, having height variations of only 30 metres.

7.3 Conclusions

The purpose of this section has been to demonstrate the viability of a FAFFA Q3D implementation. The simplest, single level, form of the scheme has been demonstrated, and although substantial improvements on run time are made, the FAFFA times are still somewhat excessive beyond 435 MHz. This may be alleviated using an optimal choice of group size or indeed, variable group size. Considering the comparative size of the error between the exact Q3D solution and the measured field, the level of agreement between Q3D FAFFA and exact Q3D need not be as high as in the examples shown here. The author also indicates that the codes used were developmental codes and might be implemented considerably more efficiently. The *cross-polar* field is calculated and shows excellent agreement with that predicted by

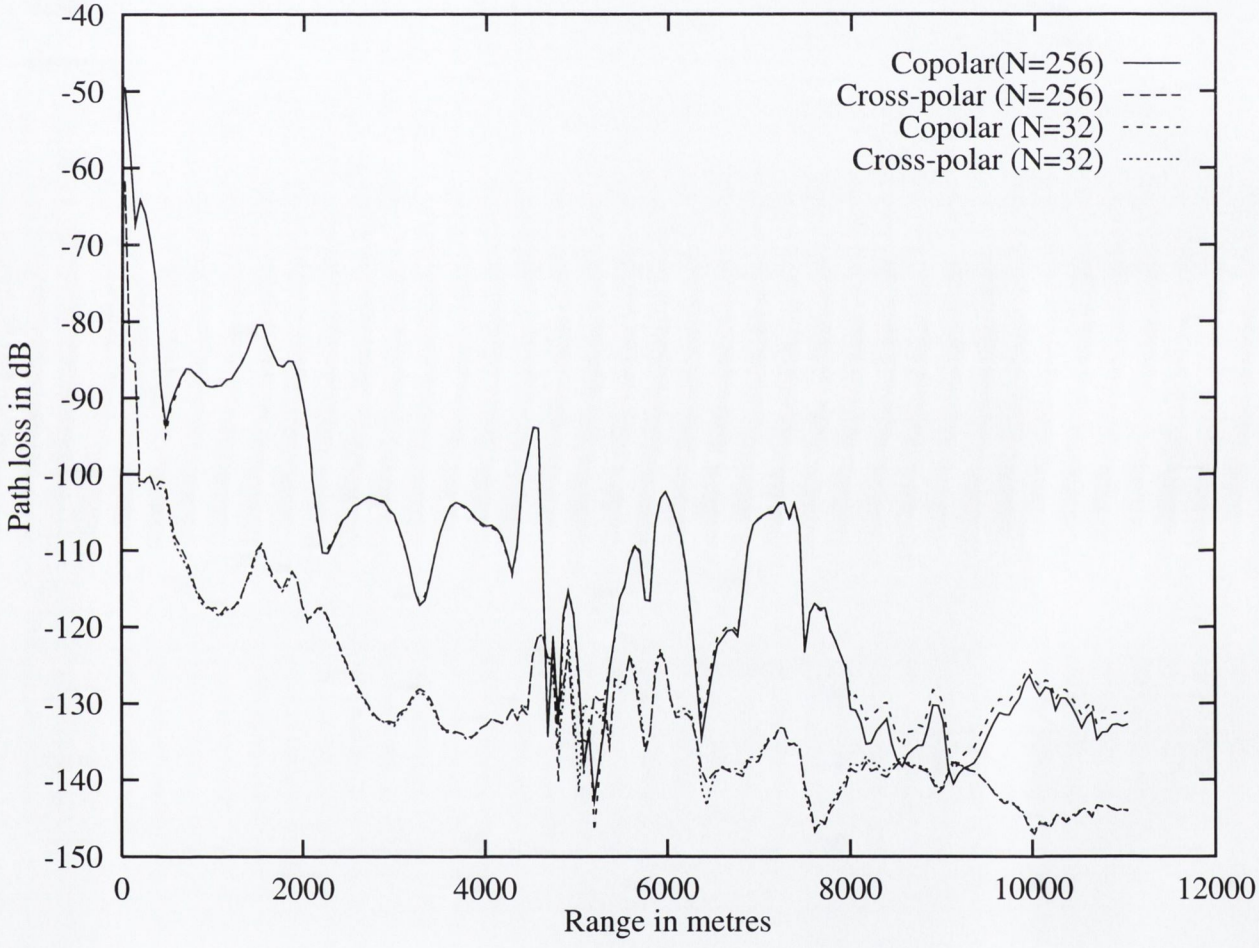


Figure 7-12: Hjorring profile at 970 MHz. Exact solution v Faffa: N = 256

the full Q3D solution.

More powerful methods than the FAFFA exist, for terrain propagation. The TIM [11] achieves solutions several hundred times faster than the FAFFA, for UHF problems with range $\approx$ 10km. By tabulating the field scattered from an arbitrarily inclined strip, having terrain type reflection characteristics, it seems plausible that a Q3D form of TIM would be possible. The size of the TIM plates would be necessarily limited however, by the discontinuities between successive TIM plates. The development of a Q3D TIM is the subject of further investigation.

Chapter 8

Discussion

A quasi three dimensional propagation modeling tool has been developed for UHF terrain problems. Rigorous three dimensional propagation models are still largely intractable due to heavy computational burden, and it has been necessary to make many approximations to capture even some of the features of a 3D terrain boundary. Scattering from terrain features off the axis of propagation is ignored, along with secondary terrain features such as buildings and vegetation. A surface approximation that creates a discontinuous boundary is introduced. Further approximations are made to the vector joining the scattering to the observation point, and to the plane of incidence of impinging field components at a surface match point. Nevertheless, these approximations are quite reasonable for undulating terrain. The alternative is in fact to ignore the presence of transverse terrain gradients altogether, and this is the conventional approach.

We have demonstrated that transverse gradients may be included in an integral equation propagation tool without a major increase in numerical complexity. Predictions indicate significant *cross-polar* scattering, particularly in geometrical shadow regions. It is intended that the technique be combined with more rapid integral equation solvers, such as the Tabulated Interaction Method[10], thereby reducing run times to the order of a few seconds, or less, depending on terrain height variation.

The author notes that the method is still some considerable way from tackling

the full three dimensional propagation problem, but believes that the first generation of rigorous 3D terrain integral equation models, will be derived by the direct extension of 2D radial models. The 2D radial approach has already be demonstrated to yield reasonable results, and characterizes the principal propagation path, that in the vertical plane connecting source and receiver. Making the 2D corrugated surface approximation denies us the opportunity of solving first for a set of radial paths, and subsequently adding in cross path scattering, as the corrugation removes the transverse gradients that cause this scattering. This shortcoming is not present in the Q3D model. The tangent plane to the surface at a radial match point is fully represented and the current vectors on the surface have three degrees of freedom[1].

The simplest approach would be to directly solve for the terrain surface currents with Q3D, for a set of terrain radials. The field strength over the terrain would then be calculated including contributions from a number of the nearest neighbour radials as depicted in Figure 8-1.

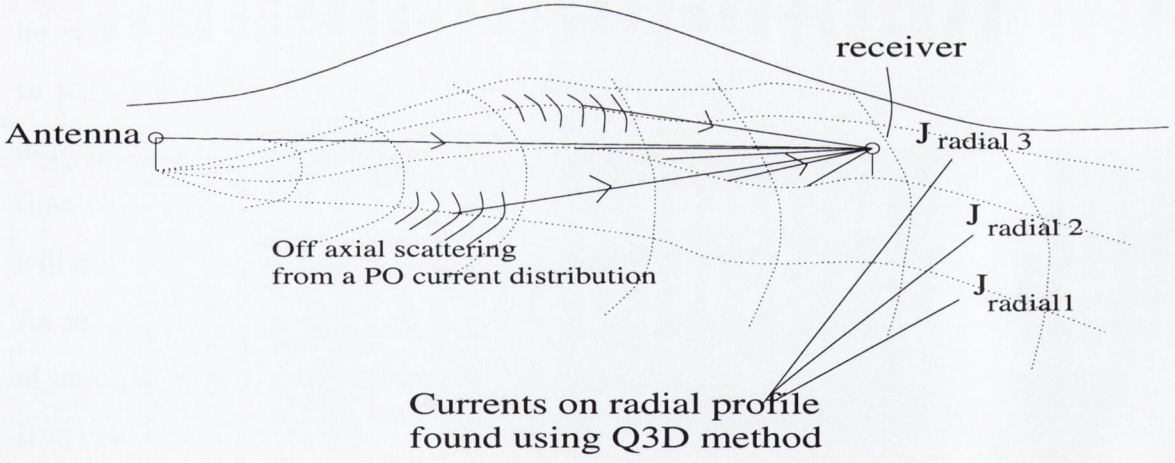


Figure 8-1: Contributions to scattered field from neighbouring terrain radials. The current on each radial found using the Q3D approach.

We observe that for terrain problems, off axial propagation will be very restricted and a single scattering off-axial model might be expected to deliver most of the possible benefits in anything other than very mountainous terrain. The means of calculating

[1]In the global sense. Locally the current vector is confined to the tangent plane

the field scattered from these adjacent radials is less clear. The current along the radial itself will be known. The next step may be to assume a physical optics phase variation in the current around the radial, allowing an area scattering integral to be formulated. Analytical expressions for the integral over a surface element will be required to avoid the large numerical integrations that prohibit conventional 3D integral equation methods. We note that analytical expressions may be formulated for the scattered field from a planar surface carrying a physical optics type current distribution[8][49][50]. Furthermore, it is conceivable that by making an intelligent search for the primary off-axial scattering regions, which may be found by appeal to GTD arguments, we may considerably limit the secondary integration. This is similar to the use of a stationary phase point search, although in this case the phase in the integrand at off-axial points may not in fact be stationary.

Further complications arise if off radial scattering contributions are included in the surface integral equation itself. The approximation made in Q3D that $k_y \ll 1$ will no longer be applicable, and a single incidence plane approximation will no longer be valid for the impinging field at a match point. In this case it will be necessary to satisfy a number of equations at a single match point, corresponding to fields impinging at different angular intervals[2]. The complexity increases when we consider that these impinging components excite currents at the match point element, that will not be adequately modeled within the physical optics phase front approximation. As set of PO current excitations will arise corresponding to the angular distribution of incoming waves.

It is evident that we have nearly arrived back at the low resolution method described in Chapter 3 section 3.10.3, where the terrain was modeled using large triangular elements, supporting a superposition of currents corresponding to plane wave physical optics excitations. That method however, fails to prioritise certain interactions. The author believes that the retention of the underlying radial propagation mechanism allows us to prioritize the strongest interactions. How much may be gained by the inclusion of multiple of axis scattering, is as yet unclear. It is clear that large

[2]The alternative is to solve the coupled integral equations where no approximate boundary condition is required

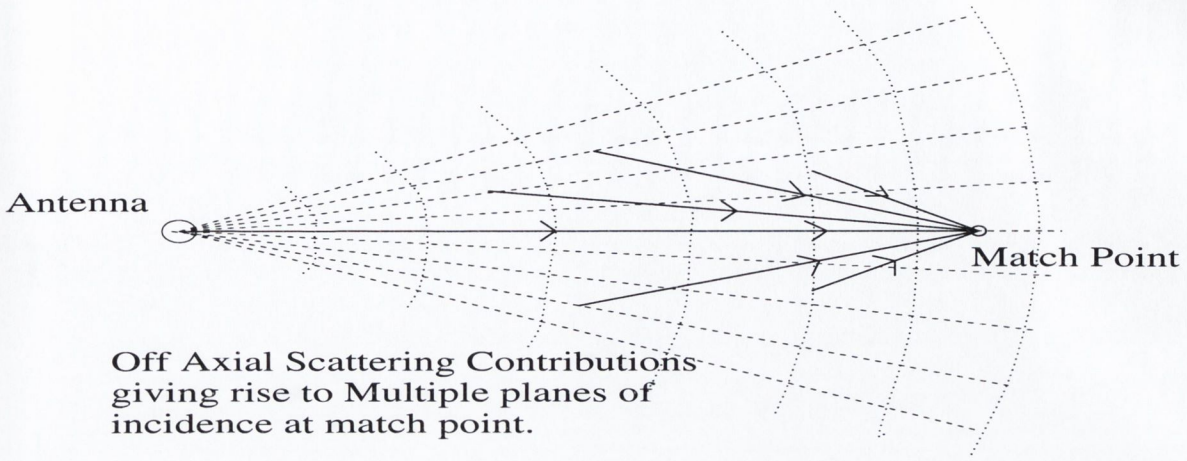


Figure 8-2: *Contributions to surface integral equation from neigbouring terrain radials. Current at match point found by satisfying boundary conditions for impinging components at a number of angular intervals, at each match point .*

scale three dimensional terrain scattering still represents a formidable computational problem, but considering the advances that have been made in numerical propagation modeling in only the last decade, it is a problem which will inevitably be overcome.

Bibliography

[1] M. Abramowitz and I. A. Stegun. *Handbook of Mathematical Functions.* New York, Dover, 1965.

[2] F. K. Akorli and E. Costa. An efficient solution of an integral equation applicable to simulation of propagation along irregular terrain. *IEEE Trans. AP*, Vol. 49, No. 7:1033–1036, 2001.

[3] B. B. Baker and E. T. Copson. *The Mathematical Theory of Huygen's Principle.* Clarendon, Oxford, 1950.

[4] C. Balanis. *Advanced Engineering Electromagnetics.* Wiley, 1989.

[5] R. H. Barfield. *Journal of the Institute of Electrical Engineers*, Vol 75:214, 1934.

[6] S. A. Bergman and H. W. Arnold. Polarization diversity in portable communications environments. *Electronics Letters*, Vol. 22:609–610, 1986.

[7] H. L. Bertoni. *Radio propagation for modern wireless applications.* Prentice Hall PTR ; London, 2000.

[8] M. Born and E. Wolf. *Principles of Optics*, volume 6th ed. Pergamon, New York, 1980.

[9] C. Brennan and P. Cullen. Application of the fast far field approximation to the compututions of uhf pathloss over irregular terrain. *IEEE AP*, 46 , 6:881–890, 1998.

[10] C. Brennan and P. J. Cullen. Multilevel tabulated interaction method applied to uhf propagation over irregular terrain. *IEEE Trans. AP*, 2000.

[11] C. Brennan and P. J. Cullen. Tabulated interaction method for uhf terrain propagation problems. *IEEE Trans. AP*, Vol. 46:738–739, May 1998.

[12] F. X. Canning. Improved impedance matrix localization method. *IEEE Trans. AP*, Vol. 41, No. 5:659–667, 1993.

[13] P. C. Clemmow. *The Plane-Wave-Spectrum Representation of Electromagnetic Fields.* Pergamon, New York, 1966.

[14] Jr. D. Holliday L.L. DeRaad and G.J.St.-Cyr. A new method for computing low grazing angle scattering. *IEEE AP*, 44:722–729, 1998.

[15] G.Brown D.A. Kapp. A numerical method for rough surface scattering calculations. *IEEE AP*, 44:711–721, 1998.

[16] G. D. Dockery and J. R. Kutler. An improved impedance-boundary algorithm for fourier split-step solutions of the parabolic equation. *IEEE Trans. AP*, Vol. 44, No. 12:1592–1599, 1996.

[17] L. B. Felsen and N. Marcuvitz. *Radiation and Scattering of waves.* Prentice-Hall, 1973.

[18] N. Patwari G. Durgin and T.S. Rappaport. An advanced 3d ray launching method for wireless propagation prediction. *IEEE 47th Vehicular Technology Conference(VTC) 1997, Phoenix, S*, pages 785–789, 1997.

[19] A. R. Nix G. E. Athanasiadou, E. K. Tameh. Channel impulse three-dimensional rural-urban simulator(citrus): an integrated micro-macro ray-based propagation model which employs raster and vector building databases simultaneously. *10th International Symposium on Personal, Indoor and Mobile Radio Communications*, Vol 3:1072–6, 1999.

[20] A. Glassner. *An Introduction to ray tracing.* Academic Press, San Diego, 1989.

[21] I. S. Gradshsteyn and I. M. Ryzhik. *Tables of Integrals Series and Products.* Academic Press, 1980.

[22] K. Hacking. Rf propagation over rounded hills. *IEE Proc.*, Vol. 117:499–511, 1970.

[23] R. H. Hardin and F. D. Tappert. Applications of the split-step fourier method to the numerical solution of nonlinear and variable coefficient wave equations. *SIAM Review*, Vol. 15:423, 1973.

[24] M. Hata. Empirical formulae for propagation loss in land modile radio services. *IEEE Trans. Vehicular Technology*, 29:317–325, 1980.

[25] J.D. Hoffmann. *Numerical Methods for Engineers and Scientists.* McGraw-Hill, New York, 1992.

[26] G.A. Hufford. An integral equation approach to the problem of wave propagation over an irregular surface. *Quarterly Appl. Maths*, 9:391–404, 1952.

[27] J.T. Hviid, J. Bach Andersen, J. Toftgard, and J. Boyer. Terrain-based model for rural area -an integral equation approach. *IEEE Transactions on Antennas and Propagation.*, 43 No. 1:41–46, 1995.

[28] A. S. Il'inskiy and G. Ya Slepyan. Impedance boundary conditions and their applications for calculating the absorption of electromagnetic waves in conducting media. *Scripta Technika, Soviet Journal of Communications Technology and Electronics*, Vol. 36, No. 6:118, 1991.

[29] Akira Ishimaru. *Electromagnetic Wave Propagation, Radiation, and Scattering.* Prentice Hall, 1991.

[30] G. L. James. *The Geometrical Theory of Diffraction for Electromagnetic Waves.* Peregrinus, 1976.

[31] U. Janaswamy. A curvilinear coordinate based split-step parabolic equation method for propagation predictions over terrain. *IEEE*, 46:1089–1097, 1998.

[32] M. A. Jensen. A recursive scheme for efficient modeling of inhomogeneous, penetrable objects. *Phys. Rev.*, 1997.

[33] J.T. Johnson, R. T. Shin, J. C. Eidson L., Tsang, and J. A. Kong. A method of moments model for vhf propagation. *IEEE AP*, 45 , 1:115–125, 1997.

[34] D. S. Jones. *The Theory of Electromagnetism*, volume Macmillan, New York. New York, Dover, 1964.

[35] L. W. Li K. Y. Kam, L. Y. Chew. Multipath propagation of radio waves in 3-dimensional terrain. *Journal of Electromagnetic Waves and Applications*, Vol. 15, No. 3:411–31, 2001.

[36] J. B. Keller. Geometric theory of diffraction. *Jnl. Optical Society of America*, 52:116–130, 1962.

[37] M. F. Levy K.H. Craig. Parabolic equation modelling of the effects of multipath and ducting on radar systems. *IEE Proc F*, 138:153–162, 1991.

[38] R.G. Kouyoumjian and P.H. Pathak. A uniform geometrical theory of diffraction for an edge in a perfectly conducting surface. *Proc. IEEE*, Vol 62, No.11:1448–1461, 1974.

[39] P. J. Cullen L. Rossi and C. Brennan. An analytical approximation of the tim look-up table. *COST259 TD(99) Meeting, Thessaloniki*, 1999.

[40] D. Lee, D. C. Resasco, M. H. Schultz, and F. Saied. A parallel 3d parabolic wave equation solver. *Theoretical and Computational Acoustics*, Vol. 2:627, 1994.

[41] W. C. Lee and Y. S. Yeh. Polarization diversity system for mobile radio. *IEEE Transactions on Communications*, Vol. Com-20:912–913, 1972.

[42] M. A. Leontovich. Method of solution for problems of electromagnetic wave propagation along the earth surface. *Bulletin of Academy of Sciences, USSR, Physical Series*, 1944:1622, Vol 8, No. 1.

[43] M. F. Levy. Diffraction studies in urban environment with wide-angle parabolic equation method. *Electronics Letters*, Vol. 28, No. 16:1491–1492, July, 1992.

[44] M. F. Levy. Parabolic wave equation techniques for radiowave propagation. *URSI Radio Science Bulletin*, No. 282:6–13, September 1997.

[45] C. C. Lu and W. C. Chew. A near-resonance decoupling approach for scattering solution of near resonant structures. *Center for Computational Electromagnetics, University of Illinois*, 1997.

[46] C.C. Lu and W.C. Chew. Fast far field approximation for calculating the rcs of large objects. *Micro. Opt. Tech. Lett.*, Vol. 8:pp.238–241., 1998.

[47] R.J. Luebbers. Propagation prediction for hilly terrain using gtd wedge diffraction. *IEEE AP*, Vol:32, 1984.

[48] A. R. Mitchell and D. F. Griffiths. *The Finite Difference Method in Partial Differential Equations.* Wiley, New York, 1980.

[49] K. Miyamoto and E. Wolf. Generalization of the maggi-rubinowicz theory of the boundary diffraction wave - part i. *Journal of the Optical Society of America*, Vol. 52, No. 6:615 – 625, 1962.

[50] K. Miyamoto and E. Wolf. Generalization of the maggi-rubinowicz theory of the boundary diffraction wave - part ii. *Journal of the Optical Society of America*, Vol. 52, No. 6:626 – 637, 1962.

[51] D. Moroney and P. J. Cullen. A fast integral equation approach to uhf coverage estimation. *Proc. of the 2nd Joint Cost 277/231 Workshop on Mobile and Personal Communications*, pages 343–350, April 1995.

[52] D. A. Mac Namara, C. W. I. Pistorius, and J. A. G. Malherbe. *Introduction to the Uniform Theory of Diffraction.* Artech House, 1990.

[53] Y. Okumura, E. Ohmori, T. Lawano, and K. Fukuda. Field strength and its variability in vhf and uhf land-mobile radio service. *Rec. Electronics Communications Laboratory*, Vol 16:825–873, 1968.

[54] G. Pelosi and P. Ya. Ufimtsev. The impedance-boundary condition. *IEEE Antennas and Propagation Magazine*, Vol 38, No1:31–35, 1996.

[55] E. Plouhinec, G. Chassay, B. Uguen, and T. Marsault. Study of multiple diffraction with a digital terrain model using a cascaded cylinder and knife-edge propagation model. *PIERS*, July 2000, Cambridge, Massachusetts.

[56] S. Wanzura R. Coifman, V. Rokhlin. The fast multipole method for the wave equation: A pedestrian description. *IEEE Antennas and Propagation Magazine*, Vol. 35, No. 3:7–12, 1993.

[57] G. Wolfe R. Hoppe and F.M. Landstorfer. Fast 3-d ray tracing for the planning of microcells by intelligent preprocessing of the data base. *3rd European Personal Mobile Communications Conference(EPMCC)*, 1999.

[58] A. F. Peterson S. L. Ray and R. Mittra. *Computational Methods for Electromagnetics.* IEEE Press, 1998.

[59] R.F.Harrington. *Field Computation by Moment Methods.* MacMillan, New York, 1968.

[60] V. Rokhlin. Rapid solution of integral equations of classical potential theory. *J. Computational Physics*, Vol. 60, No. 2:187–207, 1985.

[61] L. Rossi. Efficient methods for the computation of high frequency electromagnetic wave scattering from piecewise smooth surfaces using the integral equation formulation. *PhD Thesis, Trinity College Dublin*, 1999.

[62] L. Rossi and P. J. Cullen. An implementation of a multilevel fast far-field algorithm for solving electric field integral equations. *PIERS 99 Conference, Taipei*, March 1999.

[63] P. A. Sharples and M. J. Mehler. Cascaded cylinder model for predicting terrain diffraction loss at microwave frequencies. *IEE Proceedings*, Vol. 136, No. 4:331–337, August 1989.

[64] A. N. Shchukin. *Propagation of Radio Waves.* Svyazizdat, 1940.

[65] A. Sommerfeld. *Jber der D.M.V.*, Vol 21:309, 1912.

[66] J. M. Song and W. C. Chew. Multilevel fast-multipole algorithm for solving combined field integral equations for electromagnetic scattering. *Micro. Opt. Technol. Lett.*, Vol. 10, No. 1:14–19, 1995.

[67] J. M. Song, C. C. Lu, and W. C. Chew. Multilevel fast-multipole algorithm for electromagnetic scattering by large complex objects. *IEEE Trans. AP*, 1997.

[68] S. A. Torrico, H. L. Bertoni, and R. H. Lang. Modelling tree effects on path loss in a residential environment. *IEEE Trans. Antennas and Propagation*, Vol. 46:872–880, 1998.

[69] P. Ia. Ufimtsev. Approximate computation of the diffraction of plane electromagnetic waves at certain metal bodies. *Zh. Tekhn. Fiz. (USSR)*, Vol. 27, No. 8:1708–1718, 1957.

[70] R. G. Vaughn. Polarization diversity in mobile communications. *IEEE Transactions. Vehicular Technology*, Vol VT-39:177–186, 1990.

[71] L. E. Vogler. An attenuation function for multiple knife-edge diffraction,. *Radio Science*, Vol. 17 No. 6:1541–1546, November-December 1982.

[72] J. Walfish and H. L. Bertoni. A theoretical model of uhf propagation in urban environments. *IEEE Trans. Antennas and Propagation*, Vol. 36 No. 12:1788–1796, 1988.

[73] J. H. Whitteker. Fresnel-kirchhoff theory applied to terrain diffraction problems. *Radio Science*, Vol. 25 No. 5:837–851, 1992.

[74] A. A. Zaporozhest and M. F. Levy. Radar cross-section calculation with marching methods. *Electronics Letters*, Vol. 34 No. 20:1971–1972, Oct. 1998.

[75] C. A. Zelley and C. C. Constantinou. A three-dimensional parabolic equation applied to vhf/uhf propagation over irregular terrain. *IEEE AP*, 47, No 10:1586–1598, 1999.